TECHNISCHE UNIVERSITÄT MÜNCHEN

Lehrstuhl für Flugsystemdynamik

Precise Flight Trajectory Reconstruction Based on Time-Differential GNSS Carrier Phase Processing

Johannes Philipp Traugott

Vollständiger Abdruck der von der Fakultät für Maschinenwesen der Technischen Universität München zur Erlangung des akademischen Grades eines

Doktor-Ingenieurs

genehmigten Dissertation.

Vorsitzender: Univ.-Prof. Dr.-Ing. habil. Boris Lohmann.

Prüfer der Dissertation:
1. Univ.-Prof. Dr.-Ing. Dr. h. c. Gottfried Sachs (i.R.)
2. Priv.-Doz. Dr. rer. nat. habil. Oliver Montenbruck
3. Univ.-Prof. Dr.-Ing. Florian Holzapfel

Vorwort

Die vorliegende Arbeit entstand während meiner Tätigkeit als wissenschaftlicher Mitarbeiter am Lehrstuhl für Flugmechanik und Flugregelung (ab 2008: Lehrstuhl für Flugsystemdynamik) der Technischen Universität München in den Jahren 2005 bis 2010.

Ich danke dem Inhaber des Lehrstuhls für Flugmechanik und Flugregelung, Herrn Univ.-Prof. Dr.-Ing. Dr. h. c. Gottfried Sachs (i.R.) für die Anregung zu diesem Projekt, sein großes Interesse und die fortwährende Unterstützung der Arbeit. Ebenso gilt mein Dank Herrn Univ.-Prof. Dr.-Ing. Florian Holzapfel, der mir eine Fortführung der Arbeit am Lehrstuhl für Flugsystemdynamik ermöglichte. Sehr bedanken möchte ich mich bei Herrn Priv.-Doz. Dr. rer. nat. habil. Oliver Montenbruck vom GSOC des DLR in Oberpfaffenhofen. Durch unzählige Ratschläge und durch die Bereitstellung einer Navigations-Bibliothek unterstützte er mich wesentlich bei der Entwicklung des vorgestellten Navigationsverfahrens. Herrn Univ.-Prof. Dr.-Ing. habil. Boris Lohmann danke ich für die Führung des Prüfungsausschusses.

Mein Dank gilt auch allen Kollegen am Lehrstuhl für ihre Unterstützung und Hilfsbereitschaft sowie die stets angenehme und kreative Arbeitsatmosphäre.

Des weiteren gilt mein Dank Frau Dr. Anna Nesterova und Herrn Dr. Francesco Bonadonna vom Centre d'Ecologie Fonctionelle et Evolutive in Montpellier. Ohne ihre Hilfe hätte die Vermessung des Fluges von Albatrossen unmöglich realisiert werden können.

Bei den Firmen e-obs, TechnoSmArt und Art-of-Technology bedanke ich mich für die Unterstützung in allen Hardware Angelegenheiten. Auch diese Hilfe war von zentraler Bedeutung für das Gelingen des "Projektes Albatros".

Mein Dank gilt Susanne, die mich während der gesamten Arbeit nach Kräften unterstützte und sich selbst durch meine monatelange Expedition zu den Albatrossen nicht davon abhalten ließ mich zu heiraten!

Besonders danken möchte ich meinen Eltern. Sie haben mich (nicht erst) während der Jahre meiner Ausbildung auf vielfältige Weise unterstützt und gefördert.

Garching, im Oktober 2010   Johannes Traugott

Zusammenfassung / *Abstract*

Die Entwicklung eines Ortungsverfahrens zur präzsisen Flugbahnvermessung mittels miniaturisierter GNSS (GPS) Empfänger ist das erste Ziel der vorliegenden Arbeit. Hierbei gilt es eine Möglichkeit zu schaffen, hohe relative Präzision zu erreichen, ohne dabei auf einen zweiten, nahe gelegenen Referenzempfänger (D-GPS) und (statische) Initialisierungsphasen angewiesen zu sein. Dies wird durch die Entwicklung und Implementierung eines zeitdifferentiellen, L1 trägerphasenbasierten Ansatzes zur Relativpositionierung erreicht. Die Arbeit beinhaltet eine umfassende Untersuchung des Verfahrens: Die grundlegenden mathematischen Beziehungen werden dargelegt, theoretische Aspekte der Fehlerfortpflanzung werden hergeleitet, ein effizienter Algorithmus zur Integritätsüberwachung wird vorgestellt und die Auswertung verschiedener (Flug-)Versuche erlaubt eine praxisrelevante Validation. Das entwickelte Verfahren bietet dezimetergenaue Relativpositionierung und eröffnet damit ein breites Spektrum an Einsatzbereichen.

Dies ist die Grundlage für das Erreichen des zweiten zentralen Zieles dieser Arbeit: die Vermessung von Flugbahnen wild lebender Albatrosse mit einer Präzision und Auflösung, die eine lokale flugmechanische Analyse des dynamischen Segelfluges der Vögel ermöglicht. Die Kombination des im Feld sehr einfach umsetzbaren Zeitdifferenzen-Verfahrens (kein zweiter Empfänger, keine Initialisierung) mit der Anwendung miniaturisierter und widerstandsfähiger Hardware ermöglichte erstmals die Umsetzung eines solchen Vorhabens. Der dynamische Segelflug bietet durch ein hohes Maß an Energieeffizienz interessante Perspektiven auch für technische Anwendungen. Mit der energetischen und flugmechanischen Auswertung einzelner geschlossener Flugzyklen der Albatrosse wird ein Beitrag zur Erforschung der bis heute umstrittenen Mechanismen dieses faszinierenden Fluges geleistet.

The development of a positioning approach based on miniaturized GNSS (GPS) receivers for precisely measuring flight trajectories is the first of the two central objectives of the present work. This development is striving to realize high relative precision while overcoming the need for a second nearby base receiver (D-GPS) or any kind of (static) initialization patterns. This goal is achieved by the design and implementation of a relative positioning method based on processing time-differences of raw L1 carrier phase observations. This monograph provides a comprehensive analysis of the time-difference method: The core equations are exposed, theoretical aspects of error propagation are discussed, an efficient integrity monitoring algorithm

is presented and the evaluation of various (flight) tests allows for an elaborate practical validation. Offering decimeter precision, the time-difference positioning method opens up a wide range of applications.

This is the basis for the achievement of the second central objective: the measurement of flight trajectories of feral Wandering Albatrosses with a precision and resolution sufficient for locally analyzing the dynamic soaring flight of the birds from a flight mechanical point of view. Only the combination of the time-difference method, which is easy to apply even in adverse field conditions (no second receiver, no initialization) with the use of miniaturized and rugged hardware firstly allowed the realization of a suchlike project. The efficiency of the dynamic soaring flight reveals interesting perspectives also for technical applications. With the in-depth energetic and flight mechanical analysis of individual closed flight cycles a contribution is made to a better understanding of the mechanisms underlying this fascinating flight.

Contents

x

List of Figures

List of Tables

Symbols and Abbreviations

Symbols, Sub- and Superscripts

The used units correspond to the International System of Units (BIPM, 1998). The numerical values of physical constants agree with Mohr and Taylor (2005) if not indicated differently.

Symbol			Unit	Dim.	Description
Latin					
$\mathbf{b}^{bi}$	=	$\mathbf{x}_i^R - \mathbf{x}_b^R$	m	3×1	Base vector
c	=	299,792,458.0	m/s	1×1	Speed of light in vacuum; signal propagation speed
$\mathbf{C}$				$m \times n$	Covariance matrix
D			m/s	1×1	Doppler range rate
D			N	1×1	Drag
$\mathbf{e}$			-	3×1	Unit vector
E			m	1×1	Satellite ephemeris error
E_{tot}^*			m	1×1	Specific total energy
f^j				1×1	Residual of the jth observation
f_0	=	10.23	MHz	1×1	GPS base frequency
f_1	=	1.57542	GHz	1×1	Frequency of the L1 carrier
f_2	=	1.22760	GHz	1×1	Frequency of the L2 carrier
f_D			Hz	1×1	Doppler frequency shift
g	=	9.81	m/s²	1×1	Normal gravity
h			m	1×1	Height
$\mathbf{H}$			-	$m \times n$	Jacobian (m satellites in view, $n = 4$)
I			m	1×1	Ionospheric refraction
$\mathbf{I}$			-	$m \times m$	Identity matrix
L			N	1×1	Lift
m			m	1×1	Range error due to multipath
m			kg	1×1	Mass
$\mathbf{M}_{AB}$			-	3×3	Rotation matrix: $(\mathbf{r})_A = \mathbf{M}_{AB}(\mathbf{r})_B$
N			cycles	1×1	Integer ambiguity
N'			cycles	1×1	Ambiguity
Q			N	1×1	Side force
R			m	1×1	Pseudorange (C/A code)
t			s	1×1	(GPS system) time
t			s	1×1	Clock reading

Symbol			Unit	Dim.	Description
T			m	1×1	Tropospheric refraction
T_m			s	1×1	Raw data measurement rate
$\mathbf{v}$	$=$	$(u,v,w)^T$	m/s	3×1	Kinematic velocity relative to and indicated in the E-frame. Corresponding elaborate notation: $(\mathbf{v}_K)_E^E = (u_K, v_K, w_K)_E^{E\,T}$
$\mathbf{x}$	$=$	$(x,y,z)^T$	m	3×1	Position vector indicated in the E-frame. Corresponding elaborate notation: $(\mathbf{x})_E = (x,y,z)_E^{\,T}$
Greek					
$\boldsymbol{\beta}^{bi}$	$=$	$\boldsymbol{\xi}_i - \boldsymbol{\xi}_b$	m	4×1	Base vector enhanced by receiver clock error
γ_{idx}			rad	1×1	Flight path inclination; type of angle (idx): A – aerodynamic; K – kinematic
δ			s	1×1	Clock offset from GPS system time. $\delta > 0 \leftrightarrow$ clock reading *ahead* of GPS system time
ε			m	1×1	Range error due to measurement noise
ζ			°	1×1	Satellite elevation ($90° \leftrightarrow$ zenith)
λ_1	$=$	0.1903	m	1×1	Wavelength of the L1 carrier
λ_2	$=$	0.2442	m	1×1	Wavelength of the L2 carrier
μ_{idx}			rad	1×1	Bank angle; type of angle (idx): A – aerodynamic; K – kinematic
$\boldsymbol{\xi}$	$=$	$(x^R, y^R, z^R, c\delta^R)^T$	m	4×1	Receiver position and clock error
ρ			m	1×1	Geometric range
$\sigma^2; \sigma$				1×1	Variance; standard deviation
φ			cycles	1×1	Phasing of a wave signal
ϕ			cycles	1×1	Beat phase of a wave signal
Φ			m	1×1	Carrier phase range
χ			m	1×1	Range error
χ_{idx}			rad	1×1	Flight path azimuth; type of angle (idx): A – aerodynamic; K – kinematic

Sub- and Superscripts			Description
$\dot{x}$	$=$	$\frac{dx}{dt}$	Time derivative
$\widehat{x}$			Model, computed value
$\widetilde{x}$			Observation, measured value
x^R, x^S			Receiver, satellite referred value
x_i	$=$	$x(t_i)$	Time / epoch referred value
^{bi}Dx	$=$	$x_i - x_b$	Time-difference of x
$\left(\mathbf{r}^G\right)_A$			Vector pointing from the center of the earth to point G; components indicated in the A-frame
$\left(\mathbf{v}_{idx}^G\right)_A^B$	$=$	$\left(\frac{d}{dt}\right)^B \left(\mathbf{r}^G\right)_A$	Velocity of point G relative to the B-frame; components indicated in the A-frame; type of velocity (idx): A – aerodynamic; K – kinematic; W – wind.
$\left(\mathbf{a}_{idx}^G\right)_A^{BC}$	$=$	$\left(\frac{d}{dt}\right)^C \left(\mathbf{v}_{idx}^G\right)_A^B$	Acceleration of point G relative to the B and C-frame; components indicated in the A-frame; type of acceleration (idx): compare velocity.
$\left(\mathbf{F}_{idx}^G\right)_A$			Force acting in point G; components indicated in the A-frame; type of force (idx): A – aerodynamic; G – gravitational

Abbreviations

Abbreviation	Description
C/A, C1	Coarse Acquisition code, modulated on the L1 carrier wave
C/N_0	Signal to noise ratio
CTL	Carrier tracking loop
DLL	Delay lock loop
DoF	Degree of freedom
DOP	Dilution-of-precision
RF	Radio frequency
GNSS	Global Navigation Satellite System
GPS	NAVSTAR Global Positioning System
IGS	International GNSS Service, http://igscb.jpl.nasa.gov
IMU	Inertial measurement unit
INS	Inertial navigation system
MEMS	Microelectromechanical systems
PDF	Probability density function
PLL	Phase lock loop
PRN	Pseudo random noise code modulated on the carrier signal
PSD	Power spectral density function
PT	Position and time
PVT	Position, velocity and time
RAIM	Receiver autonomous integrity monitoring
RMS	Root mean square
RTK	Real-Time-Kinematic
SP(P)	Single-point processing
SPS	NAVSTAR GPS standard positioning service
SV	Satellite vehicle
SVN	Satellite vehicle number
TEC	Total electron count
TD	Time-differential (solution)
ZBL	Zero-baseline

1 Introduction

1.1 Motivation – Dynamic Soaring of Albatrosses

The fascinating soaring flight of albatrosses and other large sea birds is a phenomenon which has attracted the attention of both mariners and researchers from the very beginning of navigation. In the absence of any vertical (thermal) upwinds the birds manage to stay aloft without flapping their large wings.

Figure 1.1: Wandering Albatross (*Diomedea exulans*) soaring through the skies of Kerguelen Archipelago.[1]

Modern research proved that they do so at virtually no cost – Wandering Albatrosses have been observed to perform sustained high speed flights while expending little more energy than birds resting on land (Weimerskirch et al., 2000). This ability allows the animals to achieve remarkable flight performances. Birds covering distances as far as 15,200 km in a single foraging trip have been reported (Jouventin and Weimerskirch, 1990) and migration flights exceeding 25,000 km are known (Tickell, 2000, p. 141). Albatrosses primarily populate the southern hemisphere at latitudes where strong winds prevail ("Roaring Fourties" and "Furious Fifties"). These winds are the precondition for their flight near to the water surface and the birds are able to pursue their trips even during severe Antarctic storms (Catry et al., 2004).

---

[1]All photographs without explicit reference indication are taken by the author.

All these interesting observations mainly stem from measurement campaigns aiming to understand the global distribution of the highly endangered birds, their large scale migration trips (BirdLife Int., 2004) and their foraging patterns (Weimerskirch et al., 2002). Much of the data was collected using the ARGOS system (Argos, 2008) but also GPS data logging continuously gains importance in tracking albatrosses. However due to insufficient precision and low sampling rates very little experimental data is available today which allows to analyze the fundamental mechanisms of the birds' dynamic soaring maneuvers from a sound flight mechanical point of view. The theory of soaring in seabirds is a controversially discussed subject and explanations given in the literature reach from the concept of wind-gradient soaring (Denny, 2009) over gust soaring (Pennycuick, 2008) to wave soaring (Tickell, 2000). A more comprehensive literature review concerning this topic is provided by Sachs (2005). Recurring to stringent optimization methodology and simulation studies, this reference shows that the primary energy gain mechanism for dynamic soaring in albatrosses is the difference of the wind speed encountered by the birds when moving in the boundary layer close to the water surface. Within the complex maneuver the upper curve is identified to be of central importance for the flight. Figure 1.2 shows a typical dynamic soaring trajectory as dropping out of the optimization algorithms.
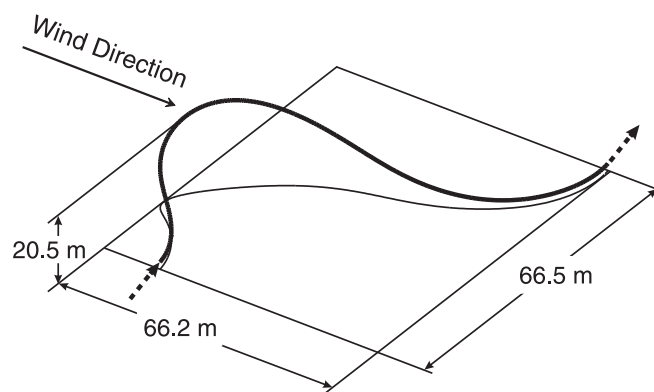
Figure 1.2: Simulation result of a typical dynamic soaring cycle of an albatross (Sachs, 2005)

Firstly collecting real in-flight measurements with a precision and sampling rate sufficient to contribute to (and to resolve) the flight mechanical controversy about dynamic soaring in albatrosses was one of the central objectives of the present project. Due to difficult field conditions this task is challenging from the perspective of positioning: The geometry of the maneuver requires precision in the decimeter range especially in the vertical direction. Typical cycle times were expected to be about 10 s. In conjunction with the high (vertical) dynamics of the birds this demands for appropriately high sampling rates. Here a minimum of 10 Hz was considered to be necessary. Flight-testing of "common" aircraft is a rather difficult matter. Having to deal with living creatures prevailing under harsh environmental conditions adds ad-

ditional complexity to this task. Mounting any kind of equipment on an albatross is not trivial. The task was conducted according to Wilson et al. (1997) and inevitably causes severe signal shadowing by the field workers – if GPS is used as was the case in the present project. Once the receiver deployed on the bird there is no guarantee that the animal remains static during a specified time interval. Hence static initialization procedures as required by most highly precise differential GPS (RTK) applications cannot be provided. Furthermore such differential techniques are limited to distances (baselines) between the base and the roving receiver not exceeding 10 km. Considering the large distances covered by foraging albatrosses, such baseline limitations would prevent the measurement of cycles flown far off-shore. Wandering Albatrosses forage in very remote areas. In the present project individual birds were equipped during the breeding season at Kerguelen Archipelago (49°S 70°E). In these regions no corrections from any wide area augmentation systems are available for GPS precision augmentation. Finally the "payload" of a Wandering Albatross is limited to about 100 g according to Phillips et al. (2003). Together with the fact that no wiring is possible on the bird but the used sensor must consist of a rugged, waterproof and self-sufficient box with maximum dimension of about 100 mm×50 mm×15 mm this is a challenging claim with respect to the used hardware. The listed positioning requirements are facilitated to a certain extent by the fact that the trajectory of the bird does not need to be calculated on-the-fly but all recorded data can be postprocessed once the receivers are recovered. Furthermore *absolute* accuracy is of secondary interest only but the trajectory relative to the starting point of a dynamic soaring cycle needs to be known with high *relative* precision only.

Modern miniaturized single frequency GPS receivers meet the hardware requirements concerning size and weight and are used as appropriate sensors within the present project. However the position solution calculated online by such modules fails to meet the mentioned precision and sampling rate requirements. This drawback is overcome by evaluating the *raw data* which are recordable by selected receiver modules. As no commercially available postprocessing software capable to achieve decimeter precision while passing on baseline restrictions and static initialization patterns was available, new ground was broken in kinematic GPS raw data processing. An innovative method based on the *time-differential* use of L1 *carrier phase* observations was developed and implemented. This method meets all requirements resulting from the albatross task. Beyond that, it opens up a wide portfolio of other applications also demanding for precise relative navigation.

With one research focus put on miniaturized aerial vehicles, there was a need at the Institute of Flight System Dynamics for precise low-cost positioning solutions also in the context of other projects. Hence a source of synergy between "classical" flight mechanics and the analysis of bird flight was identified and fully taken advantage of.

1.2 Precise GNSS Based Positioning – State-of-the-Art

Striving for accuracy and precision augmentation is inseparably related to any kind of (satellite) navigation. A wide panoply of different approaches to achieve this goal has been developed in the past and is pursued with high priority by current research. A comprehensive review of *all* corresponding efforts goes beyond the present work's scope. Here time-differenced GPS carrier phase observations are used as the basis for precise positioning and the following literature review shall be focused on various phase range based positioning approaches.

Carrier phase range measurements are highly precise observations but both very sensitive to signal obstruction and inevitably affected with an ambiguity which is unknown to the user. The "classical" way to deal with this issue are so called real-time-kinematic (RTK) approaches. Suchlike methods are based on double-differenced carrier phase observations of a rover and a second (steady) base receiver. Initially this technique was restricted to static surveying applications but is today's state-of-the-art for centimeter accuracy kinematic trajectory measuring, compare e.g. Teunissen (1994). The method is usually applied to raw data from geodetic grade receivers and is restricted to baseline lengths of about 10 km. Several minutes of static initialization data are required in order to converge the unknown ambiguities to fixed values. Most recently successful ambiguity fixing with data from low-cost receivers became feasible (Odijk et al., 2007). A way to overcome the restrictive requirement for a *static* initialization phase is realized by the commercial RTK software GrafNav which implements the option of "ambiguity resolution on-the-fly" (Waypoint, 2004). This option was extensively tested by the author with various dynamic test data recorded by low-cost receivers. However, it was observed that successful kinematic ambiguity resolution with L1 data requires extremely favorable conditions (8 satellites in view, very good signal quality) during intervals of up to 10 min. Hence this interesting possibility must be considered as a rather theoretic option when working with single-frequency receivers. Another approach to ambiguity resolution is precise point processing (PPP). PPP aims for precise static and kinematic position determination using a single, dual-frequency GNSS receiver. Applying precise satellite orbit and clock corrections as well as ionospheric correction maps, the method bears the potential to achieve centimeter precision after successful static initialization of typically more than 20 min (Gao, 2006). Time-differencing of carrier phase measurements is a way to substitute the need for ambiguity resolution by ambiguity cancelation. Already in the mid-ninety-nineties notice was attracted to this fundamental advantage. Van Graas and Lee (1995) realized highly precise baseline computations referring to triple differences (i.e. differences across two receivers, two satellites and two epochs) requiring at least 7 satellites in view, if only phase data are used. Ulmer et al. (1995) presented

a stand-alone method to process static data recorded by a single military receiver for heading determination in gun-laying applications. In more recent days this approach, enhanced by a loop misclosure procedure, was successfully applied to static measurements recorded by civil receivers (Balard et al., 2006). Time-differentiated carrier phase measurements can be used as a substitute for delta range (Doppler) observables in order to calculate stand-alone precise velocity estimates (Wieser, 2007). This option will be further discussed after introducing the basic GNSS core equations (pp. 52). Canceling ambiguities by (sequential) carrier phase differencing is the background for a diversity of combined INS/GNSS applications: In tightly coupled INS/GNSS systems triple differences can support the dynamics estimation for attitude computation by segmented Kalman filtering (position separate from dynamics) (Farrell, 2001). In a similar context, carrier phases directly differenced between subsequent epochs can be used instead of the noisier delta range (Doppler) measurements to improve velocity and attitude information without the need for a base station (Wendel et al., 2003). Farrell (2007) also shows a way to pass on the measurements provided by a base station when using the tightly coupled segmented filtering approach presented in his 2001 publication. This procedure also extends to sans-IMU operations replacing inertial measurements by a quasistatic acceleration model (leading to reduced accuracy). Overcoming some limitations of the stand-alone time-difference method, this very interesting approach has to accept both a penalty in velocity accuracy and position precision.

The kinematic time-difference method presented in this monograph is an unconventional approach emerged from the need for a high quality but low effort positioning solution which meets all introductorily mentioned requirements. The update rate of today's miniaturized low-cost single frequency receivers is limited to about 4 Hz whereas selected modules make the raw measurements available with up to 10 Hz. As a consequence only raw data processing allows to fully exploit this potential. The developed way to use carrier phase data for relative positioning guarantees high precision without restrictions concerning initialization or limited baseline length. The application of the method to flight data recorded by soaring albatrosses points out the versatility and potential of the method and firstly makes an in-depth analysis of the complex dynamic soaring maneuvers possible.

1.3 Outline of the Thesis

Chapter 2 constitutes a review of important *GPS fundamentals*. Beside a brief description of the whole system, models for all L1 observables are introduced, various measurement error sources are discussed and some focus is put on receiver technology. The latter point is important for understanding both the advantages and caveats re-

lated to any kind of carrier phase processing as opposed to code based positioning. In this context also the results of a first quality assessment test performed with the used low-cost receiver modules are presented. Finally the standard positioning equations are exposed as a starting point for the theory of the time-differential approach.

Chapter 3 gives an elaborate description of *the time-differential positioning method*. The artificial observable resulting from differencing L1 carrier phase ranges is introduced and various measurement errors are discussed from a theoretic point of view. In a next step the core positioning equations are derived and two possibilities of kinematic trajectory reconstruction based on these very equations are discussed. All theoretic considerations are underpinned by first practical results.

Chapter 4 deals with the topic of *quality and integrity monitoring*. At first a way to estimate the errors of the time-differential positioning solution in the position domain is shown. Hereupon an algorithm for monitoring the integrity of the solution is derived ensuring the detection and exclusion of cycle slips and other outlying measurements. This method is based on the adaption of a RAIM scheme as usually applied for safety critical code-based navigation in civil aviation.

Chapter 5 provides an elaborate *practical validation* of the time-difference method based on both static experiments and dynamic (flight) tests. The discussion of the test results illuminates the derived theory from different perspectives (e.g. sensitivity analysis, integrity aspects, error estimation). In many cases the comparison with a much more costly reference RTK solution is possible.

In Chapter 6 an outline of *further processing steps* is given. The determination of speed and even acceleration from the precise position fixes as dropping out of the time-differential method is discussed on the basis of quintic smoothing splines. Here upper bounds for error propagation are provided. Moreover the scenario of carrier phase outages due to excessive antenna tilting or signal shadowing is discussed and a method to bridge resulting gaps is presented.

Chapter 7 refers to the measurement campaign conducted during the southern summer 2008/09 at Kerguelen Archipelago for *investigating the dynamic soaring flight of Wandering Albatrosses*. Fundamental aspects of dynamic soaring are addressed and the methodology for verifying this theoretic concept by real measurement data is exposed. Here the birds' total energy is introduced as a suitable observable not requiring any assumptions of (aerodynamic) bird parameters or knowledge about the local wind. The high precision of the trajectories generated by time-differential processing firstly allows such in-depth analysis of real dynamic soaring cycles and provides insights into the energy management of the birds. In a next step wind information provided by external sources is used for reconstructing the specific aerodynamic forces acting during individual cycles. The latter analysis is based on the inversion of the parameter-free differential equations describing the 3-DoF motion of the birds.

2 GPS Fundamentals

Providing a truly comprehensive description of the NAVSTAR Global Positioning System (GPS) is a difficult and page filling task which has been accomplished in various textbooks (Kaplan, 1996; Farrell and Barth, 1998; Hofmann-Wellenhof et al., 2001) and (Misra and Enge, 2004).[1] The explanations given in the present Chapter – mainly based on the named sources – aim at selected technical aspects which constitute important background information before heading to the theory of the time-differential approach. After a very brief general system description, the equations, properties and mutual dependencies of the individual observables available for civil single frequency receivers are outlined in Section 2.1. Special emphasis is put on the L1 carrier phase. Subsequently the topic of receiver technology and signal tracking is addressed. This is required for appreciating the advantage of carrier phase processing as opposed to code based positioning. The analysis of zero-baseline test data from a low-cost receiver supports the theoretical considerations. Just as any other observable, also carrier phase measurements are affected with errors which are discussed hereupon. Section 2.2 lines out the algorithms required to determine both position and velocity using C/A code and Doppler measurements. These methods are implemented within the the time-differential processing software as a back-up solution in case of carrier phase outages and for initial position determination. Basic methods for range modeling and solution quality estimation already introduced here also apply to time-differential processing.

2.1 System Description

Currently 31 GPS satellites, often referred to as the *space segment*, are operated in active service by the U.S. Air Force GPS wing.[2] These satellite vehicles (SV) travel around the Earth in six circular orbits with an inclination of $55°$, an orbital altitude of about 20.200 km and a period of approximately 12 h. A worldwide ground station network (the *ground segment*) coordinated by a master control station located at

---

[1] The most recent facts about the current state of the GPS system can be found in the public ftp repository of the Time Service Department of the US Naval Observatory:
ftp://tycho.usno.navy.mil/pub/gps/

[2] Status quo September 2010. The current GPS satellite constellation is published here:
http://tycho.usno.navy.mil/gpscurr.html

Schriever Air Force Base, Colorado Springs, monitors the system. The *user segment* is split up into a civil and a US-authorized group. Civil users have free access to the standard positioning service (SPS) provided by a coarse acquisition (C/A) code and a navigation message both broadcast on the L1 frequency (1575.42 MHz). Authorized (military) users benefit from the precise positioning service (PPS) transmitted via the encrypted P(y) code on both the L1 and L2 frequency (1227.60 MHz). In the scope of the ongoing *GPS modernization campaign* an additional civil signal (L2C) for non safety critical applications has been added on the L2 frequency with bringing into service the first Block IIR-M satellite in 2005 (FAA, 2010; Tycho, 2010). A new signal on the L5 band (1176.45 MHz) will support aviation safety-of-life applications and has been introduced with the launch of the first (of a total of 12) Block II-F satellites in May 2010 (Tycho, 2010).[3] Moreover a fourth civil signal is planned for the next GPS modernization level with the first launches of Block III satellites expected in 2014 or 2015 (Gruber, 2010; Parkinson, 2010).

For the time being there exist various *satellite based augmentation systems* (SBAS) striving to increase GPS accuracy, availability and integrity. Corresponding services are implemented for many areas around the globe such as the North-American WAAS and the European EGNOS. A ground based station network calculates range corrections for each GPS satellite. These corrections are uploaded to a geostationary satellite and broadcast back to Earth together with integrity information. Users located in regions the corrections are valid for and disposing of proper receiver equipment benefit from improved positioning performance (ESA, 2005). Users located within the footprint of an SBAS satellite (which significantly exceeds the area the corrections are valid for) can still gain additional (noisy) range and rate measurements to the respective geostationary satellite.

The civil GPS *signal architecture* is illustrated by Figure 2.1. The L1 carrier signal is modulated by binary phase shift keying (BPSK) with a 1023 bit pseudorandom noise Gold code, referred to as PRN code. This kind of phase shift keying switches the underlying carrier phase by 180° in case of chip (bit) changes. Each satellite vehicle, identified by its satellite vehicle number (SVN), has a unique PRN code, e.g. SVN 51 broadcasts a signal modulated with PRN 20. Due to the stochastic orthogonality of the individual PRN codes, it is possible to separate the signals after demodulation. The technique of all satellites broadcasting on the same carrier which is spread in the frequency domain by code modulation (spread-spectrum technique) primarily improves resistance to natural interference and hostile jamming.

With increased availability of the NAVSTAR GPS and improved receiver technology (miniaturization), a variety of location (and timing) based services, unthinkable only several years ago, exerts a sustainable impact on sociocultural, technical and military

---

[3] A demonstration L5 payload was already added to SVN 49 of BLOCK IIR-M launched in 2009.
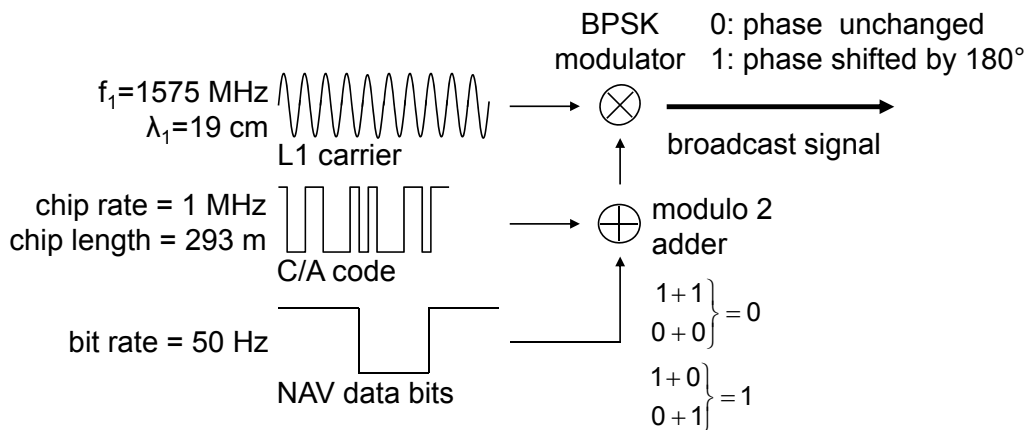
Figure 2.1: Composition of the civil component of the signal broadcasted by the GPS satellites at 1575.42 MHz (L1 band)

aspects of today's everyday life. GPS has changed the world and continues to do alike. This motivates other countries to contribute to global satellite navigation and to launch (or to reactivate) their own, independent global navigation satellite systems (GNSS). According to Revnivykh (2010), the Russian Federation has restored 98% global availability of the GLONASS system and will achieve the program in 2011. The People's Republic of China aims to expand the COMPASS system to a global network in 2020. Currently the European union is implementing the NAVSTAR interoperable GALILEO system which is scheduled to be fully operational in 2014 (Oosterlinck, 2010).[4] With the test satellites GIOVE-A and GIOVE-B already in orbit and the regular in-orbit validation phase scheduled for 2011, GALILEO will provide multiple services on an open access, a commercial, a safety-of-life and a public-regulated level. "GPS-land" is on its way to expand to a true "GNSS-land" striving for further achievements in global navigation.

2.1.1 Observables: Models and Interrelationships

The observables described in the following refer to the NAVSTAR GPS standard positioning service, i.e. to the signal components as sketched in Figure 2.1. These measurements can be recorded by low-cost, single-frequency receivers. If (civil) dual frequency equipment is used, the Doppler, carrier phase and signal strength values are also available on the L2 band by semi-codeless tracing techniques.

C/A Code Pseudorange

The Coarse Acquisition code observable (C/A or C1) is a direct, L1-code-based run-time measurement of the signal propagation from satellite to receiver antenna. The

---

[4]Open-Service, S&R and Public Regulated Service are scheduled for 2014 with 18 satellites; all 30 satellites are announced to be in orbit in 2016.

traveled distance (the geometric range) ρ between the satellite location at the time of signal emission $\mathbf{x}^S$ and the receiver location at the time of reception $\mathbf{x}^R$ is given by

$$\rho = c \left(t_{\text{reception}} - t_{\text{emission}} \right) \tag{2.1}$$

Here c is the signal propagation speed (speed of light) and t stands for the nominal (true) GPS system time. Even though general measurement errors will only be dealt with later on, there is one error which needs to be taken care of right away: the receiver clock bias from the GPS system time δ^R

$$\delta^R = \mathrm{t}^R - t \tag{2.2}$$

For $\delta^R > 0$ the receiver clock reading t^R is *ahead* of GPS system time. As a matter of fact the receiver does not feature a highly precise clock but is usually restricted to approximate the system time within millisecond precision only. As one millisecond equals a range error of roughly $300\,\text{km}$, the receiver clock bias cannot be modeled (or neglected) as other errors but needs to be treated as an additional unknown besides the three spatial receiver coordinates. As it is inevitably affected by $c\delta^R$ the range measurement is called *pseudo*range R

$$
\begin{aligned}
R &= c \left(\mathrm{t}^R_{\text{reception}} - t_{\text{emission}} \right) \\
&= c \left[\left(t_{\text{reception}} + \delta^R \right) - t_{\text{emission}} \right] \\
R &= \rho + c\delta^R
\end{aligned}
\tag{2.3}
$$

This ideal model (from hereon denoted by $\widehat{}$) differs from the real measurements ($\widetilde{}$) as output by the receiver due to various measurement errors χ:

$$
\begin{aligned}
\widetilde{R} &= \widehat{R} + \chi \\
\chi &= -c\delta^S + E + T + I + m + \varepsilon
\end{aligned}
\tag{2.4}
$$

Here δ^S is the (small) satellite clock offset from the nominal GPS system time. E represents the error in the satellite ephemeris, i.e. the uncertainty in the satellite position, which causes a bias in the estimate of the geometric range $\widehat{\rho}$. When propagating through the atmosphere, the signal is subject to both ionospheric (I) and tropospheric (T) delays. Additional user bound error sources are caused by indirect signal propagation due to ground reflections (multipath m) and random measurement noise ε. More details on these error components are given in Section 2.1.3.

Doppler

The Doppler observable is a range rate-type measurement available on both the L1 and L2 frequency. It is based on the frequency shift of the carrier wave as given by Eq. B.11 of Section B.1.2:

$$f_D = -\frac{\dot{\rho}}{\lambda} \tag{2.5}$$

with λ denoting the wavelength of the respective carrier and time derivatives indicated by a dot. Just as the pseudorange is affected by the receiver clock error δ^R, the Doppler observable is biased by the receiver clock drift $\dot{\delta}^R$ which directly stems from the offset of the receiver oscillator from the nominal GPS base frequency: $\delta f^R = f_0 \dot{\delta}^R$. Its impact on the Doppler measurement can be approximated by $\Delta f_D \approx -f \dot{\delta}^R$ with the respective nominal carrier frequency f. This requires to enhance Eq. (2.5) within the GPS context:

$$f_D = -\frac{1}{\lambda}\dot{\rho} - f\dot{\delta}^R \tag{2.6}$$

More details on (the simplifications made within) this equation are given in Kaplan (1996, pp. 50). Note that the receiver clock drift is positive ($\dot{\delta}^R > 0$) if the receiver clock is running too fast. In order to obtain an observable directly corresponding to a range-rate, Eq. (2.6) is multiplied by $(-\lambda)$[5]:

$$D = \dot{\rho} + c\dot{\delta}^R \tag{2.7}$$

In opposite to the pseudorange measurements, Eq. (2.4), Doppler measurements are, except for measurement noise, affected by the error rates only:

$$\begin{aligned} \widetilde{D} &= \widehat{D} + \dot{\chi} \\ \dot{\chi} &= -c\dot{\delta}^S + \dot{E} + \dot{T} + \dot{I} + \dot{m} + \varepsilon \end{aligned} \tag{2.8}$$

Carrier Phase

The carrier phase observable is a range-type measurement available for both the L1 and L2 frequency. It is based on the beat phase between the satellite signal (as received by the receiver, index S) and the reference carrier as internally generated by the receiver (index R). The basic physics underlying the beat phase concept are given in Section B.1.3. The following derivations are based on Hofmann-Wellenhof et al. (2001, pp. 88). Let φ^S, indicated in cycles, designate the phase of the satellite emitted wave and φ^R denote the phase of the (not yet Doppler compensated) receiver replica

---

[5]This convention is used throughout the remainder of this work such as Doppler becomes the derivative of phase. Note that this does not correspond to the definition as stated by Gurtner and Estey (2007): "The sign of the doppler shift as additional observable is defined as usual: Positive for approaching satellites."

signal. With t as an epoch[6] in GPS system time reckoned from an initial epoch $t_0(=0)$ when acquiring lock to the respective satellite one can state according to Eq. (B.4):

$$\varphi^S(t) = f\,t - f\frac{\rho(t)}{c} - \varphi_0^S(t); \qquad \varphi_0^S(t) = -\delta^S(t)\,f + \varphi^S(t_0) \qquad (2.9)$$

$$\varphi^R(t) = f\,t - \varphi_0^R(t); \qquad \varphi_0^R(t) = -\delta^R(t)\,f + \varphi^R(t_0) \qquad (2.10)$$

Here φ_0^S and φ_0^R are the satellite and receiver initial phase biases at t_0 affected with the respective clock errors. According to Eq. (B.12) the beat phase ϕ^{RS} between the received carrier and the reference signal is given by

$$\begin{aligned}
\phi^{RS}(t) &= \varphi^S(t) - \varphi^R(t) \\
&= -f\frac{\rho(t)}{c} - f\delta^R(t) + \varphi^R(t_0) - \varphi^S(t_0)
\end{aligned} \qquad (2.11)$$

The (small) satellite clock bias has been neglected for the sake of clarity – it will reappear when addressing general measurement errors. Due to the large distance ρ between satellite and receiver, Eq. (2.11) theoretically yields a large (decimal) number for ϕ^{RS}. However when acquiring lock to the respective PRN only the fractional part of this number can be measured, the initial integer number N of full cycles between satellite and receiver is unknown (*ambiguous*). Note that this ambiguity is not time dependent as long as the phase is locked continuously: $N \neq N(t)$. Hence, to model the numerical value actually output by the receiver, this unknown but constant integer term has to be subtracted from the right-hand side of Eq. (2.11). Moreover, to obtain a value directly corresponding to a range, the result is multiplied by $-\lambda$ yielding the phase-pseudorange Φ

$$\Phi(t) = \rho(t) + c\delta^R(t) + \lambda \underbrace{\left(\varphi^S(t_0) - \varphi^R(t_0) + N \right)}_{N'} \qquad (2.12)$$

Neither the initial satellite nor receiver phase biases $\varphi^S(t_0)$ and $\varphi^R(t_0)$, are known. Hence the *non*-integer ambiguity term N' is introduced in Eq. (2.12) to finally rewrite for the phaserange

$$\Phi(t) = \rho(t) + c\delta^R(t) + \lambda N' \qquad (2.13)$$

In the literature the non-integer ambiguity term N' is frequently replaced by the integer ambiguity N. This is not precise in a strict sense but the fractional receiver

---

[6]In GPS applications the time a measurement is taken or a position fix is calculated at is often referred to as an "epoch". This linguistic usage is due to the plurality of different times and clock readings related to a single measurement – the satellite clock reading at the time of signal emission, the receiver clock reading at the time of signal reception, the nominal GPS system time related to both events, etc.. The term "epoch" combines all these rather confusing time specifications and approaches to what one might usually understand by the term "time".
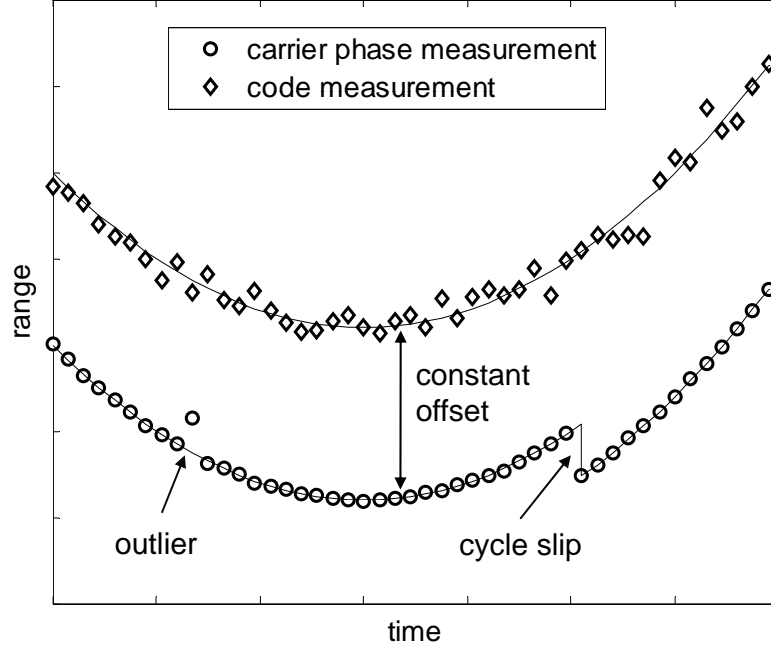
Figure 2.2: Code based pseudorange R and carrier based phaserange Φ with constant offset N' (qualitative plot)

and satellite phase terms only drop out when forming double differences. However, the non-integer character of the non-differenced phase observations does play an important role for procedures such as precise point positioning (Gao, 2006). It is important to keep in mind that the phase observable changes in the same sense as the code pseudorange but is significantly less noisy. This is qualitatively illustrated in Figure 2.2, where the constant offset $\lambda N'$ between the two measurements can also be seen. In the case of outliers or so called cycle slips, the assumption of a constant offset does not hold any longer. Special care has to be taken to identify and exclude suchlike biased phase measurements when processing the data within the positioning task. This is further explained in Section 4.2. Just as pseudoranges, Eq. (2.4), also carrier phase measurements $\widetilde{\Phi}$ differ from the respective models $\widehat{\Phi}$ as they are affected by "the usual suspects in GPS-land" such as satellite clock bias, ephemerides error, tropospheric and ionospheric refractions, measurement noise and multipath:

$$
\begin{aligned}
\widetilde{\Phi} &= \widehat{\Phi} + \chi \\
\chi &= -c\delta^S + E + T - I + m + \varepsilon
\end{aligned}
\tag{2.14}
$$

The user related error components multipath m and measurement noise ε are significantly reduced compared to code-based measurements. The remainder of the error components has the same magnitude but opposite sign in the case of the ionospheric refraction I.

Signal Strength

There are various ways to indicate the strength of a signal and different GPS receivers output this value in different ways. One widely used indication of the signal strength is known as C/N_0 ("C-to-N-zero"):

$$C/N_0 = \frac{P_C}{N_0} \text{Hz} \qquad\qquad C/N_{0\,\text{dBHz}} = 10 \log_{10} \frac{\frac{P_C}{N_0}\text{Hz}}{1\text{Hz}} \qquad (2.15)$$

with the signal power P_C in $[W]$ and the (white) noise power spectral density in $[W/Hz]$ (Misra and Enge, 2004, p. 293). A separate signal strength value is ideally given by the receiver for the various signals on the respective bands.

2.1.2 Receiver Technology

When arriving at the receiver location, the signal emitted by a GPS satellite with a power of about 27 W (available for the C/A code) has traveled a distance as far as 20,000 km and crossed Earth's atmosphere (Misra and Enge, 2004, p. 284). The signal is hereupon buried in radio frequency (RF) noise which yields very low C/N_0 values ranging from 37 to 45 dBHz. For a typical GPS receiver front end with a bandwidth of 20 MHz this means that the competing thermal noise is some 600 to 4000 times stronger than the signal power. In addition, all satellites broadcast on the same frequency band and the receiver has to untangle the different signals. Considering these circumstances one might appreciate even more the challenging task a GPS receiver is facing! The objective of this Chapter is to provide a *brief* overview of fundamental receiver technology and architecture. By far not all aspects can be addressed but the general discussion will stay on a superficial level. The interested reader is referred to the chapter "GPS Receivers" of Misra and Enge (2004) which also constitutes the main reference for the present considerations. Special attention will be contributed to the code and carrier tracking loops of the digital receiver components. Understanding their mutual interaction is key for understanding the dependencies between and the quality of the resulting measurements such as code pseudoranges, Doppler range rates and carrier phase ranges.

Receiver Layout

Figure 2.3 provides an overview of the basic receiver layout. The analog *front end* of the receiver conditions the incoming signal: it has to be amplified by a factor of 100 to 1000 and interfering natural and man-made RF noise in adjacent frequency bands has to be reduced if possible. Further, the carrier frequency of the signal is 1.5 billion cycles per second and most computers would have problems to process such high fre-
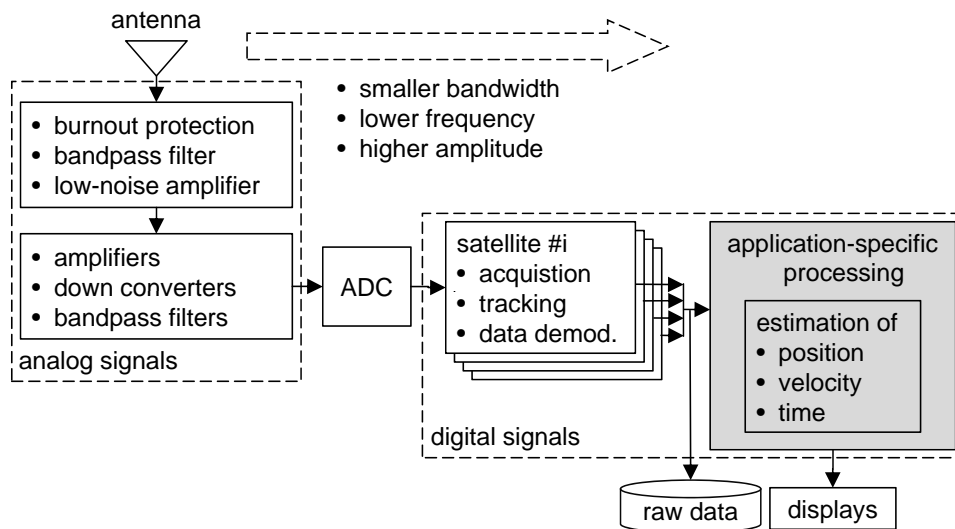
Figure 2.3: Basic design of a GPS receiver

quencies – the signal has to be down converted to something more manageable. This is accomplished by a sequential row of mixers on different intermediate frequency (IF) stages (most receivers use one or two stages). These mixers are to be preceded by carefully designed filters for removing any disturbing signals located at related image frequencies which would also be shifted to the intermediate frequency band. Mixing is followed by appropriately centered band pass filters for removing the high frequency components of the mixed signal. Note that the latter inevitably imply a phase shift. Luckily this shift is applied to the received signal from all satellites and as such does not influence the positioning solution. Finally the resulting continuous signal has to be discretized (digitalized) in both amplitude and time. Most GPS receivers use at least a two bit *analog to digital converter* (ADC, preceded by an appropriate automatic gain controller) yielding four or more levels of amplitude quantization. If the sampling rate is chosen to be at least twice the signal's cut-off frequency, this is called baseband sampling. However, most receivers refer to bandpass sampling requiring a significantly lower sampling rate which is more or less dominated by the bandwidth of the signal and not its cut-off frequency. In addition, bandpass sampling generates multiple aliases, of which the lowest ones (closest to baseband) are of special interest: bandpass sampling combines the sampling and down-conversion task. As a consequence, less IF stages are required and the transition to digital signal processing can be realized earlier. In contrast to analog signal processing, digital processing is virtually not affected by nuisance parameters such as humidity and temperature and provides increased flexibility (reprogramming instead of replacing components). Therefore an early transition from analog to digital processing is desirable. However, bandpass sampling generates a veritable raft of image frequencies which are to be removed by an anti-aliasing filter prior to sampling. The numbers created by the ADC are now

Figure 2.4: Code and carrier tracking loops of an individual channel

used within the parallel signal acquisition and tracking channels of the *digital portion* of the receiver for estimating the key triplet code time delay $\tau = R/c$, Doppler frequency shift $f_D = -D/\lambda_1$ and carrier beat phase $\phi^{(RS)} = -\Phi/\lambda_1$, compare Eqs. (2.3), (2.7) and (2.13). Modern receivers feature more than 200 of such channels. The resulting raw data is hereupon passed to the application specific positioning filter for position and velocity determination. The positioning related algorithms are to be described in detail in the subsequent Section 2.2. The majority of high quality receivers and selected low-cost modules make the raw data available to the user allowing to apply user defined positioning algorithms – such as carrier phase based time-differential postprocessing.

Signal Tracking Loops

The sampled signal as passed to the individual acquisition and tracking channels depicted in Figure 2.4 can be written as

$$S = \sqrt{P_C}N(t_l - \tau)x(t_l - \tau)\cos[2\pi(f_{IF} + f_D)t_l + \phi]$$
$$t_l = lT_S, \quad l = 0, 1, 2, 3\ldots$$

(2.16)

with the navigation data bits N, the PRN chips x (compare Figure 2.1), the final intermediate frequency f_{IF} and the sampling time T_S. The core of each channel are the numerical controlled oscillators (NCO) which generate a replica of the respective PRN code (with the current estimate of the time delay $\hat{\tau}$) and of the carrier signal
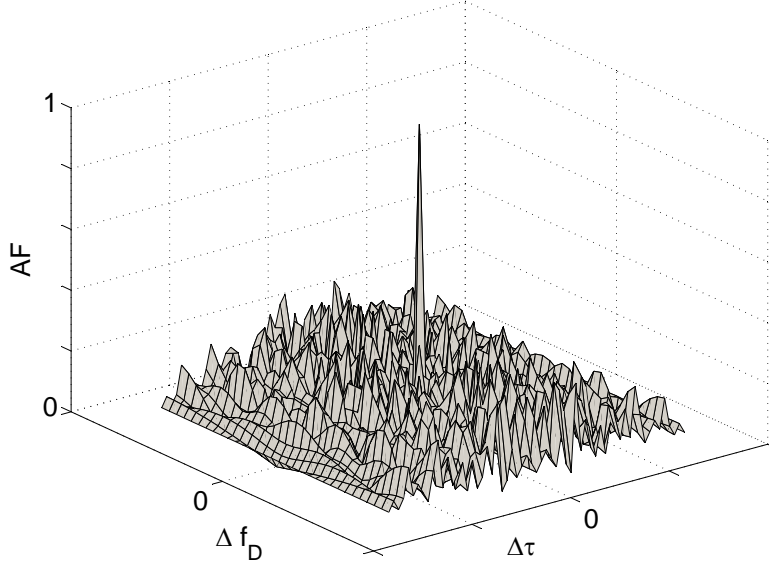
Figure 2.5: Qualitative plot of a normalized ambiguity function of a length 31 Gold code

(with $\widehat{f}_D$ and $\widehat{\phi}$). These oscillators receive inputs from a carrier tracking loop (CTL) and a delay lock loop (DLL) controller which can be operated in either acquisition or tracking mode. Multiplication of the incoming signal with an inphase and a 90 deg phase shifted (quadrature) version of the carrier replica followed by low pass filtering yields a signal which is still a function of τ but only a function of $\Delta f_D = f_D - \widehat{f}_D$ and $\Delta\phi = \phi - \widehat{\phi}$. For that reason this process is called Doppler removal or carrier wipeoff. In a next step the signal is correlated with an early, a prompt and a late replica of the PRN code which yields:

$$S_{e,p,l} = \sqrt{P_C} N \exp(j\Delta\phi) AF(\Delta\tau_{e,p,l}, \Delta f_D)$$

$$AF(\Delta\tau_i, \Delta f_D) = \frac{1}{T_{\text{cor}}} \int_0^{T_{\text{cor}}} x(t-\tau)x(t-\widehat{\tau}_i) \exp\left(j2\pi\Delta f_D t\right) dt \qquad (2.17)$$

$$\widehat{\tau}_e = \widehat{\tau} - \frac{dT_C}{2}; \quad \widehat{\tau}_p = \widehat{\tau}; \quad \widehat{\tau}_l = \widehat{\tau} + \frac{dT_C}{2}$$

Here, dT_C represents the correlator spacing which is a most important design parameter. *AF* is the ambiguity function which is closely related to the autocorrelation function as introduced in Section A.2. As it only depends on $\Delta\tau$ and Δf_D the correlation process is also called code wipeoff. Figure 2.5 illustrates the ambiguity function of a length 31 Gold code. During signal *acquisition* the CTL and DLL controllers conduct a coordinated search over the $(\Delta\tau, \Delta f_D)$ space in approximately $dT_C/2 \times 500\,\text{Hz}$ bins. Successful peak detection triggers signal *tracking* which can be performed in different control modes:

Non-coherent tracking – estimate of τ and f_D only. The discriminators used by this tracking mode in order to observe $\Delta\tau$ and Δf_D are stated in Eq. (2.18):

$$
\begin{aligned}
Z_{\Delta\tau} &= |S_e|^2 - |S_l|^2 + \text{noise}_\tau \\
Z_{\Delta f_D} &= \text{Re}\{S_p(t_1)\}\text{Im}\{S_p(t_2)\} - \text{Im}\{S_p(t_1)\}\text{Re}\{S_p(t_2)\} + \text{noise}_{f_D}
\end{aligned}
\tag{2.18}
$$

For eliminating the unknown nuisance parameters ϕ (and N) an early minus late power discriminator ($Z_{\Delta\tau}$) is used within the DLL involving increased noise due to squaring loss effects. Tracking frequency without phase, the CTL discriminator ($Z_{\Delta f_D}$) also recurs to squaring operations. As a consequence, non-coherent tracking reveals significantly increased noise and does not provide an estimate for the carrier phase. That's why modern receivers switch to coherent tracking whenever possible.

Coherent tracking – estimate of τ and ϕ. Depending on the carrier beat phase, this tracking strategy is very sensible with respect to signal obstructions. The carrier tracking loop is now also referred to as phase lock loop (PLL). The strategy implements the following discriminators for observing $\Delta\tau$ and $\Delta\phi$:

$$
\begin{aligned}
Z_{\Delta\tau} &= \big(\text{Re}\{S_e\} - \text{Re}\{S_l\}\big)N + \text{noise}_\tau \\
Z_{\Delta\phi} &= \text{Re}\{S_p\}\text{Im}\{S_p\} + \text{noise}_\phi
\end{aligned}
\tag{2.19}
$$

Assuming the navigation data to be unknown, the carrier tracking loop discriminator $Z_{\Delta\phi}$ is realized as a so called Costas discriminator again implying squaring operations. (This could be avoided by providing the navigation message from external sources, which is called Aided-GPS.) With the estimates $\hat{\phi}$ (and $\hat{\tau}$) the navigation data bits can be recovered from the inphase component of the prompt correlator. As now both ϕ and N are known, squaring operations are obsolete within the DLL discriminator $Z_{\Delta\tau}$. This yields improved noise performance compared to non-coherent tracking.

For either tracking mode the DLL controller filter is usually realized as a simple gain (P controller) commanding "speed up" or "slow down" commands ($\hat{\tau}$) to the NCO which basically integrates the incoming command. This yields PT_1 (first order) behavior of the (linearized) closed loop transfer function $G_{\text{DLL}} = \hat{\tau}(s)/\tau(s)$. The trade-off between noise performance and reference tracking is usually significantly improved by feeding a rate aiding signal from the CTL controller to the DLL controller. The CTL controller design depends on the applied tracking mode of which coherent tracking is of most interest here. As not only the phase $\hat{\phi}$ but also the phase rate $\hat{\dot{\phi}}$ is to be estimated, the controller is often realized as a PI filter again commanding "speed up" and "slow down" commands to the integrative carrier NCO. This yields PDT_2 (second order) behavior for the closed loop transfer function $G_{\text{PLL}} = \hat{\phi}(s)/\phi(s)$. As discussed in the Appendix, Doppler frequency shift and beat phase are closely related: $f_D = \dot{\phi}$,

see Eq. (B.14). Hence the phase lock loop provides both an estimate for the carrier beat phase and its Doppler frequency shift, corresponding to the final observables $\dot{\Phi} = D$ by appropriate scaling, compare Eqs. (2.7) and (2.13).

ZBL Test Results

It is important to note that the above statements explain the basic principle of GPS signal tracking. Of course, things are not that easy in the real world and each manufacturer uses his own proprietary algorithms which fit the respective design goals best. Zero-baseline (ZBL) tests are a common means for a user "outside the black box" to asses the signal tracking quality of the receiver at hand. Plugging two receivers (index a and b) of the same type to one antenna and forming double differences between measurements to two satellites (index l and k) with similar C/N_0 values

$$\begin{matrix} lk \\ ab \end{matrix} \nabla \Delta x = \left(x^{S_k, R_b} - x^{S_k, R_a} \right) - \left(x^{S_l, R_b} - x^{S_l, R_a} \right) \tag{2.20}$$

allows to estimate the variance of the receiver-due measurement error components $\sigma_{\widetilde{R}}$, $\sigma_{\widetilde{D}}$ and $\sigma_{\widetilde{\Phi}}$. Here, other noise induced e.g. by the atmosphere and multipath is eliminated by differencing.

A ZBL test has been performed with two low-cost uBlox TIM receiver modules plugged to the same high quality rooftop antenna of DLR, Oberpfaffenhofen. The measurement rate was set to 1 Hz, the recording interval was 40 min. (More details on the receivers are given in Section 5.1). The results are listed in Table 2.1. The test principally confirms the quality statements of the theoretical considerations made within the above and provides a good "impression" of the surprisingly good phase measurement precision achievable with low-cost single frequency receivers. The code noise exceeds the carrier noise by two orders of magnitude. This information is of most importance when using carrier phases for position determination.

A Note on Doppler Calculation These test results provide a good opportunity to point out some difficulties when choosing the alternative way of using Doppler data in order to directly calculate precise velocity estimates (with the option to integrate

Table 2.1: Results of a zero-baseline test with two low-cost single frequency receiver modules (uBlox TIM)

C/N_0	$\sigma_{\widetilde{R}}$	$\sigma_{\widetilde{D}}$	$\sigma_{\widetilde{\Phi}}$	$\sigma_{\widetilde{D}_\Phi}$ ($T_m = 0.1$ s)
49 dB-Hz	0.11 m	0.02 m/s	1.05 mm	0.015 m/s
43 dB-Hz	0.29 m	0.05 m/s	1.68 mm	0.024 m/s
40 dB-Hz	0.31 m	0.07 m/s	1.58 mm	0.022 m/s

for position). According to the literature (Wieser, 2007, p. 16 and p. 18) there are two common possibilities to obtain the *instantaneous* Doppler, i.e. the range rate measurements for the current epoch t_i: (1) *Assume* that the receiver is in a coherent tracking mode and that it calculates $\tilde{D}$ using *delta ranges* with the internal sampling rate T_S. This shall be indicated by the subscript Φ:

$$\tilde{D}_\Phi(t_i) = \frac{\tilde{\Phi}(t_i) - \tilde{\Phi}(t_i - T_S)}{T_S} \tag{2.21}$$

Obviously this output is corrupted by some time delay. Now further *assume* that the measurement rate T_m the raw data are made available with to the user is about the internal sampling rate T_S and project $\tilde{D}_\Phi$ to the current epoch by:

$$\begin{aligned}
\tilde{D}_{\Phi,\text{inst}}(t_i) &= \frac{1}{2}\left[\tilde{D}_\Phi(t_i) + \tilde{D}_\Phi(t_{i+1})\right] \\
&= \frac{\tilde{\Phi}(t_{i+1}) - \tilde{\Phi}(t_{i-1})}{2T_m}
\end{aligned} \tag{2.22}$$

Considering that the user neither knows T_S (which is closely related to the PLL bandwidth) nor whether the receiver *really* is in a coherent tracking mode and uses T_S for delta range calculation, it suggests itself to (2) directly use the phase measurements according to the second line of Eq. (2.22) if the latter are output by the receiver. The variance of the Delta ranges as given in Eq. (2.21) can be estimated according to

$$\begin{aligned}
\sigma^2_{\tilde{D}_\Phi} &= 2E\left\{\left[\frac{1}{T_S}\tilde{\Phi} - E\left(\frac{1}{T_S}\tilde{\Phi}\right)\right]^2\right\} \\
&= \frac{2}{T_S^2}E\left\{\left[\tilde{\Phi} - E\left(\tilde{\Phi}\right)\right]^2\right\} = \frac{2}{T_S^2}\sigma^2_{\tilde{\phi}}
\end{aligned} \tag{2.23}$$

which results to

$$\sigma_{\tilde{D}_\Phi} = \frac{\sqrt{2}}{T_S}\sigma_{\tilde{\phi}} \tag{2.24}$$

In the right-most column of Table 2.1 T_S is set to $T_m = 0.1\,\text{s}$ as this is the fastest sampling time the TIM module makes the raw data available with. Hence the according noise figures represent worst case values. The standard deviation $\sigma_{\tilde{D}}$ of the actually output measurements exceeds $\sigma_{\tilde{D}_\Phi}$ by 35 %, 110 % and 213 % for the different test cases. These results agree well with the analysis of (not double differenced) 10 Hz sampled static phase and Doppler data of the same receiver (results not depicted). Consequently the Doppler range rates output by the receiver are calculated internally with a sampling rate $T_S > T_m$ or drop out of the PLL filter by an algorithm other than the one assumed in Eq. (2.21) – which is proprietary and unknown to the user.

For concluding this digression on Doppler calculation it is important to keep in

mind two points. First, the receiver is a rather black box to the user. Deriving new observables basing on assumptions concerning receiver internal algorithms is therefore problematic. Next, directly using carrier phases if available is advantageous for both velocity and position determination. In contrast to velocity determination, direct position calculation as proposed within the time-differential method does not have to cope with time delay issues as encountered when deriving instantaneous Doppler estimates.

2.1.3 Measurement Errors and Correction Models

Just as any kind of measurements, also the GPS observations are affected by errors as firstly introduced in Eq. (2.4), p. 10. The resulting error perceived by the user, i.e. the *user equivalent range error*, is a superposition of different components such as the satellite ephemerides and clock error, atmospheric refractions caused by the ionosphere and the troposphere, and receiver and antenna dependent multipath and measurement noise (compare the ZBL test results discussed in the above). There exist various models and external correction data to compensate for these errors and navigation performance can be improved depending on the specific context such as the used receiver and whether realtime processing or postprocessing is required. Table 2.2 on p 24 summarizes the range errors resulting from the individual error sources described in this Section.

E – **Ephemerides and satellite clock error** The satellite position and an estimate for the current satellite clock error can be calculated using the ephemerides data broadcast within the GPS navigation message. The respective parameters are computed by the control segment on the basis of measurements of the GPS monitor stations. For postprocessing applications, the International GNSS Service IGS (Dow et al., 2009) offers highly precise clock and ephemerides products free of charge. *For the time-differential application 15 min sampled final orbits and 30 s sampled clock corrections are used.* Note that relativistic effects have to be accounted for when extracting the satellite clock error from the ephemerides. According to Ashby and Spilker (1996) there are three major effects: First, the orbital eccentricity causes the satellites to move with varying velocity and with varying distance from the Earth. Hence the relativistic frequency corrections applied to all satellite clocks by the control segment need to be enhanced by a satellite position and and velocity dependent correction term (up to 45 ns or 13.5 m). The time-differential approach implements this correction as specified by ICD-GPS-200C (2000, p. 89). Next, the Sagnac effect needs to be accounted for. This effect pertains to the excess path length due to receiver motion during signal propagation. It is treated implicitly by the light-time and earth-rotation correction described on pp. 28. Finally the so-called path range effect can be observed which

is related to the different gravitational potential experienced by the satellite and the receiver. The respective range (and range rate) error is negligible in the scope of time-differential processing. Relativistic effects are not listed in Table 2.2 and do not appear in error equations such as Eq. (2.4) as they can be modeled rigorously.

I – **Ionospheric refraction** The ionosphere is a region of ionized gases extending from 50 km to 1000 km above Earth. According to Seeber (1993) the ionospheric refraction can be modeled by

$$\widehat{I} = \frac{40.3}{f^2} \text{TEC}$$

$$\text{TEC} = \text{VTEC} \cdot m_{\text{iono}}(\zeta) \tag{2.25}$$

Here the total electron content TEC substitutes the integrated electron density per square meter along the signal's path and the respective carrier frequency is denoted by f. Usually only the overhead (vertical) electron content (VTEC) is known / modeled and the TEC value is obtained by referring to appropriate mapping functions m_{iono} which depend on the satellite elevation ζ. In the context of ionospheric modeling such mapping functions are often referred to as obliquity functions and typically yield factors of e.g. 2.5 for $15°$ elevation satellites. VTEC can be computed by using a model such as the one proposed by Klobuchar (1986). The current parameters of this model are transferred within the GPS navigation message. For postprocessing, more precisely measured VTEC maps are provided by IGS in the IONEX format (Schaer et al., 1998). *These maps are used for the time-differential approach in conjunction with a thin layer mapping function.* The ionosphere dispersively affects both code and phase measurements – compare inverted sign in Eqs. (2.4) and (2.14) (code delay, carrier advance).

T – **Tropospheric refraction** The neutral troposphere extends from ground to altitudes of about 9 km to 16 km. It primarily consists of the dry gases N_2 and O_2 and of water vapor. The dry fraction accounts for about 90 % of the total tropospheric delay which is usually modeled by

$$\widehat{T} = T_{\text{zenith, dry}} \cdot m_{\text{dry}}(\zeta) + T_{\text{zenith, wet}} \cdot m_{\text{wet}}(\zeta) \tag{2.26}$$

There exist various zenith delay models T_{zenith} for the dry and the wet fraction which require either atmospheric measurements at the antenna site or make do with averaged values (standard atmosphere assumptions) such as described by Hopfield (1969) and Saastamoinen (1973). There is also a variety of elevation dependent mapping functions $m_{\text{dry, wet}}$ of wich the easiest is $1/\sin\zeta$ and more accurate estimates are provided by Neill (1996). *For the time-differential approach, the Neill mapping function in combination with the UNB3 zenith path delay model (Collins et al., 1996) is used.* The

latter features three surface parameters (temperature, total pressure and water vapor pressure) in conjunction with expressions to describe their change with altitude. No external meteorological data are required for modeling.

m – **Multipath** If not only the direct version of the satellite emitted signal but also a ray reflected by nearby obstacles reaches a GPS antenna, this is called multipath. There are many variations of this cumbersome but omnipresent phenomenon which can hardly be modeled due to the virtual infinity of different environmental reflection scenarios. Multipath affects code and phase measurements in a different way. Depending on the chip length, see Figure 2.1, and the correlator spacing code multipath is restricted to $5 - 35$ m; typical values are $1 - 5$ m. Small chip length and narrow correlators suppress multipath effects. As opposed to code measurements the error in carrier phase observations due to multipath does not exceed a quarter cycle (Braasch, 1996) – being given that the direct ray is tracked within the PLL. (Otherwise, the error could theoretically be unbound.) Multipath mitigation is yet another reason to work with phase instead of code observations.

ε – **Receiver noise** In addition to all error sources addressed so far the observations output by a GPS receiver are affected with (virtually white) measurement noise. Carrier phase noise decreases with increasing signal strength, decreasing bandwidth of the PLL and increasing correlation time. In addition to these parameters code noise decreases with decreasing chip length and decreasing correlator spacing and depends on the bandwidth of the DLL instead of the CTL controller. Both kind of errors vary with the current tracking mode pursuit by the receiver, i.e. coherent or non-coherent tracking. The estimates given in Table 2.1 are confirmed by the ZBL test results presented on pp. 19 achieved with a low-cost receiver during very benign GPS conditions.

Note that little is said so far about the *drift* of the individual error components. This drift already appears in Eq. (2.8) describing the Doppler observable and will turn out to be crucial for the time-differential approach to be discussed in Chapter 3. More information on error drift will be provided on pp. 36.

Table 2.2: GPS error budget. Stochastic error characteristic (RMS, STD, etc.) indicated if available, otherwise typical values are chosen. Models and observations used for time-differential processing are *italicized*. References:
Misra and Enge (2004, pp. 140, 145, 148, 151, 152, 354)
Feess and Stephens (1987)
http://igscb.jpl.nasa.gov/components/prods.html (Apr 2010)

Error Source	Model / Observation	Range Error	Comments
Ephemerides	Broadcast orbits	~ 100 cm	Mean RMS
	Final orbits	~ 2.5 cm	Mean RMS
SV clocks	Broadcast clocks	~ 75 cm	Standard deviation; sampling interval 15 min
	Precise high rate clocks	~ 0.6 cm	Standard deviation; sampling interval 30 s
Ionosphere	No correction	$100 - 300$ cm	Zenith delay at night; $\times 2.5$ for $15°$ elevation
		$500 - 1500$ cm	Zenith delay at mid afternoon
	TVEC by Klobuchar model	$50 - 150$ cm	Zenith delay at night
		$250 - 750$ cm	Zenith delay at mid afternoon
	TVEC by IONEX maps	$30 - 130$ cm	Zenith delay, corresponds to $2 - 8$ TECU
Troposphere	No correction	$25 - 250$ cm	Zenith delay; $\times 4$ for $15°$ elevation
	Models w/o meteorological data	$5 - 10$ cm	Zenith delay
Multipath	*L1 carrier phase ranges*	$1 - 5$ cm	$< \lambda_1/4$ if receiver tracks direct signal
	C/A code ranges	$100 - 500$ cm	
Noise	*L1 carrier phase ranges*	$0.1 - 0.2$ cm	$0.5 - 1\%\ \lambda_1$
	C/A code ranges	$10 - 250$ cm	

2.2 Positioning Equations

The fundamental GPS positioning algorithms for estimating both position and time based on C/A code pseudorange and Doppler range rate measurements are described in this Section. These algorithms are implemented within the time-differential approach as backup in case of carrier phase outages. Moreover code based position fixes are used as initial estimate for time relative positioning.

2.2.1 C/A Code Based Single Point Positioning

Due to the nature of the code measurements, this position solution is noisy but very robust and represents the core functionality of any GPS receiver.

Positioning Algorithm

Pseudoranges as introduced in Eqs. (2.3) and (2.4) can be used to determine both the receiver's position $\mathbf{x}^R = \left(x^R, y^R, z^R\right)^T$ and clock bias δ^R at any epoch t. For getting started, these unknowns are combined to the position and time (PT) vector $\boldsymbol{\xi}$

$$\boldsymbol{\xi} = (\mathbf{x}^R, c\delta^R)^T = (x^R, y^R, z^R, c\delta^R)^T \tag{2.27}$$

where the receiver clock bias is scaled to range by the signal propagation speed for convenience. For the numerical solution, the position vector $\mathbf{x}^R$ will be indicated in the earth-centered-earth-fixed coordinate frame, index E (see Appendix B.2 for more details on coordinate frames). This also holds for all other variables introduced in the remainder of this Chapter if not indicated differently. For estimating $\boldsymbol{\xi}$ one needs observations $\widetilde{\mathbf{R}} = [\widetilde{R}^1, \dots, \widetilde{R}^i, \dots \widetilde{R}^m]^T$ to four or more satellites ($m \geq 4$). Matching these measurements with the respective models yields an (over-) determined, non-linear system of ordinary equations:

$$\widetilde{\mathbf{R}} = \widehat{\mathbf{R}}\left(\boldsymbol{\xi}\right) + \chi \tag{2.28}$$

With Eqs. (2.3) and (2.4) the individual pseudoranges are modeled as follows:

$$\widehat{R}^i = \rho^i + c\delta^R + \widehat{I} + \widehat{T}$$
$$\rho^i = \left|\mathbf{x}^i - \mathbf{x}^R\right| = \sqrt{(x^i - x^R)^2 + (y^i - y^R)^2 + (z^i - z^R)^2} \tag{2.29}$$

Here $\mathbf{x}^i$ is the position of the ith satellite at the time of signal emission which can be extracted from the ephemerides in order to calculate the geometric range ρ^i between receiver and satellite. Possible models for the ionospheric and tropospheric delays $(\widehat{I}, \widehat{T})$ have been addressed in Section 2.1.3. Eq. (2.28) is usually solved iteratively

by applying a Newton-Raphson algorithm and ignoring the residual measurement errors χ for the lack of better knowledge. This requires linearization in a starting point $\xi_0 = \xi - \Delta\xi$:

$$\widehat{\mathbf{R}} = \widehat{\mathbf{R}}\left(\xi_0\right) + \left.\frac{d\widehat{\mathbf{R}}}{d\xi}\right|_{\xi_0} \Delta\xi = \widehat{\mathbf{R}}\left(\xi_0\right) + \mathbf{H}_{\xi_0}\Delta\xi \tag{2.30}$$

For the sake of clarity, the Jacobian is rewritten elaborately:

$$\mathbf{H}_{\xi_0} = \begin{bmatrix} \frac{\partial\widehat{R}^1}{\partial x^R} & \frac{\partial\widehat{R}^1}{\partial y^R} & \frac{\partial\widehat{R}^1}{\partial z^R} & \frac{\partial\widehat{R}^1}{\partial(c\delta^R)} \\ \vdots & \vdots & \vdots & \vdots \\ \frac{\partial\widehat{R}^i}{\partial x^R} & \frac{\partial\widehat{R}^i}{\partial y^R} & \frac{\partial\widehat{R}^i}{\partial z^R} & \frac{\partial\widehat{R}^i}{\partial(c\delta^R)} \\ \vdots & \vdots & \vdots & \vdots \\ \frac{\partial\widehat{R}^m}{\partial x^R} & \frac{\partial\widehat{R}^m}{\partial y^R} & \frac{\partial\widehat{R}^m}{\partial z^R} & \frac{\partial\widehat{R}^m}{\partial(c\delta^R)} \end{bmatrix}_{\xi_0} \tag{2.31}$$

with

$$\frac{\partial\widehat{R}^i}{\partial x^R} \approx \frac{\partial\rho^i}{\partial x^R} = -\frac{x^i - x^R}{|\mathbf{x}^i - \mathbf{x}^R|} \qquad\qquad \frac{\partial\widehat{R}^i}{\partial\left(c\delta^R\right)} = 1 \tag{2.32}$$

Note that the variation of any atmospheric correction models and of the light time correction with time and space has been neglected. These minor effects will not impede convergence though and no additional error is caused by this simplification. As illustrated in Figure 2.6 the change of the geometric range with a change in receiver position can be interpreted as the (negative) scalar product between $\Delta\mathbf{x}^R$ and the unit vector $\mathbf{e}^i$ pointing from the receiver to the ith satellite. This allows to write for the unit vector

$$\mathbf{e}^i = \frac{\mathbf{x}^i - \mathbf{x}^R}{|\mathbf{x}^i - \mathbf{x}^R|} = -\frac{\partial\rho^i}{\partial\mathbf{x}^R}^T = -\left(\frac{\partial\rho^i}{\partial x^R}, \frac{\partial\rho^i}{\partial y^R}, \frac{\partial\rho^i}{\partial z^R}\right)^T \tag{2.33}$$
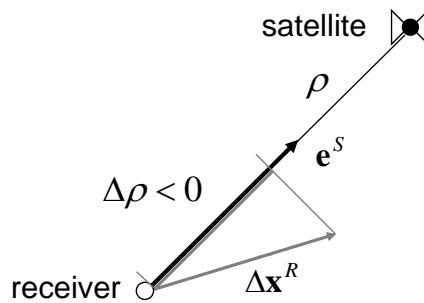

Figure 2.6: Unit vector $\mathbf{e}^S$ pointing from the receiver to a satellite. The change of the geometric range with a change of receiver position results in $\Delta\rho = -\mathbf{e}^S \cdot \Delta\mathbf{x}^R$.

Inserting Eqs. (2.32) and (2.33) in Eq. (2.31) yields for the Jacobian

$$\mathbf{H}_{\xi_0} = \begin{bmatrix} -\mathbf{e}^{1T} & 1 \\ \vdots & \vdots \\ -\mathbf{e}^{mT} & 1 \end{bmatrix}_{\xi_0} \tag{2.34}$$

The individual measurement errors χ_i are assumed to be uncorrelated and to have equal variance. In other terms, their covariance matrix is assumed to be an appropriately scaled identity matrix: $\mathbf{C}_\chi = \sigma_\chi{}^2 \mathbf{I}$. This assumption allows to solve Eq. (2.28) by non-weighted least squares as described in Section A.1, Eq. (A.5)

$$\Delta \xi = (\mathbf{H}_{\xi_0}{}^T \mathbf{H}_{\xi_0})^{-1} \mathbf{H}_{\xi_0}{}^T (\widetilde{\mathbf{R}} - \widehat{\mathbf{R}}(\xi_0)) \tag{2.35}$$

The iteration can now be continued with

$$\xi_{k+1} = \xi_k + \Delta \xi \tag{2.36}$$

until a convergence criterion such as $|\Delta \xi| < \epsilon$ is fulfilled.

Quality Estimation

If the variance of the measurement errors $\sigma_\chi{}^2$ is not known, it can be estimated by the final residuals f_i according to Eq. (A.9):

$$\begin{aligned} \sigma_\chi{}^2 &= \frac{\sum_{i=1}^{m} f^{i2}}{m-4} \\ f^i &= \widetilde{R}^i - \widehat{R}^i(\xi) \end{aligned} \tag{2.37}$$

The covariance matrix of the final position and time solution is calculated according to Eq. (A.8)

$$\mathbf{C}_\xi = \sigma_\chi^2 (\mathbf{H}_\xi{}^T \mathbf{H}_\xi)^{-1} \tag{2.38}$$

For many GPS applications an intuitive scalar number (instead of covariance matrices) is required to provide an immediate feedback about the expected positioning quality to the user. This matter is addressed by the concept of *Dilution of Precision* (DOP) which works according to the formula:

"position accuracy = measurement error × DOP"

A user who is familiar with his equipment has a rather good idea of the measurement error, i.e. the user equivalent range error, say 5 m. He can simply multiply this value with the DOP value output by the receiver, e.g. 2.0, in order to assess the current

positioning quality, resulting to $\pm 10\,\mathrm{m}$ for this example. Note that the dilution of precision works as a scalar factor accounting for the impact of the current satellite constellation *geometry*. For a more precise description of the DOP concept, let $\mathbf{D}^*$ substitute the geometry dependent term of Eq. (2.38): $\mathbf{D}^* := (\mathbf{H}_\xi{}^T \mathbf{H}_\xi)^{-1}$ and $\mathbf{D}^{**}$ denote the three upper left rows and columns of $\mathbf{D}^*$. Now one can state for the position and time covariance matrices:

$$\mathbf{C}_\xi = \sigma_\chi{}^2 \mathbf{D}^* \qquad \begin{aligned} \mathbf{C}_{(\mathbf{x})_E} &= \sigma_\chi{}^2 \mathbf{D}^{**} \\ \mathbf{C}_{(\mathbf{x})_0} &= \sigma_\chi{}^2 \mathbf{M}_{0E}{}^T \mathbf{D}^{**} \mathbf{M}_{0E} \\ &:= \sigma_\chi{}^2 \mathbf{D} \end{aligned} \qquad (2.39)$$

Here, the position covariance matrix is transformed to the north-east-down frame (n,e,d) for convenience (index 0). Comparing coefficients, e.g. $\sigma_e{}^2 = C_{(\mathbf{x})_0,\,22} = \sigma_\chi{}^2 D_{22}$, allows to define DOP values for different directions:

$$\sqrt{\sigma_n{}^2 + \sigma_e{}^2 + \sigma_d{}^2 + \sigma_{c\delta R}{}^2} = \sigma_\chi\,\mathrm{GDOP}; \quad \mathrm{GDOP} := \sqrt{D_{11} + D_{22} + D_{33} + D_{44}^*} \quad (2.40)$$

$$\sqrt{\sigma_n{}^2 + \sigma_e{}^2 + \sigma_d{}^2} = \sigma_\chi\,\mathrm{PDOP}; \quad \mathrm{PDOP} := \sqrt{D_{11} + D_{22} + D_{33}} \quad (2.41)$$

$$\sqrt{\sigma_n{}^2 + \sigma_e{}^2} = \sigma_\chi\,\mathrm{HDOP}; \quad \mathrm{HDOP} := \sqrt{D_{11} + D_{22}} \quad (2.42)$$

$$\sigma_d = \sigma_\chi\,\mathrm{VDOP}; \quad \mathrm{VDOP} := \sqrt{D_{33}} \quad (2.43)$$

$$\sigma_{c\delta R} = \sigma_\chi\,\mathrm{TDOP}; \quad \mathrm{TDOP} := \sqrt{D_{44}^*} \quad (2.44)$$

The typical accuracy achievable with C/A-code-based single point positioning varies between 2 and $15\,\mathrm{m}$ in the horizontal plane. As only satellites above the horizon are visible for a receiver, VDOP is usually about twice as high as HDOP resulting in vertical position errors of 4 to $30\,\mathrm{m}$.

Details on Range Calculation

The geometric range ρ required when modeling the pseudoranges according to Eq. (2.29) is the distance between the satellite position at the time of signal emission t_{emission} and the current estimate of the receiver position at the time of signal reception $\mathbf{x}^R(t_{\mathrm{reception}})$. Evidentially, $t_{\mathrm{reception}}$ is not known precisely but only approximated by the current estimate of the receiver clock error: $t_{\mathrm{reception}} = \mathrm{t}^R - \delta^R$, compare Eq. (2.2). For calculating ρ, the following procedure has to be performed:

1. Extract the satellite position at the time of emission from the ephemerides: $\mathbf{x}^S(t_{\mathrm{emission}})$. In the first iteration step, set $t_{\mathrm{emission}} = t_{\mathrm{reception}}$. Now calculate a first range estimate: $\rho = |\mathbf{x}^S - \mathbf{x}^R|$

2. Calculate the signal propagation time: $\Delta t = \rho/c$

3. Correct the emission time (light-time correction): $t_{\text{emission, cor}} = t_{\text{emission}} - \Delta t$

4. Get the satellite position for the corrected emission time from the ephemerides. This position is usually obtained in earth-fixed coordinates and therefore has to be corrected by the earth rotation $\omega_\oplus$:

$$(\mathbf{x}^S)_{E(t)} = \mathbf{M}_{E(t)E(t-\Delta t)} \, (\mathbf{x}^S)_{E(t-\Delta t)} \tag{2.45}$$

$$\mathbf{M}_{E(t)E(t-\Delta t)} = \begin{bmatrix} \cos(\omega_\oplus \Delta t) & \sin(\omega_\oplus \Delta t) & 0 \\ -\sin(\omega_\oplus \Delta t) & \cos(\omega_\oplus \Delta t) & 0 \\ 0 & 0 & 1 \end{bmatrix} \tag{2.46}$$

5. Recalculate the range for the corrected and transformed satellite position:

$$\rho = |\mathbf{x}^S(t_{\text{emission, cor}}) - \mathbf{x}^R| \tag{2.47}$$

6. If required, restart at 2. (Usually the iteration can be aborted after one cycle only.)

It is interesting to note that neglecting the light-time correction (step 3) can cause range errors of up to 75 m. Neglecting the coordinate transformation due to the earth rotation results in range errors as high as 35 m.

Both the light-time and the earth rotation correction are also applied when determining the unit vectors, Eq. (2.33), pointing from the receiver location at the time of reception to the satellite position at the time of emission.

2.2.2 Doppler Based Velocity Estimation

Doppler range rate observations as introduced in Eqs. (2.7) and (2.8) can be used to calculate the receiver velocity $\mathbf{v}^R = (u^R, v^R, w^R)^T$ and receiver clock drift $\dot{\delta}^R$. (If not indicated differently, velocities are always understood as kinematic velocities relative to and indicated in the earth-centered-earth-fixed coordinate frame; index E). Just as for single point positioning[7], one needs again to match at least four observations $\widetilde{\mathbf{D}} = [\widetilde{D}^1, \ldots, \widetilde{D}^i, \ldots, \widetilde{D}^m]^T$ with the respective models in order to obtain an (over-) determined set of equations:[8]

$$\widetilde{\mathbf{D}} = \widehat{\mathbf{D}}(\mathbf{v}^R, \dot{\delta}^R) + \dot{\chi} \tag{2.48}$$

---

[7]Note that *velocity* determination is often understood as an element of the *position*ing task. This wording aims to distinguish velocity and position determination ("Where am I and what's the speed I'm moving with?") from *navigation* ("Where do I want to go next and how do I get there?").

[8]The method presented in this Section assumes that "common" Doppler measurements as output by the receiver are used. For precise velocity determination , carrier based instantaneous delta ranges as addressed in Eqs. (2.21) and (2.22) could be used, too.

With Eq. (2.7) and the geometric considerations provided by Figure 2.7 the individual range-rates can be modeled as follows:

$$\widehat{D}^i = \dot{\rho}^i + c\dot{\delta}^R \tag{2.49}$$

$$\dot{\rho}^i = -\mathbf{e}^{iT}(\mathbf{v}^R - \mathbf{v}^i) \tag{2.50}$$

$$\mathbf{e}^i = \frac{\mathbf{x}^i - \mathbf{x}^R}{|\mathbf{x}^i - \mathbf{x}^R|} \tag{2.51}$$

Just as the position also the velocity of the ith satellite $\mathbf{v}^i$ can be extracted from the ephemerides. The receiver position required for calculating the unit vectors can be determined via code-based single point positioning with sufficient accuracy. As opposed to pseudorange modeling, see Eq. (2.29), range-*rate* errors caused by the atmosphere can be neglected here. Inserting in Eq. (2.48) and neglecting the residual range rate error $\dot{\chi}$ yields the normal equations

$$\begin{pmatrix} \widetilde{D}^1 - \mathbf{e}^{1T}\mathbf{v}^1 \\ \vdots \\ \widetilde{D}^m - \mathbf{e}^{mT}\mathbf{v}^m \end{pmatrix} = \begin{bmatrix} -\mathbf{e}^{1T} & 1 \\ \vdots & \vdots \\ -\mathbf{e}^{mT} & 1 \end{bmatrix} \begin{pmatrix} \mathbf{v}^R \\ c\dot{\delta}^R \end{pmatrix} \tag{2.52}$$

This linear system of equations can directly be solved for the unknowns $\mathbf{v}^R$ and $c\dot{\delta}^R$ by applying the least squares method.

For estimating the solution accuracy the DOP concept can be addressed in analogy to single point positioning. Being given that the system matrix of Eq. (2.52) coincides with the Jacobian as stated in Eq. (2.34), the DOP values from single point positioning can be used "as is" – the user simply has to interchange the measurement noise for getting a velocity accuracy estimate. Under good circumstances (HDOP < 2), the horizontal velocity accuracy is in the low decimeter per second range and accordingly worse in the vertical direction (Misra and Enge, 2004). An analysis of Doppler velocity
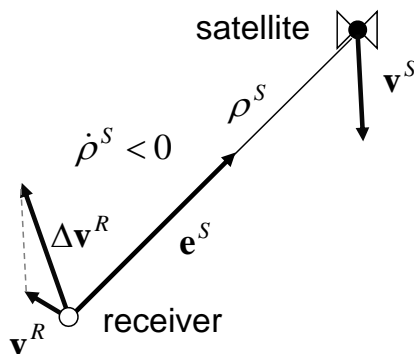

Figure 2.7: Unit vector $\mathbf{e}^S$ with receiver and satellite velocity. The range rate results to $\dot{\rho}^S = -\mathbf{e}^S \cdot (\mathbf{v}^R - \mathbf{v}^S) = -\mathbf{e}^S \cdot \Delta\mathbf{v}^R$

estimates resulting from real test data can be found in Möller (2008).

Due to the large distance between receiver and satellite of about 20,200 km the receiver location does not need to be known very precisely for (coarse) velocity determination. For example a position error as high as 10 m causes a maximum tilting of the unit vectors of $\arctan(10\,\mathrm{m}/20,200 \cdot 10^3\,\mathrm{m}) \approx 5 \cdot 10^{-7}\,\mathrm{rad}$. With range rates of up to 800 m/s this yields a maximum range-rate error of about $0.2 - 1.5\,\mathrm{mm/s}$, compare Eq. (2.50). This is much less than the average Doppler noise. However, the light-time and Earth-rotation correction should be applied when calculating the unit vectors.

Finally it is worth noting that the estimate of the receiver speed

$$V^R = \left|\mathbf{v}^R\right| = \sqrt{u^{R2} + v^{R2} + w^{R2}} \tag{2.53}$$

is biased. The expectation of this bias is always positive. This holds even though the individual error components of the velocity ideally are zero mean normally distributed random variables:

$$V_{\mathrm{bias}}^R > 0 \tag{2.54}$$

with

$$\begin{aligned} V_{\mathrm{bias}}^R &= E\left[V^R - \mu\right] \\ \mu &= \left|\left(E\left[u^R\right], E\left[v^R\right], E\left[w^R\right]\right)^T\right| \end{aligned} \tag{2.55}$$

A simple graphical explanation of this effect for the two dimensional case is provided by Figure 2.8. Statistically speaking, $V^R - \mu$ reveals a non-central χ^2-distribution.[9] The non-central characteristics of this distribution decrease with an increasing ratio of μ/σ
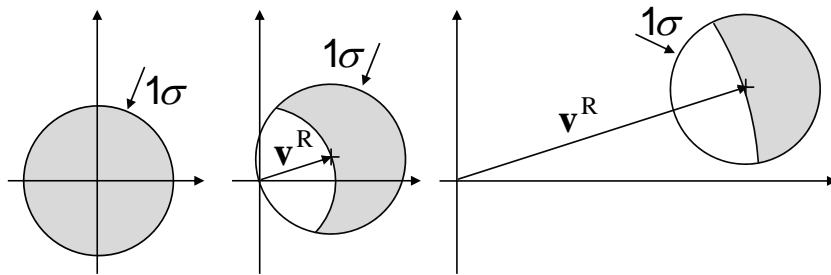

Figure 2.8: Vectorial explanation of the bias in the speed estimate V^R. For the sake of simplicity $\sigma_{u^R} = \sigma_{v^R} = \sigma$ is assumed. The *left plot* shows the case $\mu = 0$. In this case $V_{\mathrm{bias}}^R > 0$ always holds. The *center plot* shows the case $\mu = \sigma$. Now the 1σ circle is divided by the the $V^R - \mu = 0$ line represented by a circle centered in the origin with radius μ. V^R is more likely to be estimated long than short as the area of the shaded partition of the circle significantly exceeds the white area, i.e. $V_{\mathrm{bias}}^R > 0$. The *right plot* shows the case $\mu \gg \sigma$. Now both fractions of the 1σ circle reveal virtually the same area which means $V_{\mathrm{bias}}^R \approx 0+$.

---

[9]This holds if the individual velocity components are independent and equally distributed. In the general case more complex statistics are required, but the effect of a positive bias remains unchanged.

and it tends towards a zero-mean normal distribution for large speeds. Nonetheless the speed bias is in the order of $0.1 - 1\%$ for typical applications such as car navigation and has to be taken into account especially when integrating in order to obtain the distance traveled. A comprehensive treatment of this issue can be found in Wieser (2007, pp. 117).

3 Time-Differential Positioning

Time-differential positioning is a way to implement precise carrier phase based differential GPS with a single low-cost GPS receiver, without ambiguity resolution and without (static) initialization patterns. These advantages allow to realize centi- to
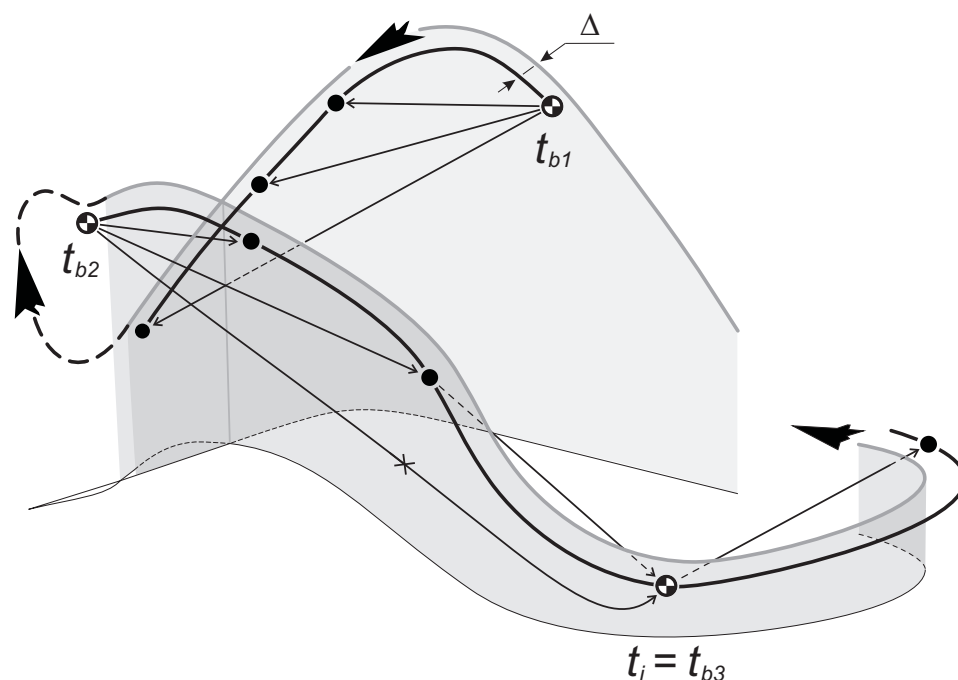
Figure 3.1: Measuring kinematic trajectories using the time-difference method

decimeter precision in applications where "classical" geodetic methods fail. A wide portfolio of implementations becomes possible, ranging from the precise analysis of flight maneuvers to biomechanical studies – even if the respective project is limited to a low budget and difficult field conditions impede the use of a nearby base station and any kind of initialization patterns. As a matter of fact such fundamental advantages do not come for free – only relative precision[1] as opposed to absolute accuracy[2] can be achieved and maintained during time spans limited to several minutes. These shortcomings require the user to always be aware of what she or he is about to do and to know the limitations and possible pitfalls related to (any kind of) carrier based

---

[1]Precision: the degree to which repeated measurements under unchanged conditions show the same results (Taylor, 1999).

[2]Accuracy: the degree of closeness of measurements of a quantity to its actual (true) value.

processing. Figure 3.1 illustrate the basic concept of the approach and the idea of (relative) precision: In this exemplary scenario a starting point is defined at an arbitrary time t_{b1} at the beginning of a flight maneuver of interest. The corresponding position of the vehicle is not known exactly but estimated by techniques such as coarse code based single point positioning. Therefore it is biased from the true location by Δ. The subsequent trajectory is now determined by time-differential processing relative to this starting point. In other terms the base vectors pointing from the starting epoch to the current position are determined exactly. Hence all fixes are affected by the same bias Δ – meaning that accuracy is not improved at all with respect to single point positioning but *precision* significantly is! Phase measurements are sensible to signal shadowing – a short upside-down interlude is likely to cause complete signal obstruction and to prevent further processing. As no initialization patterns are required by the time-difference method, a new starting point (t_{b2}) can be determined (affected with a new, different bias) and processing can immediately be resumed. Evidentially such event will lead to a gap in the final solution, but no unnecessarily long outage due to any re-initialization procedures is caused. (The third base change in the scenario given in Figure 3.1 will be addressed later on in Section 3.3).

This Chapter is intended to investigate the theoretical basics of the time-differential method. The artificial time-difference observable is described including measurement error considerations, the core-algorithm required to find the relative solution between two individual epochs is derived and finally two strategies for processing kinematic data for trajectory reconstruction are discussed.

3.1 The Observable

Carrier phase measurements as introduced in Section 2.1.1 are the basis for the time-differential approach. These observations are not directly used in the positioning equations but a new, artificial observable has to be created before heading to the core positioning task.

3.1.1 Time-Differences of Phase Measurements

As derived by Eqs. (2.9) through (2.13) phase range observations are biased by an unknown ambiguity N':

$$\Phi(t) = \rho(t) + c\delta^R(t) + \lambda N' \tag{3.1}$$

Provided continuous phase lock to the respective PRN in the receiver PLL, this ambiguity is a time-invariant constant: $N' \neq f(t)$, compare Figure 2.2. Hence, forming differences of phase observations to the same satellite between a "base-epoch" t_b and

a current epoch t_i implies ambiguity cancelation – *the* advantage of the present approach:

$$\Phi(t_i) - \Phi(t_b) = \rho(t_i) - \rho(t_b) + c\left(\delta^R(t_i) - \delta^R(t_b)\right) + \lambda \underbrace{(N' - N')}_{0} \qquad (3.2)$$

Introducing the time-difference operator $^{bi}Dx = x(t_i) - x(t_b)$ allows to rewrite Eq. (3.2):

$$^{bi}D\Phi = {}^{bi}D\rho + c\, {}^{bi}D\delta^R \qquad (3.3)$$

For positioning the time-differenced measurements ($\tilde{\ }$) are to be approximated by suitable mathematical models ($\hat{\ }$). Just as for direct phase ranges, Eq. (2.14), there is an inevitable difference between measured and computed observation:

$$
\begin{aligned}
^{bi}D\widetilde{\Phi} &= {}^{bi}D\widehat{\Phi} + {}^{bi}D\chi \\
^{bi}D\chi &= -c\, {}^{bi}D\delta^S + {}^{bi}DE + {}^{bi}DT - {}^{bi}DI + {}^{bi}Dm + {}^{bi}D\varepsilon
\end{aligned}
\qquad (3.4)
$$

The standard deviation of the noise component (and to a certain extent also of multipath) is raised by a factor of $\sqrt{2}$ compared to non-differenced measurements as there is virtually no autocorrelation between subsequent epochs. However this is not true for the remaining error components which can be considered as individual random processes with high autocorrelation depending on the physical nature of the respective error source and the applied correction models. In a linear sense one can approximate the measurement error for the time-difference case:

$$
\begin{aligned}
^{bi}D\chi = & \left[-c\frac{\partial \delta^S}{\partial t} + \frac{\partial E}{\partial t} + \frac{\partial T}{\partial t} + \frac{\partial I}{\partial t} + \frac{\partial m}{\partial t} \right] (t_i - t_b) + \\
& + \left[\frac{\partial T}{\partial \mathbf{x}^R} + \frac{\partial I}{\partial \mathbf{x}^R} \right] \left(\mathbf{x}^R(t_i) - \mathbf{x}^R(t_b) \right) + \\
& + {}^{bi}D\varepsilon^*
\end{aligned}
\qquad (3.5)
$$

with the enhanced error term $^{bi}D\varepsilon^*$ also comprising non-correlated error contributions such as ionospheric scintillation and the noise-like change of multipath with receiver motion. The error component related to the change of the receiver's position (second line in the above equation) mainly depends on the baseline length, i.e. the line-of-sight distance the receiver has traveled in the elapsed time interval. [3] This error is also encountered when working with "classical" differential techniques requiring a second base receiver. For instance, centimeter accuracy RTK applications based on ambiguity resolution are limited to baselines of 10 to 20 km due to this error component (Landau et al., 2007). As baselines mainly limited to below one kilometer are

---

[3]The term "baseline" originally stems from surveying applications where it describes the distance between reference and roving receiver.

of interest in the scope of the present application, the very small position dependent error component is not investigated further on within this monograph. Estimating the error due to the temporal variation, i.e. the *drift* of the individual components is of much more interest as it is the most important limiting factor when applying the time-difference method.

3.1.2 Error Considerations

Absolute ranging errors and respective correction data and models have already been outlined in Section 2.1.3. However, Eq. (3.5) indicates that due to differencing, the major components of each error cancel and only the (cumulative) range error drift affects the measurements $^{bi}D\widetilde{\Phi}$. Table 3.1 on p. 38 provides a coarse estimate of the individual error drift components which are briefly discussed in in the below. More detailed explanations and very helpful estimates can be found in Wieser (2007, pp. 25).

E **– Ephemerides and satellite clock error** The satellite position as extracted from the ephemerides is affected with an along-track, a cross-track and a radial error component. Geometry considerations show that both the absolute along-track error and the change of the radial position error (radial satellite velocity error) significantly impact the cumulative range error drift $^{bi}DE = \partial E / \partial t \cdot (t_i - t_b)$. In contrast to satellite position, the satellite clock drift $\dot{\delta}^S$ directly maps into a range rate error. A strict discrimination between the error drift caused by satellite position and satellite clock drift in terms of rate error is difficult and Table 3.1 indicates the combined error according to the SPS Performance Standard for the broadcast navigation data (SPS, 2008). The use of final IGS satellite clocks and orbits is assumed to further improve accuracy by one to two orders of magnitude. Neglecting relativistic corrections for the orbit eccentricity and the Sagnac effect would cause range rate errors of up to 6 mm/s.

I **– Ionospheric refraction** Three effects influence the change of the range error due to the ionosphere $^{bi}DI = \partial I / \partial t \cdot (t_i - t_b)$: First the temporal variation of TVEC with changing ionospheric activity, next the change of the mapping function with time varying satellite elevation, see Eq. (2.25), and finally ionospheric scintillation. The latter phenomenon usually contributes less than 1 mm/s range rate error. It is very hard to model and neglected for time-differential processing. The range rate errors caused by the remaining effects are listed in Table 3.1. (Note: The value indicated in Table 3.1 for the range rate error when applying IONEX maps (<2.5 mm/s) is estimated to be half the error compared to using the Klobuchar model. However IONEX maps often serve as reference for validating other ionosphere models – such as the Klobuchar model. Due to this circular reasoning the indicated value should be understood as very coarse estimate only.)

T – **Tropospheric refraction** Two effects influence the change of the range error due to the troposphere $^{bi}DT = \partial T/\partial t \cdot (t_i - t_b)$. First the temporal variation of the zenith path delay depending on the current weather and next the change of the mapping functions with varying satellite elevation, compare Eq. (2.26). The first component will typically not exceed $0.2\,\text{mm/s}$. Hence using the new IGS product for estimating the zenith path delay on the basis of global atmospheric measurements (Byun and Bar-Sever, 2009) is not required when working with time-differences but the UNB3 model is largely sufficient. The variation of the elevation causes range rate errors of approximately $13\,\text{mm/s}$ for satellites above $10\,°$ elevation and up to $80\,\text{mm/s}$ for elevations lower than $3\,°$. However these rates are virtually perfectly modeled by the use of the Neill mapping function which is reported to be accurate to within 1% (Wieser, 2007, p. 38).

m – **Multipath** Just as the range error due to multipath also its temporal variation $^{bi}Dm = \partial m/\partial t \cdot (t_i - t_b)$ strongly depends on the respective reflection environment. In fact the carrier phase range error oscillates with the additional distance traveled by the reflected signal (with a period of λ_1 under certain assumptions (Braasch, 1996)). This distances varies with both satellite and receiver motion. The variation due to satellite motion is relatively slow and can cause range rate errors in the cm/s to dm/s range for a static receiver. If the receiver moves fast enough, the limited bandwidth of the PLL filter (see p. 18) will cause the phase observations to be affected with an averaged instead of an instantaneous multipath error which will typically be in the mm/s range – provided that there is no loss of lock.

ε – **Receiver noise** Receiver noise can reasonably be assumed to be Gaussian white noise without any systematic drift, see Eq. (A.26) p. 133. When working with time differences between subsequent epochs (t_{i-1}, t_i) the standard deviation of the measurement noise error component of $^{i-1,i}D\widetilde{\Phi}$ is therefore raised by a factor of $\sqrt{2}$. When working with a clamped base epoch t_b the standard deviation will not be affected but the differenced observation $^{bi}D\widetilde{\Phi}$ will be slightly biased by the noise error at t_b.

Receiver Position An error in the base position causes a "geometric" range error in all observations $^{bi}D\widetilde{\Phi}$. This effect will be investigated further on in Section 3.2.3.

Table 3.1: GPS error drift budget. Stochastic error characteristic indicated if available, otherwise typical values are chosen. Models and observations used for time-differential processing are *italicized*. References:
SPS (2008, p. 23)
Wieser (2007, pp. 29, 32, 38, 49, 69)

Error Source	Model / Observation	Range Error Drift	Comments
Ephemerides and clocks (SV position and velocity)	Broadcast	$< 6\,\text{mm/s}$	95 % global average over any 3 s interval
	Final orbits	$\sim 0.5 - 0.05\,\text{mm/s}$	
Ionosphere	No correction	$1 - 18\,\text{mm/s}$	
	TVEC by Klobuchar model	$<5\,\text{mm/s}$	
	TVEC by IONEX maps	$<2.5\,\text{mm/s}$	Refer to the text
Troposphere	No correction	$1 - 10\,\text{cm/s}$	
	Models w/o meteorological data	$0.2 - 1\,\text{mm/s}$	
Multipath	*L1 carrier phase ranges*	$\text{mm/s} - \text{cm/s}$ range	Moving receiver
		$\text{cm/s} - \text{dm/s}$ range	Static receiver
Noise	*L1 carrier phase ranges*	-	
	C/A code ranges	-	Autocorrelation negligible

Note that there is no need to recur to explicit range *rate* error models when working with time-differences. The direct range corrections as described in Section 2.1.3 are rather applied to the raw measurements $\widetilde{\Phi}$ before forming $D\widetilde{\Phi}$.

None of the listed error components can be eliminated completely by the use of the precise measurements and dedicated models as applied for time-differential processing. A residual range error drift (superseded by random noise in the mm-range) will remain. According to Brown and Hwang (1997, p. 426) this error drift resembles a Gauss-Markov process with a long time constant ($> 1\,h$). This assumption agrees well with the drift estimates in the mm/s-range summarized in Table 3.1. Restricting possible processing intervals to time-spans well below the time constant of the range error is key when applying the time-differential approach. Precision in the cm- to dm-range can be achieved during intervals of up to 5 min. This promising assessment will be confirmed by the evaluation of experimental results in Chapter 5.

3.2 Core-Algorithm

This Section basically treats the conversion of the time-differenced measurements $^{bi}D\widetilde{\Phi}$ to a base vector pointing from the receiver location at the time t_b to its location at t_i, i.e. the transition from the measurement to the position (and time) domain. The stand-alone solution between two epochs is derived and equations to propagate range- to position errors are provided. Finally the impact of the temporal variation of the satellite constellation on time-differential processing is discussed. This theoretical background is required before heading to the reconstruction of kinematic trajectories.

3.2.1 Stand-Alone Solution between Two Epochs

Assume the receiver's position $\mathbf{x}^R$ to be known at a base epoch t_b. The base vector pointing from the position at t_b to the position at the epoch of interest t_i is defined by

$$\mathbf{b}^{bi} = \mathbf{x}^R(t_i) - \mathbf{x}^R(t_b) \tag{3.6}$$

Figure 3.2 gives an overview of the problem's geometry and illustrates the base vector. In addition to its position the receiver clock bias δ^R has to be estimated which requires to introduce the enhanced base vector

$$\boldsymbol{\beta}^{bi} = \boldsymbol{\xi}(t_i) - \boldsymbol{\xi}(t_b) \tag{3.7}$$

In order to determine this relative position and clock error $\boldsymbol{\beta}^{bi}$, time differences $^{bi}D\boldsymbol{\Phi} = [\,^{bi}D\Phi^1, \ldots, \,^{bi}D\Phi^j, \ldots, \,^{bi}D\Phi^m]^T$ to at least four satellites ($m \geq 4$) are required
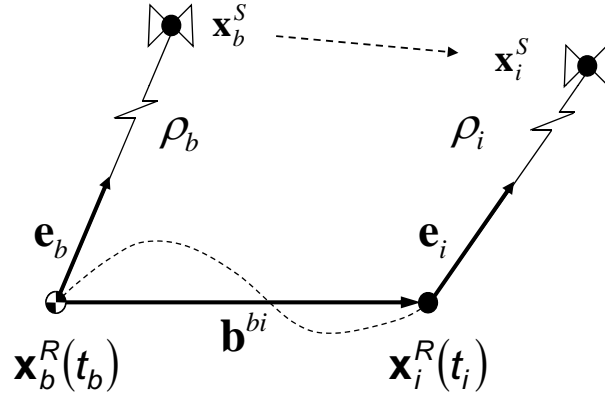
Figure 3.2: Time-differential relative positioning: $\mathbf{b}^{bi}$ is the base vector pointing from the receiver's position at t_b to its position at the current epoch t_i. The dashed line shows the trajectory traveled by the receiver in the time interval $\Delta t = t_i - t_b$. Mainly due to the motion of each satellite within Δt the direction of the unit vectors changes (only one satellite depicted here).

and the core positioning equations can be set up:

$$^{bi}D\widetilde{\mathbf{\Phi}} = {}^{bi}D\widehat{\mathbf{\Phi}} + {}^{bi}D\chi \tag{3.8}$$

With Eqs. (2.29) and (3.3) and by accounting for models of atmospheric refraction the individual time-differences for the jth satellite are computed as follows:

$$
\begin{aligned}
^{bi}D\widehat{\Phi}^j &= {}^{bi}D\rho^j + c\,{}^{bi}D\delta^R + {}^{bi}D\widehat{T}^j + {}^{bi}D\widehat{I}^j \\
&= \sqrt{(x_i^j - x_i^R)^2 + (y_i^j - y_i^R)^2 + (z_i^j - z_i^R)^2} - \sqrt{(x_b^j - x_b^R)^2 + (y_b^j - y_b^R)^2 + (z_b^j - z_b^R)^2} + \\
&\quad + c(\delta_i^R - \delta_b^R) + (\widehat{T}_i^j - \widehat{T}_b^j) - (\widehat{I}_i^j - \widehat{I}_b^j) \\
&= f(\boldsymbol{\xi}_i, \boldsymbol{\xi}_b, \mathbf{x}_i^j, \mathbf{x}_b^j, t_i, t_b)
\end{aligned}
\tag{3.9}
$$

with the subscript x_i as a shortcut for $x(t_i)$. Note that $^{bi}D\widehat{\Phi}$ is not a direct function of $\boldsymbol{\beta}^{bi}$ only. For that reason Eq. (3.8) will nominally be solved for $\boldsymbol{\xi}_i$ in the following. However it will become apparent that $\boldsymbol{\beta}^{bi}$ is the intrinsic solution of the problem and only relative precision can be achieved. Just as in standard single point processing, Eq. (3.8) is an (over-)determined set of nonlinear equations which is solved iteratively by a Newton-Raphson algorithm and a least squares estimation (see Section A.1) within each iteration loop. For that purpose the right-hand side of Eq. (3.8) has to be linearized neglecting higher order terms and the unknown range errors $^{bi}D\chi$:

$$^{bi}D\widehat{\mathbf{\Phi}}(\boldsymbol{\xi}_i, \boldsymbol{\xi}_b) = {}^{bi}D\widehat{\mathbf{\Phi}}(\boldsymbol{\xi}_{i,0}, \boldsymbol{\xi}_b) + \mathbf{H}_{\boldsymbol{\xi}_{i,0}}\Delta\boldsymbol{\xi}_i \tag{3.10}$$

with $\Delta \boldsymbol{\xi}_i = \boldsymbol{\xi}_i - \boldsymbol{\xi}_{i,0}$. The linearization point $\boldsymbol{\xi}_{i,0}$ is either the result of the last iteration cycle of the current epoch or the final result of the previous epoch. The Jacobian is given by

$$\mathbf{H}_{\boldsymbol{\xi}_{i,0}} = \frac{d\, {}^{bi}D\widehat{\boldsymbol{\Phi}}}{d\boldsymbol{\xi}_i}\bigg|_{\boldsymbol{\xi}_{i,0}} = \begin{bmatrix} \frac{\partial\, {}^{bi}D\widehat{\Phi}^1}{\partial x_i^R} & \frac{\partial\, {}^{bi}D\widehat{\Phi}^1}{\partial y_i^R} & \frac{\partial\, {}^{bi}D\widehat{\Phi}^1}{\partial z_i^R} & \frac{\partial\, {}^{bi}D\widehat{\Phi}^1}{\partial(c\delta_i^R)} \\ \vdots & \vdots & \vdots & \vdots \\ \frac{\partial\, {}^{bi}D\widehat{\Phi}^j}{\partial x_i^R} & \frac{\partial\, {}^{bi}D\widehat{\Phi}^j}{\partial y_i^R} & \frac{\partial\, {}^{bi}D\widehat{\Phi}^j}{\partial z_i^R} & \frac{\partial\, {}^{bi}D\widehat{\Phi}^j}{\partial(c\delta_i^R)} \\ \vdots & \vdots & \vdots & \vdots \\ \frac{\partial\, {}^{bi}D\widehat{\Phi}^m}{\partial x_i^R} & \frac{\partial\, {}^{bi}D\widehat{\Phi}^m}{\partial y_i^R} & \frac{\partial\, {}^{bi}D\widehat{\Phi}^m}{\partial z_i^R} & \frac{\partial\, {}^{bi}D\widehat{\Phi}^m}{\partial(c\delta_i^R)} \end{bmatrix}_{\boldsymbol{\xi}_{i,0}} \tag{3.11}$$

With Eq. (3.9) the following relationships hold:

$$\frac{\partial\, {}^{bi}D\widehat{\Phi}^j}{\partial \mathbf{x}_i^R} \approx \frac{\partial \rho_i^j}{\partial \mathbf{x}_i^R} = -\mathbf{e}_i^{j\,T} \qquad\qquad \frac{\partial\, {}^{bi}D\widehat{\Phi}^j}{\partial(c\delta_i^R)} = 1 \tag{3.12}$$

Again the spatial variations of the atmospheric correction models are neglected in these approximations - a fact which does not cause any additional error as convergence will not be impeded by such a slight change in the Jacobian. The unit vector $\mathbf{e}$ has already been introduced in Eq. (2.33) and is illustrated by Figure 3.2. Accordingly the Jacobian for the time-difference approach coincides with the one used for code-based single point processing, Eq. (2.34):

$$\mathbf{H}_{\boldsymbol{\xi}_{i,0}} = \begin{bmatrix} -\mathbf{e}_{i,0}^{1\,T} & 1 \\ \vdots & \vdots \\ -\mathbf{e}_{i,0}^{m\,T} & 1 \end{bmatrix} \tag{3.13}$$

Once linearized Eq. (3.8) can be solved by least squares

$$\Delta \boldsymbol{\xi}_i = (\mathbf{H}_{\boldsymbol{\xi}_{i,0}}{}^T \mathbf{H}_{\boldsymbol{\xi}_{i,0}})^{-1} \mathbf{H}_{\boldsymbol{\xi}_{i,0}}{}^T \left({}^{bi}D\widetilde{\boldsymbol{\Phi}} - {}^{bi}D\widehat{\boldsymbol{\Phi}}(\boldsymbol{\xi}_{i,0}, \boldsymbol{\xi}_b) \right) \tag{3.14}$$

and the next iteration cycle can be started with $\boldsymbol{\xi}_{i,k+1} = \boldsymbol{\xi}_{i,k} + \Delta \boldsymbol{\xi}_i$. Iteration will be aborted if a convergence criterion such as $|\Delta \boldsymbol{\xi}_i| < \epsilon$ is fulfilled. Due to the least-squares approach the converged solution is the one minimizing the errors (residuals respectively), compare Eq. (A.3):

$$\sum_{j=1}^{m} ({}^{bi}D\widetilde{\Phi}^j - {}^{bi}D\widehat{\Phi}^j)^2 = \min \tag{3.15}$$

Due to the inevitable error drift as stated in Eq. (3.5) the final residual level rises and precision decreases with increasing processing time spans Δt.

3.2.2 Quality Estimation

The optimality statements made in Section A.1 concerning the least squares solution for ξ_i only hold if the individual measurements $^{bi}D\widetilde{\Phi}^j$ are mutually uncorrelated, unbiased and of equal variance. This assumption only partly holds for time-differential positioning. Referring to Eq. (3.5) and the discussion in Section 3.1.2 it becomes clear that the residual measurement errors are independent and unbiased for short time intervals only as error drift not yet impacts the observations but measurement noise is the predominant error source. However, error drift takes the lead for increasing time spans and the zero mean assumption doesn't hold any longer. The basic equations given in the following for the case of short time intervals are intended as the starting point for the more elaborate discussion provided in Section 4.1: Just as in single point positioning, the variance of the observations can be estimated by the residuals according to Eq. (A.9):

$$
\begin{aligned}
\sigma_{D\widetilde{\chi}}^2 &= \frac{\sum_{j=1}^{m} {}^{bi}Df^{j2}}{m-4} \\
{}^{bi}Df^j &= {}^{bi}D\widetilde{\Phi}^j - {}^{bi}D\widehat{\Phi}^j
\end{aligned}
\tag{3.16}
$$

The covariance matrix of the final relative position and time solution is calculated according to Eq. (A.8)

$$
\mathbf{C}_{\xi_i} = \sigma_{D\widetilde{\chi}}^2 \left(\mathbf{H}_{\xi_i}{}^T \mathbf{H}_{\xi_i}\right)^{-1}
\tag{3.17}
$$

Also for time-differential positioning, it is convenient to work with the concept of dilution-of-precision as introduced by Eqs. (2.39) through (2.44) for now estimating no longer absolute accuracy but relative precision by a simple scalar value. Being given that the same Jacobian is used for time-differential and single point positioning (Eqs. (3.13) and (2.34)), comparable satellite constellations yield comparable DOP values for both approaches. Like this a user familiar with conventional processing techniques can interpret DOP values "as usual".

3.2.3 Impact of Time-Varying Satellite Constellation

Not only the receiver moves within the time elapsed between t_b and t_i but the Earth keeps on turning and also the satellites travel with up to 3.9 km/s along their orbits. This causes a variation of the satellite constellation geometry within Δt which leads to a tilting of the unit vectors as qualitatively depicted by Figure 3.2. It is interesting to note that this variation does not explicitly appear in the core positioning equations, Eqs. (3.6) through (3.14). Does that mean that changing geometry has no impact on the relative precision achievable with the time-difference approach? Not quite. To further investigate this point, another effect has to be discussed which seems to be

independent of the initial question at a first glance: How does an error in the base position (and time) influence relative precision, i.e. the base vector? This issue is addressed by Figure 3.3. Here $\mathbf{x}^R_{b,\text{true}}$ shall be the true receiver position at t_b and $\mathbf{b}^{bi}$
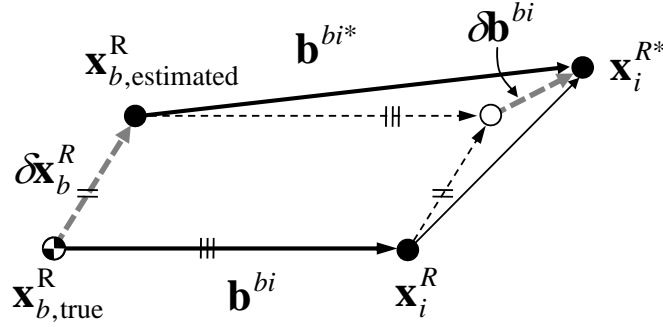

Figure 3.3: Impact of a bias of the base position on relative precision

is the base vector resulting from time-differential processing relative to such ideal base position. Of course the true initial position is not known but usually estimated by coarse single point positioning biased by $\delta\mathbf{x}^R_b$ in the low meter range. It suggests itself that such shift of the initial position will, first of all, also translate the resulting base vector by $\delta\mathbf{x}^R_b$ as indicated by the light dotted arrow parallel to $\mathbf{b}^{bi}$ in the figure. Evidentially, such pure translation is no degradation of relative precision. However, as it will be derived hereafter, a shift of the initial position not only translates but also distorts $\mathbf{b}^{bi}$ and the new base vector differs from the one calculated with an ideal base position by $\delta\mathbf{b}^{bi}$. As a consequence, also the final receiver position $\mathbf{x}^{R*}_i$ is affected by this distortion and relative precision is degraded. For a mathematical analysis of this effect, the model of the time-difference observation shall be linearized in both $\boldsymbol{\xi}_i$ and $\boldsymbol{\xi}_b$, compare Eq. (3.10):

$$^{bi}D\widehat{\boldsymbol{\Phi}} = \,^{bi}D\widehat{\boldsymbol{\Phi}}(\boldsymbol{\xi}_{i,0}, \boldsymbol{\xi}_{b,\text{true}}) + \mathbf{H}_{\boldsymbol{\xi}_{i,0}}\Delta\boldsymbol{\xi}_i - \mathbf{H}_{\boldsymbol{\xi}_{b,\text{true}}}\delta\boldsymbol{\xi}_b \qquad (3.18)$$

with $\mathbf{H}_{\boldsymbol{\xi}_{i,0}}$ according to Eq. (3.13) and $\delta\boldsymbol{\xi}_b = \boldsymbol{\xi}_b - \boldsymbol{\xi}_{b,\text{true}}$. Referring to Eq. (3.9) one gets for the second Jacobian

$$\mathbf{H}_{\boldsymbol{\xi}_{b,\text{true}}} = -\frac{\partial\,^{bi}D\widehat{\boldsymbol{\Phi}}}{\partial\boldsymbol{\xi}_b}\bigg|_{\boldsymbol{\xi}_{b,\text{true}}} = \begin{bmatrix} -\mathbf{e}^1_{b,\text{true}}{}^T & 1 \\ \vdots & \vdots \\ -\mathbf{e}^m_{b,\text{true}}{}^T & 1 \end{bmatrix} \qquad (3.19)$$

The minus sign is used for convenience only in order to obtain congruence between $\mathbf{H}_{\xi_{i,0}}$ and $\mathbf{H}_{\xi_{b,\text{true}}}$. These matrices are closely related which allows to approximate:

$$\mathbf{H}_{\xi_{b,\text{true}}} = \mathbf{H}_{\xi_{i,0}} + \dot{\mathbf{H}}_{\xi_i}(t_b - t_i) = \mathbf{H}_{\xi_{i,0}} + \begin{bmatrix} -\dot{\mathbf{e}}_{i,0}^{1\,T} & 0 \\ \vdots & \vdots \\ -\dot{\mathbf{e}}_{i,0}^{m\,T} & 0 \end{bmatrix}(t_b - t_i) \tag{3.20}$$

Note that again only changes of the unit vectors due to the elapsed time but not due to receiver motion are taken into account. Inserting Eq. (3.20) in Eq. (3.18) yields

$$^{bi}D\widehat{\mathbf{\Phi}} = {}^{bi}D\widehat{\mathbf{\Phi}}(\xi_{i,0}, \xi_{b,\text{true}}) + \mathbf{H}_{\xi_{i,0}}(\Delta\xi_i - \delta\xi_b) - \dot{\mathbf{H}}_{\xi_i}(t_b - t_i)\delta\xi_b \tag{3.21}$$

The term $\Delta\xi_i - \delta\xi_b$ is the change in receiver position compensated by the bias of the base position, i.e. the effective change in the base vector $\Delta\boldsymbol{\beta}^{bi}$. With $\Delta t = t_i - t_b$ one gets for the linearized positioning equations, compare Eq. (3.8)

$$^{bi}D\widetilde{\mathbf{\Phi}} = {}^{bi}D\widehat{\mathbf{\Phi}}(\xi_{i,0}, \xi_{b,\text{true}}) + \mathbf{H}_{\xi_{i,0}}\Delta\boldsymbol{\beta}^{bi} + \dot{\mathbf{H}}_{\xi_i}\Delta t\,\delta\xi_b + {}^{bi}D\chi \tag{3.22}$$

As the base epoch bias $\delta\xi_b$ is not known it has to be neglected just as the remaining unknown range errors $^{bi}D\chi$ when solving for $\Delta\boldsymbol{\beta}^{bi}$. For that reason the corresponding term can be understood as additional "geometric" range error

$$^{bi}D\chi_{\text{geo}} = \dot{\mathbf{H}}_{\xi_i}\Delta t\,\delta\xi_b \tag{3.23}$$

Eqs. (3.22) and (3.23) answer both introductorily asked questions: A bias in the base position acts like an additional range error and significantly degrades relative precision. With $|\dot{\mathbf{e}}|$ as high as $1.9 \cdot 10^{-4}\,1/\text{s}$ for a satellite passing right above the observer, a bias of $20\,\text{m}$ in the base position can cause relative errors as high as $1.9 \cdot 10^{-4}\,1/\text{s} \cdot 20\,\text{m} \cdot 30\,\text{s} = 11.4\,\text{cm}$ over a $30\,\text{s}$ interval. As the change in constellation geometry is represented by $\dot{\mathbf{H}}_{\xi_i}$ this result also points out the answer to the second question. The temporal variation of satellite geometry influences time relative positioning only if there is a bias in the base position (which in general is inevitable). In this case it acts like a range error growing with increasing processing time spans. These results coincide with the statements given by Ulmer et al. (1995). When working with the time-differential approach it is therefore important to determine the initial base position as accurately as possible. This can be realized by applying all corrections listed in Table 2.2, p. 24, when estimating the base position. Like this accuracies in the low meter range can be achieved and the geometric range error is reduced to the order of magnitude of the other residual errors.

3.3 Kinematic Trajectory Reconstruction

Determining the base vector between two individual epochs is sufficient for static applications but not for measuring kinematic[4] trajectories. Indeed there are different strategies for accomplishing the latter task starting from the core equations given so far. Figure 3.4 shows two possible approaches which are to be discussed here with their respective advantages and caveats.
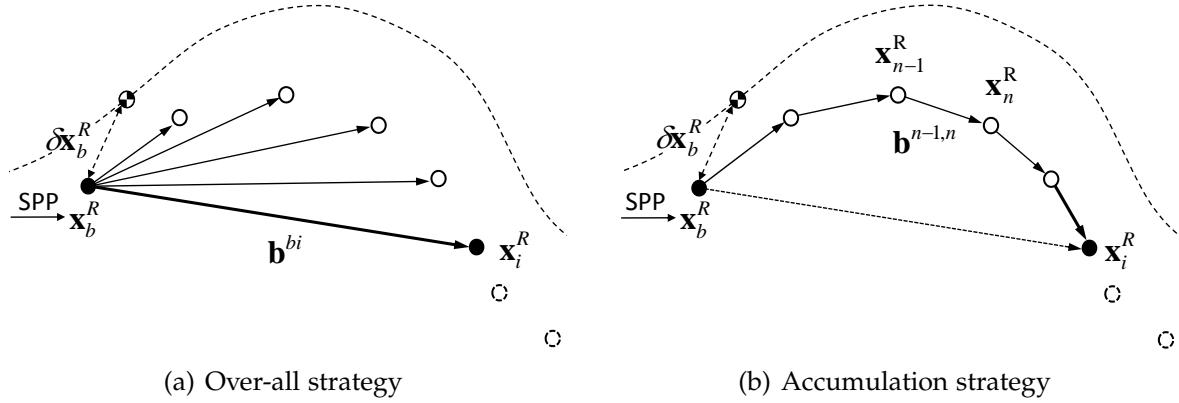

(a) Over-all strategy   (b) Accumulation strategy

Figure 3.4: Two strategies for kinematic trajectory reconstruction by the time-difference approach. The dashed line is the (unknown) true trajectory.

3.3.1 Two Strategies for Trajectory Reconstruction

Over-all strategy Each epoch is solved independently from previous measurements – the "over-all" solution between t_b and t_i is calculated as depicted by Figure 3.4(a). This strategy implements the following scheme:

1. Determine the receiver position and time solution $\boldsymbol{\xi}_b$ at a base epoch t_b. This is usually done by code based single point processing (SPP) as described in Section 2.2.1. The base solution is biased by several meters as indicated by $\delta \mathbf{x}_b^R$. The following trajectory will be precise relative to $\mathbf{x}_b$ ($\boldsymbol{\xi}_b$ respectively).

2. If there are four or more ($m \geq 4$) phase observations available at both t_b and t_i calculate $\boldsymbol{\beta}^{bi}$ (and $\boldsymbol{\xi}_i$) according to Eqs. (3.6) through (3.14). This "over-all" solution is independent of previous epochs.

3. If there are neither enough ($m < 4$) valid common phase observations between t_b and t_i nor between t_i and t_{i-1} abort processing and recalculate a new base by SPP as soon as possible. Such an event is illustrated by the first base change in Figure 3.1. It will cause a gap in the resulting trajectory.

---

[4]Note that strictly speaking the word "kinematic" could be omitted here as obviously any trajectory is of "kinematic" nature. The term is rather used following expressions such as "RTK - Real Time Kinematic" in order to make a difference to static positioning applications based on time-differences such as described by Ulmer et al. (1995).
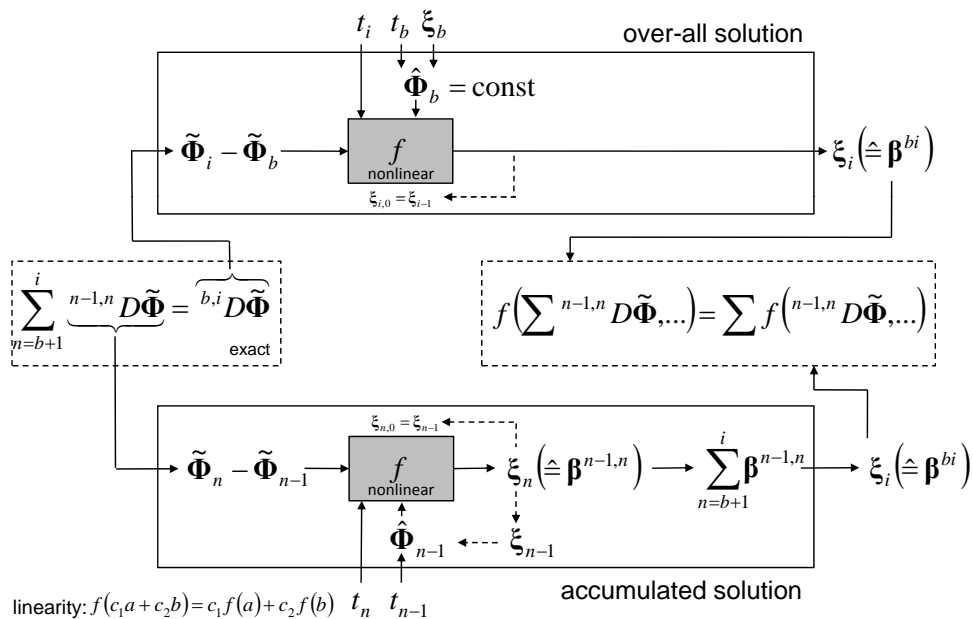
45

Figure 3.5: Comparison of over-all and accumulation strategy

4. If there are not enough ($m < 4$) valid common phase observations between t_b and t_i but sufficient common measurements between t_{i-1} and t_i ($m \geq 4$) calculate $\beta^{i-1,i}$ and declare t_{i-1} as new base. Such event is called "base hand-over" in the following and prevents a gap in the resulting trajectory. The second base-change in Figure 3.1 illustrates such base hand-over.

Accumulation strategy This strategy calculates the "incremental" solution between subsequent epochs t_{n-1}, t_n and determines the final base vector by accumulating the resulting position increments. Hence each fix strongly depends on the previous ones. The strategy implements a pattern as illustrated by Figure 3.4(b):

1. Same as in over-all strategy.

2. If there are enough ($m \geq 4$) valid common phase observations between t_{n-1} and t_n calculate the respective position (and time) increment $\beta^{n-1,n}$. Calculate the final fix by $\xi_n = \xi_{n-1} + \beta^{n-1,n}$ (with $\xi_{n-1} = \xi_b$ for the first increment).

3. If there are not enough valid common measurements between t_{n-1} and t_n abort processing and re-import a SPP solution as soon as possible (compare point 3 of the over-all strategy.

At first glance both approaches may appear to be equivalent and the accumulation strategy probably seems to have a lead in real world applications where signal shadowing is a severe issue. Anticipating this Section's central conclusion, this first impression is perfectly correct. However, a closer analysis and comparison of the two approaches shows that the first evidence is not trivial but a rather surprising result. Be aware that accumulating measurements affected with random errors always holds the risk of unbound, random-walk effects (see Section A.2).

Figure 3.5 shows a comparative flow chart of both processes. Let's start with the input. For the ith epoch, the over-all strategy takes ${}^{bi}D\widetilde{\Phi}$ whereas the input of the accumulation strategy is ${}^{n-1,n}D\widetilde{\Phi}$. It can be shown by simply writing out the sums that the statement in the diagram's left-most box is exact:

$$\sum_{n=b+1}^{i} {}^{n-1,n}D\widetilde{\Phi} = \sum_{n=b+1}^{i} (\widetilde{\Phi}_n - \widetilde{\Phi}_{n-1})$$

$$= \sum_{n=b+1}^{i} [(\Phi_n + \delta\Phi_n) - (\Phi_{n-1} + \delta\Phi_{n-1})]$$

$$= [(\Phi_{b+1} + \delta\Phi_{b+1}) - (\Phi_b + \delta\Phi_b)] +$$

$$+ [(\Phi_{b+2} + \delta\Phi_{b+2}) - (\Phi_{b+1} + \delta\Phi_{b+1})] +$$

$$+ [(\Phi_{b+3} + \delta\Phi_{b+3}) - (\Phi_{b+2} + \delta\Phi_{b+2})] + \ldots \tag{3.24}$$

$$+ [(\Phi_{i-1} + \delta\Phi_{i-1}) - (\Phi_{i-2} + \delta\Phi_{i-2})] +$$

$$+ [(\Phi_i + \delta\Phi_i) - (\Phi_{i-1} + \delta\Phi_{i-1})]$$

$$= [(\Phi_i + \delta\Phi_i) - (\Phi_b + \delta\Phi_b)]$$

$$\sum_{n=b+1}^{i} {}^{n-1,n}D\widetilde{\Phi} = {}^{b,i}D\widetilde{\Phi}$$

Even though this sum is never actually calculated but accumulation implicitly takes place in the position domain instead, this result is important for showing the equivalence of the two methods. As all measurement errors perfectly cancel it also gives a strong first hint that random-walk is no problem when applying the accumulation strategy. In the over-all case, the model of the phase range vector for the base epoch is constant whereas it has to be recomputed at each epoch for the accumulation case basing on the solution of the previous epoch. Here the final solution is obtained by accumulating the incremental base vectors whereas it drops out directly from the over-all approach. Assuming equivalence of the respective results, there is an interesting "additive input-output linearity" as indicated by the two dashed boxes in the flow chart. This very equivalence shall be investigated graphically for the case of a "pinned" satellite geometry by Figure 3.6(a): The base position at $t_{1=b}$ is known as is the change of the phase range to each satellite within $t_2 - t_1$ in terms of the time-differenced measurements. This results in nothing else but fixing the ambiguities – with values which are wrong but consistent to each satellite. Ignoring the clock error for the sake of clarity one can now draw a circle (a sphere in the 3D case) with radius ρ_2^j and center in the jth satellite's location. Intersecting these circles for all observations yields the receiver position at t_2.[5] As shown in the figure this is repeated for

---

[5]For the sake of clarity only the circles centered in a second satellite are indicated by the gray arcs in Figure 3.6(a).

the subsequent epochs when working with the accumulation strategy. Applying the over-all approach means to directly calculate ρ_5 for each satellite and to intersect the respective circles skipping the intermediate steps, see the grey, bold dashed arc. With the range equivalence demonstrated in Eq. (3.24) it becomes clear that one winds up at exactly the same position no matter which strategy is applied. For the sake of clarity satellite motion has been ignored so far but is now introduced in Figure 3.6(b). As depicted the same methodology can be applied for this "real world" scenario and again both approaches result in the same position – they are virtually equivalent.

These findings can be confirmed by the evaluation of real experiments. Figure 3.7 shows according results from processing 5 min of static L1 phase data[6] collected by the IGS network station BRUS. As the reference "trajectory" is known for a static receiver, the analysis of such data is particularly illuminating. Any offset from zero is known to be an error caused either by measurement noise or error drift. This is shown by the left diagram of Figure 3.7(a) for both the over-all and the accumulation strategy. Within both approaches the same subset of satellites is used and the respective solutions virtually coincide. Surprisingly the remaining difference is of systematic nature – but of second order only. It is depicted by the right-hand diagram. This difference is smaller than the position error by an order of magnitude for limited time intervals. It is likely to be caused by a bias of the base position as discussed in Section 3.2.3. As it is of no practical interest in the scope of the present applications this difference will not further be investigated on. The central conclusion of the results presented in Figure 3.7(a) is the confirmation (no proof!) that *no random-walk effects* are encountered when applying the accumulation strategy.

When processing kinematic (flight test) data signal shadowing and loss-of-lock events are a severe problems which reveal the assets and drawbacks of each strategy in real-world scenarios. Such scenario has been created by artificially excluding healthy satellites from the static BRUS data. Figure 3.7(b) illustrates the consequences: (I-II) 9 PRNs are available for both strategies, see the right-hand diagram.[7] The results coincide and yield the same three dimensional error as shown in the left-hand side plot. (II-III) A low elevation satellite is excluded for both approaches (PDOP $1.6 \rightarrow 1.9$). From now on the over-all strategy uses 8 PRNs for calculating the base vector pointing from t_I to t_{II+} whereas the accumulation strategy only calculates the incremental base vectors for $t > t_{II}$ with 8 satellites. They are added up to the unchanged trajectory interval I-II and the two solutions begin to diverge. (III-IV) An additional higher elevation PRN is excluded for both approaches (PDOP $1.9 \rightarrow 2.7$). This could happen e.g. due to antenna tilting. Within the over-all solution a step of

---

[6]Observation file: brus121b00.09o; ephemerides: igs15295.sp3; satellite clocks: igs15295.clk_30s; TEC map: igsg1210.09i

[7]An elevation mask lower than the one set for Figure 3.7(a) is used here. Therefore there are 9 satellites available instead of 8 at the very beginning of the processing interval.
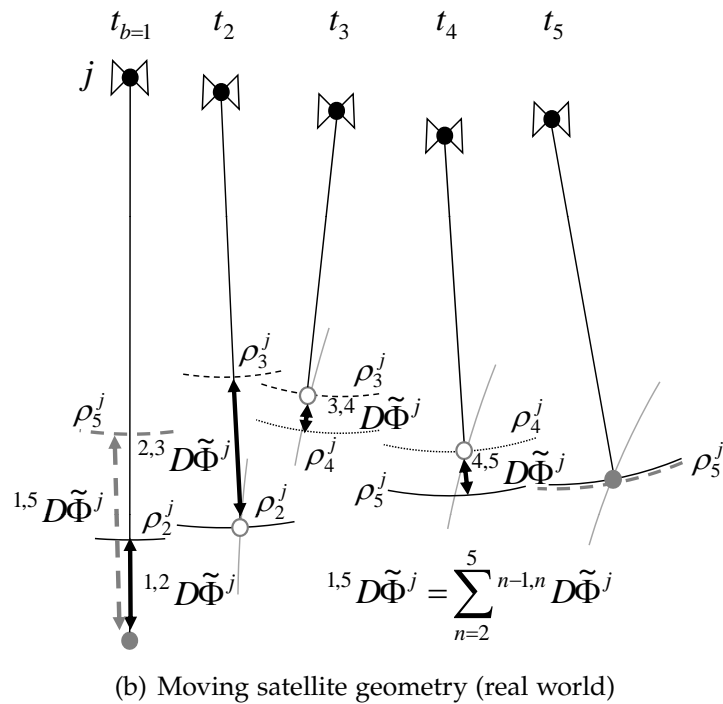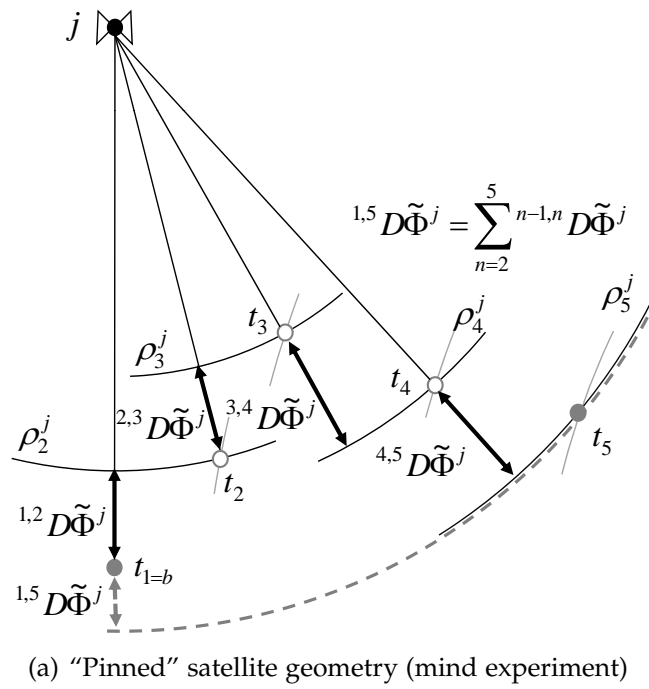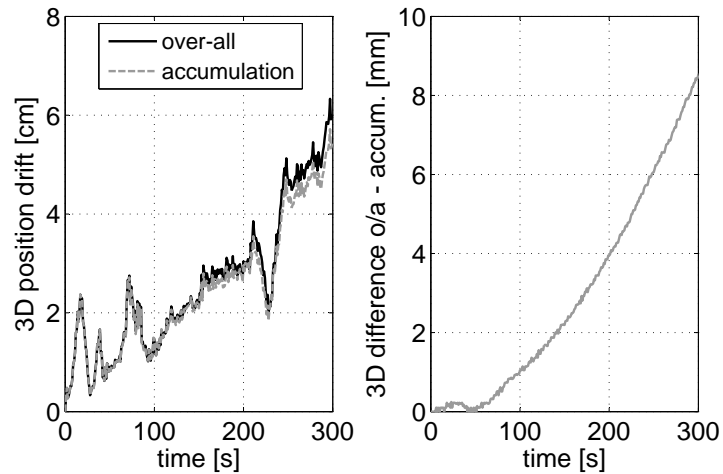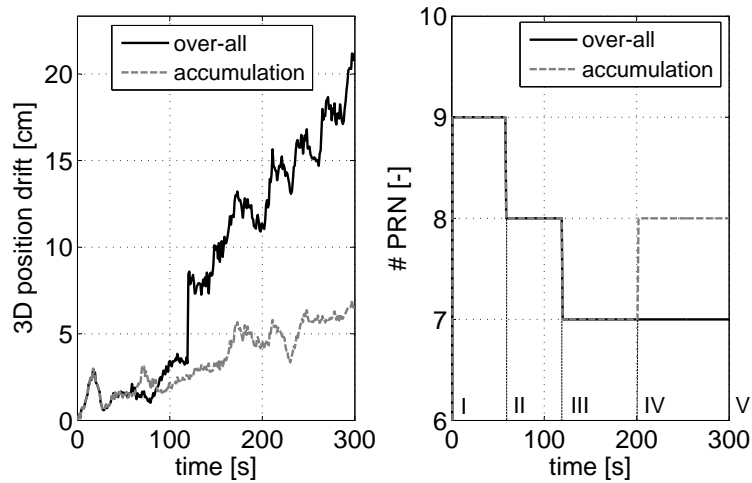
(a) "Pinned" satellite geometry (mind experiment)

(b) Moving satellite geometry (real world)

Figure 3.6: Graphical proof of equivalence of the over-all and the accumulative trajectory reconstruction strategy

(a) 3D position error (*left-hand side*) and 3D difference between the over-all and the accumulation strategy (8 used PRN, PDOP 1.8)

(b) 3D Position error (*left-hand side*) and number of used satellites for a scenario with changing number of available satellites

Figure 3.7: Comparison of two time-difference solution strategies for static L1 phase data sampled with 1 Hz by the IGS reference station in Bruxelles (BRUS)

several centimeters appears: the base-vector calculated with 8 PRNs between t_I and t_{III-} is different from the one calculated between t_I and t_{III+} with seven satellites only . Also the accumulation solution has to cope with the reduced set of satellites, but evidentially no discontinuity in terms of a step-shaped jump appears in the final solution. (IV-V) The PRN excluded at t_{III} is reused in the accumulation solution – say the receiver managed to re-acquire phase-lock to the respective satellite. Being given that this means a change in the ambiguity it is *impossible re-use a once excluded PRN in the over-all solution*. For the incremental solution however, this is no problem at all! The prodigal son can simply be welcomed back and processing is continued with 8 satellites and improved PDOP.

This discussion points out the fundamental advantages of the *accumulation strategy*:

- No random-walk effects are encountered - this constitutes the basic prerequisite for applying this strategy at all.

- Considering that only position increments are calculated, the drop-out of individual satellites cannot cause discontinuities in the resulting trajectory. This is especially important when it comes to velocity determination via numeric differentiation in the position domain.

- A common subset of satellites is required between subsequent epochs (t_{i-1}, t_i) only, not between the beginning of the processing and the current epoch (t_b, t_i). As a consequence, satellites which have not been tracked at t_b can be used right after phase-lock acquisition. This also holds for PRNs which dropped out along the way due to e.g. antenna tilting or cycle slipping. The latter can be reused even though their ambiguity inevitably changes when the receiver reacquires phase-lock. This is impossible within the over-all approach. As a consequence, there is no need to distinguish between cycle slips and other outlying measurements when monitoring the solution integrity, see Section 4.2.2.

- As it will be shown in Chapter 4 the incremental solution as used for the accumulation strategy has to be calculated for each epoch also for the over-all approach when noise estimation and integrity monitoring is an issue (which is usually true). Hence the accumulation strategy outperforms the over-all approach also when it comes to the required numerical effort.

These advantages are opposed by the following restrictions:

- Usually phase lock is not lost without a reason. Hence it has been observed while evaluating multiple experimental data that reusing a frequently lost satellite necessarily improves DOP values but not compulsively the final solution – despite strict quality monitoring as described in Chapter 4. As usually no reference trajectory is available, it is often hard to tell whether it is better to exclude such candidate at all or not.

- A time-difference solution is affected by error drift. For its real-life application, the prediction of an upper bound of this drift is crucial. This will be addressed in Chapter 4. However it will turn out when processing difficult static and dynamic data in Chapter 5 that the determination of such upper bound becomes difficult when using the accumulation strategy. Especially when there is a frequent variation of the used subset of PRNs, the error bound prediction gets overly pessimistic.

For concluding this discussion one can summarize: If the data to be processed are of good quality, i.e. if there are no satellites lost on the way, it is recommended to use the over-all strategy because the error estimate will be more reliable. In all other cases the accumulation strategy should be preferred – for very difficult data it is often the only way to achieve satisfying results at all.

3.3.2 A Note on Velocity Determination

"Calculating position increments means calculating speed and this is what is basically happening here, right?" This question is asked with good cause. Indeed delta range based (Eqs. (2.21) and (2.22)) speed calculation may look very similar to position estimation by time-differences, especially when it comes to the accumulation strategy. This Section intends to point out some fundamental differences between both approaches and to show advantageous aspects of the time-differential approach.

Just as the over-all strategy also the accumulation strategy recurs to the core equations derived in Section 3.2.1, pp. 39. The input are phase observations differenced between subsequent epochs $^{n-1,n}D\widetilde{\Phi}$, see Eq. (3.4). The net result of these equations are position (and receiver clock error) increments. These increments are implicitly accumulated (not integrated!) to a base vector β^{bi} pointing from a starting epoch t_b to the current epoch t_i. With the initial receiver position and clock error ξ_b known from code based single point processing, the current receiver position ξ_i is calculated and output by the algorithm.

As opposed to positioning, velocity determination is based on equations according to Section 2.2.2, pp. 29. The required inputs are range rate type observations. For this purpose either the raw Doppler observations as directly output by the receiver, Eq. (2.21), or delta ranges calculated from raw phase observations according to Eq. (2.22) can be used. As raw phase measurements are available in the present context, the latter method is assumed here to apply for precise velocity estimation. [8]

Both approaches are opposed in Figure 3.8. Applying adequate methods for differentiating position to velocity (see Section 6.1, pp. 95) or integrating velocity to

---

[8]Note that the use of (subsequent) raw phase observations for speed determination as used within the accumulation approach is a necessary precondition for avoiding random walk when integrating to position.
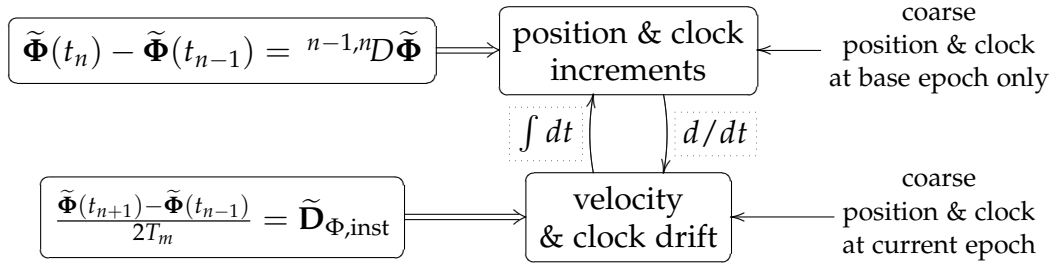
Figure 3.8: Positioning by time-differences opposed to velocity calculation by delta ranges

position, both methods yield equivalent outputs. As they use the same input one can expect equivalent precision – assuming that corresponding correction models are used. Despite this alikeness in terms of interface, both methods do implement *very different core equations* – resulting in different problems and caveats. It is the latter point where the benefits of the time-differential approach come to force:

Precise velocity determination is a linear problem wich requires a priori knowledge about the current receiver position in order to determine the unit vectors pointing form the receiver to the satellites, see Eq. (2.52). Here the current receiver position can be (and usually is) calculated via single point positioning which constitutes an additional operation on top of the solution of the velocity problem. For the time-differential approach, this operation only has to be performed once when determining the base position. Hence the computational load is reduced.

Another advantage when working with time-differences is the fact, that the raw data measurement rate T_m does not need to be known precisely but implicitly drops out of the solution. Especially when working with low-cost receivers, this rate is not constant but subject to variations in the millisecond range. Moreover all observations are tagged by the receiver clock reading. In general the oscillator stability of low-cost receivers is poor and clock steering is often performed in a discrete manner leading to millisecond jumps in the receiver clock error, see Odijk et al. (2007, Figure 1). It is possible – but difficult – to correct for these effects when determining speed based on delta ranges and again the coarse C/A code solution is required. When working with time-differences, these problems are automatically solved because the sampling rate is not part of the observable.

The primary goal of the majority of GPS applications is position determination based on range-type measurements. As a consequence a wide choice of range correction models and measurements for different signal errors is available in the literature or provided by IGS, see pp. 21. These corrections can be used "as is" for time-differential processing. For velocity determination, they first need to be converted to range rate corrections. This bears the risk of precision degradation due to neglecting higher order terms.

Finally the time-differential approach has the potential to estimate both high fre-

quency position noise and low frequency, systematic position *drift*. Estimating the latter means nothing else but estimating velocity *bias* – which is very hard to achieve (if possible at all) when working in the velocity domain only. The next Chapter will address this topic besides general integrity monitoring aspects.

4 Quality and Integrity Monitoring

In the present context the *quality* of a positioning solution refers to the noise and the error drift this solution is affected with. A meaningful error estimate enables the user to effectively tune solution parameters and to make solid statements about the final positioning precision. The general ability of a GNSS system to provide timely warnings when the system should not be used is commonly referred to by the term *integrity* (Kaplan, 1996). As integrity is probably *the* weak point of the Global Positioning System it has to be assured by some kind of Receiver Autonomous Integrity Monitoring (RAIM). The main RAIM task in the scope of time-differential processing pertains to the detection and exclusion of erroneous measurements.

4.1 Error Estimation

GPS raw data typically do not (directly) provide information about the stochastic characteristics of the recorded observations (Gurtner and Estey, 2007). For that reason the first step towards estimating the error of the final solution in the position domain is error determination in the range domain. According to the results presented in Section 3.2.2 this can be accomplished by normalizing the residual level by the system's degree of over-determination, compare Eq. (3.16):

$$\sigma_{D\tilde{\chi}}{}^2 = \frac{^{xy}D\mathbf{f}^T \; ^{xy}D\mathbf{f}}{m - 4} \tag{4.1}$$

As discussed in this Section the above statement only holds if there is a sufficient excess of available measurements (at least five but better six or seven satellites in view) and if these measurements are mutually uncorrelated, unbiased and of equal standard deviation. These conditions also pertain to the error propagation into the position (and time) domain which is accomplished by the concept of dilution of precision as previously introduced by Eqs. (2.39) through (2.44):

$$\text{solution error} = \sigma_{D\tilde{\chi}} \cdot \text{DOP} \tag{4.2}$$

The following Sections will refer to Eqs. (4.1) and (4.2) for addressing the important tasks of estimating both the noise and the error drift the time-difference solution is

affected with. This is done even though the listed conditions required for applying these equations in a mathematically blameless way cannot always be fulfilled completely or even partly. However, the analysis of real data shows that the correlation of the respective estimate with the true error is sufficient for significant quality analysis.

4.1.1 Noise Estimation

Accumulation strategy Error drift does virtually not affect subsequent epochs (t_{n-1}, t_n) and the residuals dropping out of the solution when applying the accumulation strategy, see Section 3.3.1, are directly related to the stochastic component of the range errors. (These residuals are called *"incremental residuals"* in the following.) Hence the measurement noise can be estimated by replacing the indices x and y in Eq. (4.1) by $n-1$ and n. In this case there is no correlation between the individual measurements, they are unbiased and of virtually equal variance. Hence all preconditions are fulfilled and the noise the position is affected with can be calculated by Eq. (4.2).

Over-all strategy The residuals dropping out of the solution between long(er) time intervals (t_b, t_i) are primarily related to the systematic error component but only very little to the stochastic one. Hence noise estimation is a priori impossible when applying the over-all approach. It will turn out that not only noise estimation but also RAIM is impossible when calculating the base-vector between t_b and t_i. For that reason the incremental solution between t_{i-1} and t_i has to be calculated in addition to β^{bi} if nothing is known from external sources about the expected measurement error and there is a substantial risk of outlying measurements or cycle slips. Obviously this implies a rise of numerical effort.

4.1.2 Error Drift Estimation

Over-all strategy For time intervals exceeding a few seconds the predominant component of the error in $^{bi}D\widetilde{\Phi}$ is of systematic nature. In this case all measurements are both strongly mutually correlated and biased. Empirical analysis (and Eq. (4.5)) reveals that this is directly reflected in the residual level of the solution between t_b and t_i (referred to as *"over-all residuals"* in the following). Replacing the indices x and y by b and i in Eq. 4.1 and inserting the result (which no longer corresponds to the common notation of variance) in Eq. (4.2) yields an estimate for the drift the position is affected with.

Accumulation strategy Just as there is no measure for the stochastic error component available when working with the over-all solution, there is a priori no means to estimate the error drift when applying the accumulation strategy. Luckily it turns out [1]

---

[1] by empirical investigation, derivation (yet) missing

that it is possible to artificially reconstruct the over-all residuals out of the incremental residuals by accumulation:

$$^{bi}Df^j_{\text{accum.}} \approx \sum_{n=b+1}^{i} {}^{n-1,n}Df^j \tag{4.3}$$

Of course it is tacitly assumed here that the same satellite subset is used when solving for β^{bi} and $\beta^{n-1,n}$ for all epochs. These *"accumulated residuals"* can now be used in Eq. (4.1) for estimating the error drift in the measurement domain to be propagated into the position domain by once more using Eq. (4.2).

4.1.3 Quality Monitoring of Static Sample Data

Both the possibilities and limitations of the quality monitoring methods proposed in the above are to be pointed out by their application to an exemplary 5 min interval of clean static data recorded with a low-cost L1 receiver[2]. The resulting error when using both the over-all (o/a) and the accumulation (accum.) strategy is depicted in subplot (a) of Figure 4.1. The long term drift, superimposed by high-frequency noise, amounts to 15 cm after 300 s for both approaches which, according to the discussion in Section 3.3.1, virtually coincide. 7 satellites are visible throughout the whole processing interval with PDOP values of approx. 2.1 (b). The root mean square of the incremental residuals is depicted in subplot (c). Normalization with the degree of over-determination according to Eq. (4.1) (and square-rooting) yields an estimate for the standard deviation of the noise component of the time-differenced phase-measurements (d). This noise propagates to the position domain by multiplication with PDOP according to Eq. (4.2). Subplot (e) illustrates the resulting values for $\sqrt{\sigma_n^2 + \sigma_e^2 + \sigma_d^2}$. As stated in Eq. (4.3) the incremental residuals stemming from the accumulation strategy can be summed up for approximating the over-all residuals required for drift estimation. This is shown by subplot (f) for PRN 11. The unbiased noise-like signal represents the incremental residuals (incr.): $^{n-1,n}Df^{11} = {}^{n-1,n}D\widetilde{\Phi}^{11} - {}^{n-1,n}D\widehat{\Phi}^{11}$. Summing up the incremental residuals results in the grey line representing the accumulated residuals (accum.) which agree well with the over-all residuals (o/a): $^{bi}Df^{11} = {}^{bi}D\widetilde{\Phi}^{11} - {}^{bi}D\widehat{\Phi}^{11}$. The error drift itself can now be determined either by the over-all strategy or the accumulation strategy as depicted by subplots (g) and (h). The grey lines represent the root-mean-square values of the respective residuals, the black line is the associated measurement drift estimate and the bold black lines are the final estimates of the 3D position error drift. It is desirable that the deviation of these estimates from the real drift as depicted in

---

[2]Ublox evaluation kit with patch antenna, refer to Section 5.1 pp. 73 for details. Used ephemerides: igs14143.sp3; used satellite clocks: igs14143.clk_30s; used TEC map: igsg0450.07i
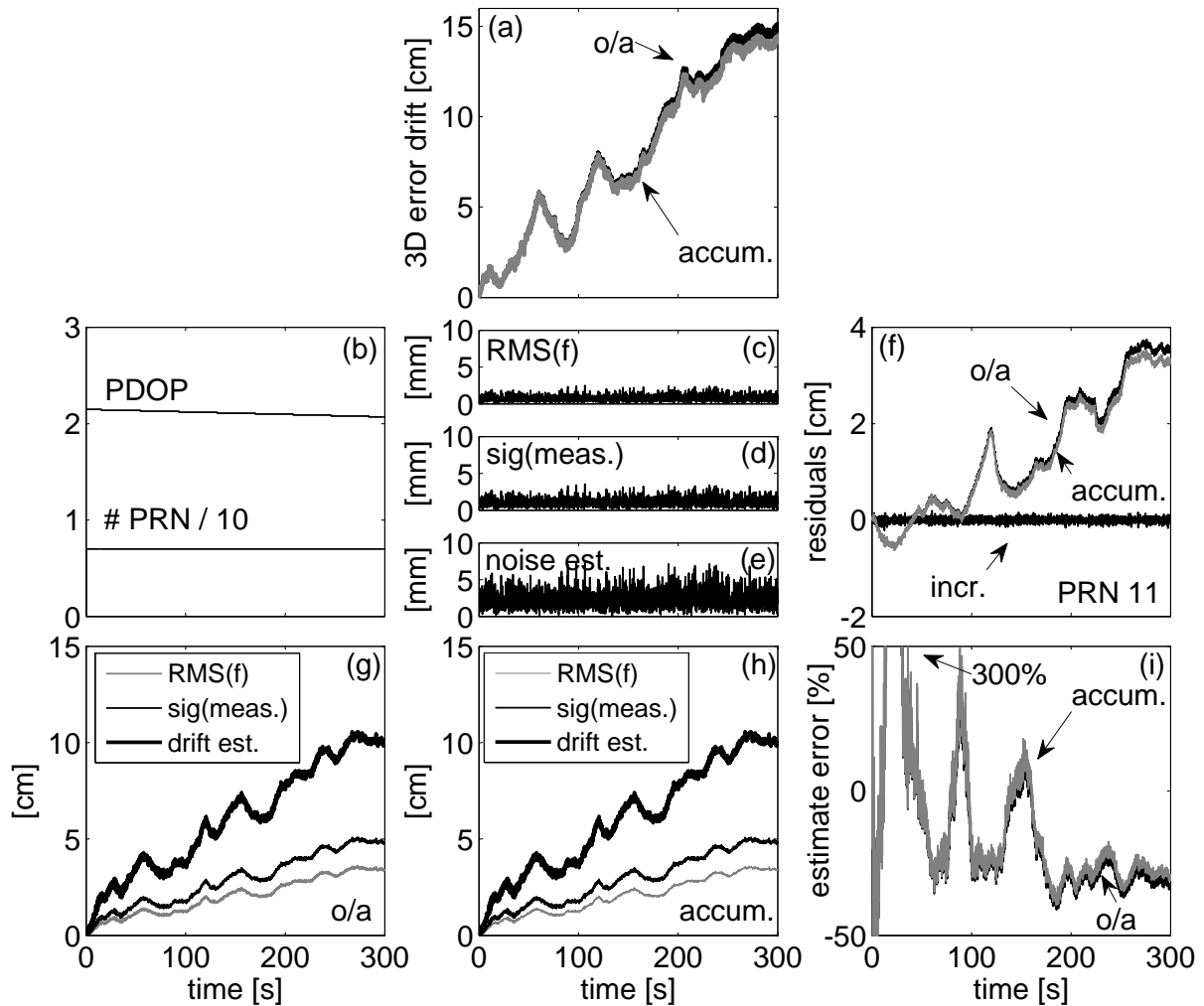
Figure 4.1: Quality monitoring for clean, static data. *(a)* 3D error drift for both over-all (o/a) and accumulation (accum.) approach. *(b)* Position dilution-of-precision and number of used satellites. *(c)* Root-mean-square of incremental residuals. *(d)* Estimated standard deviation of measurement noise. *(e)* Estimate of the noise component of the 3D position error. *(f)* Approximation (accum.) of the over-all residuals (o/a) of PRN 11 out of the incremental residuals (incr.) by accumulation. *(g)* Estimate of 3D error drift by the over-all strategy. *(h)* Estimate of 3D error drift by the accumulation strategy. *(i)* Deviation of the drift estimate from the real 3D position error drift for both approaches.

(a) is small. The relative deviation of the drift estimate from the real drift is illustrated in subplot (i). For small errors, the estimate exceeds the true error by a factor of 3 but converges to below 40 % for increasing time-spans. As indicated by the coincidence between over-all and accumulation strategy in subplot (f), also the final error estimates of both approaches are very similar and match the real error within less than an order of magnitude.

With these results a means to estimate the solution quality in the absence of a reference trajectory is found.

4.2 RAIM: Outlier and Cycle Slip Detection

Continuous phase lock is key when working with time-differences: the carrier phase range ambiguity remains constant allowing for complete cancelation by subtracting consecutive measurements, see Eq. (3.2). However, a temporary loss of lock may cause the ambiguity to change, resulting in a *cycle slip*. In addition to such slips the phase observable can be affected by other *outliers* for various reasons, e.g. multipath. Figure 2.2 on page 13 illustrates the effects of both outliers and cycle slips to the phase range measurements. Time-differencing does neither cancel slips nor outliers, so they must be *detected* and *excluded* from the solution as each slipped cycle corresponds, at the L1 frequency, to 19 cm of range error – which is much if decimeter-level or better precision is required. Cycle slip detection is typically based on geometry-free observables or measurement predictions. Canceling the range component requires either dual-frequency measurements or knowledge of the receiver dynamics from, e.g. inertial sensors (De Jong, 1998). However, these features increase hardware costs and are not available in the present project's scope with its central objective of working with low-cost single frequency receivers only. Measurement prediction can be done by simple polynomial fitting or using, e.g. a Kalman filter. The wavelet transform has also been applied to cycle slip detection (Gun et al., 2006). In a dynamic application the measurements may, however, be hard to predict or model with wavelets. RAIM has been extensively researched and successfully used in traditional pseudo-range based GNSS positioning, but such a method has also been applied to carrier observables (Odijk and Verhagen, 2007). RAIM is based on measurement redundancy which poses a requirement of an over-determined system of equations. The least squares position solution residual can be used as a measure of consistency: if the norm of the residual exceeds some predefined threshold value, an alarm is raised. Further investigations can be made to pinpoint the faulty measurement. The goal of this work is to use and to assess the performance of a RAIM method on cycle slip and outlier detection in the context of stand-alone time-differenced data.

4.2.1 Cycle Slips and Outliers in Carrier Phase Observations

The phase ambiguity N' as introduced in Eq. (2.13) is usually referred to in units of *full* carrier cycles. However there may be an additional half-cycle ambiguity due to the navigation message modulated on the signal. As the message is not known beforehand, it cannot be removed to obtain a clean sinusoidal carrier wave to track. For that reason carrier tracking loops are commonly constructed as Costas loops which are insensitive to $180\,°$ phase shifts, see Section 2.1.2. Such a loop does not know if it is tracking the carrier correctly or off by 180 degrees (Kaplan, 1996). If such receiver is used Eq. (2.13) rewrites to

$$\Phi(t) = \rho(t) + c\delta^R(t) + \frac{\lambda}{2}N' \tag{4.4}$$

The receiver can, however, resolve this ambiguity by examining the decoded navigation data bits, but if it, for some reason, fails to do so, the ambiguous part of the carrier phase measurement is $\frac{\lambda}{2}N'$ while normally it is $\lambda N'$. The receivers used in the experiments described hereafter for supporting the theoretical discussion are Costas-type half-cycle ambiguity receivers. If the signal tracking is subject to a temporary (shorter than a sampling period) discontinuity, the integer fraction of the ambiguity N' may change while its fractional part remains consistent – a *cycle slip* occurred. As it can be seen in the upper plot of Figure 4.2 cycle slips are of persistent nature, i.e.
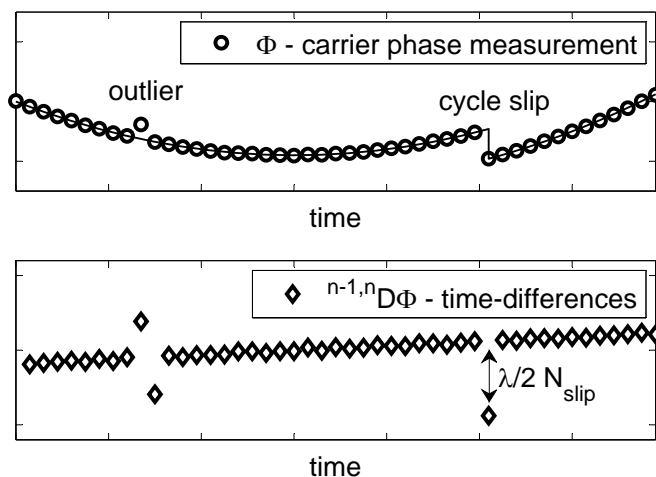
Figure 4.2: Schematic visualization of a phase measurement affected with an outlier and a cycle slip (top) and the corresponding time-differenced observable

the change in N' by $\frac{\lambda}{2}N_{\text{Slip}}$ will affect all subsequent measurements to the same satellite as well. Due to the half-cycle ambiguity, the smallest possible slip is $\pm^1/_2$ cycles, equivalent to approximately $10\,\text{cm}$ at the L1 band. Note that, in contrast to N', N_{Slip} ideally is an integer number. The receiver may also be, due to e.g. multipath, subject to random-magnitude (no integer constraint) temporary measurement blunders,

yielding *outlier* measurements. Such errors not necessarily affect subsequent epochs but are often restricted to single epochs only, refer again to Figure 4.2. For RAIM within time-differential processing, only incremental time-differences $^{n-1,n}D\Phi$ are to be used. The lower plot of the figure shows how this observable is affected by erroneous measurements: Single outliers now affect two subsequent epochs in opposite "direction" whilst cycle slips only affect one epoch with an ideal peak size of $\frac{\lambda}{2}N_{\text{Slip}}$. These characteristics are proposed as an approach for future outlier and cycle slip discrimination and repair.

4.2.2 Detection and Exclusion Using Time-Differences

In civil aviation GNSS is primarily used for coarse positioning based on C/A pseudoranges (FAA, 1994). Measurement errors are uncommon but large (dozens or hundreds of meters) and usually caused by the space segment. In a safety-critical application such as aviation, the user cannot wait – possibly for hours – for the control segment to detect the satellite malfunction and upload new satellite health data. Thus, the receiver must be able to autonomously detect and exclude biased measurements in order to meet the required positioning performance specifications. In addition the user must be informed about the maximum positioning error caused by faulty measurements which may pass unnoticed with the current false-alert and no-detection probability settings. There exist various algorithms to address this task of which three can be shown to be equivalent (Brown, 1992). This original application of RAIM totally differs from the context of cycle slip and outlier detection where errors are small, occur considerably often, and are mainly caused by the user segment, e.g. receiver dynamics and the environment. However, RAIM is based on measurement redundancy in least squares estimation. Hence it is directly applicable to the time-difference positioning task. The basic equations for slip *detection* (there is a slip within the current satellite subset at all) are reviewed in the following according to Brown and Chin (1997). In a next step an algorithm for identifying and *excluding* the biased PRN is discussed.[3]

Test Statistics

In order to transfer the results given by Brown and Chin (1997) to the time-difference problem, let's resume the core least squares equations, derived in Section 3.2, for an incremental solution: The linearized measurement equations are given by

$$^{n-1,n}D\widetilde{\boldsymbol{\Phi}} = {}^{n-1,n}D\widehat{\boldsymbol{\Phi}}(\boldsymbol{\xi}_{n,0}) + \mathbf{H}_{\xi_{n,0}}\Delta\boldsymbol{\xi}_n + {}^{n-1,n}D\boldsymbol{\chi}$$

---

[3] The presented results are mainly based on Kirkko-Jaakkola et al. (2009).

resulting in a least squares estimate for the position and time solution update for each iteration cycle

$$\Delta \boldsymbol{\xi}_n = (\mathbf{H}_{\boldsymbol{\xi}_{n,0}}^T \mathbf{H}_{\boldsymbol{\xi}_{n,0}})^{-1} \mathbf{H}_{\boldsymbol{\xi}_{n,0}}^{\ T} \left({}^{n-1,n}D\widetilde{\boldsymbol{\Phi}} - {}^{n-1,n}D\widehat{\boldsymbol{\Phi}}(\boldsymbol{\xi}_{n,0}) \right)$$

$$\boldsymbol{\xi}_{n,k+1} = \boldsymbol{\xi}_{n,k} + \Delta \boldsymbol{\xi}_n$$

The error the enhanced base-vector is affected with after convergence writes to

$$\boldsymbol{\beta}_{\text{true}}^{n-1,n} - \boldsymbol{\beta}^{n-1,n} = (\mathbf{H}_{\boldsymbol{\xi}_n}^{\ T} \mathbf{H}_{\boldsymbol{\xi}_n})^{-1} \mathbf{H}_{\boldsymbol{\xi}_n}^{\ T}\ {}^{n-1,n}D\boldsymbol{\chi}$$

with $\boldsymbol{\xi}_n$ and $\boldsymbol{\beta}^{n-1,n}$ representing the converged solution. (Note that the measurement error ${}^{n-1,n}D\boldsymbol{\chi}$ is unknown.) The residual vector in the range domain is given by

$$
\begin{aligned}
{}^{n-1,n}D\mathbf{f} &= {}^{n-1,n}D\widetilde{\boldsymbol{\Phi}} - {}^{n-1,n}D\widehat{\boldsymbol{\Phi}}(\boldsymbol{\xi}_n) \\
&= \left(\mathbf{I} - \mathbf{H}_{\boldsymbol{\xi}_n}(\mathbf{H}_{\boldsymbol{\xi}_n}^{\ T} \mathbf{H}_{\boldsymbol{\xi}_n})^{-1} \mathbf{H}_{\boldsymbol{\xi}_n}^{\ T} \right) {}^{n-1,n}D\boldsymbol{\chi}
\end{aligned}
\tag{4.5}
$$

This equation describes the propagation of errors from the measurement into the residual domain. As there is virtually no measurement error drift for subsequent epochs, it is apparent that the range residual level, i.e. the length of the residual vector $|D\mathbf{f}| = \sqrt{D\mathbf{f}^T D\mathbf{f}}$ of an incremental solution is reduced compared to the one resulting from an over-all solution between t_b and t_i. Outliers and and cycle slips will therefore cause significantly more distinct peaks in $|{}^{n-1,n}D\mathbf{f}|$ than in $|{}^{bi}D\mathbf{f}|$. For that reason $|{}^{n-1,n}D\mathbf{f}|$ is proposed as an appropriate test statistics for the cycle slip and outlier detection task. The indices $n-1, n$ will be dropped in the following for improved readability. Analyzing the stochastic characteristics of this test statistics would require a digression to the concept of *parity space*. The interested reader is referred to the tutorial-like derivations given by Brown and Chin (1997) and only the final results are summarized here:

- The statistics distribution of $|D\mathbf{f}|$ is *independent of the constellation geometry* for a given number m of used satellites. In other terms, if there are e.g. seven satellites in view, it is irrelevant for the residual level in the range domain whether this PRN subset yields DOP values of 1.5 or 7.8. Considering that varying DOP values *do* affect the final bias in the position domain, this can be considered a rather surprising finding resulting from parity space transformation. It is the basis for using $|D\mathbf{f}|$ as test statistics.

- The assumption of uncorrelated, unbiased and normally distributed range errors holds for ${}^{n-1,n}D\chi^j$ conditioned on the absence of an erroneous measurement. In this case the squared test statistics $|D\mathbf{f}|^2$ reveals a centralized (but unnormalized) chi-square distribution with $k = m - 4$ degrees of freedom. For the general, nor-
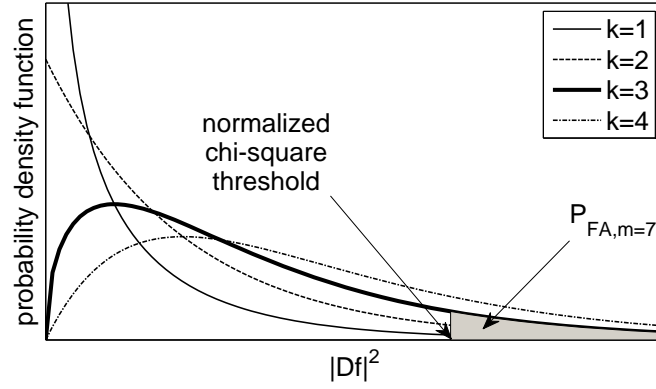
Figure 4.3: Normalized chi-square probability density function for $1 \leq k \leq 4$ degrees of freedom. The grey area corresponds to a specified false alert probability P_{FA} for the case of $m = 7$ satellites in view.

mal case, the corresponding χ^2-probability density function (PDF) for a stochastic variable x writes to

$$p(x) = \frac{x^{(\frac{k}{2}-1)}e^{-\frac{x}{2}}}{2^{\frac{k}{2}}\Gamma(\frac{k}{2})}; \quad x > 0$$

$$= 0; \quad x \leq 0$$

(4.6)

Figure 4.3 shows this relationship for different degrees of freedom.

Detection Threshold

Based on these results a decision rule for outlier and cycle slip detection can be made up: an outlier (or cycle slip) alert is issued if the condition

$$|D\mathbf{f}| \overset{?}{>} T_D \quad \text{with } T_D = f(P_{FA}, \sigma_{D\chi}, m)$$

(4.7)

holds. Here, the decision threshold T_D has to be calculated from the inverse chi-square probability density function for a given measurement standard deviation, the respective number of satellites in view and a specified *false alert rate* P_{FA} as illustrated by the grey area in Figure 4.3. P_{FA} is the probability that a detection takes place, conditioned on zero range bias. The inversion of the chi-square PDF is difficult and not for all degrees of freedom analytical solutions exist. The code snippet given below shows how to realize the inversion for exemplary values (compare Figure 4.4) using MATLAB.

```
P_FA      = 3.33e-7;                    % False alert rate
m         = 7;                          % Number of used satellites
sigma     = 33;                         % Measurement noise [m]
T_D_norm  = chi2inv(1-P_FA,m-4);        % Normalized threshold
T_D       = sigma * sqrt(T_D_norm);     % Final threshold (T_D=189.37m)
```
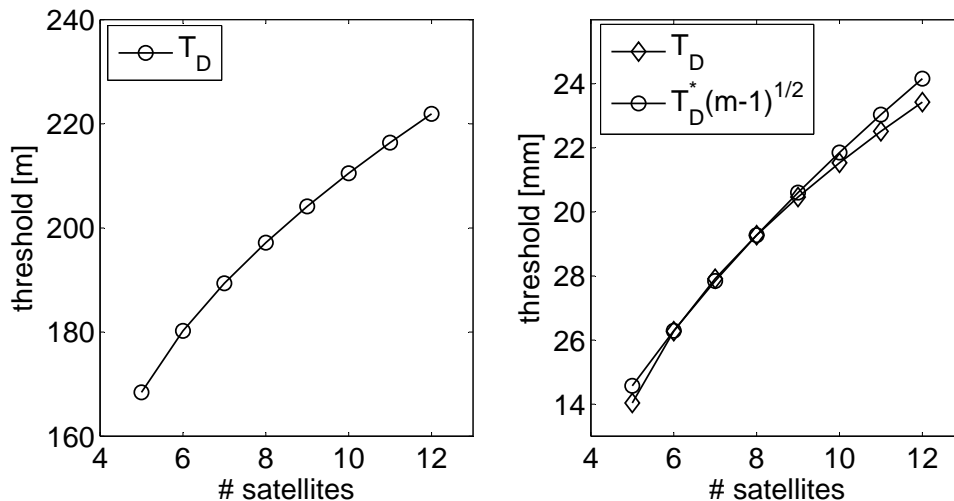
Figure 4.4: Different test statistics threshold settings for cycle slip and outlier detection. *To the left*: Reference values given by Brown and Chin (1997) for settings as applicable for C/A code receivers in safety critical civil aviation applications ($P_{FA} = 3.33 \cdot 10^{-7}, \sigma = 33\,\text{m}$). *To the right*: T_D – threshold for parameters which are typical for time-difference applications ($P_{FA} = 5 \cdot 10^{-3}, \sigma = 5\,\text{mm}$). $T_{D,\text{time-diff.}}$ – effectiv threshold for $|D\mathbf{f}|$ when working with RMS($D\mathbf{f}$) as test statistics and using the threshold T_D^*.

In this example reference values as proposed by Brown and Chin (1997) for C/A code-based civil aviation applications have been used. According results for various numbers of used satellites are given in the left-hand plot of Figure 4.4. Within the time-difference approach a test statistics slightly different from the one proposed so far is used

$$\text{test statistics} = \text{RMS}(D\mathbf{f}) = \sqrt{\frac{D\mathbf{f}^T D\mathbf{f}}{(m-1)}} \tag{4.8}$$

and an according decision rule is introduced

$$\text{RMS}(D\mathbf{f}) \overset{?}{>} T_D^* \quad \text{with } T_D^* = \text{constant} \tag{4.9}$$

$$|D\mathbf{f}| \overset{?}{>} T_D^* \sqrt{m-1} \tag{4.10}$$

Here T_D^* is independent of the number of satellites. This simplifies the implementation of the detection algorithm and alleviates computational load. The effective threshold for $|D\mathbf{f}|$ (i.e. if $|D\mathbf{f}|$ was chosen as test statistics instead of RMS($D\mathbf{f}$)) is still adaptive to the number of used satellites as it can be seen in Eq. (4.10). As shown by the right-hand side of Figure 4.4, this adaption is only off by less than 5 % from the threshold values proposed by Brown and Chin (1997) for parameters which are typical for non safety-critical time-difference applications – if T_D^* is set smartly. Smartly means: (1) Choose an appropriate false alarm rate, e.g. 0.5 % for non safety-critical applications. (2) Determine the expected measurement noise. This can be done either by empirical experience with the used equipment or by using the noise estimate as

given in Section 4.1.1. A phase noise standard deviation of 5 mm is typical for low-cost receivers in dynamic applications. (3) Determine a typical number of satellites for the data interval to be processed, e.g. $m_0 = 8$. (4) Get T_D from the inverse of the chi-square PDF for the chosen values. (5) Calculate $T_D^* = T_D / \sqrt{m_0 - 1}$.

Exclusion Algorithm

Once an appropriate threshold is defined a detection and exclusion algorithm as outlined by Figure 4.5 can be executed. Resting upon redundancy information out of
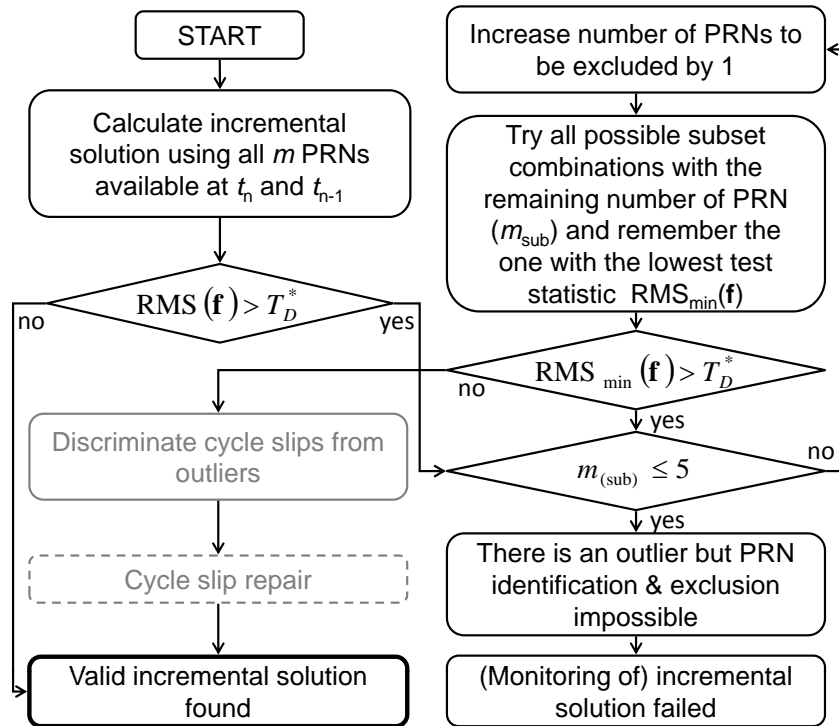
Figure 4.5: Outlier detection, identification and exclusion algorithm. Cycle slip discrimination and repairing is indicated in grey as a future option with the potential to increase the number of usable satellites.

the over-determined set of positioning equations, the test statistics will always be bound to zero for only four satellites in view. Consequently, outlier detection is impossible for the four-in-view case and exclusion is only feasible for more than five used satellites. This problem is common to all RAIM approaches. Due to Eq. (4.5) there is no direct relationship between measurement biases and range residuals on individual satellites. In other terms, if $D\widetilde{\Phi}^i$ is biased that does *not* necessarily imply a raised residual Df^i of that very satellite. For that reason a subset-based search strategy as shown in the figure has to be applied. Such strategy causes a high computational load, especially in multiple-outlier scenarios. This impedes the application of the method in real-time applications. Moreover, most RAIM schemes are based on a single-outlier assumption which does not hold in the context of cycle slip detection.

Hence RMS($D\mathbf{f}$) alone may not be ideally suited as test statistics for the multiple-outlier case, and alternative methods, as proposed e.g. by Hewitson and Wang (2006), potentially achieve improved results. As residuals of (t_{n-1}, t_n)-time-differences are the basis for outlier detection due to improved bias observability, a single error at, say t_n, always affects $^{n-1,n}D\widetilde{\Phi}$ and $^{n,n+1}D\widetilde{\Phi}$ with an offset of similar value but opposite sign, compare Figure 4.2. This can cause the erroneous exclusion of the respective PRN at t_{n+1}.

Nonetheless the discussed approach provides a suitable means of integrity monitoring based on time-differences. Being a true snapshot method, it is relatively easy to implement and can also be used as a preprocessing step for any carrier phase processing applications as no assumptions are made on, e.g. receiver dynamics. It further bears the potential of outlier and cycle slip discrimination and even repair.

4.2.3 Performance Testing

The presented method is tested using various sets of authentic GPS data, all logged by low-cost L1-only receivers. More details on the used equipment can be found in Chapter 5, pp. 73. During a flight test a stationary base receiver was available for reference RTK computations. Precise ephemerides, 30-second-sampled clock corrections and ionospheric correction data were used for all results.

Static Data

A static test is expected to be an easy starting point for validating the correctness of the theory. Stationary receivers are less prone to cycle slips than moving ones and the presence of range biases is easy to observe from the solution "trajectory" as it should not contain distinctive jumps. Figure 4.6(a) demonstrates the effect of outliers in the position domain and the upper left plot of Figure 4.6(b) shows the corresponding test statistics values. The data was recorded by a low-cost L1-only receiver with a $\frac{\lambda}{4}$ wire antenna.[4] The processed interval was short (only 22 seconds) but contained two measurement errors, both on the same satellite (PRN 4, 20° elevation) which are well visible in the trajectory computed without error detection. 9 satellites were available and only the remaining 8 were used after the outlier was detected. The measurement noise is estimated by the least squares solver to $\sigma_{D\widetilde{\Phi}} = 4\,\text{mm}$ and the detection threshold is set to $T_D^* = 7\,\text{mm}$ which corresponds to a false alert probability of $1 \cdot 10^{-3}$. The test statistics for disabled outlier detection ("off") shows three distinct spikes which are eliminated if the threshold is enabled ("on") leading to the exclusion of three measurements of PRN 4. The pattern of the corresponding time-differenced range

---

[4]Modified version of the GiPSy receiver, refer to Section 5.1, pp. 73 and to Figure 5.4, p. 79 for more information on this receiver.
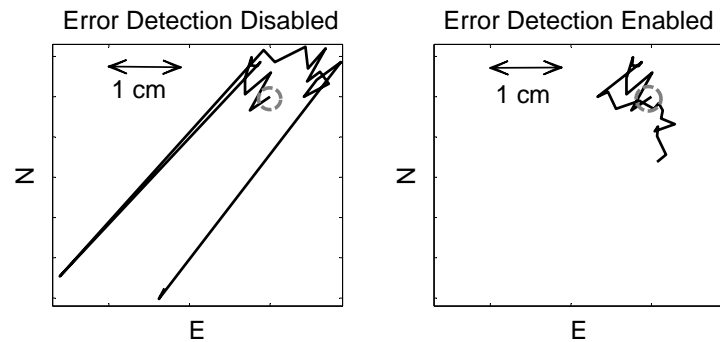
(a) Analysis in the position domain: East and north components of the trajectory resulting from processing without (*to the left*) and with (*to the right*) outlier detection and exclusion. The initial location is marked with a circle.
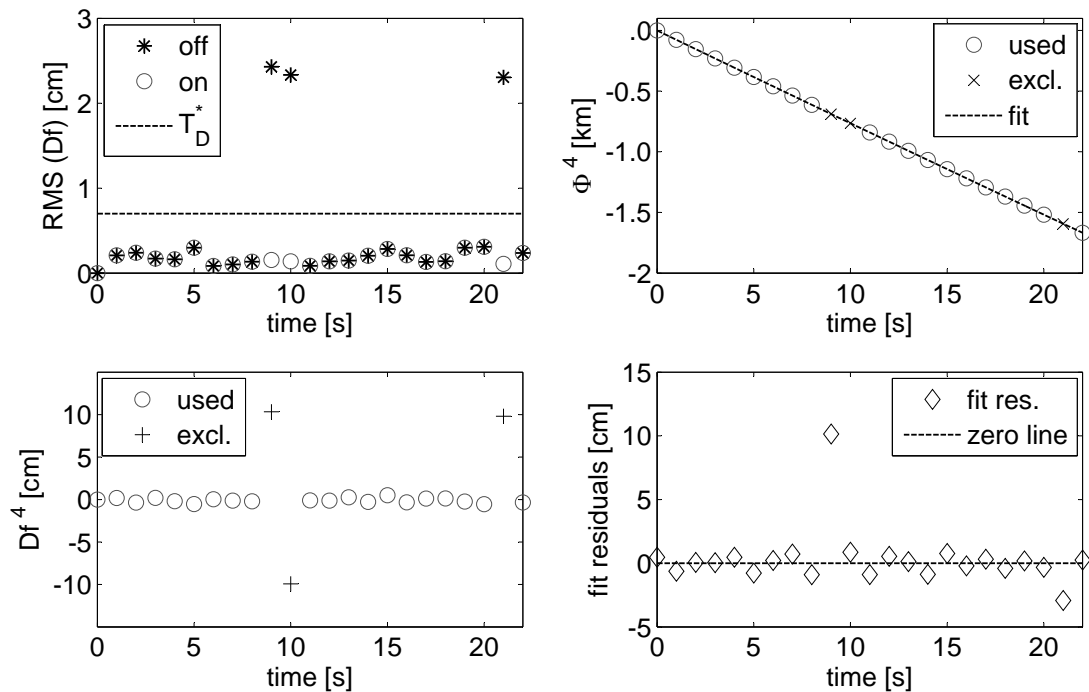
(b) *To the left*: Analysis in the range residual domain. *Top left*: Test statistics for disabled ("off") and enabled ("on") error detection with threshold T_D^*. *Bottom left*: Residuals of the time-differenced phase range measurements of the excluded satellite PRN 4. *To the right*: Analysis in the range domain. *Top right*: Non-differenced phase range measurements to PRN 4 fitted by a cubic smoothing spline. Data normalized to 0 for $t = 0$s. *Bottom right*: Fit residuals confirming the outlier hypothesis for the first exclusion.

Figure 4.6: Successful outlier detection and exclusion within 22 s of static data recorded by a L1 GPS receiver ($P_{FA} = 1 \cdot 10^{-3}$, $\sigma_{D\widetilde{\Phi}} = 4.3$ mm and $T_D^* = 7$ mm)

residuals as depicted by the bottom left plot of Figure 4.6(b) reveals a magnitude of $\frac{\lambda}{2}$ of the measurement errors proposing the presence of half-cycle slips. However, two subsequent epochs are affected in the first case. This indicates the presence of a simple outlier instead of a slip impeding a concluding discrimination. For validation purposes, the non-differenced observations to PRN 4 were interpolated using cubic smoothing splines yielding residuals (between spline and observation) with a standard deviation similar to the one expected for the range measurements, see top right plot of Figure 4.6(b). The excluded measurements where not used when fitting. The fit residuals (bottom right plot) confirm the outlier hypothesis in the first case. In the second case, the error is very small which prevents a solid discrimination.

Flight Test Data with Simultaneous Errors

As a real-life application, the time-differential method was used for estimating the take-off and landing distance of the Mü 30 "Schlacro" aircraft of AKAFLIEG München. The measurement process was repeated six times. During the landings the aircraft bounced remarkably after hitting the ground, resulting in excessive losses of lock within the data recorded by a miniaturized L1 GPS logging unit mounted on the left wing tip.[5] The reconstructed altitude profile is drawn in Figure 4.7(a). The zoomed version shows an abrupt jump of about 15 cm in the altitude. That section was processed continuously with carrier phases and as the data was logged at 10 Hz, it is not a plausible explanation that the dynamics would have changed suddenly. At the epoch of interest, the presence of one or multiple outliers was detected successfully, i.e. the test statistics exceeded the current threshold setting (RMS($D\mathbf{f}$) > T_D^* = 1 cm). The subsequent identification and exclusion algorithm (according to Figure 4.5) however excluded PRN 21 and 22. It is suspected that these identifications are incorrect. Figure 4.7(b) shows the time-differenced carrier phases for the used satellites, revealing three half-cycle slips. As it can be seen in the figure, PRN 22 is not affected by any outliers. Thus, two of the remaining cycle slips remain undetected. Forcing PRN 21 to be totally excluded from the computations does not help: a false solution fits well enough in the measurement subset containing two biased measurements, and thus the exclusion algorithm terminates after finding two satellites to be excluded. In this example the least squares residual itself is not a sufficient test statistics for detecting multiple simultaneous cycle slips. This agrees with the single-outlier assumption in most RAIM schemes mentioned in the above.

---

[5]Refer to Section 5.1, pp. 73 for more details on the used GiPSy receiver, and to Figure 5.8, p. 84 for details on the experiment setup.
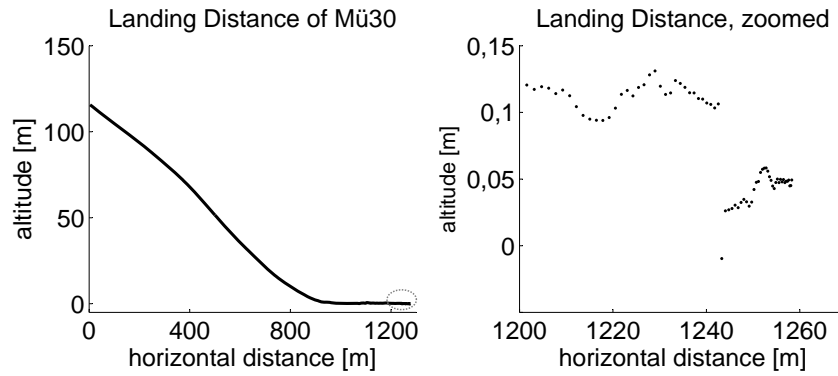
(a) Vertical profile of the time-difference solution during landing. The gap in the trajectory (see zoomed section *to the right*) is an indicator for erroneous slip identification.
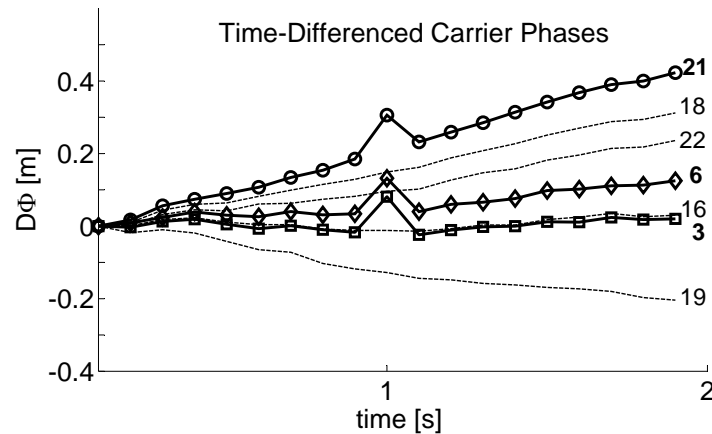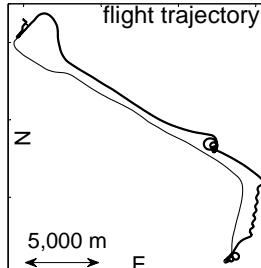

(b) Time-differences of consecutive carrier phases in the landing data. All lines have been shifted to begin at zero. The identification algorithm flags PRN 21 and 22 as faulty and excludes these measurements from further computation even though PRN 22 is healthy.

Figure 4.7: Successful slip detection but erroneous identification and exclusion within a multiple outlier scenario recorded by a miniaturized L1 receiver during an experimental aircraft hitting the ground when landing ($P_{FA} = 2 \cdot 10^{-3}$, $\sigma_{D\chi} = 6.5\,\mathrm{mm}$, $T_D^* = 1\,\mathrm{cm}$)

Flight Test Data Compared to RTK Solution

Another kinematic test was performed using a data set measured with an L1 receiver[6] during a test flight with the research aircraft G-109 of the Institute of Flight System Dynamics (see Figure 5.11, p. 88) starting from Oberpfaffenhofen. The data begins with a 15 minute stationary section to facilitate real-time kinematic (RTK) ambiguity resolution, followed by a flight containing circle and dynamic-soaring-like maneuvers. Especially during these very dynamic sections, the number of tracked satellites temporally dropped to low values (≥ 5) with accordingly poor DOP values. As opposed to time-differential processing, RTK is unaffected by error drift but requires a second base receiver and an initialization to work. More details on the RTK software are given in Section 5.3.1. Both was provided for this test flight for validation purposes. The cycle-slip detection and identification results of the time-differential solution were compared to those derived from an RTK solution computed at Delft University of Technology. A total of 165 errors, classified as cycle slips and outliers, were listed in the reference. The time-differential method detected 113 non-categorized errors. For all epochs where the time-difference method identified an error, consecutive time-differences of the carrier phase measurements of the suspected satellites were examined manually to see whether an error really had occurred or not. Table 4.1 shows how many exclusions were observed to be correct, wrong, or, as was the case for most epochs, uncertain due to, e.g. gaps in the phase data or, more frequently, non-uniform sampling of the phase measurements.[7] The detection results of the two

Detection Results	TD ✔	TD ✘	Uncertain	
TD / RTK Agree	6	3	20	
TD / RTK Disagree	9	8	30	
TD Detection only	2	4	31	

Table 4.1: Manual comparison of time-differential (TD) and real-time kinematic (RTK) measurement error detection results for kinematic data recorded during a test flight. The flight trajectory (*to the right*) is bold for the leading 26 min interval the RTK reference was available. The figures show how many of the detections were confirmed to be correct (✔) or wrong (✘), and at how many epochs the data were not suited for manual analysis.

methods were not expected to be identical as the RTK solution did not report any half-cycle slips (which was due to the software not being configured to do so) whereas the

---

[6]UBlox evaluation kit, refer to Section 5.1, pp. 73 for more information.

[7]The data was logged at 4 Hz but the measurement instants were not spaced by exactly .25 s and the timestamps had second fractions like .247, .499, .747 and .999. Data re-sampling by third-party software was not addressed as any kind of measurement manipulation was to be avoided. However, time-differencing such data yields oscillatory results making visual inspection of the presence of slips and outliers difficult – especially if the data originates from a highly dynamic scenario, as was the case.

time-differential method did detect some half-cycle slips. Moreover, the RTK solution is computed from double-differenced data which causes slips from both the rover and the reference receiver to be subtracted from each other. Thus, a slip detected in RTK can have occurred in either of the two receivers. Even though the rover receiver is more prone to cycle slipping, several RTK detections were observed to have occurred in the reference receiver. In the verifiable cases, the methods achieved a similar performance: supposing that RTK was right in cases where the time-difference method was verified to be wrong and the methods disagreed, both approaches were right in 50+x % of the verifiable epochs. Knowing that the flight data was highly dynamic and frequently suffered from a low number of tracked satellites, this can be considered as a fairly good performance. Without a second base receiver and without (static) initialization, the detection strategy as implemented in the time-difference approach yields results of a similar quality than obtained when addressing much more costly RTK methods.

4.3 Quality and Integrity Monitoring – Conclusion

The time-differential approach has the potential of both estimating the position and receiver clock solution error and monitoring the solution integrity. Concerning error estimation, the range residual level of the time-difference solution between subsequent epochs (accumulation strategy) is required for the high frequency part whereas the residuals of the over-all solution between the starting and the current epoch can be used for estimating low frequency error drift effects. As a consequence, the incremental solution has to be calculated in addition if the over-all strategy is addressed. This is also required for integrity monitoring. Vice vera, the over-all range residuals are to be reconstructed out of the incremental residuals when applying the accumulation strategy. This leads to restrictions when processing difficult dynamic data. Incremental range residuals are also the basis for integrity monitoring, i.e. the detection, identification and exclusion of biased measurements. A RAIM algorithm as usually applied within code-based aviation applications has been adapted and implemented for the detection of outliers and cycle slips with a defined false alert rate. A satellite-subset based identification and exclusion algorithm has been developed for pinning down the affected observations. For error detection, at least five satellites must be available; for identification and exclusion at least six PRNs must be tracked. The present snapshot approach can potentially be extended for outlier and cycle slip discrimination and even repair taking advantage of the respective range residual characteristics. However, when using the accumulation approach, it has been shown that neither discrimination nor repair are required. Most RAIM approaches are based on a single-outlier assumption and the in-depth analysis of real-life measurement data dis-

closed restrictions of successful error identification and exclusion in multiple outlier scenarios. Comparison with RTK reference data however indicates that the success rate of the implemented RAIM algorithm is very well on a competitive basis with much more costly approaches.

5 Practical Validation

Test results supporting the theoretical considerations have already been provided throughout the previous Chapters. For an in-depth validation of the potential of the time-differential approach within various practical scenarios, the present Chapter addresses further tests for which a reference trajectory was available. A summary of important results is given by Table 5.1, p. 94. Moreover technical details about the employed miniaturized equipment are given.

5.1 Equipment

The experiments described hereafter have partly been performed with two evaluation kits from the Swiss manufacturer Ublox featuring TIM-LL or TIM-LP receiver modules, see Figure 5.1(a). Both modules are identical except for some minor details which do virtually not affect positioning performance or measurement quality. The footprint of the modules is 25 mm × 25 mm, the mass is indicated with 3 g. Typical power consumption is 54 mA and the operation voltage is 2.7–3.3 V. The evaluation kits come with an active patch antenna in a plastic casing. The size of the patch is 25 mm × 25 mm × 4 mm. External power supply is required for operating the kits. The measured data are logged by a serial interface to a PC or laptop.

The miniaturized combined receiver and data logger GiPSy from the Italian manufacturer TechnoSmArt was used as a stand-alone alternative to the evaluation kits. The core device depicted in Figure 5.1(b) is as small as 44 mm × 21 mm × 4 mm and has a mass of only 4.25 g (without antenna and battery). A passive 25 mm × 25 mm × 4 mm patch antenna mounted on a 35 mm × 35 mm ground plate was used throughout the present experiments adding up the mass of the whole construction to 18,4 g.[1] GiPSy features the Ublox module LEA-4T with a footprint of 17 mm × 22.4 mm and a mass of 2.1 g. A USB interface allows the free setting of all module parameters. The data is logged to an integrated 8 MB flash memory and/or an external 2 GB SD card via an additional logging device similar to the Neurologger described by Vyssotski et al. (2006). The size of this external logging device is 50 mm × 36 mm × 5 mm; its mass it 6 g. The typical power consumption of GiPSy is approximately 40-45 mA driven

---

[1]Other antenna types (chip antennas, helix antennas, $\lambda/4$-wire antennas, coaxial antennas) did not reach the performance of the patch antenna in comparative tests.

(a) Ublox evaluation kit with TIM-LL receiver module
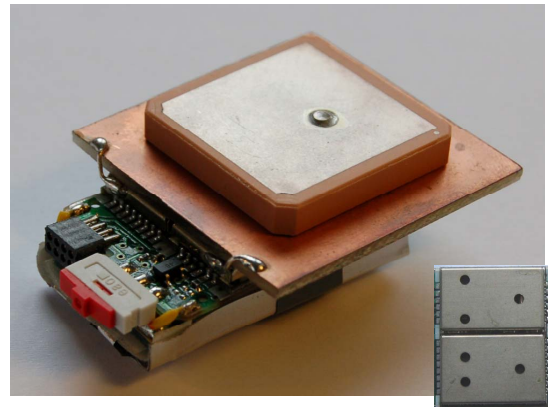
(b) Miniaturized receiver and data logger GiPSy from the manufacturer TechnoSmArt featuring a Ublox LEA-4T receiver module [Photo: TechnoSmArt]

Figure 5.1: GPS receivers used for practical tests (photos of GPS modules not true to scale)

by 2.9–3.7 V. The external logging device additionally requires approximately 6.7 mA. GiPSy and Neurologger were operated by a 3.7 V lithium-polymeric battery with a mass of 7.1 g.

Both the TIM and the LEA modules are single frequency receivers which output raw data in addition to the online positioning solution using the UBX proprietary protocol (ANTARIS, 2003). Whilst the latter can only be calculated with un update rate of 4 Hz, the raw measurements are available with up to 10 Hz. As problems where encountered when forcing the receiver to output both the online solution and the raw data with the respective maximum rates, the online solution was usually set to 1 Hz only when logging raw data with 10 Hz. A set of raw data (C/A code pseudoranges, Doppler range rates, L1 carrier phase ranges and signal to noise ratios) for e.g. 11 tracked satellites has a volume of 280 bytes (ubx-message RXM-RAW). For a measurement rate of 10 Hz this results in a data flow of 164 KB/min or 9.6 MB/h. Logging only the standard PVT solution and some quality indicators (ubx-message NAV-SOL) requires 60 bytes per fix independently of the number of tracked satellites. This yields 14 KB/min or 0.8 MB/h at an update rate of 4 Hz.

According to Ublox' technical support the LEA and TIM modules primarily differ in size, weight and power consumption whereas signal quality and positioning performance are identical. Hence the promising carrier range precision estimates of the TIM ZBL-test (refer to Table 2.1, p. 19) also hold for the LEA module.

5.2 Static Tests

The reference "trajectory" for static data is known a priory – it should ideally be represented by a single point. Due to noise and drift effects, this does not hold in real applications. As all deviations (from zero) can easily be observed, static data are a suitable starting point to assess the quality of the time-differential positioning solution.

5.2.1 Sensitivity Analysis by the Evaluation of Clean Static Data

The time-differential position solution is affected by both a high frequency noise-like error and a low frequency error drift component. The underlying physical effects in the range domain have been discussed in Sections 2.1.3, 3.1.1 and 3.1.2 and are summarized in the Tables given on p. 24 and p. 38. The error propagation to the position domain was addressed theoretically and a first evaluation of static measurement data gathered by the IGS network station BRUS was given in Section 3.3, p. 50.

The first part of the present results refers once more to these very clean data and analyzes the *impact of the used atmospheric correction models and precise clock and ephemerides data* on the solution quality.

In Section 3.2.3, pp. 42 the effect of a *bias in the base position on relative precision* was discussed from a theoretic point of view. Now the practical consequences of the found interrelations are demonstrated by artificially shifting the base solution used when processing static data. For this test data collected by a Ublox TIM evaluation kit in a benign environment are used.

Apart from sensitivity analysis the comparison of data from this low-cost receiver with the ones gathered by the geodetic grade BRUS receiver additionally provides an impression of the high performance-cost ratio of modern low-cost equipment.

Impact of Correction Models and Precise Ephemerides

The IGS network station in Bruxelles uses an Ashtech Z-XII3T GPS receiver in conjunction with an ASH701945B_M rooftop antenna as depicted in Figure 5.2. A randomly chosen 5 min interval (brus121b00.09o) of the 1 Hz sampled data has been processed by time-differences using the accumulation strategy. IGS final ephemerides (igs15295.sp3), high rate satellite clock corrections (igs15295.clk_30s) and a ionospheric TEC map (igsg1210.09i) have been used to calculate both an estimate of the initial position $\mathbf{x}_0$ by coarse single point processing and for subsequent carrier based processing. The troposphere was modeled using the UNB3 model. With 8 used satellites, PDOP values did not exceed 2.0.

Figure 5.2: IGS network site in Bruxelles [Photo: IGS]

The bold black line (1) of both plots of Figure 5.3(a) represents the resulting solution. The high-frequency noise-like error component is estimated to $\sqrt{\sigma_n^2 + \sigma_e^2 + \sigma_d^2} = 3.8\,\text{mm}$. The total 3-dimensional error with respect to the starting point $|\mathbf{x}_i - \mathbf{x}_0|$ stays below 6 cm which corresponds to a drift of not more than 0.2 mm/s. This drift goes below the lumped estimate of Table 3.1 by more than one order of magnitude – an indicator (no proof!) that these theoretic drift estimates are pessimistic. The blue line (2) shows the same solution when omitting the 30 s clock data for the time-differential solution[2] but using all other corrections comprising precise ephemerides. The total 3-dimensional error after 5 min rises to 22 cm whereas the high-frequency noise remains virtually unaffected (which also holds for the remaining scenarios discussed here). Omitting both high rate clocks and precise ephemerides but using the broadcast data instead increases the error drift to 1.7 mm/s, see green line (3). This significant decrease of precision corresponds to the difference of the respective estimates for broadcast and final orbit accuracies given in Table 3.1. The impact of the atmosphere was analyzed by omitting either the ionospheric correction (red line (4)) or the troposphere model (cyan line (5)) while using precise ephemerides and high rate clocks. Considering that no ionospheric model was used at all when omitting the IONEX map corrections, the increase in position drift is comparatively modest. Note that omitting ionospheric corrections degrades absolute range accuracy to a greater extent than the precision of carrier range time-differences. Omitting tropospheric corrections however causes a significant degradation of the present solution – 58 cm of 3-dimensional error after 5 min. Being given that good tropospheric corrections can be estimated without recurring to external data, such correction is highly advisable when working with time-differences.

---

[2]The initial code based single-point solution was kept unchanged during all scenarios.
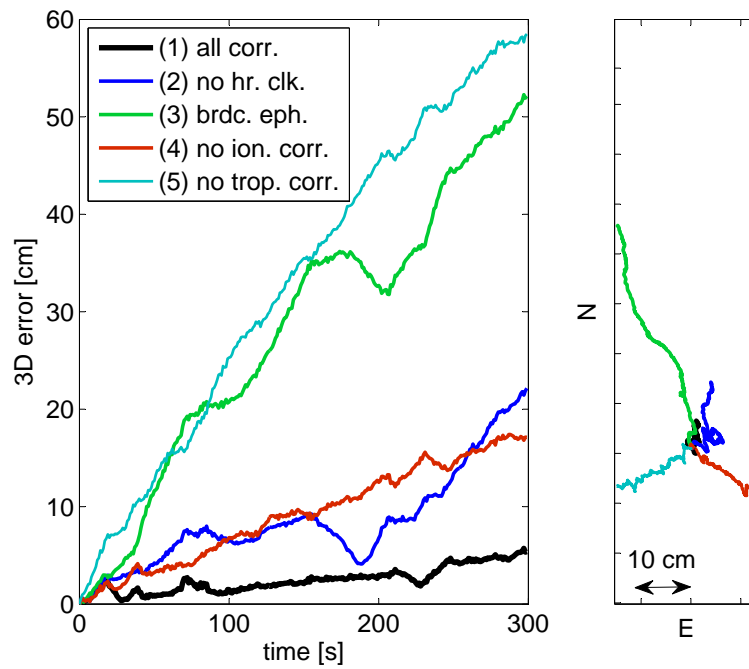
(a) 5 min of static data collected by the geodetic grade receiver of the IGS network station BRUS with the impact of various correction data and models
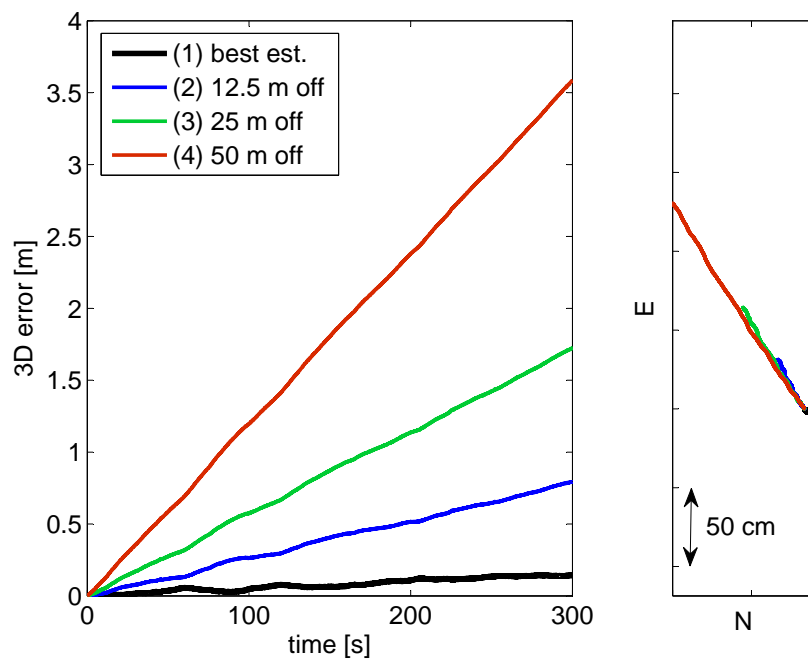
(b) 5 min of static data collected by the low-cost receiver module TIM with the impact of an artificial bias in the base position

Figure 5.3: Sensitivity analysis of the time-differential solution. *To the left:* Time history of the 3-dimensional error $\left|\mathbf{x}_i - \mathbf{x}_0\right|$. *To the right:* 2-dimensional footprint of the "trajectory" (vertical error component not visible).

Impact of a Bias in the Base Position

It has been shown by Eqs. (3.18) through (3.23) that a bias in the base position acts like an additional "geometric" range error. This is to be verified by artificially shifting the base position of a 5 min interval of static data collected by the TIM evaluation kit, see Figure 5.1(a). The data was collected under very clean environmental conditions on open fields near Munich on February 14th, 2007. All afore mentioned correction data and models have been applied for calculating the base position and the subsequent time-differential solution. With 7 satellites in view PDOP values did not exceed 2.15. The bold black line (1) of both plots of Figure 5.3(b) shows the best time-differential solution. Error drift is as low as 0.5 mm/s yielding a bias of 14 cm after 300 s. The high-frequency noise is estimated to $\sqrt{\sigma_n^2 + \sigma_e^2 + \sigma_d^2} = 2.3$ mm. Note that these values are competitive to the ones achieved by the BRUS Ashtech receiver. Shifting the base position by 12.5 m results in the blue line (2), an offset of 25 m yields the green line (3) and the red line (4) corresponds to a bias of 50 m. The base position was shifted in the same (random) direction for all 3 scenarios. The corresponding 3-dimensional position error after 5 min is 79 cm, 172 cm and 358 cm. These results agree with the linear dependency of the geometric range error on the base position bias stated in Eq. (3.23).

Sensitivity Analysis – Conclusion

The present results are not intended to make up with a (significant) statistical analysis. Such analysis would require an extremely (unrealistic) high amount of data as the number of effects to be captured is very high: the ephemeris error (drift) changes with the age of data and its impact on ranging depends on the current user position (and speed and motion direction for dynamic data), the residual satellite clock error depends on the oscillator type used by the currently tracked satellites, ionospheric activity reaches peaks within a period of several years, the weather (troposphere) changes on a daily basis and atmospheric errors strongly depend on the user's altitude, etc. However, in conjunction with the theoretic error (drift) estimates of the Tables 2.2 and 3.1 the results provide a valuable impression of the various effects and the benefits of the individual correction models.[3] The negative impact of a base position bias shows the importance of absolute range corrections when calculating the base position. Besides analyzing the solution's sensitivity these results also point out the high potential of the time-differential approach. Precision in the cm range is possible for time spans of several minutes when all corrections are applied. Furthermore it is shown that the high precision of the carrier phase measurements revealed by the ZBL tests results (see pp. 19) yields a very low noise level in the position domain.

---

[3]A similar sensitivity analysis with different test data can be found in Traugott et al. (2008b).

5.2.2 Error Drift Estimation with Difficult Static Data

Error drift effects cannot be avoided when working with time-differences. However the results of the previous Section show that this drift is small. High precision throughout intervals of up to several minutes is sufficient for a large number of applications – provided that an estimate of the current drift is reported to the user. The theory of error drift estimation has been investigated in Section 4.1.2 and was demonstrated by the evaluation of clean static data on pp. 57. Estimating the error drift is somewhat more challenging when the data is not so clean, especially when the accumulation approach is to be applied. In Eq. (4.3) it has been assumed that there is no change in the used satellite subset (the constellation) – this assumption does not hold when processing difficult data. In the case of a constellation change at the epoch t_i, ${}^{bi}Df^j_{\text{accum.}}$ has to be reset to ${}^{i-1,i}Df^j$ for *all* tracked PRNs. Consequently the range error drift estimate according to Eq. (4.1) drops in a steplike way. This directly propagates to the 3-dimensional position error estimate according to Eq. (4.2). However, the position error indicator can be appropriately "stitched" such as to finally yield a valid estimate. This shall be demonstrated by the evaluation of difficult static data gathered with a modified version of GiPSy featuring a $\frac{\lambda}{4}$ wire antenna as depicted in Figure 5.4.[4]
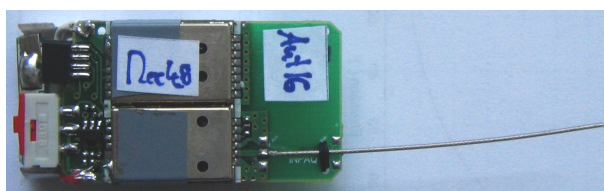
Figure 5.4: GiPSy with $\frac{\lambda}{4}$ wire antenna.

Just as during the analysis on pp. 57 the data was processed by both the accumulation (accum.) and the over-all (o/a) strategy. As depicted in the top left plot of Figure 5.5 not all 8 satellites in view where usable during the 5 min processing interval due to several phase outages of PRN 4 and 14 (22° and 36° elevation). Once dropped out, the respective satellite was not used anymore within the over-all solution causing PDOP values to increase from 1.9 to 2.35. When applying the accumulation strategy the dropped out satellites could be used again after phase lock reacquisition. The top right plot of the Figure exemplarily shows ${}^{bi}Df^9_{\text{accum.}}$ calculated by the accumulation solution and ${}^{bi}Df^9$ of the over-all solution. Note that both lines begin to diverge when PRN 4 drops out for the first time. Each time the constellation changes, the bold black line is reset close to zero: ${}^{bi}Df^9_{\text{accum.}} = {}^{i-1,i}Df^9$. The step in ${}^{bi}Df^9$ (grey line) at 211 s

---

[4]This configuration was tested within the assessment of antennas other than the patch antenna finally used. As shown here, even static data gathered with a wire antenna causes problems when processing carrier phase observations. Hence this antenna was discarded.
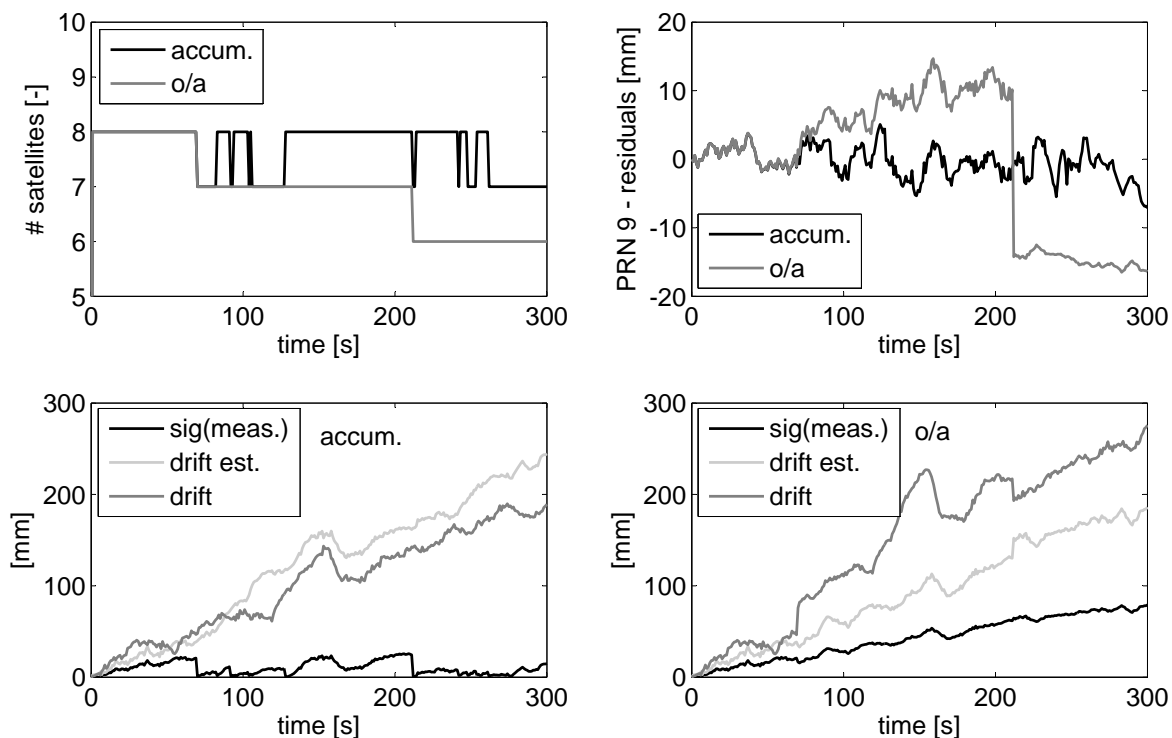
Figure 5.5: Error drift estimation with difficult static data. *Top left:* Number of satellites used throughout the accumulated and the over-all solution. *Top right:* Residuals of PRN 9 for both strategies. *Bottom left:* 3-dimensional error drift (estimation) for the accumulated solution. *Bottom right:* 3-dimensional error drift (estimation) for the over-all solution.

is due to the drop out of PRN 14 from the over-all solution. This event also causes a gap in the position solution (not depicted). Such effects have been addressed previously in the discussion related to Figure 3.7. The bottom left plot of Figure 5.5 shows the 3-dimensional error $|\mathbf{x}_i - \mathbf{x}_0|$ of the accumulated solution (dark grey line). The basis for estimating this drift is $\sigma_{D\widetilde{\chi}}$ reconstructed based on the individual ${}^{bi}Df_{\text{accum.}}^j$ of all tracked satellites according to Eq. (4.1) (black line). In analogy to the top right plot, this line shows steps close to zero whenever the satellite constellation changes. However, the implemented algorithm for stitching the final 3-dimensional error estimate according to Eq. (4.2) yields the light grey line. This estimate matches the real error drift well. The bottom right plot of Figure 5.5 shows the according results for the over-all solution. Considering that less satellites are used here, increased PDOP values cause a slightly higher 3-dimensional error drift (dark grey line). This drift can be estimated (light grey line) via $\sigma_{D\widetilde{\chi}}$ based on the carrier range residuals ${}^{bi}Df^j$ (black line) directly dropping out of the solution.

For the present case, the error drift estimate of the accumulated solution coincides with the real error even better than the one stemming from the over-all solution. These results demonstrate that also for a changing satellite constellation a valid error drift estimate is found for both the accumulation and the over-all time-differential strategy.

5.3 Dynamic Tests

Depending on DLL and PLL bandwidth, receiver motion does influence signal tracking quality. For that reason, the promising results of the static tests cannot be projected "as is" to dynamic applications but a comparison with reference solutions is desirable for validation purposes. According tests are provided within the present Section.

Most (low-cost) receivers provide the option to specify the type of receiver motion. Within the Ublox configuration software the user can choose between "stationary", "pedestrian", "automotive" "sea", and "airborne" (1 - 4 g). According to Ublox' customer support [oral communication], these settings only affect the positioning algorithm transforming the raw data to the online PVT solution but not the parameters of the tracking loops themselves. As all subsequently presented results are based on the raw data, they are not affected by any user settings.

5.3.1 Car Driving

A car driving test was performed on February 14th, 2007 on open fields in the north of Munich with the Ublox TIM evaluation kit. Driving speed did not exceed $14\,\mathrm{m/s}$ and the view to the skies was not restricted by buildings or trees. The experimental setup is depicted in Figure 5.6. With such such benign environmental conditions this test is chosen as an appropriate starting point for dynamic analysis.

For the sake of generating a reference trajectory, a second base receiver (Ublox TIM evaluation kit) was setup on a nearby tripod and a static initialization period of about $10\,\mathrm{min}$ was provided before starting to drive.

The reference solution is computed in a differential real-time-kinematic (RTK) mode using data of the base receiver. The double-differenced phase and code data of both receivers are processed using inhouse Kalman filter software of the Department of Earth Observation & Space Systems of Delft University of Technology. In this Kalman

Figure 5.6: Experimental setup. The white arrow points to the patch antenna of the evaluation kit.

filter the (float) L1 ambiguities are kept constant but no constraints are imposed on the dynamics of the rover coordinates. The software automatically detects cycle slips and outliers in the data and in case a cycle slip is identified the ambiguity state vector is adapted for this. The float ambiguity solution had converged after about 5 min such that the integer values could be estimated by means of the LAMBDA method (Teunissen, 1994). After checking whether these integer ambiguities would pass the Ratio Test with fixed failure rate (Verhagen and Teunissen, 2006), the ambiguity fixed solution for the rover position was computed. The solution is accurate to within a view millimeters and represents the state of the art in geodetic differential GPS processing.

The footprint of the driven trajectory is depicted by the upper plot of Figure 5.7. Throughout 170 s driving, 7 PRNs were tracked by the TIM module yielding PDOP values of about 2.1. The lower left plot of the Figure shows the time history of the vertical component of the TD (time-differential) solution.[5] The "spikes" are due to the bumpy gravel road – not due to noise! This noise is estimated to $\sigma_d = 2.3$ mm only. The black line of the lower right plot of Figure 5.7 shows the 3-dimensional relative deviation between the TD and the RTK solution $\left| \mathbf{x}_{\text{TD}} - \mathbf{x}_{\text{RTK}} \right|$. (Both solutions have been shifted such as to begin in the same point). After about 3 min they differ by only 9 cm. The grey line represents the error estimate of the TD solution (based on the accumulation approach). The congruence between drift estimate and the difference between the two solutions is striking.

In this experiment the setup of a nearby base receiver and static initialization was feasible – this is often not the case in more challenging field conditions. For such dynamic scenarios the present results endorse the time-differential method as a both efficient and precise alternative to much more costly differential approaches. This will be confirmed by the analysis of highly dynamic flight test data.

---

[5]Ephemerides: igs14143.sp3; satellite clocks: igs14143.clk_30s; TEC map: igsg0450.07i
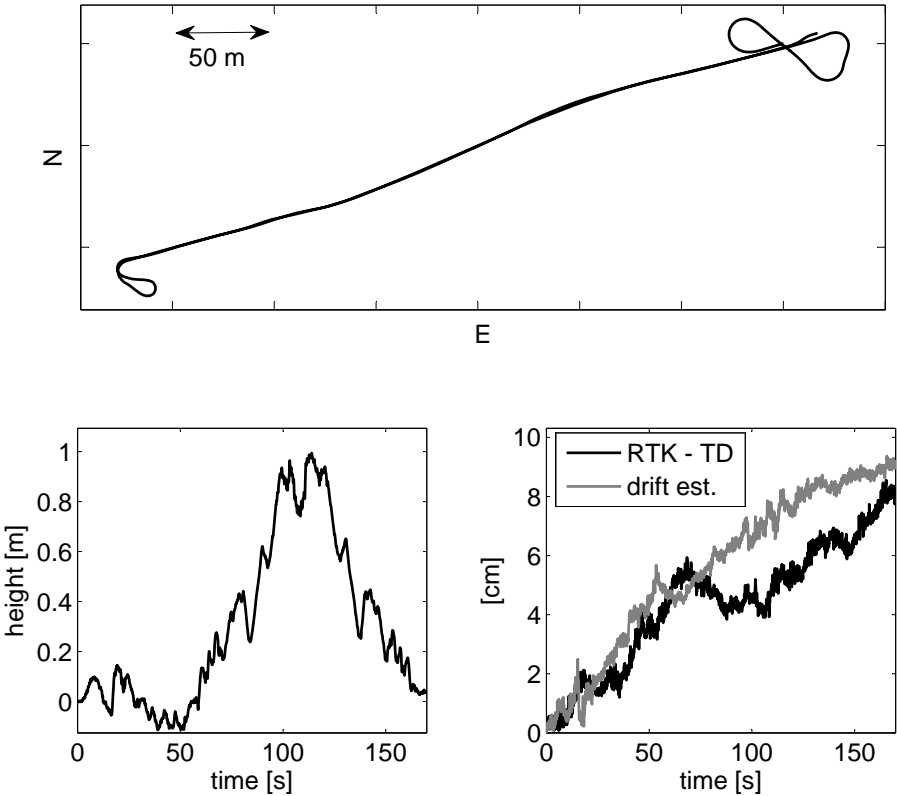
Figure 5.7: Car driving test on open fields with RTK reference solution. *Top:* Footprint of the trajectory. *Bottom left:* Time history of vertical trajectory component (bumpy gravel road). *Bottom right:* 3-dimensional error drift estimate and deviation of time-differential (TD) and RTK soltution.

5.3.2 Flight Tests – MÜ 30 "Schlacro" and G-109B Research Aircraft

A variety of flight tests has been performed – not only for validating the method but also for supporting maneuver reconstruction and flight performance analysis with the recorded data. A closer look on the respective results is intended to provide deeper insights into both the limitations and the possibilities of the time-differential approach in the scope of flight test applications.

MÜ 30 "Schlacro"

MÜ 30 "Schlacro" is an aircraft designed and built by the student organization AKA-FLIEG of Technische Universität München. The project was in the airworthiness certification phase in 2008 and some performance parameters have been identified supported by the time-differential approach. For that reason the aircraft was equipped with the miniaturized receiver GiPSy mounted at the left wing tip as depicted by Figure 5.8. Just as for the car driving test, static data were collected by a reference

Figure 5.8: MÜ 30 "Schlacro" with the miniaturized receiver and data logger GiPSy mounted at the very outside of the wing

station (TIM evaluation kit) mounted close to the airfield in Fürstenfeldbruck (about 25 km west of Munich). Again a converged RTK solution could be calculated by the department of Earth Observation & Space Systems of Delft University of Technology serving as a highly accurate reference. Precise IGS ephemerides, 30 s sampled clock corrections and TEC maps were used for processing.[6] The test was performed on May 15th, 2008.

The top left plot of Figure 5.9 shows the footprint of the eight-like maneuver analyzed in detail here. The according vertical profile of the 110 s trajectory section is given in the upper right plot. Both the over-all and the accumulation strategy have been applied to the raw data for the sake of comparison. The results are provided by the lower left (over-all) and lower right (accumulation) plots of the Figure. The

---

[6]Ephemerides: igs14794.sp3; satellite clocks: igs14794.clk_30s; TEC map: igsg1360.08i
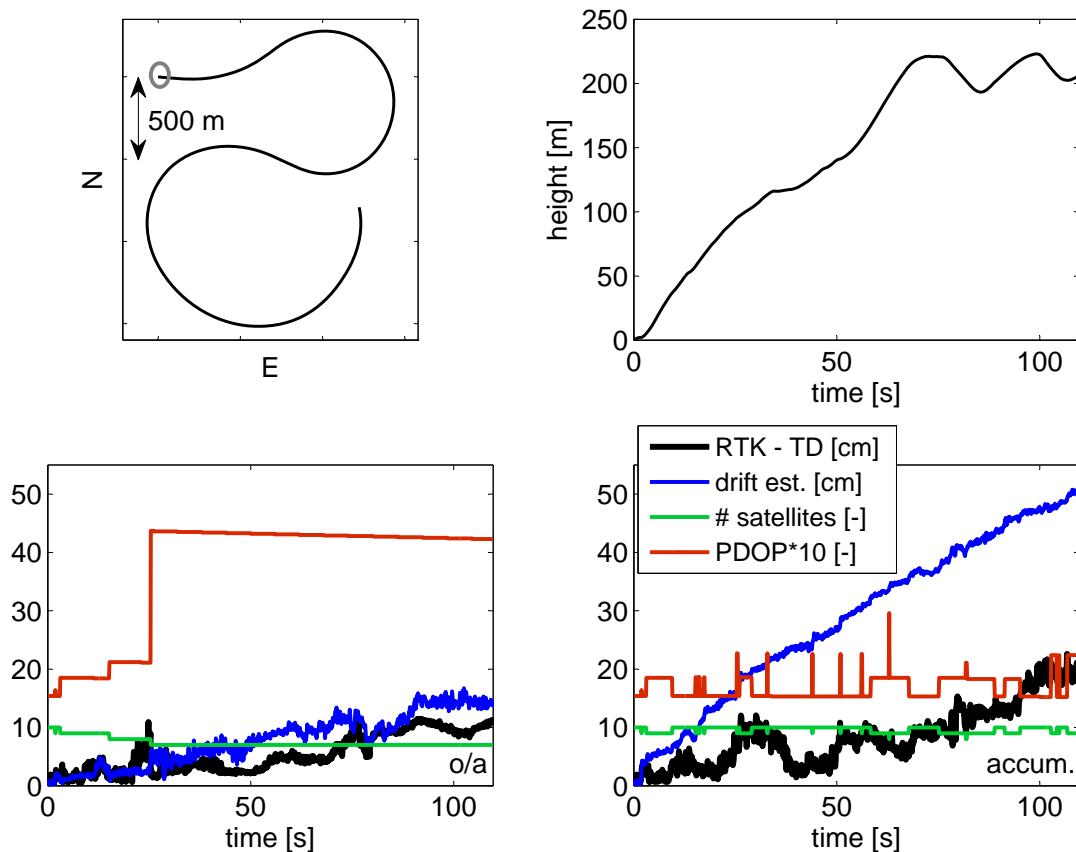
Figure 5.9: MÜ 30 "Schlacro" flight test with RTK reference solution. *Top left:* Trajectory of the "eight" maneuver analyzed by time-differences. Start marked by grey circle. *Top right:* Time-history of the vertical solution component. *Bottom:* Deviation between the time-differential solution and the RTK reference solution and 3-dimensional error estimate. (The *left* plot refers to the TD solution by the over-all approach, the *right* plot shows the results of the accumulation strategy. The legend is identical for both plots.)

black line is the 3-dimensional aberration of each TD solution from the RTK trajectory $|\mathbf{x}_{TD} - \mathbf{x}_{RTK}|$. For the over-all solution the difference is as small as 11.4 cm after 110 s, the accumulated solution winds up at 20.5 cm difference. This corresponds to an average drift of 1.04 mm/s and 1.86 mm/s. As already pointed out in Section 5.2.1 this drift is significantly lower than what can be expected by the (pessimistic) range error rate estimates given in Table 3.1. Due to the dynamics of the maneuver, the carrier phase of the PRNs 4, 23 and 24 (24°, 13° and 8° elevation, elevation mask used for processing: 7°) is not tracked continuously by the LEA-4T module. As a consequence, the number of satellites used within the over-all solution successively reduces from 10 to 7 (green line) with an according increase of PDOP values (red line). The lost satellites are re-used as soon as possible when applying the accumulation strategy. This results in significantly better PDOP values. Nevertheless this solution reveals a higher error drift. This can be explained by the increased measurement noise caused by the "unstable" satellites. With 7 used PRNs, the measurement noise of the over-all solution is estimated to 2.1 mm whereas it is 2.9 mm for the accumulation solution using all satel-

lites. Even though the high frequency measurement noise is theoretically unbiased, this practical analysis exhibits some coupling to systematic drift effects. This does not only affect error drift, but – to a worse extent – error drift estimation, too. Whereas in previous experiments the drift estimate resulting (blue line) from both approaches coincided well with the observed error, the accumulation based drift estimate is now pessimistic by a factor of 2.3. Considering that this is an *estimate* only, such result is acceptable but should be kept in mind when addressing data of even worse quality.

The integrity of the current solution has been monitored as described in Section 4.2. For validation purposes, here an additional solution has been calculated (by the accumulation strategy) with loose outlier detection threshold settings. The deviation of both the original (tight) and the new (loose) solution from the RTK reference is depicted by the upper left plot of Figure 5.10. For the tight solution T_D^* was set to 10 mm resulting in 6 exclusions as depicted by the center left plot of the Figure. Comparison with the grey line of the upper left plot reveals that the loose TD solution shows a bias with respect to the RTK solution in case of an undetected outlier (except for the first time T_D^* is exceeded). The right hand side plots of Figure 5.10 illustrate the residuals $^{i-1,i}Df^j$ of the corrupted satellites excluded from the tight solution at the epochs when the threshold is exceeded: $\mathrm{RMS}(Df) > T_D^*$. (These residuals are computed even though the respective satellite is *not* used within the tight solution at the moment an outlier is detected.) Both the comparison to the RTK solution and this analysis confirm the functionality of the exclusion algorithm. The deviation of the uncorrected solution from the reference points out yet another time the urgent need for such internal monitoring when processing difficult dynamic data as is the case.

As discussed in Section 4.2.1, (half-) cycle slips and other outliers affect the time-differenced observable in a different way. As explained on p. 61 this property bears the potential of cycle slip and outlier *discrimination*. The present results confirm this statement. PRN 23 is excluded at 4 epochs. Each time the residual analysis shows values close to $\lambda_1/2$ (95.1 mm). This proposes the presence of half-cycle slips. Such slips necessarily affect all subsequent epochs – as mirrored by the steps in the grey line of the upper left plot of Figure 5.10. Such a step is also observed at $t = 84.5\,\mathrm{s}$ when PRN 4 is identified to be biased. Here the residual pattern proposes the presence of 2 or even 3 subsequent half-cycle slips. The situation is different at $t = 2.0\,\mathrm{s}$ when PRN 10 is flagged as outlier. Here the zig-zag residual pattern does not indicate a cycle slip but the measurement is affected by some differently caused bias. In accordance there is no step-like divergence between the loose TD and the RTK solution. As a consequence, PRN 10 potentially could be re-used also in the over-all solution, compare the bottom left plot of Figure 5.9. (Note: The current implementation of the time-differential processing software realizes a basic cycle-slip and outlier discrimination logic, which was disabled here for generating the over-all solution. For
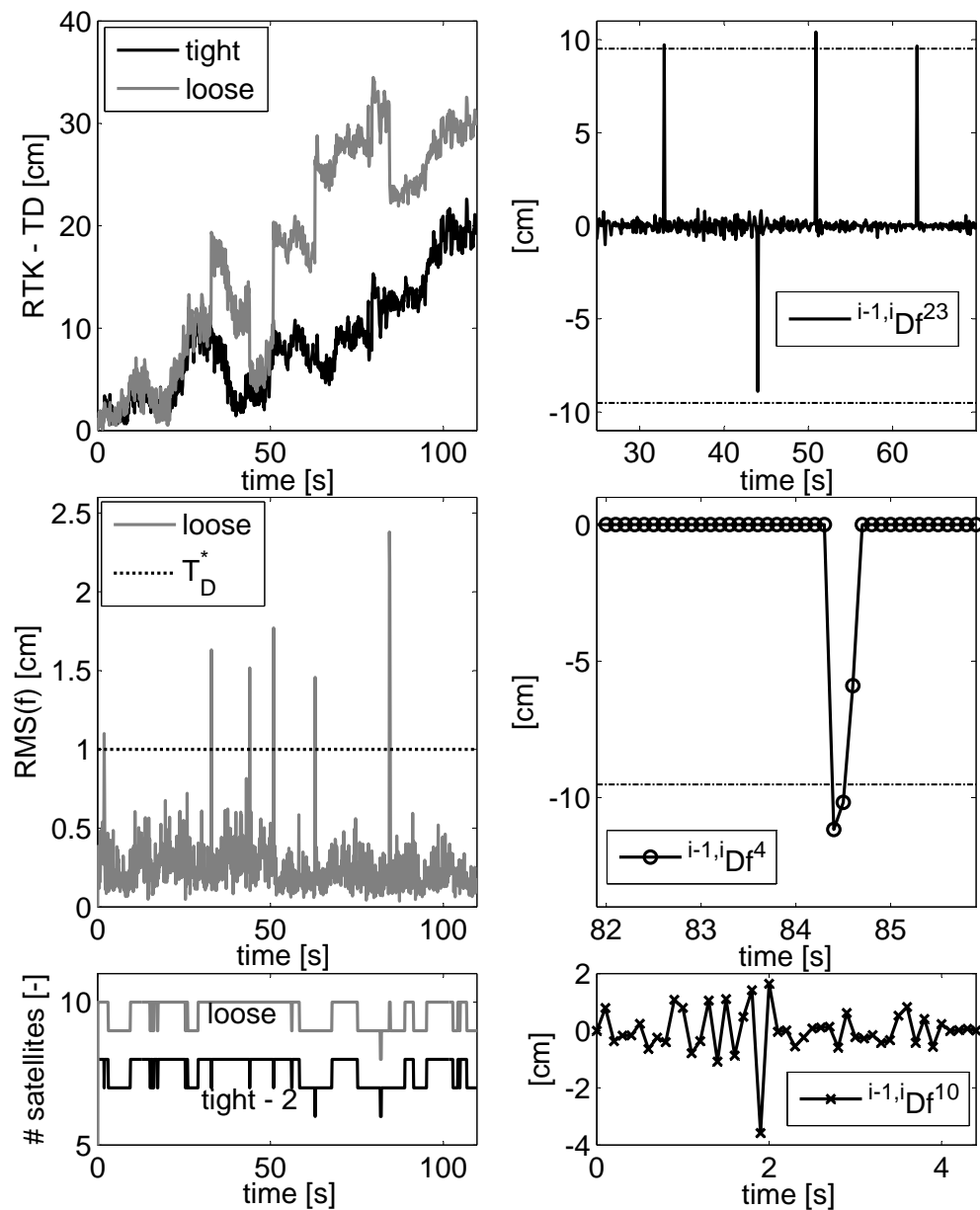
Figure 5.10: Integrity analysis of the MÜ 30 flight test data. *Top left:* Difference between TD and RTK solution $|\mathbf{x}_{\text{RTK}} - \mathbf{x}_{\text{TD}}|$ for loose and tight threshold settings. *Center left:* Test statistics RMS($D\mathbf{f}$) for loose threshold settings and threshold T_D^* applied as tight setting. *Bottom left:* Number of used satellites for tight and loose threshold settings. (For improved readability, the black line has been shifted by 2.) *To the right:* Carrier range residuals $^{i-1,i}Df^j$ of the tight solution for the corrupted PRNs 23, 4 and 10.

reliably applying such discrimination approach to real-world measurements further development to solid code still requires some effort – which is obsolete in the scope of the present project when working with the accumulation strategy. However this interesting option could be further investigated on when using the time-differential method e.g. as a means for raw data quality screening.)

The present results point out the applicability of the time-differential approach in conjunction with miniaturized low-cost receivers in the context of flight testing. The built-in integrity monitoring capabilities correctly screened out 6 outlying measurements and the trajectory of interest was reconstructed with low decimeter precision.

Research Aircraft Grob G-109B

For further exploring the time-differential approach under highly dynamic conditions, raw data recorded during a test flight with the research aircraft Grob G-109B of the Institute of Flight System Dynamics are processed and analyzed in this Section. The used receiver was the TIM evaluation kit with the patch antenna mounted right behind the cockpit as depicted by Figure 5.11. The test was performed on July 17th,

Figure 5.11: Research aircraft Grob G-109B of the Institute of Flight System Dynamics

2007 starting from the airfield in Oberpfaffenhofen (20 km west of Munich) within the scope of an experimental campaign. All data were recorded with 4 Hz. A reference receiver (TIM evaluation kit) was setup near the airfield and static initialization was provided in order to generate a reference RTK solution as for previously described tests. 9 min of static data was required for ambiguity convergence. However the RTK solution was only available for the first half of the flight, before complex maneuvers caused complete loss of lock. Evaluation by time-differences is possible also in the second half of the flight as no re-initialization is required. The recorded data was previously used for validating the TD outlier and cycle slip detection and exclusion algorithm, refer to pp. 68. (A brief overview over the complete flight trajectory is given by the plot next to Table 4.1.) Final ephemeris, 30 s sampled precise satellite clocks, TEC maps and the UNB3 troposphere model were used for processing two

interesting sections of the whole flight which are analyzed in the following.[7]

The footprint of a circle-like maneuver is depicted by the left plot of Figure 5.12(a). Such maneuver is especially challenging as the visible part of the sky changes continuously due to the aircraft's bank angle of approximately 35°. As a consequence the number of satellites used for time-differential processing (accumulation strategy) varies between 8 and 5 yielding PDOP values ranging from 1.6 to 6.5. The upper right plot of the Figure shows the 3-dimensional deviation between the RTK and the TD solution (black line) and the TD error drift estimate (grey line). The relative deviation between both solutions stays below 38 cm during the whole maneuver. Assuming the RTK solution to be "true", the error estimate is again quite pessimistic – as was the case for the MÜ 30 flight test. The RTK and the TD solution differ in a steplike way at $t = $ 28-31 s, 47-51 s and 53.75 s (marked by small arrows in the plot) – an indication of undetected cycle slips and outliers. Within the time-differential solution, the detection threshold was set to the stringent value of $T_D^* = 5$ mm corresponding to a false alert rate of $P_{FA} = 1 \cdot 10^{-3}$.[8] The plots of Figure 5.12(b) show the velocity estimates of both solutions calculated by direct numerical differentiation for the north and the vertical channel. In all three cases it is the RTK solution which exhibits unlikely spikes. The pattern of the left and the center plot are probably due to a cycle slip affected PRN not excluded from the solution whereas the double spike in the right plot might be caused by a single outlying measurement. This result is somewhat flattering to the TD solution which apparently captures outliers better for the current data section. Note that this is not always the case, compare Table 4.1.

As another trajectory section of special interest the take-off and climb to 50 m is analyzed here in more detail. The associated vertical profile is illustrated by the left plot of Figure 5.13. Note that the loss of altitude before rotation is due to the slope of the runway, noted with 8 % in the official ILS/DME Approach Chart. It is 8.2 % according to the precise time-differential GPS solution! Now there are no conspicuous differences between the RTK reference and the TD solution during the 45 s interval and the maximum relative deviation is as low as 6 cm. The high frequency noise of the TD solution is $\sqrt{\sigma_n^2 + \sigma_e^2 + \sigma_d^2} = 5.9$ mm – a slightly improved value compared to the more complex circle maneuver. With 7-8 tracked PRN PDOP values do not exceed 2.1.

For concluding this Chapter on practical validation of the time-differential method, a solution which has not been addressed at all so far (but very well deserves to be mentioned!) shall be presented – the solution calculated online by the proprietary Ublox positioning engine of the receiver. It is assumed that this solution is calculated

---

[7]Ephemerides: igs14362.sp3; satellite clocks: igs14362.clk_30s; TEC map: igsg1980.07i

[8]The high frequency measurement noise $\sigma_{D\chi}$ needed for calculating P_{FA} is estimated to 3.1 mm yielding $\sqrt{\sigma_n^2 + \sigma_e^2 + \sigma_d^2} = 6.6$ mm in the position domain.
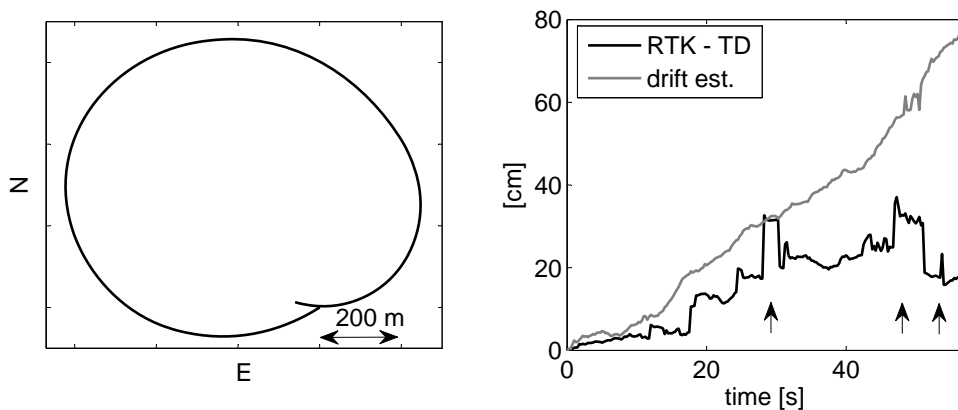
(a) *To the left:* Footprint of the maneuver (circle flown clockwise). *To the right:* 3-dimensional relative deviation of the time-differential solution from the RTK reference $\left| \mathbf{x}_{RTK} - \mathbf{x}_{TD} \right|$ and error drift estimate.
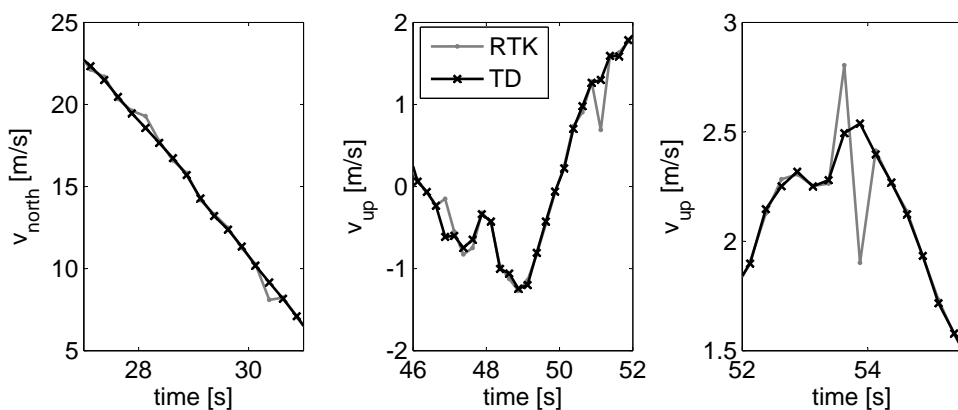
(b) Velocity estimates (for the north and the vertical direction) by difference quotients of the RTK and the TD position solution at the moments marked by arrows in the right plot of (a).

Figure 5.12: G-109B circle maneuver with RTK reference solution
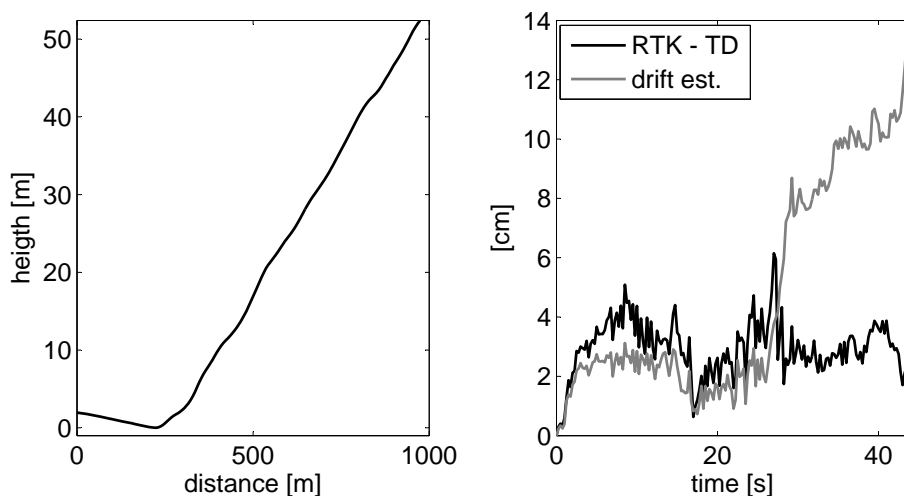
Figure 5.13: G-109B take-off. Vertical profile (*to the left*) and deviation from RTK solution $\left| \mathbf{x}_{RTK} - \mathbf{x}_{TD} \right|$ with error estimate.

based on a Kalman filter algorithm similar to the one presented by Kaplan (1996, p. 53). The dynamic platform model has been set to "Airborne < 4 g" (the maximum possible acceleration setting). The Kalman filter acts like a smoother to the noisy CA code pseudoranges which causes the PVT solution to be much smoother than the stand-alone pseudorange and Doppler solution addressed in Section 2.2. However, the price to be paid for this is a loss in dynamic performance, a time-lag in the solution, and – at least as problematic as that – the user's ignorance of what *really* happens inside the receiver. For the current flight the Ublox (UBX) solution has been sampled with the same rate of 4 Hz as the raw data. This allows a direct comparison of the RTK, the TD and the UBX solution as depicted by Figure 5.14. The upper left plot illustrates the vertical component of the maneuver. The shown interval is preceded by a constant climb which is now likely to be disturbed by a wind gust yielding the depicted profile. The deviation of both the TD and the UBX solution to the RTK reference is given by the lower left plot. The deviation of the UBX solution is systematic and exceeds 1 m. This is also mirrored in the vertical velocity, given by the upper right plot of the Figure. The UBX solution is smooth, but affected with a time delay of about 1 s leading to differences of up to -0.92 m/s with respect to the time-differential solution.[9] These results show that the precision of the UBX solution is probably better than what one initially would expect – but cannot meet the requirements in the scope of the present project.

---

[9]Note that the RTK solution shows some unrealistic spikes in the vertical speed which are probably caused by undetected cycle slips. These are also suspected to cause the step-like deviations of the vertical position component between RTK and TD solution as noticeable in the lower left plot of Figure 5.14.
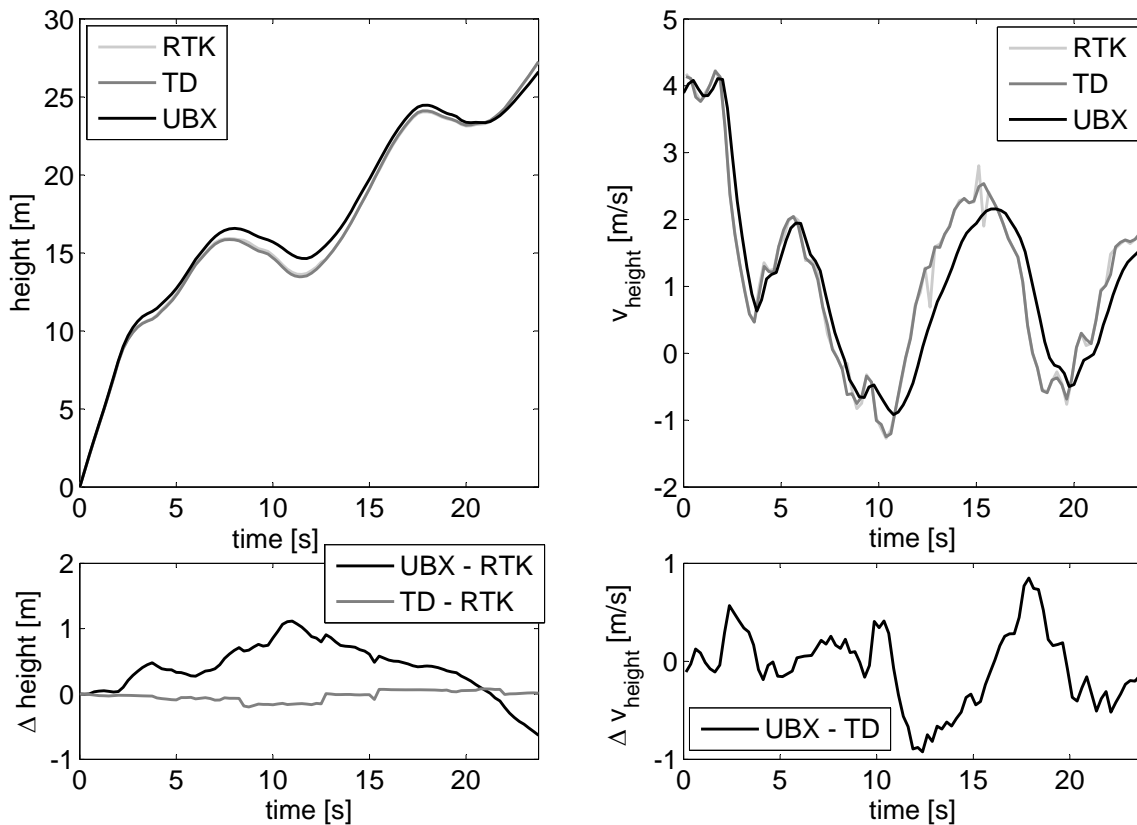
Figure 5.14: G-109B test flight – comparison of RTK, TD and UBX solution during a wind gust. *To the left:* Vertical component of all three solutions (*top*) and relative deviation of TD and UBX from RTK reference. *Top right:* Vertical speed calculated by difference quotients for the TD and the RTK solution and directly output by the UBX receiver. *Bottom right:* Relative deviation between TD and UBX solution.

5.4 Practical Validation – Conclusion

Table 5.1 summarizes the essential key data of all tests.[10] The central conclusions resulting from these numbers are: (1) The measurement noise $\sigma_{D\chi}$ of the low cost Ublox receivers is very low, not only in static but also in highly dynamic applications. This corresponds well with the zero-baseline test results given on p. 19. (2) The systematic error drift increases with increasing data complexity but stays far below of what can be deduced from theoretic carrier range error rate estimates as given in Table 3.1. Decimeter precision or even better is possible for intervals of up to 5 min. (3) An estimate of the systematic error drift is found. For the accumulation strategy, this parameter tends to be pessimistic (roughly by a factor of 2). Such estimate enables the user in an intuitive way to determine the maximum time span to be processed.

Beside the identification of these numerical performance parameters the validity of theoretical derivations could be verified practically, e.g. the impact of a base position bias on relative precision. More test results pertaining to this are given by Traugott et al. (2008a). The importance and efficiency of the used ranging models and external corrections for precision augmentation was pointed out by a sensitivity analysis of static data, also compare Traugott et al. (2008b). These results are especially important when considering the time-differential approach for real-time applications where neither precise ephemerides and satellite clocks nor ionosphere maps are available. Aside from precision, integrity is an important issue and needs to be monitored. The functionality of the implemented outlier detection and exclusion algorithms was demonstrated by the in-depth analysis of flight test data.

Finally it is worth noting that the availability of a RTK reference solution during most of the presented tests was not expected a priori. Actually the used software from the Department of Earth Observation & Space Systems was applied for the first time to data stemming from truly low-cost receivers. The successful convergence of the ambiguities was a great success, compare Odijk et al. (2007). However, the realization of the necessary static initialization period was not always easy. Before the flight tests, wind gusts risked to move the (small) aircraft on the ground and special care had to be taken when boarding for preventing antenna shadowing by the pilot's body or cockpit doors. For even more challenging field applications (which will be addressed in Chapter 7) such initialization is simply impossible and the time-differential solution is the only means to achieve the desired high precision.

---

[10]Not all results given in the Table have been explicitly addressed throughout the respective discussions. More practical (flight) tests can also be found in Traugott and Sachs (2007) and Traugott et al. (2008c)

Table 5.1: Summary of key results of practical tests. "$\sigma_{D\chi}$" is the estimate of the (high frequency) measurement noise; "3D Noise"($=\sqrt{\sigma_n{}^2 + \sigma_e{}^2 + \sigma_d{}^2}$) is the estimate of the propagation of this noise to the position domain (compare p. 56 for both columns); "3D Drift" is the rate of the solution deviation from the initial position $|\mathbf{x} - \mathbf{x}_0|$ for static data and the rate of the deviation from the RTK reference solution $|\mathbf{x}_{\text{TD}} - \mathbf{x}_{\text{RTK}}|$ for dynamic tests; "3D Drift Est." is the estimate of the error drift (according to p. 56). "acc." refers to the accumulation strategy whereas "o/a" stands for the over-all solution strategy.

Test	Receiver	$\sigma_{D\chi}$ [mm]	3D Noise [mm]		3D Drift [mm/s]		3D Drift Est. [mm/s]	
			acc.	o/a	acc.	o/a.	acc.	o/a
BRUS (stat.)	Ashtech Z	2.0	3.8	3.8	0.2	0.2	0.5	0.2
Open Fields (stat.)	Eval. Kit	1.1	2.3	2.3	0.5	0.5	0.3	0.3
$\lambda/4$ Antenna (stat.)	GiPSy	2.0	3.8	4.3	0.6	0.9	0.8	0.6
Car Driving	Eval. Kit	1.2	2.5	2.5	0.5	0.5	0.5	0.5
MÜ 30 (Eight)	GiPSy	2.5/2.9	4.8	9.1	1.9	1.0	4.6	1.3
G-109B (Circle)	Eval. Kit	3.1	6.6	-	(5)	-	13	-
G-109B (Take-Off)	Eval. Kit	3.6	5.9	-	1.3	-	2.9	-

6 Further Processing Steps

The time-differential positioning algorithm has been coded to a program described in detail in Appendix C. The final processing results are saved in ASCII files and can now be processed further on such as to comply with the goals of the respective application.

6.1 Velocity and Acceleration Determination

The determination of velocity and acceleration is of high interest within most kinematic investigations. A discussion of different methods to accomplish this task based on carrier phase measurements has already been given on pp. 52. Time-differential processing yields precise position fixes which have to be converted to velocity and acceleration by appropriate (numerical) differentiation methods.

6.1.1 Difference Quotients as Upper Bound for Noise Propagation

The easiest way to get velocity and acceleration from position is numerical differentiation by difference quotients:

$$\left(\mathbf{v}_K^R\right)_N^N(t_{i-1/2}) = \left(\dot{\mathbf{x}}^R\right)_N^N = \frac{\left(\mathbf{x}^R\right)_N(t_i) - \left(\mathbf{x}^R\right)_N(t_{i-1})}{\Delta t} \tag{6.1}$$

$$\left(\mathbf{a}_K^R\right)_N^{NN}(t_i) = \left(\ddot{\mathbf{x}}^R\right)_N^{NN} = \frac{\left(\mathbf{v}_K^R\right)_N^N(t_{i+1/2}) - \left(\mathbf{v}_K^R\right)_N^N(t_{i-1/2})}{\Delta t} \tag{6.2}$$

with the sampling time usually corresponding to the measurement rate: $\Delta t = T_m$. N denotes a local tangent navigation coordinate frame and K indates kinematic quantities. (As no other frames and only kinematic quantities are used throughout this Section, the sub- and superscripts will be dropped from now on – they will reappear in the next Chapter.) As a matter of fact, such simple calculation leads to increased noise for the individual components of the velocity $\mathbf{v} = [u, v, w]^T$ and the acceleration $\mathbf{a} = [\dot{u}, \dot{v}, \dot{w}]^T$ (written out here for the north component only):

$$\sigma_u = \frac{\sqrt{2}}{\Delta t} \sigma_n \tag{6.3}$$

$$\sigma_{\ddot{u}} = \frac{\sqrt{6}}{\Delta t^2} \sigma_n \tag{6.4}$$

The noise estimation given by Eq. (6.3) is based on the assumption of the position fixes to be unbiased and to be affected with normally distributed noise $N(0, \sigma_{n,e,d})$. The correlation between subsequent velocity estimates is taken into account in Eq. (6.4). These assumptions are used here as a worst case estimates for any numerical differentiation.

The time-differential position solution is affected with error drift. This drift leads to a slightly biased velocity. The size of this small bias can directly be calculated from the 3-dimensional error drift estimate and results to 1.2 to 30 cm/min for the experiments summarized in Table 5.1. Eq. (6.3) does not account for the velocity bias but only propagates the normally distributed high frequency component of the position noise to the velocity domain. Acceleration is virtually not affected by position drift effects. The minimum measurement interval of the used GPS receivers is $T_m = 0.1$ s. The resulting variances for the test results presented in Chapter 5 are indicated in Table 6.1. Note that the indicated values are very conservative *upper bounds* for the precision achievable with the time-differential approach - more suitable differentiation methods significantly improve velocity and acceleration accuracy.

Table 6.1: Worst case estimates for velocity and acceleration noise for the test data evaluated in Chapter 5. The indicated values result from direct numerical differentiation by difference quotients according to Eqs. (6.3) and (6.4). The 3D position noise estimates ("3D Noise") given in Table 5.1 are split up into their horizontal (north n, east e) and vertical (down d) component assuming $\mathrm{VDOP} \approx 2 \cdot \mathrm{HDOP}$.

$T_m = 0.1$ s	Position [mm]	Velocity [cm/s]	Acceleration [m/s²]
Horizontal	$\sigma_{n,e} = 0.6 - 2.8$	$\sigma_{u,v} = 0.9 - 4.0$	$\sigma_{\ddot{u},\ddot{v}} = 0.1 - 0.7$
Vertical	$\sigma_d = 1.8 - 8.0$	$\sigma_w = 2.5 - 11.4$	$\sigma_{\ddot{w}} = 0.4 - 2.0$

6.1.2 A Kinematic Approach: Quintic Smoothing Splines

Natural quintic smoothing splines according to Reinsch (1967) are used as a kinematic approach for velocity and acceleration determination. Based on variational calculus, this method finds a piecewise 6th order polynomial function $x_i = \sum_{j=0}^{5} k_{ij}(t - t_i)^j$ between all $i = 0 \ldots n$ measurements which minimizes the jerk $\dddot{x}$ in an integrative sense:

$$\int_{t_0}^{t_n} \left(\dddot{x}(t) \right)^2 dt = \min! \tag{6.5}$$

In contrast to common spline interpolation, smoothing splines do not hit the given measurements (here: the position fixes of the time-differential solution) exactly but

permit residuals $f_{\text{spline}}(t_i) = x_{\text{TD}}(t_i) - x(t_i)$.[1] The resulting function is continuous in the sampling points up to the 4th derivative:

$$x_i^{(4)}(t_i) = x_{i-1}^{(4)}(t_i) \tag{6.6}$$

Natural boundary conditions are usually applied to the 3rd and 4th derivative yielding

$$\begin{aligned}\dddot{x}_0(0) &= \dddot{x}_{n-1}(t_n) = 0 \\ x_0^{(4)}(0) &= x_{n-1}^{(4)}(t_n) = 0\end{aligned} \tag{6.7}$$

More details on the theory of the algorithm and it's performance when applied to GPS measurements can be found in Bierling (2007) and Hütter (2008). Instructions on how to easily implement smoothing splines using MATLAB are given in the Appendix, p. 149.

The smoothing spline approach turns out to be suitable for flight trajectory reconstruction to multiple intents: Due to the continuity constraints of quintic splines, also higher order aircraft dynamics can be captured precisely, compare Eq. (6.6). The ratio of sampling rate, expected dynamics and polynomial order is chosen in a way such as to avoid overfitting – which was never observed during practical data evaluation. The minimization of the jerk, Eq. (6.5), is plausible from the point of view of dynamics and the congruence between expected noise and spline residual variance allows to eliminate random noise to a large extent. Finally the algorithm uses information from *all* measurements at a time and thus fully exploits the possibilities of postprocessing.

A practical example of velocity and acceleration reconstruction by quintic smoothing splines confirming the above statements is given by Figure 6.1.

---

[1]Note that a separate spline is calculated for the north, east and down direction yielding the residuals $f_{\text{spline},n}$, $f_{\text{spline},e}$ and $f_{\text{spline},d}$.
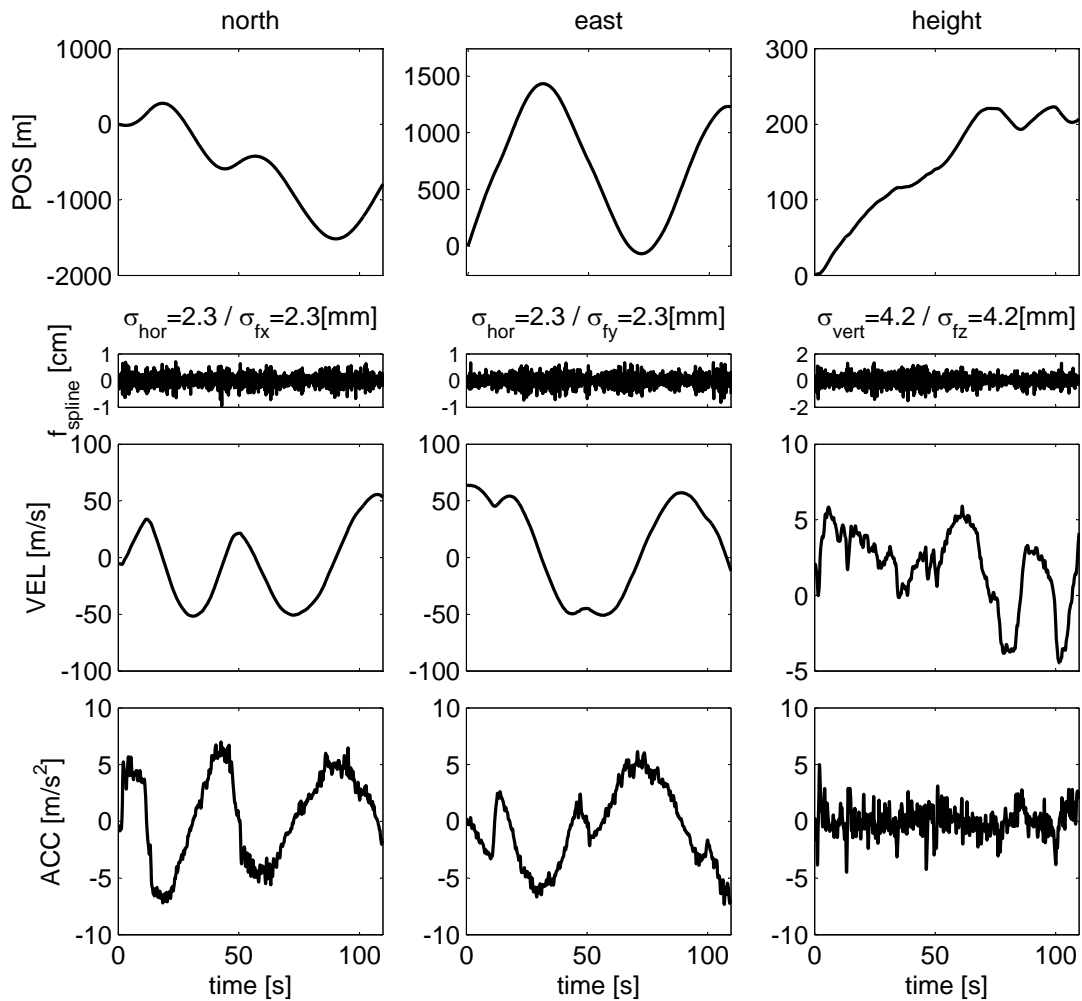
(a) Position, velocity and acceleration in the north, east and vertical direction. The spline smoothing parameters are chosen such as to match the standard deviation of the spline residuals (*second line*) with the estimate of the horizontal and vertical noise as calculated by the time-differential software. There is no systematic bias in the residuals which indicates that the flight dynamics are properly captured by the fit.
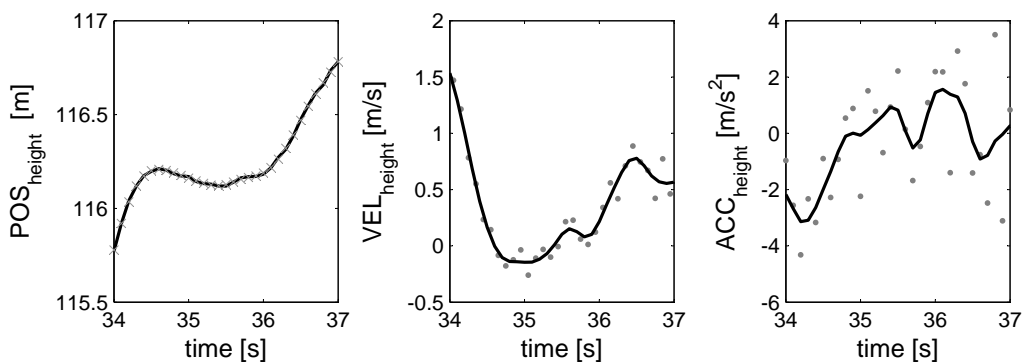
(b) Zoomed trajectory interval (probably during a wind gust). *To the left:* Vertical profile as directly calculated by time-differential processing (grey markers) and quintic spline fit (black line) *Center:* Vertical speed. The black line is the analytically differentiated spline whereas the grey dots represent the speed resulting form difference quotients, Eq. (6.1). *To the right:* Acceleration from the 2nd analytical derivative of the spline (black line) and as resulting from difference quotients according to Eq. (6.2).

Figure 6.1: Velocity and acceleration determination during the MÜ 30 "eight" flight maneuver (pp. 84) by quintic smoothing splines

6.2 Bridging Phase Outages

In case of excessive loss of lock (carrier phase of less than 4 satellites tracked) both the over-all and the accumulated time-differential solution may fail during one or several epochs. In this case, code-based single-point position (and velocity) fixes, compare Section 2.2, are used to bridge the problematic interval. Such event is qualitatively depicted by Figure 3.1, p. 33 (see "t_{b2}") and inevitably leads to a gap in the resulting trajectory. A method in order to cope with such cumbersome events has been developed by Utschick (2010) basing on local smoothing in the time domain as described by Klein and Morelli (2006, pp. 355). Only a brief outline of this algorithm shall be given in the present Section, more details (on error propagation) can be found in the former reference.

Assume the following dynamic motion model:

$$\dot{\mathbf{x}} = \mathbf{v}$$
$$\dot{\mathbf{v}} = \mathbf{a} \tag{6.8}$$
$$\dot{\mathbf{a}} = \mathbf{0}$$

Note that this model is used here for illustrating the basic algorithm. It yields a 3rd order polynomial as local interpolation function. The model can readily be enhanced to higher orders by only constraining higher derivatives to zero. (This is realized within the practical example given later on.) Integration from a starting point t_k to a (past) epoch t_{k-l} results to

$$\mathbf{x}(t_{k-l}) = \frac{1}{2}\mathbf{a}_k(t_{k-l} - t_k)^2 + \mathbf{v}_k(t_{k-l} - t_k) + \mathbf{x}_k$$
$$\mathbf{v}(t_{k-l}) = \mathbf{a}_k(t_{k-l} - t_k) + \mathbf{v}_k \tag{6.9}$$

This relationship can be set up for all time-differential position fixes of the local problematic interval:

$$\begin{pmatrix} \mathbf{x}_{\mathrm{TD},k-l} \\ \vdots \\ \mathbf{x}_{\mathrm{TD},k-1} \\ \mathbf{x}_{\mathrm{TD},k} \end{pmatrix} = \begin{bmatrix} \mathbf{I} & (t_{k-l} - t_k)\mathbf{I} & (t_{k-l} - t_k)^2\mathbf{I} \\ \vdots & \vdots & \vdots \\ \mathbf{I} & (t_{k-1} - t_k)\mathbf{I} & (t_{k-1} - t_k)^2\mathbf{I} \\ \mathbf{I} & \mathbf{0} & \mathbf{0} \end{bmatrix} \begin{pmatrix} \mathbf{x}_k \\ \mathbf{v}_k \\ \mathbf{a}_k \end{pmatrix} + \begin{pmatrix} \varepsilon_{\mathrm{TD},k-l} \\ \vdots \\ \varepsilon_{\mathrm{TD},k-1} \\ \varepsilon_{\mathrm{TD},k} \end{pmatrix} \tag{6.10}$$

Here $\varepsilon_{\mathrm{TD}}$ is the position noise of the time-differential solution. Eq. (6.10) can principally be solved by least-squares, compare Appendix A.1. However the approach must yet be adapted in order to comply with the fact that the time-differential solution is only available at the $p + 1$ leading and $p + 1$ trailing epochs of the local interval.For

the remaining time only the coarse single-point (SP) position and velocity solution is available:

$$
\begin{pmatrix}
\mathbf{x}_{\text{TD},k-l} \\
\vdots \\
\mathbf{x}_{\text{TD},k-l+p} \\
\mathbf{x}_{\text{SP},k-l+p+1} \\
\mathbf{v}_{\text{SP},k-l+p+1} \\
\vdots \\
\mathbf{x}_{\text{SP},k-p-1} \\
\mathbf{v}_{\text{SP},k-p-1} \\
\mathbf{x}_{\text{TD},k-p} \\
\vdots \\
\mathbf{x}_{\text{TD},k}
\end{pmatrix}
=
\begin{bmatrix}
\mathbf{I} & (t_{k-l}-t_k)\mathbf{I} & (t_{k-l}-t_k)^2\mathbf{I} & \mathbf{I} & \mathbf{0} \\
\vdots & \vdots & \vdots & \vdots & \vdots \\
\mathbf{I} & (t_{k-l+p}-t_k)\mathbf{I} & (t_{k-l+p}-t_k)^2\mathbf{I} & \mathbf{I} & \mathbf{0} \\
\mathbf{I} & (t_{k-l+p+1}-t_k)\mathbf{I} & (t_{k-l+p+1}-t_k)^2\mathbf{I} & \mathbf{0} & \mathbf{0} \\
\mathbf{0} & \mathbf{I} & (t_{k-l+p+1}-t_k)\mathbf{I} & \mathbf{0} & \mathbf{0} \\
\vdots & \vdots & \vdots & \vdots & \vdots \\
\mathbf{I} & (t_{k-p-1}-t_k)\mathbf{I} & (t_{k-p-1}-t_k)^2\mathbf{I} & \mathbf{0} & \mathbf{0} \\
\mathbf{0} & \mathbf{I} & (t_{k-p-1}-t_k)\mathbf{I} & \mathbf{0} & \mathbf{0} \\
\mathbf{I} & (t_{k-p}-t_k)\mathbf{I} & (t_{k-p}-t_k)^2\mathbf{I} & \mathbf{0} & \mathbf{I} \\
\vdots & \vdots & \vdots & \vdots & \vdots \\
\mathbf{I} & \mathbf{0} & \mathbf{0} & \mathbf{0} & \mathbf{I}
\end{bmatrix}
\begin{pmatrix}
\mathbf{x}_k \\
\mathbf{v}_k \\
\mathbf{a}_k \\
\Delta\mathbf{x}_{\text{begin}} \\
\Delta\mathbf{x}_{\text{end}}
\end{pmatrix}
+
\begin{pmatrix}
\boldsymbol{\varepsilon}_{\text{TD},k-l} \\
\vdots \\
\boldsymbol{\varepsilon}_{\text{TD},k-l+p} \\
\boldsymbol{\varepsilon}_{\text{SP},k-l+p+1} \\
\boldsymbol{\varepsilon}_{\text{SP},\mathbf{v},k-l+p+1} \\
\vdots \\
\boldsymbol{\varepsilon}_{\text{SP},k-p-1} \\
\boldsymbol{\varepsilon}_{\text{SP},\mathbf{v},k-p-1} \\
\boldsymbol{\varepsilon}_{\text{TD},k-p} \\
\vdots \\
\boldsymbol{\varepsilon}_{\text{TD},k}
\end{pmatrix}
$$

$$(6.11)$$

The "artificial" states $\Delta\mathbf{x}_{\text{begin}}$ and $\Delta\mathbf{x}_{\text{end}}$ account for the gap in the trajectory resulting from resuming time differential processing with respect to the last SP solution before phase lock reacquisition. The elements of the unknown errors $\boldsymbol{\varepsilon}$ have significantly different variances, corresponding to the noise-like component of the time-differential position solution and the position and velocity noise of the coarse single-point solution. As all corresponding variances are output by the time-differential software, Eq. (6.11) can be solved by properly *weighted* least squares, compare Eqs. (A.11) through (A.14). The resulting offsets $\Delta\mathbf{x}_{\text{begin}}$ and $\Delta\mathbf{x}_{\text{end}}$ can now be added to the previous and subsequent healthy TD solution yielding a properly bridged trajectory. This result is used as a basis for smoothing spline interpolation as described in the above.

Figure 6.2 demonstrates the practical applicability of the bridging algorithm with highly dynamic data recorded during the G-109B flight test described on pp. 88. An RTK reference solution was available for that flight which is addressed once more for validating the bridging algorithm. As shown by the Figure the gap in the TD trajectory is bridged in a way to allow for reasonable speed and even acceleration determination by subsequent smoothing. No steps or spikes are observed in the respective plots. Especially when it comes to the evaluation of difficult data as was the case in this example, the developed bridging algorithm is a convenient enhancement to time-differential positioning.
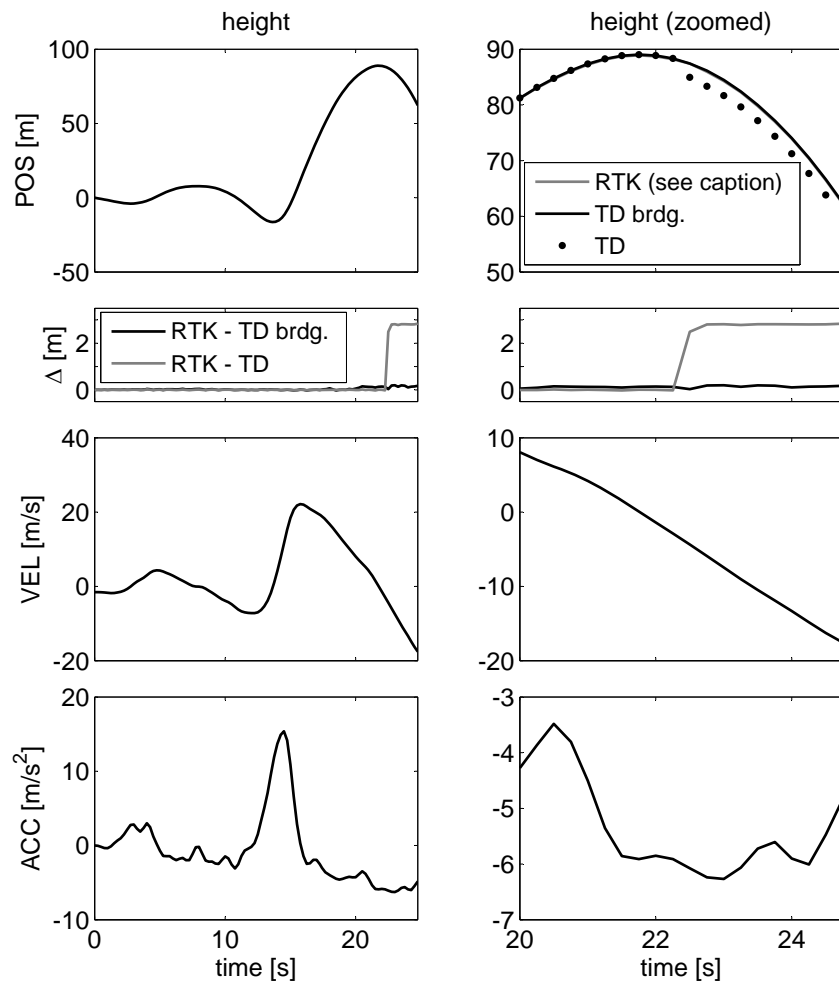
Figure 6.2: Bridging of a phase outage during a dynamic soaring like maneuver flown with the research aircraft G-109B. *1st line:* Vertical profile of the maneuver with a phase outage at $t = 22.4\,\text{s}$ due to excessive bank angle (bank angle not depicted). The deviation between RTK reference (grey line, not visible as overlapped by black line) and original TD solution after the outage is clearly visible by the black dots in the upper right plot. After applying the algorithm, the bridged TD (black line) and RTK solution virtually coincide. *2nd line:* Deviation between RTK reference and original (grey) and bridged (black) TD solution in the vertical direction. *3rd & 4th line:* Vertical velocity and acceleration derived from the bridged TD solution by smoothing spline interpolation.

7 Measuring the Dynamic Soaring of Albatrosses

Albatrosses and other large seabirds manage to fly huge distances across the ocean without flapping their large wings. Considering the absence of thermal upwinds over open waters, this flight is of special interest for both ornithologists and aeronautical engineers. A literature review of the outstanding flight performance of the birds and of various approaches to explain the phenomenon of sustained non-flapping flight has already been provided in Section 1.1, pp. 1. However, due to the high requirements in terms of measurement precision and hardware miniaturization in conjunction with the harsh environmental conditions the birds are living in, there is a lack of suitable experimental data. Hence none of the hypotheses proposed in the literature could be validated so far. Finally closing this gap by means of the precise positioning methodology presented in the previous Chapters was the goal of a measurement campaign to Kerguelen Archipelago – a breeding site of the Wandering Albatross in the southern Indian Ocean.

7.1 The Measurement Campaign

In close cooperation with the Centre d'Ecologie Fonctionelle et Evolutive (CEFE - UMR 5175) and the Institut Polaire Français Paul Emile Victor (IPEV, Program No. 354) a research expedition to Kerguelen Islands (49°S 70°E) was realized during December 2008 through March 2009. A permission to equip 20 Wandering Albatrosses with GPS data loggers according to the guidelines established by IPEV and the French research center CNRS for Ethical Treatment of Animals was granted by the administration of the Kerguelen territories (TAAF).

Wandering Albatrosses (Diomedea exulans[1]) pertain to one of seven species of Great Albatrosses (Diomedea) which, with a wingspan of 2.7-3.2 m and a mass of 5-12 kg, are by far the biggest birds of the ocean (Tickell, 2000, p. 25). They also exceed all other albatrosses in both size and weight. With the exception of the North Pacific Albatrosses (Phoebastria) all existing genera range in the southern hemisphere

---

[1] Class: Aves – Order: Porcellariiformes (Tubenoses) – Family: Diomedeidae (Albatrosses) – Genus: Diomedea (Great Albatrosses) – Species: Diomedea exulans (Wandering Albatrosses)

at rather high latitudes where strong winds prevail. With their long and narrow wings (aspect ratio in the range of 15) and and a special mechanism "locking" the extended wings during gliding flight (Tickell, 2000, p. 28), albatrosses spend most of their lifetime on open seas soaring close to the water surface. Only during the breeding season the birds return to the regions where they were reared in order to meet their partner for mating, breeding and chick feeding. During incubation the couples take turns in foraging, each partner leaving for trips extending from one day to more than a month while the other one remains at the nest.

During this time a permanent observation of the breeding colony at Cap Ratmanoff, located at the very east of Kerguelen's Courbet peninsula, allowed the author to identify birds ready to leave for a foraging trip, to equip them with GPS loggers and to recover the devices with the recorded data after the birds had homed to their nests. Valid flight data could be recorded from 80% of the equipped birds (16 out of 20) resulting in a total of about 36 days of valid GPS measurements. Figure 7.4(a), pp. 110 illustrates the longest of all recorded trajectories, which are provided completely in Appendix D.1.

7.1.1 Miniaturized Equipment

All loggers were attached to the back feathers of the birds using adhesive tape. The recommended upper limit of the mass of the self-contained devices was 100 g, the upper limit of the size was 100 mm×50 mm×15 mm [F. Bonadonna, oral communication]. The electronics had to be protected from rain, seawater[2] and the birds' bills by a sealed and rugged casing. When equipping the birds the GPS antennas were completely shadowed by the field workers. This fact impeded the realization of any static initialization patterns as required by RTK differential techniques. After the equipment some birds immediately left for foraging, others remained with their partner for another couple of hours or even days before heading to the sea. After leaving the nest, some birds landed on the water close to the shore, again waiting for several hours or even a day before most likely favorable winds enabled them to finally start their foraging trip. The used measurement equipment had to match size and weight requirements while being capable to bridge the gap between deployment on the bird and the animals finally soaring over open seas.

Three different types of GPS data loggers were used during the campaign. The core of each device was a Ublox LEA-4T GPS module. Compare the ZBL test results presented in Section 2.1.2, pp. 19 and the information provided in Section 5.1, pp. 73 for more details on this miniaturized L1 module. For power supply all devices were

---

[2]Wandering Albatrosses usually don't dive but obtain their food (mainly carrion and squids) by seizing and scooping from the surface (Tickell, 2000, p. 164).
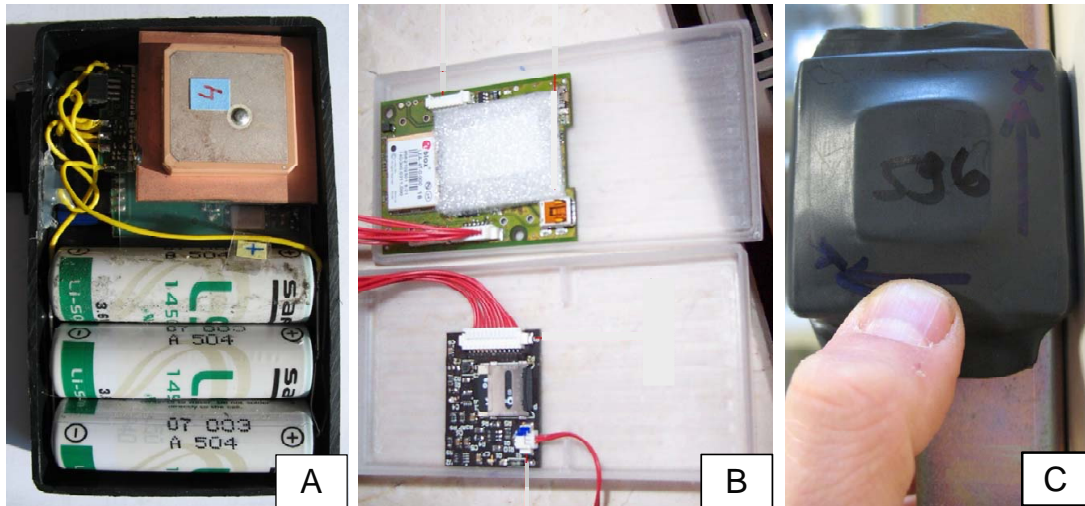
(a) GPS data loggers. A: TechnoSmArt "GiPSy"; B: Art-of-Technology "OEM GPS Data Logger" (without batteries); C: e-obs "GPS-Tag". (Photos not true to scale.)

(b) Wandering Albatross equipped with GPS data logger (red circle). The logger is attached to three bunches of feathers right between the wings using adhesive tape. No logger was lost during flight and all devices could be recovered without causing substantial damage to the feathering.

Figure 7.1: GPS equipment used for the albatross measurement campaign

connected to 3.6 V primary lithium-thionyl chloride (Li-SOCl$_2$) AA-size bobbin cells from the French Saft company (typical weight per cell: 16.2 g). Tests in a low temperature environment (expected ambient temperature 3-10 °C) with currents of 40-70 mA identified the models LS 14500 and LS 14500 C as the best choice for the albatross application.[3] Figure 7.1(a) shows the three different logger types which are described in more detail in the following:

A TechnoSmArt GPS data logger GiPSy. Most specifications of this device have already been given in Section 5.1, pp. 73. As 10 Hz raw data logging started immediately when deploying the device on the bird, a minimum runtime of 60 h

---

[3]Heat transfer from the body of the birds to the batteries may have risen the actual operating temperature. As this effect could not be quantified it was not considered when selecting the power supply source.

had to be guaranteed to bridge the delay between bird equipment and the bird (most likely) flying offshore. This was realized by using 3 LS 14500 cells for power supply and by recording all logged data to a 2 GB external SD card via the additional logging device "Neurologger". The casing was a commercially available 89 mm×55 mm×22 mm ABS thermoplastic bifid box sealed with Sikaflex®-221. The overall mass of the device was 103 g (18.4 g GiPSy, 6.0 g Neurologger, 48.6 g batteries, 30.0 g casing). The longest recorded trajectory was a $6\frac{1}{2}$ day flight. (Note that the raw data quality significantly degraded during the last 2 days due to reduced battery voltage.)

B Art-of-Technology OEM GPS Data Logger. This device closely resembles GiPSy in terms of used GPS antenna and module, power consumption, used batteries and memory. The board also features 8 MB on-chip flash memory which was extended by an external logger addressing a 2 GB Micro-SD card. The form factor of the OEM board is 60 mm×45 mm×7 mm with a mass of 16.2 g including antenna. The used casing was a 108 mm×55 mm×19 mm custom made bifid polycarbonate (Makrolon®) box with a mass of 21.8 g also sealed with Sikaflex®-221. The overall mass of the device aggregated 92.6 g comprising 3 LS 14500 cells and the extended memory. The casing was transparent which allowed to read out the board's status LEDs. The device was operated magnetically by a reed switch.

C e-obs GPS-Tag. This device was delivered ready-to-use by the manufacturer, i.e. comprising batteries (2 Saft LS 14500) and casing (sealed shrinking tube). It also featured a LEA-4T module but was confined to 8 MB internal memory for raw data recording only. In addition to the GPS sensor, the device allowed to record 3D acceleration data measured by an integrated MEMS accelerometer. Due to limited memory (approx. 30 min of raw 10 Hz GPS and acceleration data), a "smart" way to bridge the time interval between receiver deployment and the birds finally flying was implemented by e-obs in cooperation with the author: After equipping the bird, the GPS module was set to a sleep mode only determining its position and speed every 60 min via the (coarse) online solution calculated by the module (just as most other operating parameters, also the wake-up interval could be redefined in the field). Now the actual position was compared with a specified latitude-longitude window: if the bird was outside this window, i.e. offshore, and was moving with a speed exceeding a threshold of 5.5 m/s, i.e. not swimming on the water but flying, permanent raw-data recording was enabled. This strategy yielded five valid 30 min flight records out of five deployments of this type of receiver. As an additional option the devices offered the possibility to download all recorded data to a handheld base station from a distance of up to 20 m.

Figure 7.1(b) shows a female Wandering Albatross spreading its wings right after

deploying one of the described devices. The male has already taken over the egg and the female is ready to leave for a foraging trip.

7.1.2 Wind Information

Wind information is obtained using SeaWinds on QuikSCAT Level 3 Daily Gridded Ocean Wind Vectors (JPL SeaWinds Project). The data is sampled on an approximately $0.25° \times 0.25°$ global grid twice a day (which equals approx. 28 km in north-south direction and 18 km in east-west direction at 49°S). The data provides local wind velocity vectors at a reference altitude of 10 m with an accuracy of $2\,\mathrm{m/s}$ (or 10% for velocities above $20\,\mathrm{m/s}$) and the wind direction within $\pm20°$ (JPL, 2006). Figure 7.2 shows an exemplary QuickSCAT wind map of the Kerguelen area. For calculating
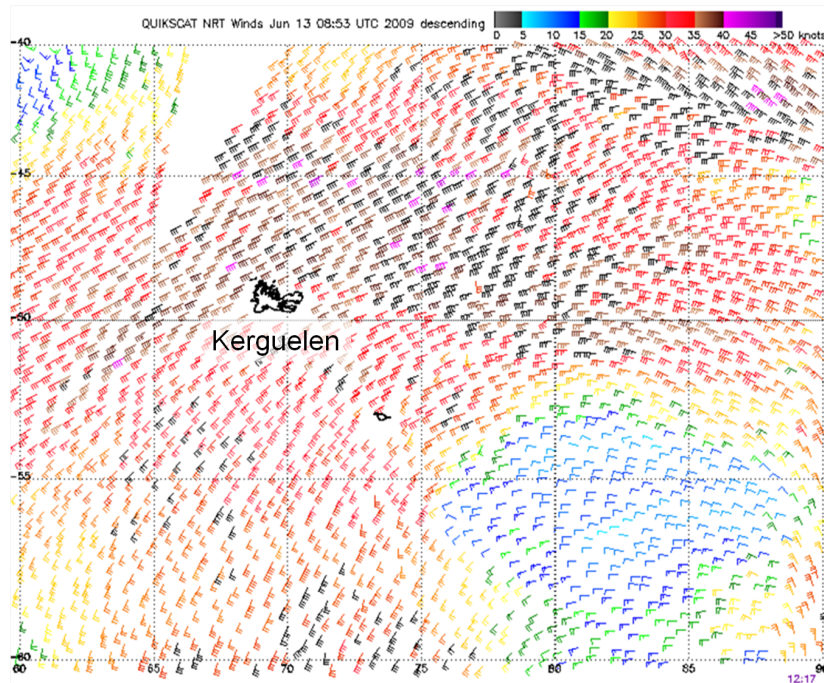
Figure 7.2: QuickSCAT wind map of the Kerguelen area (JPL, 2006)

the wind at defined trajectory points one-dimensional linear interpolation is used in the time domain and bivariate Akima interpolation is addressed in the position domain. More details on the wind data and the interpolation methods can be found in Müller (2009). The change of the wind speed in the boundary layer close to the water surface is modeled according to Sachs (2005):

$$V_W(h) = V_{W,\mathrm{ref}} \frac{\ln \frac{h}{h_0}}{\ln \frac{h_{\mathrm{ref}}}{h_0}} \tag{7.1}$$

with the absolute value of the local wind speed V_W, the height above the sea surface h, the minimum height h_0 and the wind speed $V_{W,\mathrm{ref}}$ at the reference height h_{ref}. For

the present studies h_0 is set to $3\,\text{cm}$. A value of $10\,\text{m}$ is used as reference height such as to directly enable the use the QuickSCAT winds as $V_{W,\text{ref}}$. Figure 7.3 illustrates Eq. (7.1).
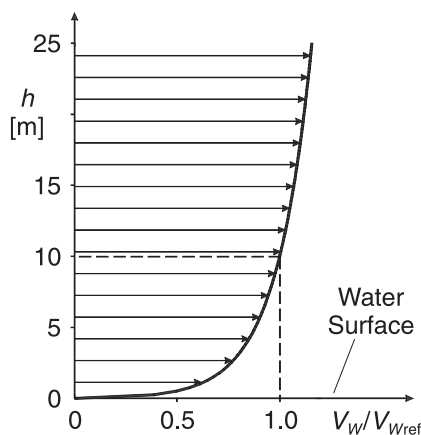
Figure 7.3: Boundary layer wind model (Sachs, 2005)

Already here it shall be pointed out that any wind information will only be used to better explain aerodynamic aspects of dynamic soaring in albatrosses. Obviously there are many uncertainties – one might think of the motion of the sea by itself (tides and unknown swell of several meters), wave related turbulences and the sparse spatial and temporal sampling rate of the QuickSCAT data. Hence it is not possible to rely on the wind information in a strict sense.

7.2 Trajectory Analysis

The analysis of the recorded albatross trajectories aims for experimentally solving the controversy about dynamic soaring in albatrosses. The analysis is conducted in three consecutive stages:

1. A visual inspection of the position fixes provides first insights into the nature of the dynamic flight of the birds. The informative value of this level of analysis is comparable to just watching the animals either in real life or on video tape – enhanced by the possibility to readily choose the observation zoom level, the viewing angle and monitor the flight over a much larger distance range.

2. The energy management during the flight is investigated by looking at both the birds' specific total energy state and the temporal variation (derivative) of this observable. Such analysis does not require any assumptions of (aerodynamic) bird parameters or local winds. However it firstly provides insights into the energy gaining mechanisms employed by the animals: In which parts of the flight does the energy level increase, where does it decrease? If the energy decreases whenever

the bird is close to the water surface, can waves and related turbulences contribute significantly to the energy gain required for overcoming drag? Answering such-like questions is key for understanding the energy transfer mechanisms required for sustained non-flapping flight. The analysis is performed on the basis of an exemplary closed flight cycle. Here "closed" means that the bird adopts the same energy level and flight direction at the beginning and the end of the trajectory section (the flight cycle). This confirms the periodicity of the maneuver in the sense of a mathematical proof of induction as opposed to the statistical evaluation of a plurality of cycles. (More cycles with corresponding analysis plots are provided in Appendix D.2, pp. 163.)

3. Only in a last step the wind information introduced in Section 7.1.2 is used in conjunction with the differential equations describing the (specific) point mass dynamics of an albatross in order to estimate the (specific) aerodynamic forces acting on the bird during the selected flight cycle. Note that still no assumptions of (aerodynamic) bird parameters are made and only rotational dynamics are neglected. If the forces resulting from an inversion of the differential equations based on the measured precise position, velocity and acceleration fixes are plausible, this strongly indicates (no proof!) the following: (1) The made wind assumptions are sufficient in order to explain the observed flight. (2) As any vertical winds caused by waves or related turbulences are not included in the model, the secondary influence of suchlike effects is confirmed.

7.2.1 Visual Inspection

Figure 7.4 illustrates the flight of a Wandering Albatross on three different zoom levels. Figure 7.4(a) shows the recorded trajectory on a global scale – the tracked bird covered a distance of about 4,850 km in a period of about 6 days. (The whole foraging trip lasted 30 days). Figure 7.4(b) shows the footprint (in the north-east plane) of a 13.5 km interval of this flight. Here the winding and curving character of the trajectory clearly comes to light. (In none of the recorded trips the birds were ever observed to fly in straight lines or in altitude regions other than very close to the water surface.) Finally Figure 7.4(c) picks out a single flight cycle. Here four typical phases can be distinguished: a windward climb (1), a curve from wind- to leeward (2), a leeward descent (3) and finally a reverse turn at very low altitudes initializing the next cycle (4). Note the resemblance of this cycle with the simulation results depicted in Figure 1.2, p. 2.

Figures 7.4(a) and 7.4(b) are based on the coarse 1 Hz solution calculated online by the GPS receiver. Figure 7.4(c) is calculated by precise time-differential processing. The wind direction is plotted according to the QuickSCAT data.
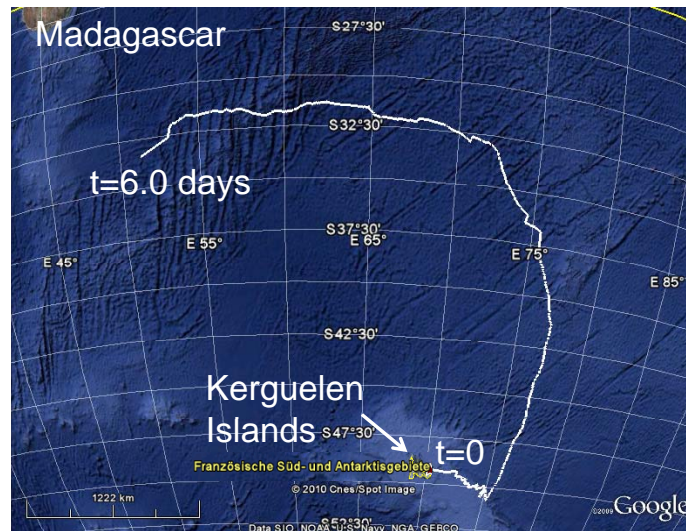
(a) Breeding site Kerguelen Islands (49°S 70°E) with a 6.1 day recording of a foraging trip of a Wandering Albatross (total trip duration: 30 days).
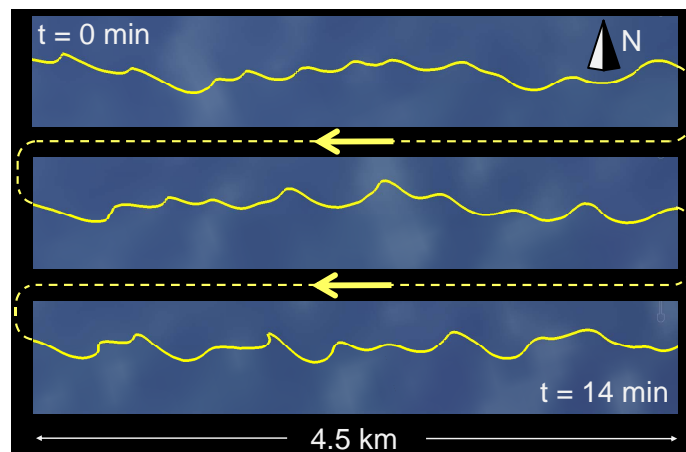
(b) Typical dynamic soaring flight pattern of a Wandering Albatross. The whole flight is made up of curved elements – the individual dynamic soaring cycles.
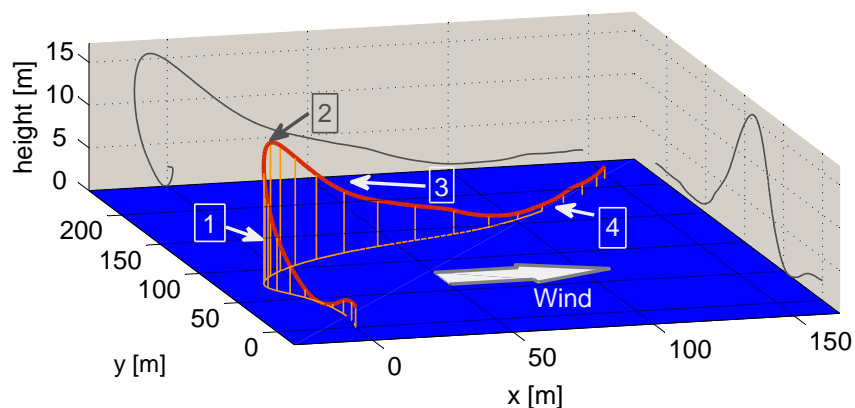
(c) Individual dynamic soaring cycle consisting of (1) a windward climb, (2) a curve from wind- to leeward at peak altitude, (3) a leeward descent and (4) a reverse turn close to the sea surface initializing the next cycle. The duration of the maneuver is 15 s.

Figure 7.4: The dynamic soaring flight of Wandering Albatrosses (Diomedeae exulans) at different zoom levels.

7.2.2 Energy Analysis

The specific total energy E_{tot}^* is defined as the sum of potential and kinetic energy referred to mass and gravity:

$$
\begin{aligned}
E_{\text{tot}}^* &= \frac{1}{mg}\left(\frac{1}{2}mV_k{}^2 + mgh\right) \\
&= \frac{1}{2g}V_K{}^2 + h
\end{aligned}
\tag{7.2}
$$

Here V_K is the speed relative to the ground (elaborate notation: $V_K = \left|\left(\mathbf{v}_K^G\right)^N\right|$ with G denoting the bird's center of gravity). The height above ground (sea level) is represented by h. Note that E_{tot}^* is not an absolute quantity but strongly dependent on the coordinate frames used to define velocity and height. For this purpose the navigation frame N is addressed in the present context, compare Appendix B.2. The frame is rotated around the z-axis such that the new x-axis coincides with the direction of the wind flow as indicated by the QuickSCAT data. The horizontal origin of this frame is clamped at the starting point of the precisely processed trajectory section. The vertical origin is located at the lowest point of the subsequent flight cycle usually shifted by an offset of $0.5\,\text{m}$.[4] Note that such origin definition only impacts the absolute value of the potential energy, not its derivative, i.e. its relative course. As opposed to potential energy, the kinetic component of E_{tot}^* does not depend on the definition of the origin but on the nature of the used velocity. Here the kinematic velocity, i.e. the velocity of the bird's center of gravity relative to the ground (not relative to the air!) is used.

A perspective visualization of a typical dynamic soaring cycle is provided by Figure 7.5(a). (The location of the cycle is indicated in Figure D.1(a), p. 160.) The upper left plot of Figure 7.5(b) shows the time history of h (black line) and V_K (grey line) during this maneuver. The corresponding course of E_{tot}^* (black line) and $\dot{E}_{\text{tot}}^*$ (grey line) is depicted by the lower left plot of Figure 7.5(b). The right diagram of the Figure shows the footprint of the maneuver color-coded with E_{tot}^*.

Note that these plots are exclusively based on real measurements – no assumptions of the (local) wind or of any bird parameters are made. Hence the following statements are of central importance:

1. The height h and the speed V_K are similar at the beginning and the end of the maneuver where the bird flies virtually in the same direction. Hence the (dynamically coupled) flight states repeat and the depicted maneuver is cyclic – the bird can fly

---

[4]The starting point of any soaring cycle is calculated by code based single point positioning and affected with an error of several meters (compare Figure 3.1, p. 33). Further the true location of the sea level is unknown due to waves and swell. As the birds often nearly touch the water surface with their wing tips in the lower curve, a bias of $0.5\,\text{m}$ has been defined in order to obtain somewhat realistic absolute numbers for the potential energy.
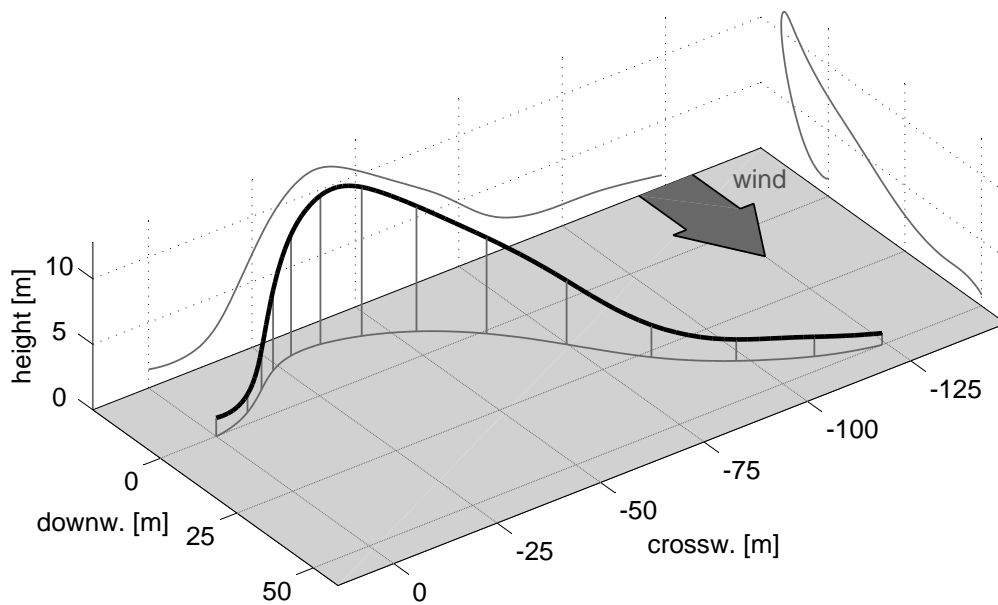
(a) 3-dimensional trajectory. The vertical direction is exaggerated by a factor of three; the grey arrow indicates the wind direction according to QuickSCAT.
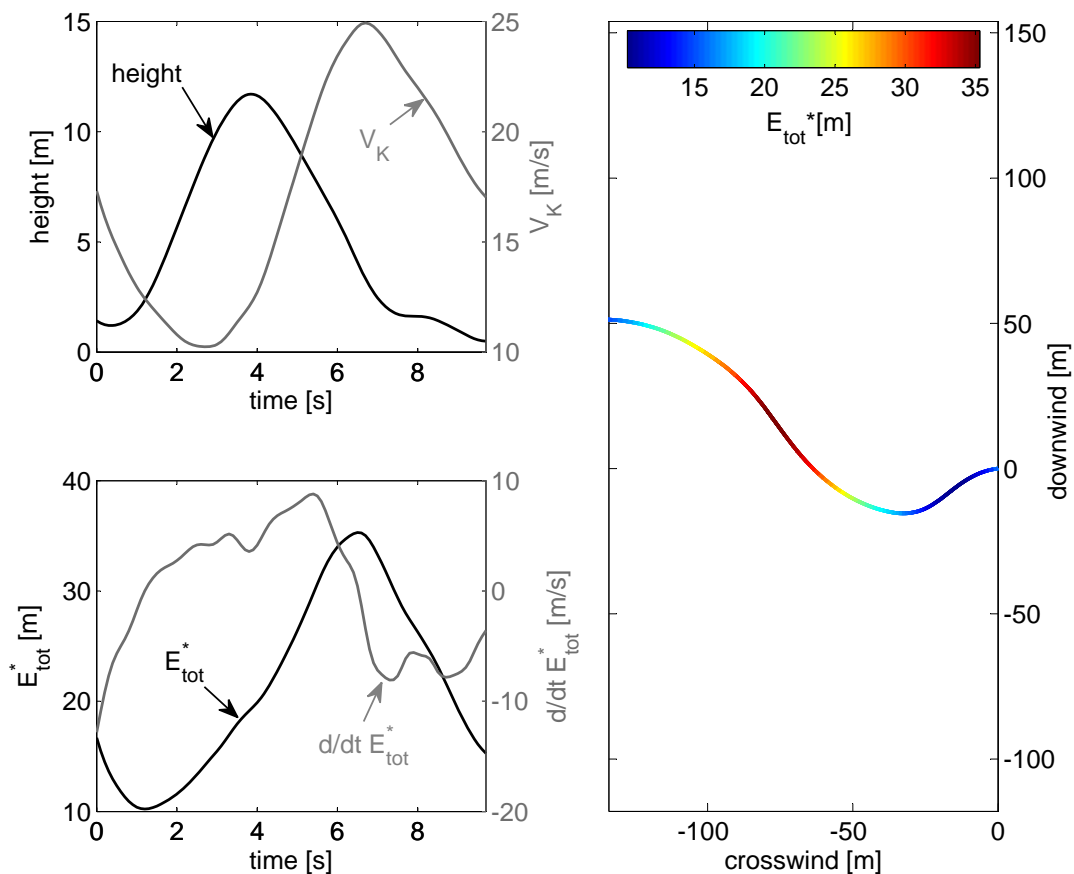
(b) Energy analysis. *Top left:* Height and kinematic speed (speed relative to the ground). *Bottom left:* Specific total energy and its time derivative. *To the right:* Footprint of the maneuver color-coded with total energy. The positive "downwind" axis points in the direction the wind is blowing in.

Figure 7.5: Analysis of a typical, closed dynamic soaring maneuver. With the same energy level at the beginning and the end and the bird flying in similar direction and at similar height, the maneuver has cyclic nature and can be repeated periodically.

continuously by periodically repeating the same maneuver.

2. The total energy decreases ($\dot{E}_{tot}^* < 0$) at flight phases where the bird is close to the water surface. As a consequence, vertical winds induced by waves or turbulences can be excluded as (primary) sources of energy gain.[5] Only during upper parts of the maneuver there is a net gain of energy ($\dot{E}_{tot}^* > 0$).

3. The change of the total energy is continuous; there are no distinct spikes in $\dot{E}_{tot}^*$ (no energy pulses). This is an indicator that turbulences do not play an important role in the energy transfer mechanisms.

Being subject to the laws of nature, the birds *have* to compensate for the dissipative effect of drag. Eliminating many other effects, the above results strongly suggest that they do so by dynamic soaring as very comprehensively explained by Lissaman (2007): *"When a bird [...] is oriented with a horizontal component of its lift vector aligned with the natural wind, work is done on the flight system. Consequently, by suitable trajectories, variations in wind speed can be used to add energy to the system."* By applying optimization calculus to an albatross simulation model, Sachs (2005) successfully demonstrated that a wind model according to Eq. (7.1) represents a "variation in wind speed" which is suitable to explain the sustained flight of albatrosses. This shall be verified by *real flight data* in the next Section.

A Note on Data Quality   Before heading to further explanations on dynamic soaring, let's have a quick look on the GPS data underlying the discussed trajectory: The quality of the raw phase data is restricted due to the difficult environmental conditions (permanent antenna tilting, reflecting water surface, etc.). Hence the accumulation strategy is addressed for processing the data, compare Section 3.3.1, pp. 45. 6 to 9 satellites are used under very frequent constellation changes yielding PDOP values of 1.9 to 3.0 throughout the interval. The 3-dimensional error drift is estimated to 6.5 dm at the end of the maneuver corresponding to a speed bias of 6.8 cm/s. For typical speed values of 15 m/s this is an absolute speed error of approximately 0.5% and an energy error of about 1%. (Note that this estimate tends to be pessimistic by a factor of 2 or 3, compare p. 52, p. 85.) The standard deviation of the noise component of the position error is estimated to 1.05 cm. For directly differentiating the 10 Hz sampled data, this results in upper bounds of 14.8 cm/s for the speed noise and 0.26 g for the acceleration noise, compare p. 95. Note that smoothing by splines significantly reduces this error. A threshold $T_D^* = 7$ mm has been used for integrity monitoring resulting in 11 exclusions of corrupted measurements, see Eq. (4.9).

---

[5]This confirms the fact that albatrosses can perform non-flapping flight in areas with strong winds but very little swell as leewards of an island or even over solid land when approaching their nests (personal observation by the author).

7.2.3 Aerodynamic Force Analysis

As opposed to the assumption-free energy analysis, models describing the instantaneous local wind and the dynamics of the soaring bird are required for this last analysis stage:

Wind model According to the QuickSCAT data, the wind speed in $10\,\text{m}$ altitude at the time and the location of the analyzed flight cycle was $11.3\,\text{m/s}$ and the wind direction[6] was $66°$. Hence $V_{W,\text{ref}} = 11.3\,\text{m/s}$ in Eq. (7.1).

Point mass dynamics The point mass dynamics of the bird are modeled as follows:

$$\left(\dot{\mathbf{v}}_K^G\right)_N^{NN} = \frac{1}{m}\left(\mathbf{F}_A^G\right)_N + \begin{pmatrix} 0 \\ 0 \\ g \end{pmatrix}_N \tag{7.3}$$

This basic model neglects both earth curvature and earth rotation, which is obviously reasonable considering the short flight distances of a cycle and the comparably low speed level. Further the rotational dynamics of the bird are not taken into account and the (short) lever arm between the GPS antenna and the (unknown) center of gravity G of the bird is neglected. The bird's acceleration is solely determined by gravity and the acting aerodynamic forces $\left(\mathbf{F}_A^G\right)_N$. In the aerodynamic frame A, the latter forces are defined as follows:

$$\left(\mathbf{F}_A^G\right)_A = \begin{pmatrix} -D \\ Q \\ -L \end{pmatrix}_A \quad \text{with } Q \overset{\beta_A=0}{=} 0 \tag{7.4}$$

with the drag D, the lift L and the side force Q. This force vanishes with the assumption of zero angle of sideslip $\beta_A = 0$. The GPS measurements deliver the birds position indicated in the navigation frame $\left(\mathbf{x}^G\right)_N$. Differentiation (by smoothing splines) yields the kinematic velocity $\left(\mathbf{v}_K^G\right)_N^N$ and the acceleration $\left(\dot{\mathbf{v}}_K^G\right)_N^{NN}$ relative to the N-frame. Both quantities are indicated in this frame, too. The kinematic velocity is directly linked to the aerodynamic velocity by the wind as stated in the following equation and illustrated in Figure 7.6:

$$\left(\mathbf{v}_K^G\right)_N^N = \left(\mathbf{v}_A^G\right)_N^N + \left(\mathbf{v}_W^G\right)_N^N \tag{7.5}$$

With these two models, the specific lift L/m, the specific drag D/m and the aerodynamic bank angle μ_A can be determined (without any assumptions concerning bird

---

[6]As opposed to common conventions, the QuickSCAT "wind direction" is the direction the wind is blowing in.
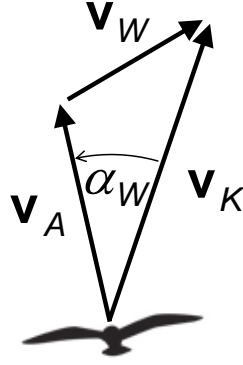
Figure 7.6: Definition of aerodynamic (A), kinematic (K) and wind (W) velocity vectors

parameters) according to Müller (2010):

The aerodynamic azimuth χ_A and flight path inclination angle γ_A are defined by the individual components of the aerodynamic velocity $\left(\mathbf{v}_A^G\right)_N^N = \left(u_A^G, v_A^G, w_A^G\right)_N^{N^T}$. The latter is calculated by Eq. (7.5) in conjunction with the wind model Eq. (7.1) and the height h:

$$
\tan \chi_A = \frac{\left(v_A^G\right)_N^N}{\left(u_A^G\right)_N^N}
$$
$$
\sin \gamma_A = -\frac{\left(w_A^G\right)_N^N}{V_A}
\tag{7.6}
$$

with the absolute value of the aerodynamic velocity V_A. Now the transformation matrix $\mathbf{M}_{\bar{A}N}$ between the navigation frame N and the aerodynamic frame $\bar{A}$ is determined:

$$
\mathbf{M}_{\bar{A}N} = \begin{bmatrix} \cos \chi_A \cos \gamma_A & \sin \chi_A \cos \gamma_A & -\sin \gamma_A \\ -\sin \chi_A & \cos \chi_A & 0 \\ \cos \chi_A \sin \gamma_A & \sin \chi_A \sin \gamma_A & \cos \gamma_A \end{bmatrix}
\tag{7.7}
$$

The components of the acting specific aerodynamic forces in the N-frame $\frac{1}{m}\left(\mathbf{F}_A^G\right)_N$ are known by solving Eq. (7.3) based on the GPS-derived accelerations, i.e. by inverting the point mass dynamics. Now the components of this force in the $\bar{A}$-frame can be calculated:

$$
\frac{1}{m}\left(\mathbf{F}_A^G\right)_{\bar{A}} = \frac{1}{m}\mathbf{M}_{\bar{A}N}\left(\mathbf{F}_A^G\right)_N
\tag{7.8}
$$

With the relationship

$$
\left(\mathbf{F}_A^G\right)_{\bar{A}} = \begin{pmatrix} X_A^G \\ Y_A^G \\ Z_A^G \end{pmatrix}_{\bar{A}} \overset{\beta_A = 0}{=} - \begin{pmatrix} D \\ L \sin \mu_A \\ L \cos \mu_A \end{pmatrix}
\tag{7.9}
$$

the bank angle can finally be determined:

$$\tan \mu_A = \frac{\frac{1}{m}\left(Y_A^G\right)_{\bar{A}}}{\frac{1}{m}\left(Z_A^G\right)_{\bar{A}}} \tag{7.10}$$

With Eqs. (7.4) and (7.9) one gets for the components of the aerodynamic force in the *A*-frame:

$$\frac{1}{m}\left(\mathbf{F}_A^G\right)_A = \frac{1}{m}\begin{pmatrix} \left(X_A^G\right)_{\bar{A}} \\ 0 \\ \frac{\left(Z_A^G\right)_{\bar{A}}}{\cos \mu_A} \end{pmatrix} \tag{7.11}$$

Hence the specific drag and the specific lift result to

$$\begin{aligned} \frac{1}{m}D &= -\frac{1}{m}\left(X_A^G\right)_{\bar{A}} \\ \frac{1}{m}L &= -\frac{1}{m\cos \mu_A}\left(Z_A^G\right)_{\bar{A}} \end{aligned} \tag{7.12}$$

The left plot of Figure 7.7 illustrates the reconstructed bank angle during the investigated flight cycle (black line) and the time history of the angle α_W between the kinematic velocity $\left(\mathbf{v}_K^G\right)^N$ and the aerodynamic velocity $\left(\mathbf{v}_A^G\right)^N$ (grey line). It is the latter angle which explains the fact that both the lift and the drag have a non-zero component in the kinematic flight direction acting as propulsive[7] and dissipative forces defined as follows:

$$\begin{aligned} \frac{1}{m}F_{\text{Prop}} &= \mathbf{e}_x^T \mathbf{M}_{KN}\mathbf{M}_{NA}\left(0 \quad 0 \quad \frac{L}{m}\right)_A^T \\ \frac{1}{m}F_{\text{Diss}} &= \mathbf{e}_x^T \mathbf{M}_{KN}\mathbf{M}_{NA}\left(-\frac{D}{m} \quad 0 \quad 0\right)_A^T \end{aligned} \tag{7.13}$$

where the multiplication with $\mathbf{e}_x = (1,0,0)^T$ picks out the lift and drag component in flight direction. The rotation matrices are defined as

$$\mathbf{M}_{NA} = \begin{bmatrix} \cos\chi_A\cos\gamma_A & \sin\chi_A\cos\gamma_A & -\sin\gamma_A \\ \cos\chi_A\sin\gamma_A\sin\mu_A - \sin\chi_A\cos\mu_A & \sin\chi_A\sin\gamma_A\sin\mu_A + \cos\chi_A\cos\mu_A & \cos\gamma_A\sin\mu_A \\ \cos\chi_A\sin\gamma_A\cos\mu_A + \sin\chi_A\sin\mu_A & \sin\chi_A\sin\gamma_A\cos\mu_A - \cos\chi_A\sin\mu_A & \cos\gamma_A\cos\mu_A \end{bmatrix}^T \tag{7.14}$$

and

$$\mathbf{M}_{KN} = \begin{bmatrix} \cos\chi_K\cos\gamma_K & \sin\chi_K\cos\gamma_K & -\sin\gamma_K \\ -\sin\chi_K & \cos\chi_K & 0 \\ \cos\chi_K\sin\gamma_K & \sin\chi_K\sin\gamma_K & \cos\gamma_K \end{bmatrix} \tag{7.15}$$

with the kinematic flight path angles γ_K and χ_K calculated in analogy to Eq. (7.6) out of the components of the kinematic velocity $\left(\mathbf{v}_K^G\right)_N^N$. F_{Prop} and F_{Diss} are linked to the

---

[7]Note that F_{Prop} has a dissipative characteristic during the lower parts of the trajectory, too.
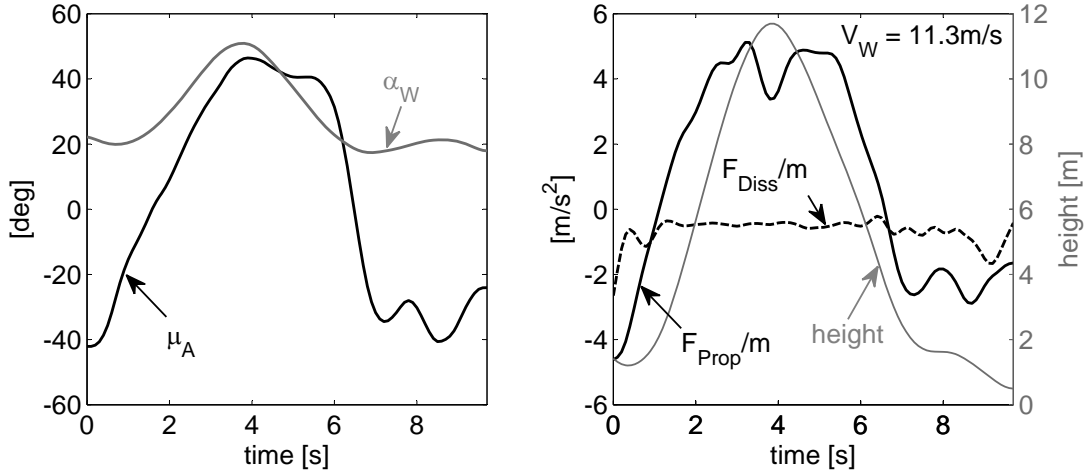
Figure 7.7: Aerodynamic analysis of the dynamic soaring cycle investigated in Figure 7.5. *To the left:* Aerodynamic bank angle μ_A and wind angle α_W according to Figure 7.6. *To the right:* Specific propulsive and dissipative forces. Wind speed V_W according to the QuickSCAT measurements and the logarithmic boundary model, Eq. (7.1).

total energy by the integral relationship:

$$
\begin{aligned}
\Delta E_{\text{tot}}^* &= \frac{1}{mg} \int_{t_1}^{t_2} \mathbf{F}_A^G \cdot \left(\mathbf{v}_K^G\right)^N dt \\
&= \frac{1}{mg} \int_{t_1}^{t_2} \left(F_{\text{Prop}} + F_{\text{Diss}}\right) V_K dt
\end{aligned}
\tag{7.16}
$$

The right plot of Figure 7.7 shows the the time history of F_{Prop} and F_{Diss}[8] for the current flight cycle.

These results allow the following statements:

1. The reconstructed bank angle μ_A is plausible – meaning that the obtained values fairly agree with what can be expected from both the theoretical considerations according to Sachs (2005)[9] and from either personal or video taped observations of soaring Wandering Albatrosses. This is a first indicator that the underlying local wind model reflects the real conditions.

2. The resulting dissipative force due to drag F_{Diss} is negative throughout the whole maneuver.[10] Hence the partition of the acting aerodynamic force in lift L and drag D is plausible. This fact also supports the local wind assumptions.

3. This local wind causes a divergence between the bird's kinematic and aerodynamic velocity. The resulting angle α_W leads to a tilting of the lift vector such as to have a component aligned with the instantaneous flight path direction. This component

---

[8]The high values of F_{Diss} at the bginning and the end of the plotted interval are due to the natural boundary constraints used when interpolating, Eq. (6.7).

[9]The results of this reference refer to *minimum* wind conditions, which are exceeded in the present case.

[10]The unsteady behavior at the limits of the cycle is likely to be caused by the natural boundary conditions used for smoothing spline interpolation, see Eq. (6.7).

acts like a propulsive force F_{Prop} (replacing thrust) during the upper turn from wind- to leeward. The decelerating effect of this force throughout the opposite curve is attenuated by the reduced wind speed at the low altitudes this turn is flown at. After integration a net energy gain remains which is just sufficient to compensate for drag, compare Eq. (7.16).

4. According to Figure 7.3 the maximum change in wind speed occurs directly above the water surface. However with a peak altitude of 11.7 m the bird leaves the area with high gradients. This points out that it is not primarily the wind gradient per se but the absolute difference in wind speed encountered by the bird during the upper and the lower turn which is responsible for energy extraction.

7.3 Dynamic Soaring of Albatrosses – Conclusion

The periodic nature of the analyzed flight cycle allows to generalize the statements made in the above in order to explain the dynamic soaring of albatrosses and other large seabirds. Here special importance pertains to the results stemming from the energy analysis as the latter is solely based on direct, precise measurements. The aerodynamic force analysis is based on two models – a parameter-free point mass model and a boundary layer wind model in conjunction with satellite measured wind speeds. This analysis shows that the used wind model provides a flight mechanical explanation for the measured total energy.

Future work to be done on the flight data gathered during the campaign to Kerguelen Archipelago pertains to the measurements of the three-dimensional MEMS accelerometers. These data were recorded during five flights aside the raw GPS output and have not been used so far. A description of the data quality of these sensors can be found in Müller (2010). The sensor-frame related measurements bear the potential of reconstructing additional flight parameters. Moreover the built-up of a dynamic soaring "library" is in progress allowing the classification of individual cycles according to different criteria such as wind speed and wind-relative flight direction. This information will help to learn even more about the fascinating flight of the great wanderers.

8 Conclusion and Outlook

8.1 Time-Differential Positioning

The GPS positioning approach presented in this work allows to measure trajectories with a precision in the decimeter range. This is possible without requiring a second receiver (a reference station) and without the need for dedicated (static) initialization patterns. As a consequence measurements under difficult field conditions are considerably facilitated and even new applications become possible. The method exploits L1 carrier phase ranges – a measurement type which is much more precise than the C/A code range measurements commonly used for (civil) positioning. However, carrier phase measurements are inevitably affected with an ambiguity. In other terms, the range information output by the receiver is precise (to the millimeter level) but not at all accurate. As already implied by the term *time-differential* processing, the method overcomes this problem by forming single differences between phase measurements taken by the same receiver at different moments in time. The starting point of a trajectory section of interest is determined by standard code based single point positioning within an accuracy of a few meters. The following position fixes are determined via time-differential processing with decimeter precision relative to the starting point. Hence neither a second receiver nor any initialization as addressed by other techniques using the same type of measurements is needed. The drawback opposed to such fundamental advantages is the fact that the resulting position fixes are affected with a drifting error component which limits possible processing intervals. This error can be mitigated significantly by the use of external correction data, i.e. corrections pertaining to satellite clocks, satellite predicted positions (the ephemerides) and atmospheric signal delays. Like this trajectories extending over 30 s to up to 5 min can be reconstructed precisely, depending on various environmental conditions. Carrier phase measurements are very fragile causing any kind of phase based processing to be sensitive to signal obstructions caused e.g. by antenna tilting or antenna shadowing. These effects may enforce a reset of the time-differential solution possibly causing a gap in the resulting trajectory. Besides the core positioning capabilities, the developed postprocessing software features algorithms for both solution quality and solution integrity monitoring. Whereas the former is essential for providing feedback of the actual error (drift) to the user, the latter ensures that erroneous phase measurements

(e.g. affected by cycle slips) are detected and excluded such as to assure correct results. Moreover the provided quality indicators allow to properly tune interpolation parameters used in further processing steps for estimating speed and even acceleration. In a final processing step eventual trajectory gaps are bridged by fusing C/A code based position and Doppler based velocity information with the time-differential solution. The whole approach is generally applicable to raw L1 carrier phase data recorded by any kind of GPS receivers. In the context of the present project the goal was to use miniaturized low-cost receivers. Whereas the majority of the devices of this class do not allow the user to access the raw (phase) data, some manufacturers do provide this feature as add-on to selected receivers. However the on-board memory of these modules is usually designed to store the final position fixes rather than the much higher data flow resulting from raw data recording. This necessitates the use of additional external memory for logging data during extended time periods. The successful time-differential processing of raw data gathered by low-cost receivers constitutes a significant added value and enhances the area of operation of such devices. This was demonstrated by a variety of static and dynamic (flight) tests serving as a validation of the proposed method. The test results both provide a general proof of concept of time-differential processing and exhibit the quality of the resulting solution. This solution was shown to be affected with a noise-like error in the millimeter range and an error drift of several centimeters up to several decimeters per minute only. Furthermore the in-depth comparison with a RTK reference solution allowed to validate the quality and integrity monitoring algorithmic. The test phase was followed by a demanding application: the measurement of the dynamic soaring of albatrosses. This task implied harsh environmental conditions (low ambient temperatures, salt water, high dynamics of the birds) and restrictive requirements concerning size, weight and ruggedness of the used hardware. Moreover the field conditions encountered when mounting measurement equipment on the birds impeded the realization of any initialization patterns. The huge distances covered by the birds when foraging made the setup of a close-by base station impossible. The successful evaluation of the recorded raw data by the time-differential approach allowed the reconstruction of the birds' maneuvers with unmatched precision.

The temporal limitation of possible processing intervals may appear as a severe restriction of the time-differential method in terms of applicability at a first glance. However it turns out that there are many applications that do not demand longer trajectory sections – ranging from flight testing to the measurements of any short-term motion on a much smaller scale. In many scenarios even the use of improved (and heavier) antennas would be feasible to further alleviate the problem of loss of phase lock. However the installation of a second base receiver and the realization of initialization patterns as needed by other precise postprocessing approaches would

be a no-go requirement in many cases. If not directly applied for positioning, the time-differential method could also be used as an independent means for raw data screening, paving the way for other postprocessing tools: Within the development of the integrity monitoring algorithm the potential of outlier and cycle slip discrimination and even repair has been revealed. Some more development efforts would be necessary to translate this idea to stable and reliable code further enhancing the versatility of the approach. Time-differential processing fully exploits latest achievements in terms of receiver technology and miniaturization. It will also benefit from the breathtaking advancements of GNSS systems around the globe. The high number of satellites trackable by multi-GNSS receivers will allow to process data recorded during even more difficult conditions in the not too far future. Today positioning solutions for all thinkable applications and virtually all required accuracies are available – to those who can afford to both spend a lot of money and to use large and heavy equipment. Scientists and engineers all around the globe have opened the race to make high positioning performance available also for (mass market) applications with strict budget limitations and stringent size and weight requirements – enabling the location of a cell phone to within a one meter accuracy may be the next sound-barrier to be broken in (civil) positioning! Showing the high potential of carrier phase time-differences when exploiting the measurements of truly low-cost, miniaturized and stand-alone GPS receivers in highly dynamic applications, the present work intends to contribute to these ongoing efforts.

8.2 The Flight of Albatrosses

During the past decade GNSS systems made position information as available and as self-evident as the time displayed on a wristwatch. This was not granted at all during long centuries, causing countless accidents in the history of seafaring. This history was always associated with the large white albatrosses which seemingly effortless – without flapping their large wings – followed the vessels venturing in southern seas. Whereas the determination of a ship's position succeeded with the invention of precise chronometers at the end of the 18th century, understanding the mechanisms of the fascinating flight of albatrosses was impossible due to deficient measurement equipment and methods until today. Coarse position determination by means of the Global Positioning System already became possible in the nineteen-eighties. However only the development of the precise time-differential positioning method in combination with the latest achievements in terms of receiver miniaturization and power efficiency allowed to firstly measure albatross flight trajectories with very high precision serving as a sound basis for flight mechanical investigations.

   In the scope of a successful measurement campaign to a breeding site of Wandering

Albatrosses at the Kerguelen Islands (49°S 70°E), thirty-six days of GPS flight data of the world's largest flying birds were recorded and analyzed back in the office. This analysis was carried out in multiple stages: A first visual examination of the recorded trajectories confirmed that the birds always fly close to the water surface, that they barely ever fly in a straight line but that their tracks reveal a highly winding, cyclic shape. The animals were observed to cover long distances during their foraging trips – one individual traveled close to 5,000 kilometers over open waters within six days. In a next step the birds' energy management was analyzed by observing their specific total energy level during individual dynamic soaring cycles. Such a cycle typically consists of four distinguished phases: a turn from lee- to windward directly above the water surface, a windward climb to altitudes of ten to twenty meters, an upper turn from wind to leeward at peak altitude, and a leeward descent after which the whole maneuver is repeated. Passing on any assumptions concerning (aero)dynamic bird parameters or local winds, this analysis revealed that the birds are loosing energy when flying directly above the water surface. In conjunction with the smooth change of the total energy over time, this shows that wave or turbulence induced vertical winds or gusts do not play a key role for the energy gain required for a sustained flight without flapping. It is during the upper turn, high above the rough sea surface, that a maximum gain of total energy can be observed. Only now an analysis of the specific aerodynamic forces based on local wind assumptions was carried out – still without falling back to (unknown) estimates of any bird parameters. Here it could be shown that it is the "smart" swiveling of the lift vector towards the inertial speed vector which allows the birds to extract energy from the air during the upper turn of their maneuvers.

As a matter of fact a highly energy efficient flight technique as observed in albatrosses is of major interest also in a technical context. The presented findings constitute a starting point for the development of respective applications. This is left up for future projects. The central objective of the present research was to understand – to finally understand – how these mysterious ocean travelers manage to continuously fly without flapping their large wings.

Bibliography

ANTARIS (2003). *Positioning Engine Protocol Specification*. Ublox AG. Doc ID GPS.G3-X-03002-D.

Argos (2008). *Argos Users's Manual – Worldwide Tracking and Environmental Monitoring by Satellite*. Argos, Toulouse, France.

Ashby, N. and Spilker, J. J. (1996). Introduction to relativistic effects on the Global Positioning System. In Parkinson, B. W. and Spilker, J. J., editors, *Global Positioning System: Theory and applications*, volume 1, pages 623–697. AIAA, Washington DC.

Balard, N., Santerre, R., Cocard, M., and Bourgon, S. (2006). Single GPS receiver time-relative positioning with loop misclosure corrections. *GPS Solutions*, 10(1):56–62.

Bierling, T. (2007). *Kinematische Flugbahnrekonstruktion aus Positions-Messdaten mittels glättender Spline Interpolation*. Semsterarbeit, Institute of Flight System Dynamics, Technische Universität München. Supervision: Traugott, J.

BIPM (1998). *Bureau International des Poids et Mesures: Le Système International d'Unités (SI) - The International System of Units (SI)*. Pavillon de Breteuil, F-92312 Sèvres Cedex, France, 7th edition.

BirdLife Int. (2004). *Tracking Ocean Wanderers: The Global Distribution of Albatrosses and Petrels. Results from the Global Procellariiform Tracking Workshop*. BirdLife International, Gordon's Bay, South Africa.

Braasch, M. S. (1996). Multipath effects. In Parkinson, B. W. and Spilker, J. J., editors, *Global Positioning System - Theory and Applications*, volume 1, pages 547–568. AIAA, Washington DC.

Brown, R. G. (1992). A baseline RAIM scheme and a note on the equivalence of three RAIM methods. In *Proc. of the 1992 National Technical Meeting of the Institute of Navigation*, San Diego, CA.

Brown, R. G. and Chin, G. Y. (1997). GPS RAIM: Calculation of threshold and protection radius using chi-square methods - a geometric approach. *Global Positioning System: Institue of Navigation*, 5:155–178.

Brown, R. G. and Hwang, P. Y. C. (1997). *Introduction to Random Signals and Applied Kalman Filtering*. John Wiley & Sons, New York, 3rd edition. ISBN 0-471-12839-2.

Byun, S. H. and Bar-Sever, Y. E. (2009). A new type of troposphere zenith path delay product of the International GNSS Service. *Journal of Geodesy*, 83:367–373. DOI 10.1007/s00190-008-0288-8.

Catry, P., Phillips, R. A., and Croxall, J. P. (2004). Sustained fast travel by a Gray-Headed Albatross (Thalassarche Chrysostoma) riding an arctic storm. *The Auk*, 121(4):1208–1213.

Collins, P. C., Langley, R., and LaMance, J. (1996). Limiting factors in tropospheric propagation delay error modelling for GPS airborne navigation. In *Proc. of ION 52nd Annual Meeting*, Cambridge, MA.

De Jong, K. (1998). Real-time integrity monitoring, ambiguity resolution and kinematic positioning with GPS. In *Proc. of the 2nd European Symposium on Global Navigation Satellite Systems*.

Denny, M. (2009). Dynamic soaring: Aerodynamics for albatrosses. *European Jounal of Physics*, 30:75–84.

Dow, J. M., Neilan, R. E., and Rizos, C. (2009). The International GNSS Service in a changing landscape of Global Navigation Satellite Systems. *Journal of Geodesy*, 83:191 – 198. doi:10.1007/s00190-008-0300-3.

ESA (2005). EGNOS fact sheet 14 - SBAS interoperability explained - delivering a global service. published online at www.egnos-pro.esa.int.

FAA (1994). *Advisory Circular 90-94: Guidelines for using GPS equipment for IFR en route and terminal operations and for nonprecision instrument approaches in the U.S. national airspace system*.

FAA (2010). GPS Modernization: The Future of Navigation. Online article published at www.faa.gov.

Faraway, J. J. (2005). *Linear Models with R*, volume 63 of *Texts in Statistical Science*. Chapman & Hall/CRC. ISBN 1-58488-425-8.

Farrell, J. L. (2001). Carrier phase processing without integers. In *Proc. of ION 57th Annual Meeting*, pages 423–428, Albuquerque, NM.

Farrell, J. L. (2007). *GNSS Aided Navigation & Tracking*. American Literary Press, Baltimore, MD. ISBN-13: 978-1-56167-979-9.

Farrell, J. L. and Barth, M. (1998). *The Global Positioning System and Inertial Navigation*. Progress in Astronautics and Aeronautics. McGraw-Hill, New York, NY.

Feess, W. A. and Stephens, S. G. (1987). Evaluation of GPS ionospheric model. *IEEE Transactions on Aerospace Science and Electronic Systems*, AES-23(3):332–228.

Gao, Y. (2006). What is precise point positioning (PPP), and what are its requirements, advantages and challenges? *Inside GNSS*, 1(8):16–18. ISSN 1559-503X.

Gruber, B. (2010). GPS program update to ION 2010. In *Proc. of the ION 23rd International Conference of the Satellite Devision*, Portland, OR.

Gun, L., Yong-Hui, H., and Wei, Z. (2006). A new algorithm of detecting and correction cycle slips in dual frequency GPS. In *Proc. of the IEEE Intl. Frequency Control Symposium and Exposition*. IEEE.

Gurtner, W. and Estey, L. (2007). *RINEX: The Receiver Independent Exchange Format Version 2.11*. Astronomical Institute University of Berne, CH, and UNAVCO, Boulder, CO.

Hewitson, S. and Wang, J. (2006). GNSS receiver autonomous integrity monitoring (RAIM) for multiple outliers. *The European Journal of Navigation*, 4(4):47–57.

Hofmann-Wellenhof, B., Lichtenegger, H., and Collins, J. (2001). *Global Positioning System - Theory and Practice*. Springer, Wien, New York, 5th edition.

Hopfield, H. S. (1969). Two-quadratic tropospheric refractivity profile for correction sattellite data. *Jounal of Geophysical Research*, 74(18):4487–4499.

Hütter, H. (2008). *Untersuchungen von Methoden zur Rekonstruktion von 3-Freiheitsgrad Bewegungen auf der Grundlage von Positionsmessungen über ausgleichende Splines*. Diplomarbeit, Institute of Flight System Dynamics, Technische Universität München. Supervision: Traugott, J.

ICD-GPS-200C (2000). *Navstar GPS Space Segment / Navigation User Interfaces*. U.S. Air Force.

Jouventin, P. and Weimerskirch, H. (1990). Satellite tracking of Wandering Albatrosses. *Nature*, 343:746–748.

JPL (2006). *QuikSCAT Science Data Product User's Manual – Overview and Geophysical Data Products*. Jet Propulsion Laboratory, CA.

Kaplan, E. D., editor (1996). *Understanding GPS - Principles and Applications*. Artech House, Inc., Norwood, MA, 16th edition.

Kirkko-Jaakkola, M., Traugott, J., Odijk, D., Collin, J., Sachs, G., and Holzapfel, F. (2009). A RAIM approach to GNSS outlier and cycle slip detection using L1 carrier phase time-differences. In *Proc. of the IEEE Workshop on Signal Processing Systems*, pages 273–278, Tampere, Finland. IEEE.

Klein, V. and Morelli, E. A. (2006). *Aircraft System Identification – Theory and Practice*. AIAA Education Series. ISBN 1-56347-832-3.

Klobuchar, J. (1986). Design and characteristics of the GPS ionospheric time-delay algorithm for single frequency users. In *Proc. of PLANS'86 – Position Location and Navigation Symposium*, pages 280–286, Las Vegas, NV.

Kuchling, H. (1999). *Taschenbuch der Physik*. Fachbuchverlag Leipzig im Carl Hanser Verlag, München, Wien.

Landau, H., Chen, X., Kipka, A., and Vollath, U. (2007). Network RTK - getting ready for GNSS modernization. *GPS World*, 18(4):50 – 55.

Lissaman, P. (2007). Fundamentals of energy extraction from natural winds. *Technical Soaring*, 31(2):36 – 41.

MATLAB (2008). *R2008b Product Help*. The MathWorks.

Misra, P. and Enge, P. (2004). *Global Positioning System - Signals, Measurements and Performance*. Ganga-Jamuna Press, Lincoln, MA. 2nd printing.

Mohr, P. and Taylor, B. (2005). CODATA recommended values of the fundamental physical constants. *Reviews of Modern Physics*, 77(1). http://physics.nist.gov/cuu/Constants/.

Möller, C. (2008). *Entwicklung und Implementierung eines Moduls zur Geschwindigkeitsermittlung aus GPS Dopplermessdaten*. Semesterarbeit, Institute of Flight System Dynamics, Technische Universität München. Supervision: Traugott, J.

Müller, H. (2009). *QuikSCAT L3 Global Wind Data – Projection on Local Flight Trajectories and 3D Interactive Visualization*. Semesterarbeit, Institute of Flight System Dynamics, Technische Universität München. Supervision: Traugott, J.

Müller, H. (2010). *Investigations on Dynamic Soaring of Albatrosses Based on Precise GPS and Accleration Data*. Diplomarbeit, Institute of Flight System Dynamics, Technische Universität München. Supervision: Traugott, J.

Neill, A. E. (1996). Global mapping functions for the atomosphere delay at radio wavelength. *Journal of Geophysical Research*, 101(b2):3227–3246.

NIMA (2000). Department of Defense World Geodetic System 1984 – Its definition and relationships with local geodetic systems. Technical Report 8350.2, National Imagery and Mapping Agency.

Odijk, D., Traugott, J., Sachs, G., Montenbruck, O., and Tiberius, C. C. J. M. (2007). Two approaches to precise kinematic GPS positioning with miniaturized L1 receivers. In *Proc. of ION GNSS 20th International Technical Meeting of the Satellite Division*, pages 827–838, Fort Worth, TX. The Institute of Navigation.

Odijk, D. and Verhagen, S. (2007). Recursive detection, identification and adaption of model errors for reliable high-precision GNSS positioning and attitude determination. In *Proc. of 3rd Intl. Conference on Recent Advances in Space Technologies*.

Oosterlinck, R. (2010). Galileo programme status. In *Proc. of ION 23rd International Technical Meeting of the Satellite Devision*, Portland, OR.

Parkinson, B. (2010). Looking ahead for GPtS. In *Proc. of ION 23rd International Technical Meeting of the Satellite Devision*, Portland, OR.

Pennycuick, C. J. (2008). *Modelling the Flying Bird*. Elsevier / Academic Press. ISBN 978-0-12-374299-5.

Phillips, R. A., Xavier, J. C., and Croxall, J. P. (2003). Effects of satellite transmitters on albatrosses and petres. *The Auk*, 120:1082–1090.

Reinsch, C. H. (1967). Smoothing by spline functions. *Numerische Mathematik*, 10:177–183.

Revnivykh, S. (2010). GLONASS status and progress. In *Proc. of ION 23rd International Technical Meeting of the Satellite Devision*, Portland, OA.

Saastamoinen, J. (1973). Contributions to the theory of atmospheric refraction. *Journal of Geodesy*, 46:279–298.

Sachs, G. (2005). Minimum shear wind strength required for dynamic soaring of albatrosses. *Ibis*, 147(1):1–10. doi:10.1111/j.1474-919x.2004.00295.x.

Schaer, S., Gurtner, W., and Feltens, J. (1998). IONEX: The IONosphere map EXchange format version 1. In *Proc. of the IGS AC Workshop*, pages 3127–3131, Darmstadt, Germany.

Seeber, G. (1993). *Satellite Geodesy - Foundations, Methods, and Applications*. Walter de Gruyter, Berlin, New York.

SPS (2008). *Global Positioning System Standard Positioning Service Performance Standard*. US Department of Defense, 4th edition.

Stöcker, H., editor (2000). *Taschenbuch der Physik*. Harri Deutsch Verlag, Thun, Frankfurt a. M., 4th edition.

Taylor, J. R. (1999). *An Introduction to Error Analysis - The Study of Uncertainties in Physical Measurements*. University Science Books. ISBN 0-935702-75-X.

Teunissen, P. J. G. (1994). A new method for carrier phase ambiguity estimation. In *Proc. of IEEE PLANS*, pages 862–873, Las Vegas, NV.

Tickell, W. L. N. (2000). *Albatrosses*. Pica Press, Robertsbridge.

Traugott, J., Dell'Omo, G., Vyssotski, A., Odijk, D., and Sachs, G. (2008a). A time-relative approach for precise positioning with a miniaturized L1 GPS logger. In *Proc. of ION GNSS 21th International Technical Meeting of the Satellite Division*, pages 1883–1894, Savannah, GA. The Institute of Navigation.

Traugott, J., Odijk, D., Montenbruck, O., Sachs, G., and Tiberius, C. C. J. M. (2008b). Making a difference with GPS. *GPS World*, 19(5):48 – 57.

Traugott, J. and Sachs, G. (2007). Präzisionsvermessung von Flugbahnen mittels miniaturisierter L1-GPS-Empfänger durch ein Zeitdifferenzen-Verfahren. In *Proc. of PosNav*, Magdeburg, Germany. DGON.

Traugott, J., Sachs, G., and Holzapfel, F. (2008c). Präzise Flugbahnrekonstruktion mittels miniaturisierter L1-GPS Empfänger durch ein Zeitdifferenzen-Verfahren. In *Jahrbuch 2008 der Deutschen Gesellschaft für Luft- und Raumfahrt*, volume 3, Darmstadt, Germany. DGLR.

Tycho (2010). Block II satellite information. Available online at ftp:// tycho.usno.navy.mil.

Ulmer, K., Hwang, P., Disselkoen, B., and Wagner, M. (1995). Accurate azimuth from a single PLGR+GLS DoD GPS receiver using time relative positioning. In *Proc. of ION GPS-95*, pages 1733–1741, Palm Springs, CA. The Institute of Navigation.

Utschick, M. (2010). *Entwicklung eines Verfahrens zur Fusion, Glättung und Differentiation verschiedenartiger GPS Positions- und Geschwindigkeits-Lösungen.* Semesterarbeit, Institute of Flight System Dynamics, Technische Universität München. Work supported by Wendel, J. and Butzhammer, P.; supervision: Traugott, J.

Van Graas, F. and Lee, S. W. (1995). High-accuracy differential positioning for satellite-based systems without using code-phase measurements. *Navigation: Journal of the Institute of Navigation*, 42(4):605–618.

Verhagen, S. and Teunissen, P. J. G. (2006). New Global Navigation Satellite System ambiguity resolution method compared to exitsting approaches. *Journal of Guidance, Control and Dynamics*, 29(4):981–991.

Vyssotski, A. L., Serkov, A. N., Itskov, P. M., Dell'Omo, G., Latanov, A. V., Wolfer, D. P., and Lipp, H. P. (2006). Miniature neurologgers for flying pigeons - multichannel EEG and action and field potentials in combination with GPS recording. *Journal of Neurophysiology*, 95:1263–1273.

Waypoint (2004). *GrafNav/GrafNet, GrafNav lite, GrafMov, Inertial Explorer Operating Manual.* NovAtel Inc. (Waypoint Products Group).

Weimerskirch, H., Bonadonna, F., Bailleul, F., Mabille, G., Dell'Omo, G., and Lipp, H. P. (2002). GPS tracking of foraging albatrosses. *Science*, 295:1259.

Weimerskirch, H., Guionnet, T., Martin, J., Shaffer, S. A., and Costa, D. P. (2000). Fast and fuel efficient? Optimal use of wind by flying albatrosses. *Proc. of The Royal Society, Series B*, 267:1869–1874.

Wendel, J., Obert, T., and Trommer, G. F. (2003). Enhancement of a tightly coupled GPS/INS system for high precision attitude determination of land vehicles. In *Proc. of ION 59th Annual Meeting/CIGTF 22nd Guidance Test Symposium*, pages 200–208, Albuquerque, NM.

Wieser, A. (2007). *GPS Based Velocity Estimation and its Application to an Odometer.* Shaker Verlag, Aachen.

Wilson, R. P., Putz, K., Peters, G., Culik, B., Scolaro, J. A., Charrassin, J. B., and Ropert-Coudert, Y. (1997). Long-term attachment of transmitting and recording devices to penguins and other seabirds. *Wildl. Soc. Bull.*, 25:101–106.

Zarchan, P. and Musoff, H. (2000). *Fundamentals of Kalman Filtering – A Practical Approach*, volume 190 of *Progress in Astronautics and Aeronautics*. AIAA Education Series, Reston, VA.

A Maths

A.1 Least Squares

Let $\widetilde{\mathbf{y}} = (\widetilde{y}_1, \ldots, \widetilde{y}_i, \ldots, \widetilde{y}_m)^T$ be a set of measurements affected with experimental errors ε_i. These measurements are (linearly) modeled as a function of the unknown parameters $\mathbf{x} = [x_1, x_2, \ldots, x_n]^T$ with $n \leq m$:

$$\widetilde{\mathbf{y}} = \mathbf{H}\mathbf{x} + \varepsilon \tag{A.1}$$

The $m \times n$ coefficients of $\mathbf{H}$ (the predictors) are constants or functions of an independent variable such as the sample time. The goal of a least squares estimator is to determine $\mathbf{x}$ such as to minimize the errors ε in a least squares sense:

$$\varepsilon = \widetilde{\mathbf{y}} - \mathbf{H}\mathbf{x} \tag{A.2}$$

$$\varepsilon^T \varepsilon = \sum_{i=1}^{m} \varepsilon_i^2 = \text{min!} \tag{A.3}$$

Following the derivation given in statistics textbooks such as Faraway (2005), Eq. (A.3) yields the normal equations

$$\mathbf{H}^T \mathbf{H} \mathbf{x} = \mathbf{H}^T \widetilde{\mathbf{y}} \tag{A.4}$$

which can finally be solved for an estimate of the parameters $\widehat{\mathbf{x}}$ (the estimator) and the observations $\widehat{\mathbf{y}}$:[1]

$$\widehat{\mathbf{x}} = (\mathbf{H}^T \mathbf{H})^{-1} \mathbf{H}^T \widetilde{\mathbf{y}} \tag{A.5}$$

$$\widehat{\mathbf{y}} = \mathbf{H}\widehat{\mathbf{x}} = \mathbf{H}(\mathbf{H}^T \mathbf{H})^{-1} \mathbf{H}^T \widetilde{\mathbf{y}} \tag{A.6}$$

If the measurement errors ε_i are mutually uncorrelated, have zero mean and equal variance, and the structural part of the model (Eq. (A.1)) is correct, Eq. (A.5) is the best linear unbiased estimate of $\mathbf{x}$. This relationship is known as the Gauss-Markov theorem. To understand this theorem the concept of an estimable function is required. A linear combination of the parameters $\psi = \mathbf{c}^T \mathbf{x}$ is estimable iff there exists a linear

---

[1]It is no good practice to invert the normal equation matrix as shown here for the sake of simplicity. If $\mathbf{H}^T \mathbf{H}$ is well conditioned and positive-definite, the normal equations can be solved directly by using Cholesky decomposition.

combination $\mathbf{a}^T\widetilde{\mathbf{y}}$ such that

$$E\left[\mathbf{a}^T\widetilde{\mathbf{y}}\right] = \mathbf{c}^T\mathbf{x} \quad \forall\mathbf{x} \tag{A.7}$$

The theorem states that in the class of all unbiased linear estimates of ψ, $\widehat{\psi} = \mathbf{c}^T\widehat{\mathbf{x}}$ has the minimum variance and is unique.

If, in addition to the above conditions, the errors are normally distributed, least squares corresponds to the maximum likelihood criterion.

The covariance matrix of the parameters can be determined by

$$\mathbf{C}_{\widehat{\mathbf{x}}} = \sigma^2(\mathbf{H}^T\mathbf{H})^{-1} \qquad\qquad \text{with } \mathbf{C}_\varepsilon = \sigma^2\mathbf{I} \tag{A.8}$$

If there are enough measurements ($m \gg n$) and the variance σ^2 of the measurement errors is not known, the latter can be estimated by

$$\sigma^2 = \frac{\mathbf{f}^T\mathbf{f}}{m-n}; \quad \text{with} \tag{A.9}$$

$$\mathbf{f} = \widetilde{\mathbf{y}} - \widehat{\mathbf{y}} \tag{A.10}$$

Here $\mathbf{f}$ represents the residual vector, i.e. the difference of the measured and the computed observations.

If the observations are not equally reliable, a more general objective function may be addressed:

$$\varepsilon^T\mathbf{V}^{-1}\varepsilon = \min!; \quad \text{with } \mathbf{V} \sim \mathbf{C}_\varepsilon \tag{A.11}$$

where $\mathbf{V}$ is an m-by-m real symmetric positive definite matrix which is proportional to the measurement covariance matrix. If the individual measurement errors ε_i are uncorrelated, $\mathbf{V}$ has diagonal shape: $\mathbf{V} \sim diag(\sigma_i^2)$. As a consequence the objective function simplifies to $S = \sum_{i=1}^{m}(1/\sigma_i^2 f_i^2) = \min!$ For the general case Eq. (A.11) yields the following normal equations

$$\mathbf{H}^T\mathbf{V}^{-1}\mathbf{H}\mathbf{x} = \mathbf{H}^T\mathbf{V}^{-1}\widetilde{\mathbf{y}} \tag{A.12}$$

which can be solved for $\widehat{\mathbf{x}}$ either by inversion or Cholesky decomposition. The covariance matrix of the measurement errors is assumed to be known only up to a scale factor *mse* (mean squared error) which can be estimated according to standard least squares equations if there is a sufficient number of measurements ($m \gg n$) (MATLAB, 2008, function "lscov"):

$$mse = \frac{\widetilde{\mathbf{y}}^T(\mathbf{V}^{-1} - \mathbf{V}^{-1}\mathbf{H}(\mathbf{H}^T\mathbf{V}^{-1}\mathbf{H})^{-1}\mathbf{H}^T\mathbf{V}^{-1})\widetilde{\mathbf{y}}}{m-n} \tag{A.13}$$

This yields an estimate for the parameter covariance matrix

$$\mathbf{C}_{\widehat{\mathbf{x}}} = (\mathbf{H}^T \mathbf{V}^{-1} \mathbf{H})^{-1} mse \tag{A.14}$$

Of course, if the absolute variances of the measurement errors are known and $\mathbf{V}$ is chosen accordingly ($\mathbf{V} = \mathbf{C}_\varepsilon$), *mse* should be set to one in Eq. (A.14).

A.2 Random Processes

The very brief explanations given here are mainly quoted from Brown and Hwang (1997).

Before heading to the description of a random process some basic definitions concerning an individual random variable X (with respective sample realizations x) shall be repeated: The expected or mean value of X is calculated by

$$
\begin{aligned}
E[X] = m_X &= \sum_{i=1}^{m} p_i x_i \quad \text{(discrete case)} \\
&= \int_{-\infty}^{\infty} x f_X(x) \, dx \quad \text{(continuous case)} \\
&= \frac{\sum_{i=1}^{n} x_i}{n}; \quad \text{(numerical sample calculation)}
\end{aligned}
\tag{A.15}
$$

where p_i are the probabilities related to the m possible realizations of the discrete random variable X. The probability density function of X in the continuous case is denoted by $f_X(x)$. Basing on these definitions some other frequently used quantities are introduced according to Zarchan and Musoff (2000, p. 27):

$$\text{Mean square value} = E[X^2] = \frac{\sum_{i=1}^{n} x_i^2}{n-1} \tag{A.16}$$

$$\text{Root mean square RMS} = \sqrt{E[X^2]} \tag{A.17}$$

$$\text{Variance } \sigma^2 = E[(X - m_X)^2] = \frac{\sum_{i=1}^{n}(x_i - m_X)^2}{n-1} \tag{A.18}$$

$$\text{Standard deviation } \sigma = \sqrt{\sigma^2} \tag{A.19}$$

For the zero mean case only (!) the mean square value equals the variance and the RMS coincides with the standard deviation.

In opposite to a random variable related to an individual event like throwing a dice, a random process is related to the time history of some physical quantity such as the voltage driving the speakers of a radio tuned away from any station frequency. Figure A.1 illustrates a typical realization of a continuous-time random process. In order to describe such a signal, something about the relative distribution of the process
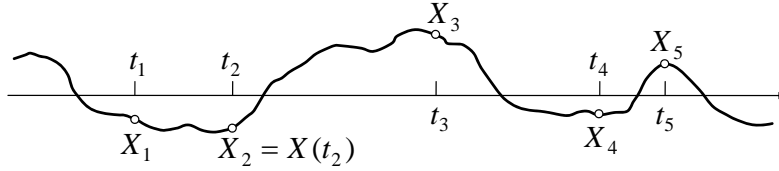
Figure A.1: Sample signal of a typical noise process

amplitude as well as its mean and mean square value must be known. This information is provided by the first-order probability density functions $f_{X_1}(x_1), f_{X_2}(x_2), \ldots$. In addition some knowledge about how rapidly the signal is changing, i.e. its spectral content, is required. This is achieved by analyzing the joint densities $f_{X_1 X_2}(x_1, x_2)$, $f_{X_1 X_3}(x_1, x_3), \ldots$ relating any pair of random variables. These second order density functions would provide, in conjunction with even higher-order ones, a lot of probabilistic information about the process. As it is very difficult to specify them explicitly, other means to properly describe a random process are required:

Stationarity A random process is said to be *(time-) stationary* if the density functions describing the process are invariant under a translation of time.

Ergodicity A random process is said to be *ergodic* if a single sample time signal of the process as shown in Figure A.1 contains all possible statistical variations of the process. (This would not be the case for a random process such as $X(t) = A$ with A being a random variable "determined" once when starting the process (turn-on bias)).

Autocorrelation Function The autocorrelation function holds information about how well the process is correlated with itself at two different times:

$$R_X(t_1, t_2) = E[X(t_1)X(t_2)]) \qquad \text{(general case)} \qquad \text{(A.20)}$$

$$R_X(\tau) = E[X(t)X(t+\tau)] \qquad \text{(stationary case)} \qquad \text{(A.21)}$$

For a both stationary and ergodic signal, the autocorrelation function can be calculated according to

$$R_X(\tau) = \text{time average of } X(t) \cdot X(t+\tau)$$
$$= \lim_{T \to \infty} \frac{1}{T} \int_0^T X(t)X(t+\tau)dt \qquad \text{(A.22)}$$

Figure A.2 shows the autocorrelation function for an exemplary random process. If the autocorrelation function decreases rapidly, the process changes rapidly with time and vice versa – the autocorrelation function contains important information about the frequency content of a process.

Power Spectral Density Function For stationary processes, the Wiener-Khinchine theorem establishes a direct relation between the (power) spectral density function (PSD)
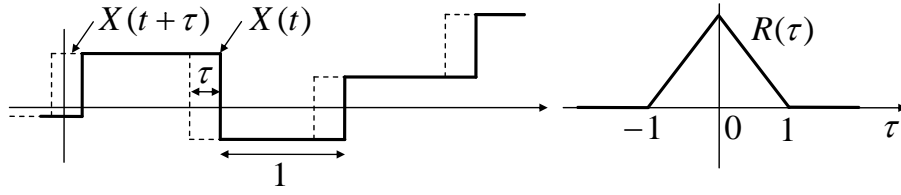
Figure A.2: Exemplary random process with autocorrelation function (stationary, ergodic case)

of the process and its autocorrelation function:

$$S_X(j\omega) = \mathscr{F}[R_X(\tau)] = \int_{-\infty}^{\infty} e^{-j\omega\tau} R_X(\tau) d\tau \tag{A.23}$$

As known from Fourier transform theory, the inverse of the PSD accordingly yields the autocorrelation function

$$R_X(\tau) = \mathscr{F}^{-1}[S_X(j\omega)] = \frac{1}{2\pi} \int_{-\infty}^{\infty} e^{j\omega\tau} S_X(j\omega) d\omega$$

$$R_X(0) = E[X^2(t)] = \frac{1}{2\pi} \int_{-\infty}^{\infty} S_X(j\omega) d\omega \tag{A.24}$$

Note that for a zero-time shift, the autocorrelation function provides a convenient means to calculate the mean square value of the process. Obtaining the power in a finite band is achieved by integrating over the appropriate range of frequencies, that is

$$\begin{bmatrix} \text{"Power" in} \\ \text{range } \omega_1 \leq \omega \leq \omega_2 \end{bmatrix} = \frac{1}{2\pi} \left(\int_{-\omega_2}^{-\omega_1} S_X(j\omega) d\omega + \int_{\omega_1}^{\omega_2} S_X(j\omega) d\omega \right) \tag{A.25}$$

Gaussian Random Process A Gaussian or normal random process is defined as one in which all (higher-order) density functions are normal in form.

White Noise White noise is a stationary random process with PSD:

$$S_X(j\omega) = A \qquad\qquad R_X(\tau) = A\delta(\tau) \tag{A.26}$$

where $\delta(\tau)$ denotes Dirac's delta. Both the autocorrelation function and the spectral density function are illustrated by Figure A.3(a). With the second line of Eq. (A.24) the variance of such signal is infinite - white noise jumps around infinitely far, infinitely fast. Being given that real physical systems are bandlimited to some extent, white noise is a mathematically simple assumption which is suitable as input for many simulation scenarios as the output will always be a limited - meaningful - process. The analogous discrete-time process, a (Gaussian) white sequence, is defined as a sequence of zero-mean, uncorrelated (Gaussian) random variables.

Gauss-Markov Process A stationary Gaussian process with exponential autocorrela-

tion is called Gauss-Markov Process.

$$R_X(\tau) = \sigma^2 e^{-\beta|\tau|} \qquad\qquad S_X(j\omega) = \frac{2\sigma^2\beta}{\omega^2 + \beta^2} \qquad\qquad \text{(A.27)}$$

The autocorrelation approaches zero with $\tau \to \infty$, see Figure A.3(b). The process has zero mean, its variance is σ^2 and its time constant results to $1/\beta$. The discrete version of the process is described by

$$X(t_{k+1}) = e^{-\beta\Delta t} X(t_k) + W(t_k) \qquad\qquad \text{(A.28)}$$

with $W(t_k)$ as an uncorrelated, zero-mean Gaussian sequence.

(a) White noise

(b) Gauss-Markov process
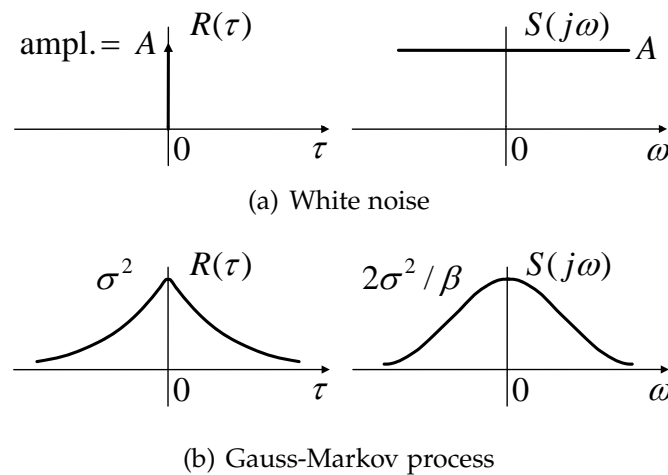
Figure A.3: Autocorrelation function (to the left) and PSD for two frequently used random processes

Wiener Process (Random-Walk) The classical random-walk problem is stated as follows: Start at the origin. Take n steps of same size forward (positive) or backward (negative) with equal likelihood of stepping in either direction. What is the average distance traveled after n steps (in an ensemble sense)? — $m = 0$. What is average square of the distance after n steps? — $\sigma^2 = n$. An exemplary random walk process is shown in Figure A.4. Note that σ is unbounded with n and the process is nonstationary. The continuous analog of random-walk is the output of an integrator driven by white noise. If the input is Gaussian white noise[2], the resulting continuous random-walk process is also normal and known as the *Wiener* or *Brownian-motion*

---

[2]Due to the "infinite variance" problem it is somewhat difficult to define what is meant by (continuous) white Gaussian noise. Usually the argumentation is reversed stating that hypothetical white noise it that process, which, when integrated, yields a Wiener process.

process with the following properties:

$$E[X(t)] = 0 \qquad E[X^2(t)] = t \qquad R_X(t_1, t_2) = \begin{cases} t_2, & t_1 \geq t_2 \\ t_1, & t_1 < t_2 \end{cases} \qquad \text{(A.29)}$$
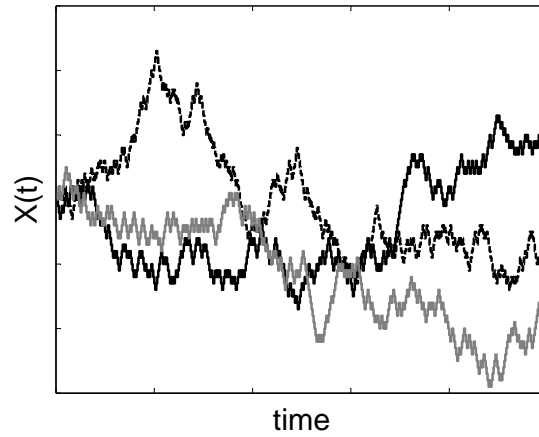
Figure A.4: Ensemble of three realizations of the same random walk experiment

B Physics

B.1 Wave Fundamentals

B.1.1 Wave Equations

An harmonic wave y with amplitude y_0, frequency f, period $T = 1/f$ and wavelength λ is a both time (t) and space (x) dependent oscillation which can be described by the following equation:

$$y(x,t) = y_0 \sin\left[2\pi\left(ft - \frac{x}{\lambda}\right)\right] = y_0 \sin\left(2\pi\,\varphi\,(x,t)\right) \tag{B.1}$$

compare standard physics textbooks such as Kuchling (1999, p. 223). Here φ is the phase indicated in revolution cycles. The propagation speed c is only a function of the medium (no medium is required in the case of electromagnetic waves):

$$c = \lambda f \tag{B.2}$$

The instantaneous frequency of a wave signal at a given (receiver) location is defined by the change of its phase φ (Hofmann-Wellenhof et al., 2001)

$$f = \frac{\partial \varphi}{\partial t} \qquad\qquad \varphi = \int_{t_0}^{t} f(\tau)\,d\tau \tag{B.3}$$

If the emitter (E) of a signal with constant frequency is separated from the receiver (R) by a range ρ one obtains the respective phasings by integration

$$\varphi^E(t) = ft \qquad\qquad \varphi^R(t) = f\left(t - \frac{\rho}{c}\right) \tag{B.4}$$

Figure B.1 illustrates a wave signal.

B.1.2 Doppler Frequency Shift

The Doppler frequency shift is caused by receiver and emitter motion. Here one has to distinguish between medium-bound signals, such as sound waves in acoustics, and electromagnetic waves.
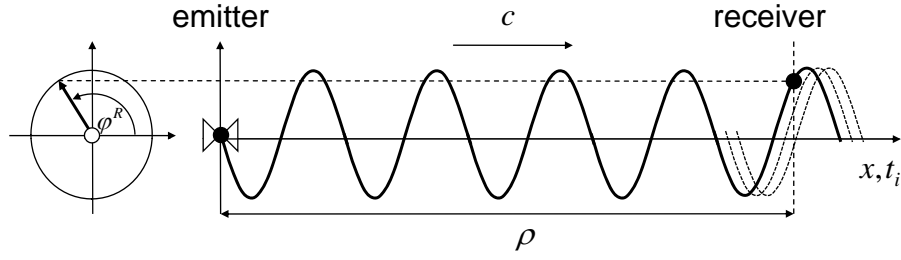
Figure B.1: Snapshot of a wave signal at t_i. Note: $\rho \uparrow \Rightarrow \varphi^R \downarrow$ but $t \uparrow \Rightarrow \varphi^R \uparrow$

Doppler Shift in Acoustics

Let the emitter oscillate with the (nominal) frequency f and the signal propagate through the medium (e.g. air) with the constant speed c. If the emitter moves with a line-of-sight speed v^E relative to the medium, the effective signal wavelength in this direction is altered to

$$\lambda = \frac{c}{f} - v^E T = \frac{c - v^E}{f} \tag{B.5}$$

If the receiver moves with a line-of-sight speed v^R relative to the medium, this changes the receiver relative signal propagation speed to $c - v^R$. Hence one gets for the frequency f^R as perceived by the receiver:

$$f^R = \frac{c - v^R}{\frac{c - v^E}{f}} = f \frac{c - v^R}{c - v^E} \tag{B.6}$$

The sign convention for v^E and v^R is illustrated in Figure B.2. The *Doppler frequency shift* is now defined as the difference between the received and the nominal frequency:

$$f_D = f^R - f \tag{B.7}$$

For $c \gg v^E, v^R$ Eq. (B.6) is often approximated by only considering the resulting range rate $\dot{\rho} = v^R - v^E$

$$f^R = f\left(1 - \frac{\dot{\rho}}{c}\right) \qquad\qquad f_D = -\frac{\dot{\rho}}{\lambda} \tag{B.8}$$
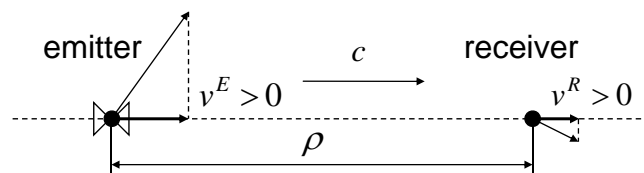
Figure B.2: Sign convention for emitter and receiver motion
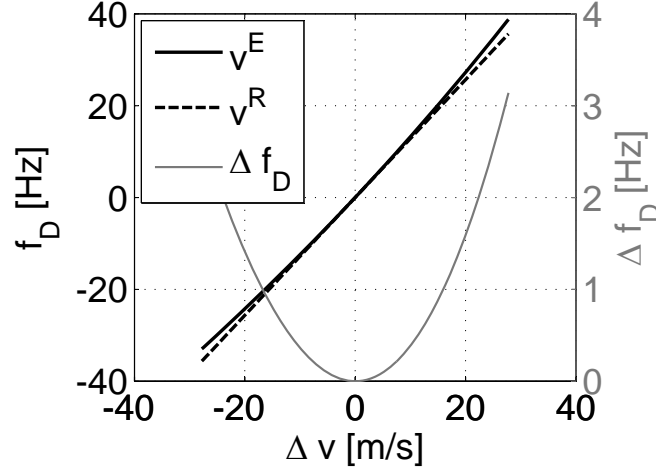
Figure B.3: Difference between the Doppler frequency shift caused by emitter (v^E) and receiver (v^R) motion for a nominal frequency of 440 Hz (standard pitch) and $c = 343$ m/s (acoustic velocity).

Note that Eq. (B.8) corresponds to Eq. (B.6) for receiver motion only. However, Figure B.3 shows that the error made by such simplifications is already in the order of 10 % for everyday life examples.

Doppler Shift for Electromagnetic Waves

Electromagnetic waves are not bound to any medium. Their propagation speed (speed of light) in vacuum is defined as $c = 299,792,458.0$ m/s (Mohr and Taylor, 2005). According to the theory of special relativity, the speed of light is a constant for any inertial observer. As a consequence, translational receiver velocity does not change the receiver relative signal propagation speed and discrimination between a moving receiver and/or a moving emitter is not possible. For high relative velocities, the concept of time dilation causes a *second order Doppler effect* for an observer moving with v vertically to the signal propagation direction (Stöcker, 2000, p. 279):

$$f^R = f\sqrt{1 - \left(\frac{v}{c}\right)^2} \tag{B.9}$$

Multiplying Eq. (B.6) for the emitter motion only case ($v^E = -\dot{\rho}, v^R = 0$) by this relativistic correction yields the longitudinal *Doppler shift for electromagnetic signals*

$$f^R = f\frac{1}{1 + \frac{\dot{\rho}}{c}}\sqrt{1 - \left(\frac{\dot{\rho}}{c}\right)^2} = f\sqrt{\frac{c - \dot{\rho}}{c + \dot{\rho}}} \tag{B.10}$$

For range rates which are small with respect to the speed of light ($\dot{\rho} \ll c$), the relativistic correction for longitudinal motion can be neglected in Eq. (B.10), $(\dot{\rho}/c)^2 \approx 0$,

139

and one obtains as a first order approximation for the frequency shift

$$f_D = f \frac{1}{1 + \frac{\dot{\rho}}{c}} - f = -f \frac{\dot{\rho}}{c} \Big/ \underbrace{\left(1 + \frac{\dot{\rho}}{c}\right)}_{\approx 1}$$

$$f_D = -\frac{\dot{\rho}}{\lambda}$$

(B.11)

This result coincides with Eq. (B.8).

In satellite navigation with a carrier frequency of 1.5 GHz and along-track velocities of about 4 km/s, the second order Doppler frequency shift is in the range of 0.13 Hz which corresponds to range rates of 2 cm/s. This shift is further reduced by the systematic compensation of the satellite oscillators for both general and special relativistic effects with the purpose of long term clock drift reduction. Assuming maximal range rates of 0.9 km/s (Hofmann-Wellenhof et al., 2001, p.88) calculating the longitudinal Doppler via Eq. (B.11) instead of Eq. (B.10) causes an error in the order of 7e-3 Hz (1 mm/s range rate).

B.1.3 Beat Phase

The impact of relative motion between receiver and emitter cannot only be described by the received signal's Doppler frequency shift but also by its beat phase (derivation following Hofmann-Wellenhof et al. (2001, pp. 88)). Let the receiver be located at a distance ρ_0 from the emitter at an initial time t_0 and the phasing of the received signal be $\varphi^R (\rho_0, t_0)$, compare Figure B.1. After $\Delta t = t - t_0$ the range has changed by $\Delta \rho = \rho - \rho_0$ and the receiver now perceives $\varphi^R (\rho, t)$. If there was no relative motion, the received phase would be $\varphi^R (\rho_0, t)$. [1] The difference between these two phasings is defined as the *beat phase ϕ*

$$\phi(t) = \varphi^R (\rho, t) - \varphi^R (\rho_0, t)$$

(B.12)

Figure B.4 illustrates this concept. If relative motion stops, the beat phase remains constant. Otherwise, it changes with the change in range

$$\Delta \rho = -\phi \lambda \qquad\qquad \phi = -\frac{\Delta \rho}{\lambda}$$

(B.13)

where ϕ is indicated in whole and fractional cycles [rad/2π].[2] Comparing Eqs. (B.13) and (B.11) allows to establish a direct relation between the Doppler frequency shift

---

[1] This corresponds to the phasing of a reference signal generated by the receiver.
[2] Note that ϕ can take decimal values much greater than one depending on the change in range.
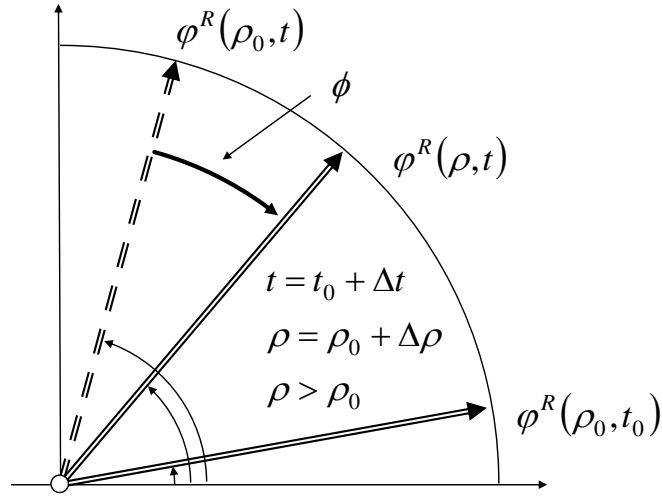
Figure B.4: Illustration of the beat phase ϕ in the complex plane

and the beat phase:

$$f_D = \dot{\phi} \tag{B.14}$$

with

$$\dot{\phi} = -\frac{1}{\lambda}\frac{d}{dt}\Delta\rho = -\frac{\dot{\rho}}{\lambda} \tag{B.15}$$

Referring to Eq. (B.3) it becomes evident that ϕ is nothing but the instantaneous phasing of an oscillation with the frequency f_D, i.e. the phasing of the *beat* resulting from a superposition of the received signal and a reference oscillation with the nominal, not Doppler-shifted frequency.

Note that just as Eq. (B.11) also Eqs. (B.13) through (B.15) are first order approximations only which provide sufficient accuracy in the scope of the satellite navigation task.

B.2 Coordinate Frames

In the following the coordinate frames required for defining all motion related quantities are defined. The World Geodetic System 1984 is used as defined in NIMA (2000).

E – Earth-Centered-Earth-Fixed Frame

x-axis In equatorial plane; points through Greenwich Meridian.

y-axis In equatorial plane to form a right-hand system with the x- and the z-axes.

z-axis Rotation axis of the Earth.

N – Local Tangent Navigation Frame

x-axis Parallel to the local WGS-84 ellipsoid surface; pointing to a direction that may deviate by χ_N from the north direction. (Here: x-axis aligned with the local wind direction.)

y-axis Parallel to the local WGS-84 ellipsoid surface; to form a right-hand system with the x- and the z-axes.

z-axis Pointing downwards; perpendicular to the local WGS-84 ellipsoid surface.

Origin User defined point clamped to Earth.

0 – North-East-Down Frame

x-axis Parallel to the local WGS-84 ellipsoid surface; pointing to the geographic north pole.

y-axis Parallel to the local WGS-84 ellipsoid surface; pointing east to form a right-hand system with the x- and the z-axes.

z-axis Pointing downwards; perpendicular to the local WGS-84 ellipsoid surface.

Origin Reference point clamped to aircraft / moving vehicle.

A – Aerodynamic Frame

x-axis Aligned with the aerodynamic velocity; pointing into the direction of the aerodynamic velocity.

y-axis Pointing to the right perpendicular to the x- and the z-axes.

z-axis Pointing downwards in the symmetry plane of the aircraft; perpendicular to the x-axis.

Origin Reference point clamped to aircraft / moving vehicle.

K – Kinematic Frame

x-axis Aligned with the kinematic velocity; pointing into the direction of the kinematic velocity.

y-axis Pointing to the right perpendicular to the x- and z-axes.

z-axis Pointing downwards parallel to the projection of the local normal to the WGS-84 ellipsoid into a plane perpendicular to the x-axis, i.e. to the kinematic velocity.

Origin Reference point clamped to aircraft / moving vehicle.
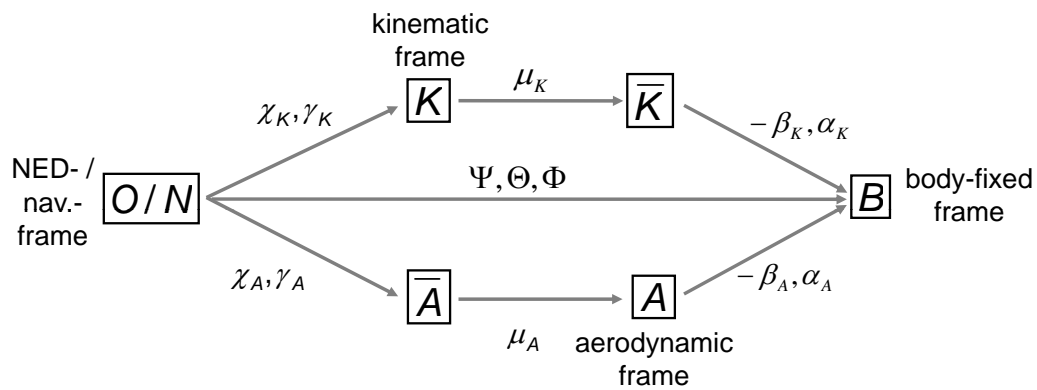
Figure B.5: Relationship between different coordinate frames

C Instructions to the Time-Differential Processing Software

The software features the options single-point processing (SPP) with or without Doppler based velocity determination and time-differential processing (kinematic relative positioning, KRP). The program comes as a Win32 console application based on a C++ GPS library by courtesy of the German Aerospace Center DLR.

C.1 Interface Description

The software interface is based on ASCII in- and output files. These files can be created and used for further analysis by any other software, e.g. MATLAB.

C.1.1 Input

State_Files.txt . This file must be located in the same directory as the main executable. Its name must not be altered. If the specified input files are located in the same directory as the main executable, the `<path>` information is optional. An exemplary syntax is given below (also see Table C.1).

```
// ...comment...
// ...comment...
-SoF-
RINEX       : <path>\91f_1514_176315_176915.09o
Ephemerides : <path>\igs15142_clk.sp3
scd         : <path>\IGS05.scd
IONEX       : <path>\igsg0130.09i
-EoF-
```

- The observation file must be provided in RINEX 2.0 (or higher) format. Use the program TEQC by UNAVCO to generate RINEX files out of any proprietary (receiver dependent) binary observation record.

- The (precise) satellite ephemerides for the current observation time are to be given in SP3 format. The final IGS orbit file for day `d` (0 =Sunday, 6 =Saturday) of GPS week `wwww` is published by IGS with a latency of about two weeks. It can be

145

downloaded by replacing the respective placeholders in the following url:

`ftp://cddis.gsfc.nasa.gov/pub/gps/products/wwww/igswwwwd.sp3.Z`[1]

- The ephemerides contain both satellite orbit and clock corrections. However, this information is only sampled in 15 min intervals. Additional 30 s sampled satellite clock corrections can be merged into the ephemerides file using the DLR program SP3AddClock.exe. Download the high-rate clock corrections here:

  `ftp://cddis.gsfc.nasa.gov/pub/gps/products/wwww/igswwwwd.clk_30s.Z`

- Ionospheric delay corrections for day `ddd` of year `yyyy` can be provided by a ionospheric map file in the IONEX format. This information is optional and the corresponding line in State_Files.txt can be omitted. For download, use

  `ftp://cddis.gsfc.nasa.gov/pub/gps/products/ionex/yyyy/ddd/igsgddd0.yyi.Z`

- The mandatory files IGS.scd (to be used before GPS week 1400 (Sunday, 5.11.2006)) or IGS05.scd (to be used after GPS week 1400) hold satellite specific information such as antenna phase center offsets.

SPP_Parameters.txt This file must be located in the same directory as the main executable. Its name must not be altered. An exemplary syntax is given below. See Table C.1 for a description of the different parameters.

```
//...comment
//...comment
-SoF-
limits         = gpsTime
  start        = 1514 176377.4
  end          = 1514 176464
elMask         = 5
epsilon        = 1e-2
residualRMS    = 4.0
stepSize       = 1
latitude       = -49.0
longitude      = 70.0
altitude       = 5
resRMS_DL1     = 2.0
choice_DL1     = y
-EoF-
```

---

[1] Don't forget to unzip before using the file.

KRP_Parameters.txt This file must be located in the same directory as the main executable. Its name must not be altered. An exemplary syntax is given below. See Table C.1 for a description of the different parameters.

```
//...comment
//...comment
-SoF-
limits              = gpsTime
   start            = 1514 176377.4
   end              = 1514 176407.7
elMask              = 5
epsilon             = 1e-4
residualRMS         = 0.01
maxDeltaEpochs      = 1
numberOfPrn         = 5
CS_tolerance        = 1.0
-EoF-
```

Excluding individual measurements The software features an outlier and cycle slip detection algorithm. However, sometimes the user might wish to manually exclude additional measurements. This can be accomplished by inserting an exclusion list in SPP_parameters.txt and/or KRP_Parameters.txt:

```
...
removedPRN
beginList
PRN = 10 type = SoW    intervals = < C1 176387 - 176392 >
PRN = 13 type = idxObs intervals = < C1 773 - 823 | D1 873 - 900 >
endList
...
```

Keep all blanks as shown in this example when working with the exclusion list. The `PRN` parameter identifies the PRN of which measurements are to excluded from the computations. The parameter `type` specifies whether the exclusion intervals are indicated in GPS seconds of week (`SoW`) or in observation indices (`idxObs`, starting with 0 for the first epoch in the RINEX file). Now the exclusion `intervals` can be specified for each PRN. Each interval is preceded by a tag flagging the type of observation to be excluded (`C1` – L1 C/A code pseudoranges; `D1` – L1 Doppler range rates; `L1` – L1 carrier ranges). Excluding pseudoranges will affect SPP position calculation whereas removing Doppler range rates will impact SPP velocity determination. Hence such intervals are to be specified in SPP_parameters.txt. Specification of intervals during which L1 carrier ranges are to be removed will affect KRP processing and must be set in KRP_Processing.txt.

C.1.2 Output

After having executed GPS_Processing.exe, the output files SPP_Results.txt and KRP_Results.txt are created holding all processing results listed in Table C.2.

C.2 Data Processing – Step-by-Step

C.2.1 Preprocessing

1. *Select data interval* to be analyzed by precise time-differential processing (GPS week and second of week of first and last epoch).

2. *Transform* receiver proprietary binary observation file *to the RINEX format*. If the binary file is large it is recommended to only transform the data interval of interest. This task can be accomplished with the tool TEQC of UNAVCO. Note that there is the possibility to instantaneously check the quality of the phase observations of the respective interval.

3. Download *external correction data* according to the instructions given in the above, pp. 145: IGS final ephemerides, IGS 30 s sampled satellite clock corrections and IONEX ionosphere maps. (A useful tool for date conversion is provided by AIUB.) Merge the high rate clock corrections and the final ephemerides using the DLR program SP3AddClock.exe.

C.2.2 GPS_Processing

1. *Set input parameters* for GPS_Processing.exe according to Table C.1. An explanation of all *output values* is given in Table C.2.

2. Get an overview of the whole data interval using *SPP processing* (chose `limits=idxObs` and set `start=0` and `end=-1` to process the whole obs file). Check solution quality according to Table C.3 and the plausibility of the chosen input parameters. Process at least the interval which is to be processed by KRP in order to allow for SPP imports if necessary.

3. Apply the time-differential method (*KRP processing*) to a selected data interval (up to 5 min for good data quality).

   - Apply the over-all approach (`maxDeltaEpochs>max(idxSol)`) if the data quality is sufficient, i.e. if no base changes (hand-over events) are triggered automatically.

   - Apply the accumulation strategy (`maxDeltaEpochs=1`) otherwise.

   - Carefully analyze the quality of the solution using the parameters given in Table C.4. Eventually improve the results by changing the outlier detection threshold (`residualRMS`). Note that very tight settings are recommended (millimeter

range). For details on outlier detection refer to Section 4.2.2, pp. 61 and the MAT-
LAB function `set_residualRMS`. If individual satellites appear to be suspicious,
exclude them manually from the computations.

- Take your time to adjust all input parameters such as to get optimal results. If
  the data quality is very poor and one or more epochs cannot be solved at all
  by KRP, an SPP solution is imported automatically. This will cause gaps in the
  solution.

4. Save the final solution together with the input files such as to ensure repeatability
   and traceability of the processing results.

C.2.3 Postprocessing

MATLAB functions for a direct import of the processing results (`readData`) and quick
visualization have been implemented. Functions for handling KRP results affected
with SPP imports are available as is are functions for speed calculation based on KRP
position fixes. The latter internally use smoothing splines.

A Note on Smoothing Splines using Matlab   MATLAB's spline toolbox implements
the smoothing spline algorithm which is adressed for velocity determination as de-
scribed within Section 6.1.2 (MATLAB, 2008, function "spaps"). Here, the deviation
of the function $x(t)$ from the data x_{TD} resulting from time-differential processing is
measured by

$$E(x) = \sum_{i=0}^{n} w_i \big(x_{\mathrm{TD}}(t_i) - x(t_i) \big)^2 \tag{C.1}$$

with the default choice for the weights w_i making $E(x)$ the composite trapezoidal rule
approximation to $\int_{t_0}^{t_n} \left(x_{\mathrm{TD}} - x \right)^2 dt$. The function features the smoothing parameter
`tol` yielding $E(x) \approx$ `tol`. A proper setting of this parameter allows to smooth the data
by matching the variance of the spline residuals with the estimate of the horizontal
and vertical position noise estimates:

$$\sigma_{n,e} \approx \sigma_{f_{\mathrm{spline},n,e}} \qquad\qquad\qquad \sigma_d \approx \sigma_{f_{\mathrm{spline},d}} \tag{C.2}$$

This can readily be implemented as shown by the listing on the next page.

```
tol_hor      = sigma2_hor  * dt * (nos-1); %  sigma2_hor: estimate of
tol_vert     = sigma2_vert * dt * (nos-1); %    variance of horizontal
                                           %    TD position fixes
[NORTH_spl] = spaps(t, NORTH_TD,...        %  sigma2_vert: estimate
              tol_hor,'m',3);              %    of variance of ver-
[EAST_spl]  = spaps(t, EAST_TD,...         %    tical TD pos. fixes
              tol_hor,'m',3);              %  dt: sampling time
[DOWN_spl]  = spaps(t, DOWN_TD,...         %  nos: number of samples
              tol_vert,'m',3);             %  m: Derivative to be
                                           %    minimized, 3 for
                                           %    quintic splines
```

Table C.1: Input parameters for GPS_Processing.exe. Angle brackets designate placeholders: %i – insert positive integer; %f – insert float.

Identifier	Value	Description
State_files.txt		
RINEX	<path>\<filename>	Observation file in RINEX format
Ephemerides	<path>\<filename>	Satellite ephemerides in SP3 format.
scd	<path>\IGS05.scd	Spacecraft description file (use IGS.scd before GPS week 1400)
IONEX	<path>\<filename>	Ionosphere map in IONEX format
SPP_Parameters.txt and KRP_Parameters.txt		
limits	gpsTime or idxObs	Processing interval in GPS weeks and seconds of week or by specification of the resp. index within the observation file
start	<%i> <%f> or <%i>	
end	<%i> <%f> or <%i>	
elMask	<%f>	Elevation mask [deg]
epsilon	<%f>	Convergence criterion [m]. Iteration is stopped if $|\Delta\boldsymbol{\zeta}| <$ epsilon
residualRMS	<%f>	Cycle slip and outlier detection threshold [m]. Corresponds to T_D^* according to Eqs. (4.8) and (4.9)
removedPrn		Manual exclusion of individual measurements as described on p. 147
beginList		
<exclusion list>		
endList		

Table C.1: continued

Identifier	Value	Description
SPP_Parameters.txt only		
stepSize	<%i>	Processing step size. stepSize=2 → only every other observation is processed
latitude	<%f>	Initial WGS-84 latitude [deg]. An initial position close (within some hundreds kilometers) to the measurement site has to be indicated in order to ensure convergence.
longitude	<%f>	Initial WGS-84 longitude [deg]
altitude	<%f>	Initial altitude [m] (height above WGS-84 ellipsoide)
choice_DL1	y or n	Choose whether to calculate Doppler based speed (y) or not (n). Only possible if there are D1 observations in the RINEX file.
resRMS_DL1	<%f>	Cycle slip and outlier detection threshold for speed calculation. See residualRMS.
KRP_Parameters.txt only		
maxDeltaEpochs	<%i>	Maximum number of epochs to be processed before issuing a hand-over event. maxDeltaEpochs = 1 corresponds to the accumulation strategy, pp. 46. If values greater than the total number of epochs to be processed are chosen, this corresponds to the over-all strategy.
numberOfPrn	<%i>	Minimum number of satellites to be used when solving. If numberOfPrn < 5, no reliable cycle slip and outlier detection is possible, Figure 4.5.
CS_tolerance	<%i>	Parameter for discrimination between cycle slips and outliers, p. 65. CS_tolerance = 1 will flag all detections as cycle slips. Use this setting if maxDeltaEpochs = 1.

Table C.2: Output of GPS_Processing.exe (items ordered as in the respective result file)

Parameter	Unit	Description
SPP_Results.txt and KRP_Results.txt [2]		
idxSol	-	Continuous epoch count. 0 for first epoch solved by current processing run.
idxObs	-	Continuous epoch count. 0 for first epoch within current observation file.
GPS_Week	-	GPS Week of current epoch
GPS_SoW	s	GPS second of week of current epoch. Time stamp not corrected by receiver clock error estimate δ^R. For corrected time calculate: GPS_SoW_cor = GPS_SoW - dt, compare Eq. (2.2).
sucFlag	-	0: solution failed, 1: solution succeeded. KRP: solution counted as success even if SPP import necessary and successful.
usedPrn	-	Number of satellites used within position solution. KRP: Hand-over: set to 0. SPP import: set to 0.
PDOP	-	PDOP of position solution, see Eq. (2.41)
HDOP	-	HDOP of position solution, see Eq. (2.42)
VDOP	-	VDOP of position solution, see Eq. (2.43)
resMean	m	Mean of range residuals. KRP: Hand-over: Value from incremental solution $\Rightarrow$ maxDeltaEpochs=1: Mean of incremental solution maxDeltaEpochs>max(idxSol): Mean of over-all solution
resRms	m	Root-mean-square of range residuals according to Eq. (4.8). KRP: Hand-over: resRms=dResRms
sigmaMeas	m	Estimate of standard deviation σ of range measurements, compare Eqs. (2.37) and (4.1): sigmaMeas=resRms*sqrt((usedPrn-1)/(usedPrn-4)) 0 if only 4 satellites in view. KRP: Hand-over: sigmaMeas=dResRms*sqrt((dUsedPrn-1)/(dUsedPrn-4)) $\Rightarrow$ maxDeltaEpochs=1: Estimate of standard deviation of $^{j-1,j}D\widetilde{\Phi}^i$ maxDeltaEpochs>max(idxSol): Estimate of measurement error *drift*, compare "over-all strategy", p. 56.

---

[2]If not indicated differently, KRP values equal respective SPP values for an SPP import event.

Table C.2: continued

Parameter	Unit	Description
posErrEst	m	Estimate of 3D position error: `sigmaMeas*PDOP`. KRP: Hand-over: Reset to 0. $\Rightarrow$ `maxDeltaEpochs=1`: To be ignored `maxDeltaEpochs>max(idxSol)`: Indicator for 3D error drift of over-all solution.
x	m	$(x^R)_E$ – x-component of receiver position indicated in ECEF coordinates
y	m	$(y^R)_E$ – y-component of receiver position indicated in ECEF coordinates
z	m	$(z^R)_E$ – z-component of receiver position indicated in ECEF coordinates
c_dt	m	$c\delta^R$ – Receiver clock error scaled to range by multiplication with the speed of light (299,792,458.0 m/s)
east	m	East component of receiver position in local-tangent frame centered at the solution of the first SPP or KRP epoch (`idxSol = 0`).
north	m	North component of receiver position (see `east`)
zenith	m	Vertical component of receiver position completing the right-hand system (see `east`)
i=1...32		...satellite specific values...
PRN_i	-	PRN number

Table C.2: continued

Parameter	Unit	Description
prnFlag_i	-	PRN edit flag indicating state of PRN within position solution: 1 Measurement not available 2 Ok, measurement used within solution 3 Ok, measurement repaired and used within solution (not yet available) 4 Missing data. Either ephemerides or measurement missing KRP: for either base or rover epoch 5 Satellite below elevation mask (see `elMask`) 6 Outlier excluded from solution 7 KRP only: Cycle-slip excluded from solution. If `CS_tolerance = 1` every outlying measurement is flagged to 7. Such measurement will not be reused in subsequent epochs for `maxDeltaEpochs > 1`. 8 KRP only: Valid measurement which was not yet valid at base epoch (e.g. satellite raising above `elMask`) 9 KRP only: Base change (either SPP import or hand-over when number of processed epochs exceeding `maxDeltaEpochs`). If `maxDeltaEpochs = 1` (accumulation strategy), every PRN is flagged to 9 at every epoch 10 Measurement manually excluded from solution. KRP, `maxDeltaEpochs > 1`: Measurement will be reused after specified exclusion interval.
R_tild_i	m	$\widetilde{R}^i$ – C/A code pseudorange, p. 10
Phi_tild_i	m	$\widetilde{\Phi}^i$ – L1 carrier based phaserange, p. 12
D_tild_i	m/s	$\widetilde{D}^i$ – L1 Doppler range rate, p. 11
SNR_i	dBHz	L1 signal to noise ratio
Az_i	deg	Azimuth
El_i	deg	Elevation
O_C_i	m	Range residual SPP: $f^i = \widetilde{R}^i - \widehat{R}^i$ KRP: $^{bj}Df^i = {}^{bj}D\widetilde{\Phi}^i - {}^{bj}D\widehat{\Phi}^i$. Hand-over: `O_C_i=dO_C_i`$\Rightarrow$ `maxDeltaEpochs=1`: Range residual of incremental solution `maxDeltaEpochs>max(idxSol)`: Range residual of over-all solution

Table C.2: continued

Parameter	Unit	Description
SPP_Results.txt only		
usedPrnDL1	-	Number of satellites used within velocity solution [3]
PDopDL1	-	PDOP of velocity solution, compare Eq. (2.41)
HDopDL1	-	HDOP of velocity solution, compare Eq. (2.42)
VDopDL1	-	VDOP of velocity solution, compare Eq. (2.43)
resRmsDL1	m/s	Root-mean-square of range rate residuals according to Eq. (4.8)
sigmaMeasDL1	m/s	Estimate of standard deviation σ of range rate measurements, compare Eqs. (2.37). (0 if only 4 satellites in view).
velErrEst	m/s	Estimate of 3D velocity error (`sigmaMeasDL1*PDopDL1`)
x_dot	m/s	First element of $(\dot{\mathbf{x}}^R)_E^E$ – x-component of receiver velocity relative to and indicated in ECEF coordinates
y_dot	m/s	Second element of $(\dot{\mathbf{x}}^R)_E^E$
z_dot	m/s	Third element of $(\dot{\mathbf{x}}^R)_E^E$
c_dt_dot	m/s	$c\dot{\delta}^R$ – Receiver clock error drift scaled to range rate by multiplication with the speed of light (299,792,458.0 m/s)
east_dot	m/s	East component of receiver velocity relative to and indicated in local-tangent coordinates centered at the first epoch.
north_dot	m/s	North component of receiver velocity (see `east_dot`)
zenith_dot	m/s	Vertical component of receiver velocity completing the right-hand system (see `east_dot`)
i=1...32		...satellite specific values...
prnFlagDL1_i	-	PRN flag indicating state of PRN within velocity solution (compare `prnFlag_i`)
O_C_DL1_i	m/s	Range rate residual: $f^i = \widetilde{D}^i - \widehat{D}^i$
KRP_Results.txt only		
idxObsB	-	Continuous count of current base epoch t_b. 0 for first epoch within observation file
dUsedPrn	-	Number of satellites used within current incremental solution (relative solution between t_{j-1} and t_j) SPP import: set to 0
dPDOP	-	PDOP of incremental position solution, compare Eq. (2.41) SPP import: set to 0.
dHDOP	-	HDOP of incremental position solution, compare Eq. (2.42) SPP import: set to 0.

---

[3] If not indicated differently, all values related to Doppler based velocity calculation default to 0 if speed calculation is disabled (`choiceDL1=n`).

Table C.2: continued

Parameter	Unit	Description
dVDOP	-	VDOP of incremental position solution, compare Eq. (2.43) SPP import: set to 0.
dResRms	m	Root-mean-square of range residuals of incremental solution according to Eq. (4.8) SPP import: set to 0.
dResRmsC	m	Root-mean-square of accumulated range residuals `dO_Cc_i`. Constellation change: `dResRmsC=dResRms` `maxDeltaEpochs>max(idxSol)`: To be ignored. SPP import: Set to 0.0.
dSigmaMeas	m	Estimate of standard deviation of $^{j-1,j}D\widetilde{\Phi}^i$ (for any `maxDeltaEpochs` setting). `dSigmaMeas=dResRms*sqrt((dUsedPrn-1)/(dUsedPrn-4))` 0 if only 4 satellites in view. `maxDeltaEpochs=1`: Coincides with `sigmaMeas` (except for SPP imports) SPP import: Set to 0.0
dSigmaMeasC	m	Approximation of measurement error drift: `dSigmaMeasC=dResRmsC*sqrt((dUsedPrn-1)/(dUsedPrn-4))` 0 if only 4 satellites in view. `maxDeltaEpochs=1`: Ideally matches `sigmaMeas` of corresponding over-all solution if there are no constellation changes. `maxDeltaEpochs>max(idxSol)`: To be ignored SPP import: Set to 0.0
dPosErrEst	m	3D error drift estimation: `dSigmaMeas*dPDOP` Constellation change: Accumulation in order to avoid reset as observed in `dSigmaMeas` and `dResRmsC`. `maxDeltaEpochs=1`: Estimate of 3D error drift `maxDeltaEpochs>max(idxSol)`: To be ignored. SPP import: Set to 0.0
GPS_SoW_B	s	GPS second of week of base epoch t_b
xB_lt	m	East component of receiver position at t_b in local-tangent frame centered at the solution of the first KRP epoch (`idxSol = 0`)
yB_lt	m	North component of receiver position at t_b (sea `xB_lt`).
zB_lt	m	Vertical component of receiver position at t_b (sea `xB_lt`).
bx_lt	m	East component of base vector $\mathbf{b}^{bj}$ in local-tangent frame centered at the solution of the first KRP epoch (`idxSol = 0`)
by_lt	m	North component of base vector between (see `bx_lt`)
bz_lt	m	Vertical component of base vector (see `bx_lt`)
i=1...32		...satellite specific values...

Table C.2: continued

Parameter	Unit	Description
dPrnFlag_i		PRN edit flag indicating state of PRN within incremental position solution, compare prnFlag_i.
dO_C_i	m	Range residual of incremental solution $^{j-1,j}Df^i = \, ^{j-1,j}D\widetilde{\Phi}^i - \, ^{j-1,j}D\widehat{\Phi}^i$, see Figure 4.1(f) SPP import: Set to 0.0
dO_Cc_i	m	Accumulated range residuals. Same satellite constellation as previous incremental solution: dO_Cc_i = dO_C_i + dO_Cc_i-1 Changed satellite constellation: dO_Cc_i = dO_C_i maxDeltaEpochs=1: Accumulated residuals, compare Figure 4.1(f). Ideally matches O_C_i of corresponding over-all solution (given that there is no constellation change). maxDeltaEpochs>max(idxSol): To be ignored. SPP import: Set ot 0.0

Table C.3: Single point processing (SPP): Noise estimation in both the measurement and the position/speed domain based on the output of GPS_Processing.exe (see pp. 27).

	Position	**Speed**
Measurement Noise $\sigma(\widetilde{R}^j)$ or $\sigma(\widetilde{D}^j)$	sigmaMeas	sigmaMeasDL1
Position or **Speed** **Noise** $\sqrt{\sigma_n^2 + \sigma_e^2 + \sigma_d^2}$	posErrEst = sigmaMeas * PDOP	velErrEst = sigmaMeasDL1 * PDopDL1

Table C.4: Time-differential processing (KRP): Noise and drift estimation in both the measurement and the position domain based on the output of GPS_Processing.exe (see Section. 4.1, pp. 55). For the over-all strategy it is is assumed that an over-all solution can be found for all epochs and no base change is issued.

	Accumulation Strategy maxDeltaEpochs = 1	**Over-All Strategy** maxDeltaEpochs > max(idxSol)
Measurement Noise $\sigma(^{i-1,i}D\widetilde{\Phi}^j)$	dSigmaMeas or sigmaMeas	dSigmaMeas
Measurement Drift "σ"$(^{bi}D\widetilde{\Phi}^j)$	dSigmaMeasC Reset to dSigmaMeas in case of constellation change.	sigmaMeas
Position Noise $\sqrt{\sigma_n^2 + \sigma_e^2 + \sigma_d^2}$ of $\mathbf{b}^{i-1,i}$	dSigmaMeas * dPDOP or sigmaMeas * PDOP	dSigmaMeas * dPDOP
Position Drift $\sqrt{\sigma_n^2 + \sigma_e^2 + \sigma_d^2}$ of $\mathbf{b}^{bi}$	dPosErrEst Accumulated in case of constellation change. To obtain estimate e.g. in horizontal plane calculate: dPosErrEst*(dHDOP/dPDOP)	posErrEst = sigmaMeas * PDOP

D Albatross Results

The following pages provide supplementary results from the 2008/09 albatross measurement campaign to Kerguelen Islands.

D.1 Measured Trajectories

All recorded foraging trips (expect for the one already depicted in Figure 7.4(a) p. 110) are provided without further comments here. The plots are based on the the coarse 1 Hz solution calculated online by the GPS receiver modules. Note that all birds returned to their nests. In case of incomplete trajectories recorded with the TechnoSmArt logger "GiPSy", the batteries (and/or the memory) expired before the bird homed (measuring complete trips was not the objective of the campaign). The figure captions indicate the nest ID[1] (e.g. 94), the sex of the bird (f or m) and the approximate duration of the foraging trip in days. In case the trip was only recorded partially, the time from the bird leaving the breeding site until the last recorded position fix is indicated here. Furthermore the used logging device (GiPSy (A), OEM GPS Data Logger (B) or GPS Tag (C))is specified.

---

[1] This identification number was attributed to each albatross nest at Cap Ratmanoff by the author while monitoring the colony.
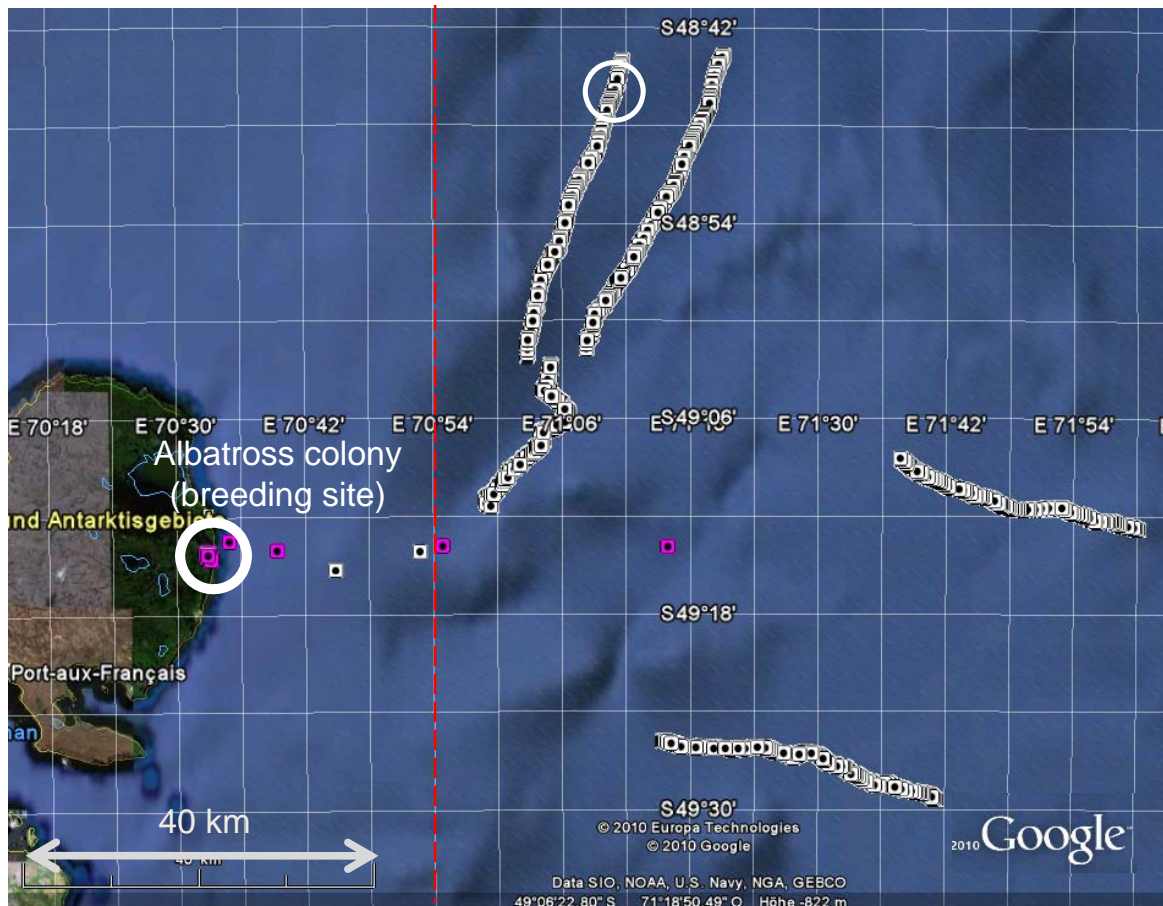
(a) Five 30 min flight trajectories recorded by e-obs GPS-Tags (C). The dashed red line represents the eastern bound of the specified lat-lon window, compare p. 106. At the pink fixes located east of the line, low speed values indicated the respective bird to be swimming. In this case 10 Hz raw data recording was delayed for another 60 min. The white circle in the upper center of the map designates the location of the flight cycle discussed in detail on pp. 111.

(b) 6m, 0.8 d, GiPSy (A)

(c) 7f, 2.7 d, GiPSy (A)

Figure D.1: Recorded albatross foraging trajectories
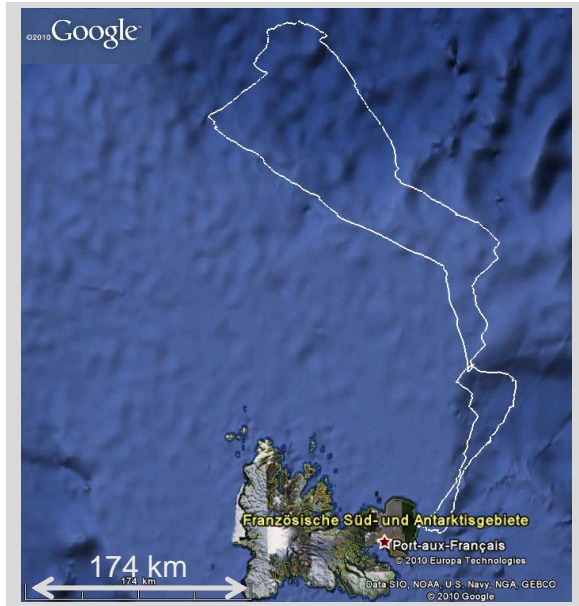
(a) 1m, 3.2 d, GiPSy (A)
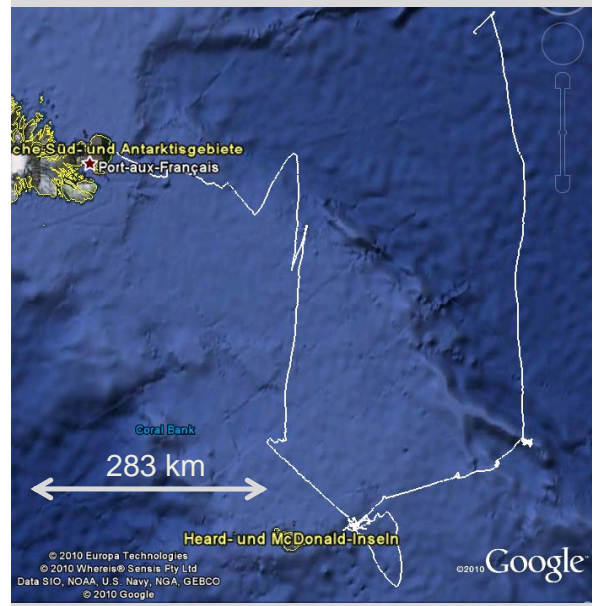
(b) 94f, 5.5 d, GiPSy (A)

(c) 3m, 4.2 d, GiPSy (A)

(d) 6f, 0.9 d, OEM Data Logger (B)

Figure D.2: Recorded albatross foraging trajectories (continued)

(a) 1201f, 0.9 d, OEM Data Logger (B)
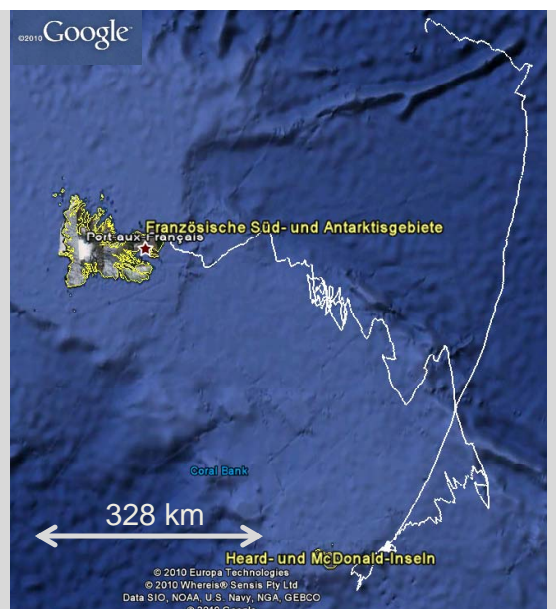
(b) 91f, 6.5 d, GiPSy (A)
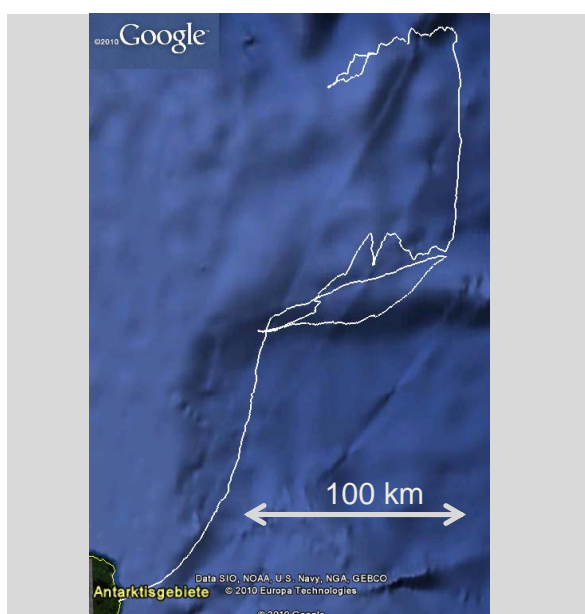
(c) 901f, 0.8 d, OEM Data Logger (B)

(d) 2f, 4.4 d (4 Hz online solution only), OEM Data Logger (B)

Figure D.3: Recorded albatross foraging trajectories (continued)

D.2 Dynamic Soaring Cycles

Eleven dynamic soaring cycles with plots as discussed in Chapter 7 (Figures 7.5 and 7.7) are provided without further comments here. The cycles have been chosen according to the following "filter" from the measured trajectories presented in the previous Section: Except for the 30 min records, all flights have been screened for sections where the birds were obviously swimming on the water (identified by low speed values). During such intervals, the birds drift on the surface. It was assumed that this drift is mainly caused by the wind (currents are not considered so far). If the direction of the drift coincided with the wind direction as interpolated from the QuickSCAT data, the quality of the raw phase data of a 10 min interval before and after the swimming phase has been checked using UNAVCO's teqc software. If this check was promising, these intervals have been analyzed precisely by time-differential processing followed by a first energy analysis. Now "closed" cycles have been picked out, i.e. cycles with virtually identical start and end states (total energy and flight direction, if possible). If the reconstructed aerodynamic forces were not plausible, the wind direction and speed has manually been altered from the QuickSCAT values. This has been done at a few cycles only and is indicated accordingly in the following plots. Note that the size of the grey wind arrow indicated in the the perspective trajectory plots is not related to the wind strength but only illustrates the wind direction. The tags provided within the figure captions (e.g. "10f_1514_345869_345885") are to be read as follows: Nest ID (10), female bird (f), GPS week of cycle (1514), GPS second of week at the beginning and the end of the cycle (345869, 345885).
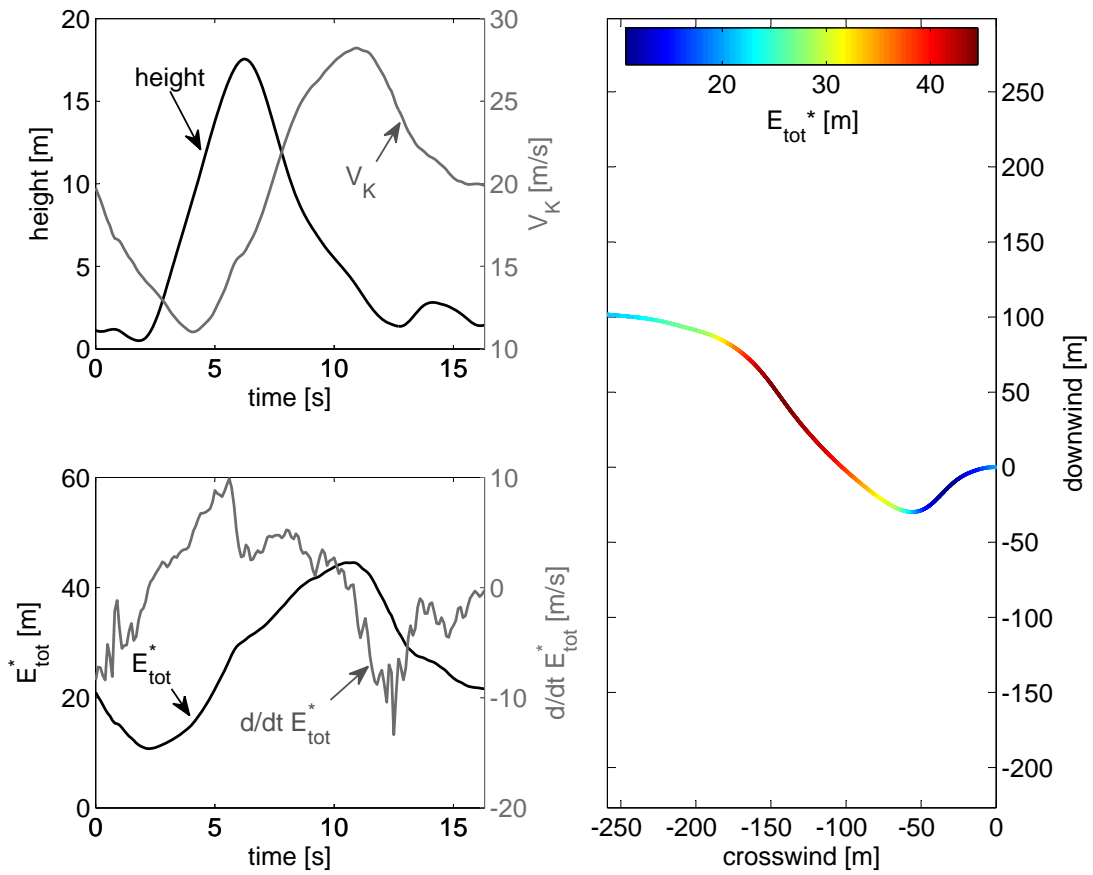
(a) Total energy
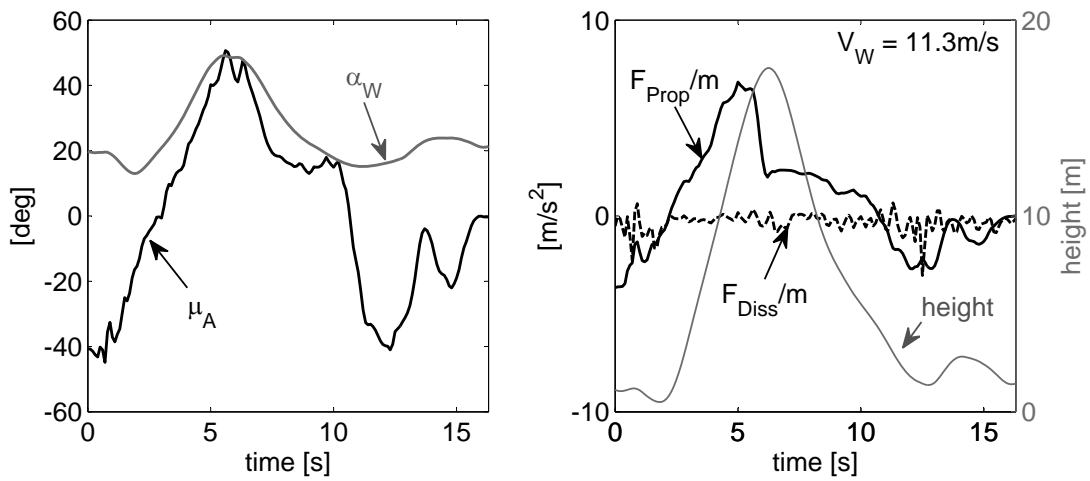
(b) Aerodynamics

Figure D.4: 10f_1514_345869_345885 – Analysis
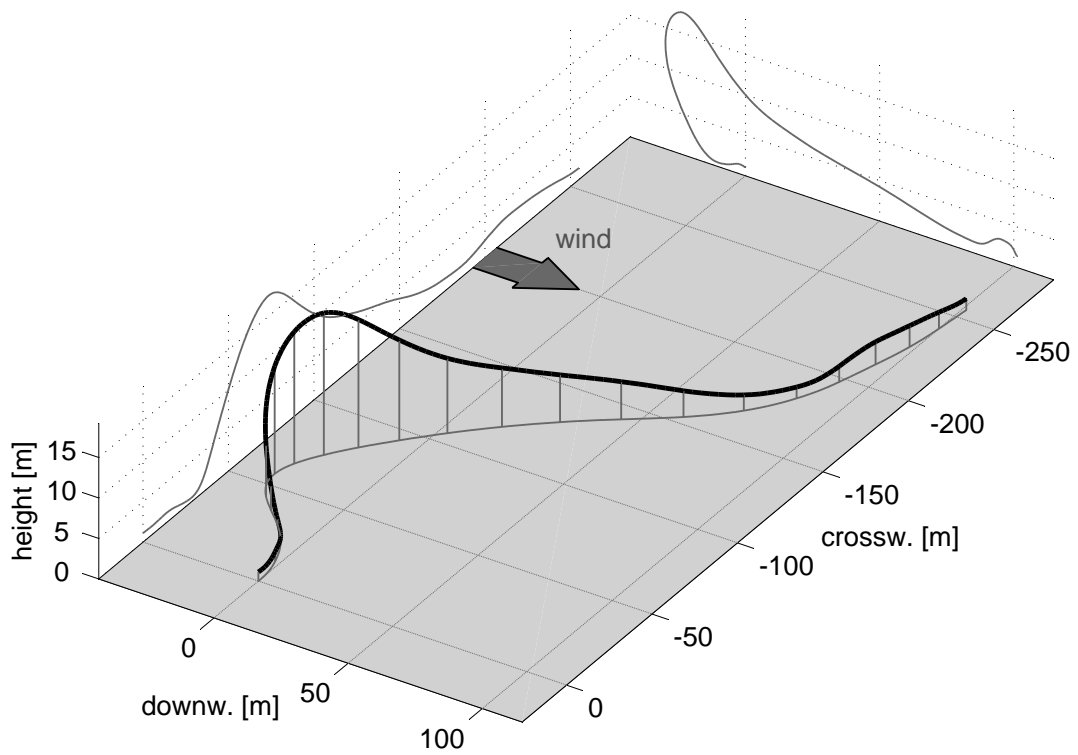
Figure D.5: 10f_1514_345869_345885 – Trajectory
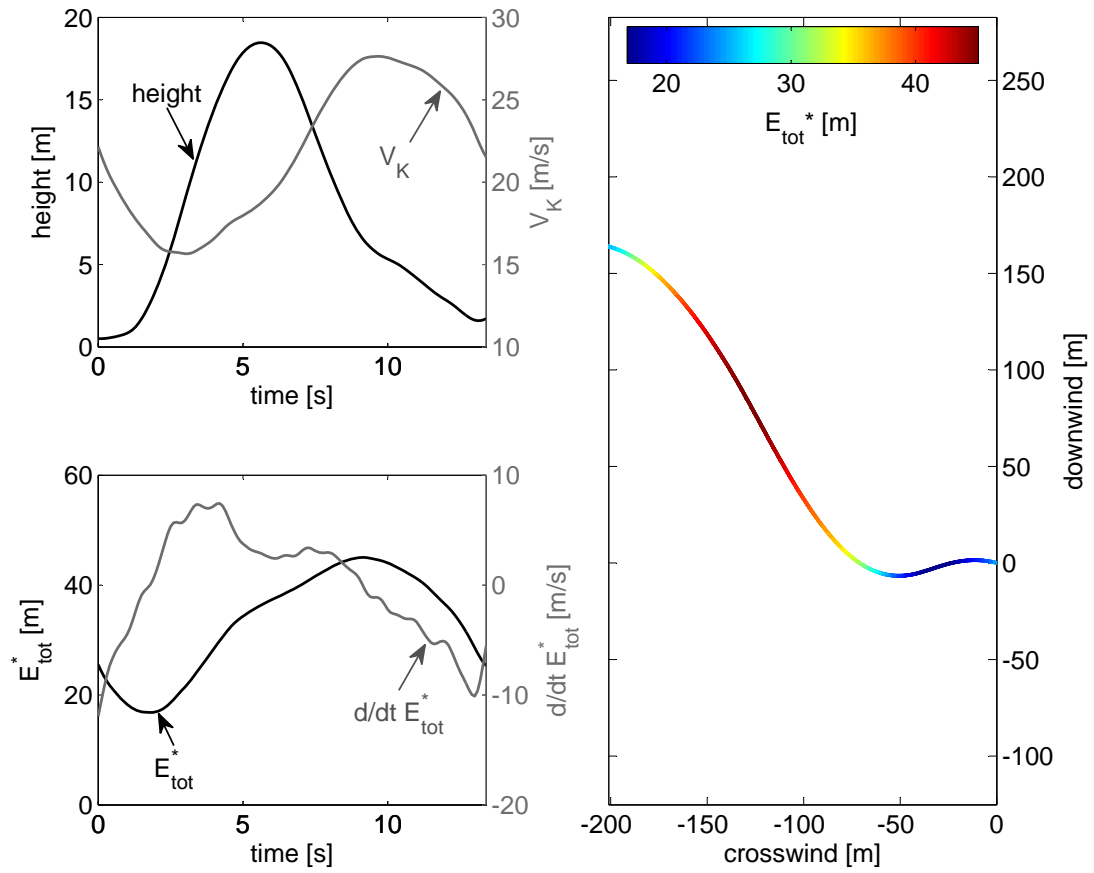
(a) Total energy
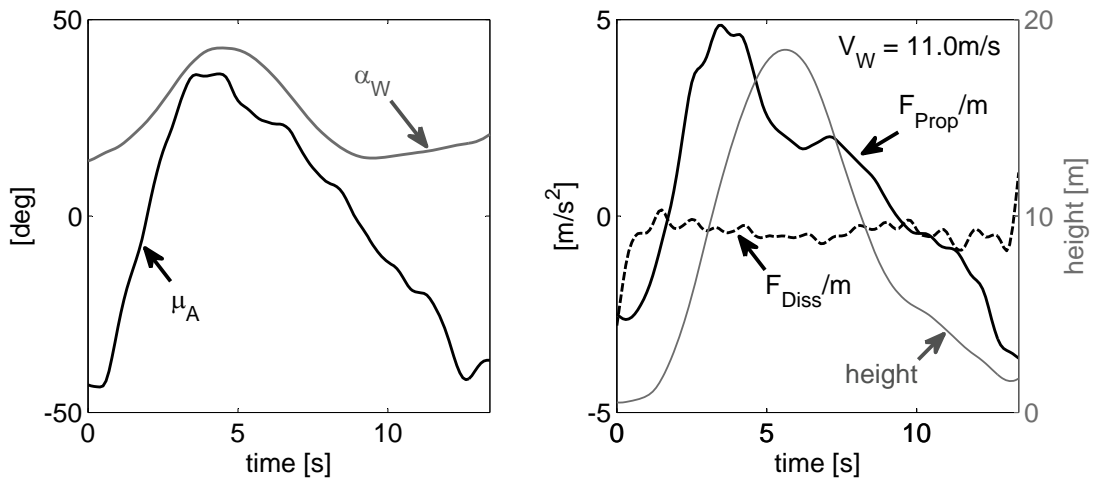
(b) Aerodynamics

Figure D.6: 10f_1514_346548_346562 – Analysis
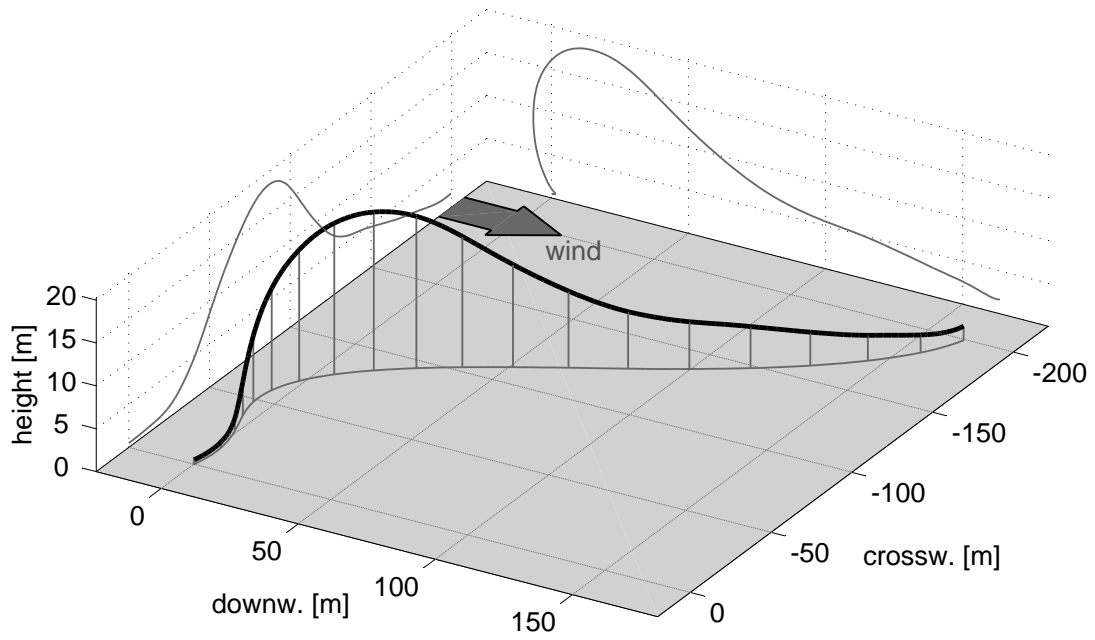
Figure D.7: 10f_1514_346548_346562 – Trajectory
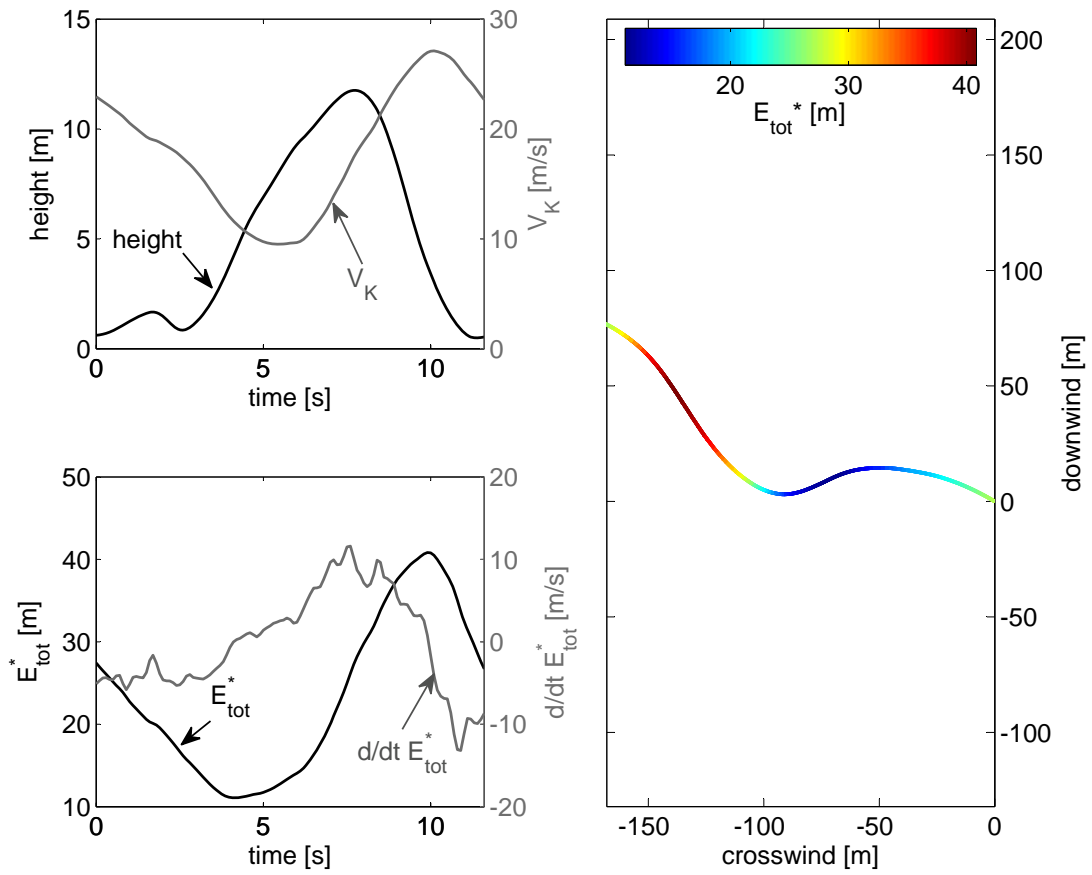
(a) Total energy
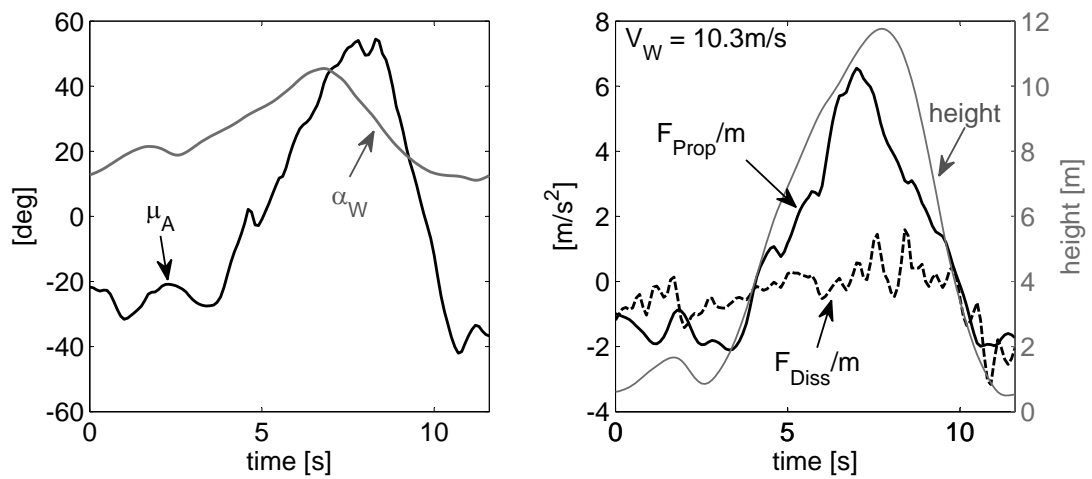
(b) Aerodynamics

Figure D.8: 94f_1513_228183_228195 – Analysis
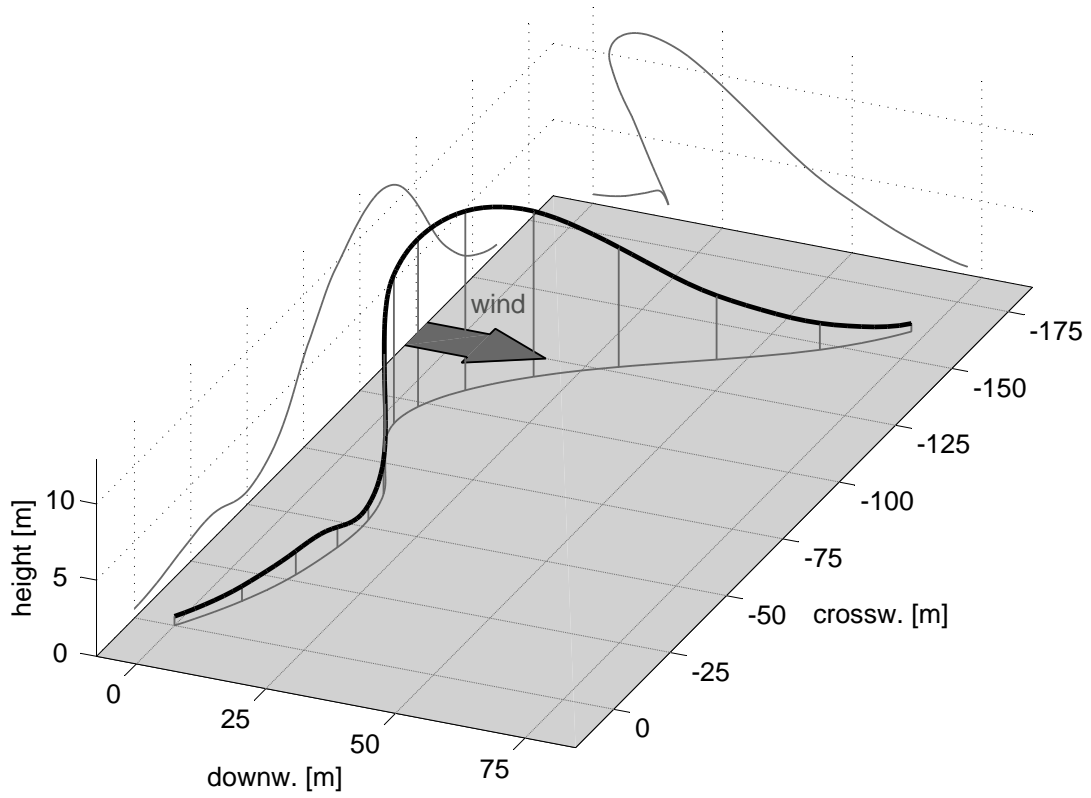
Figure D.9: 94f_1513_228183_228195 – Trajectory
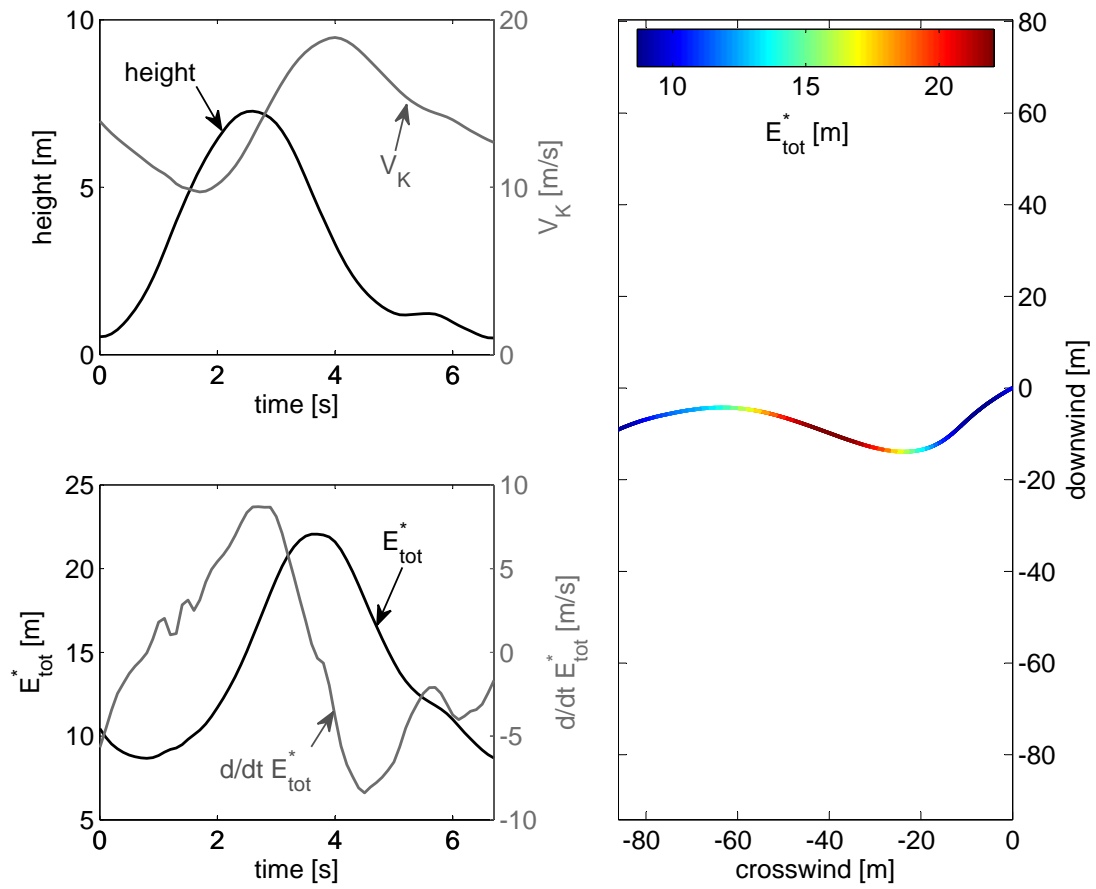
(a) Total energy
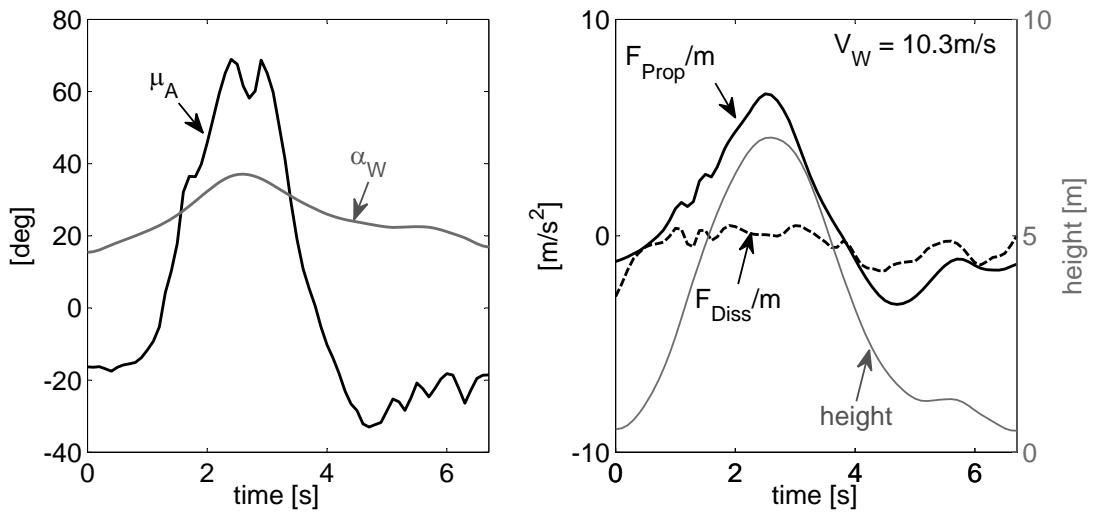
(b) Aerodynamics

Figure D.10: 3m_1514_185364_185370 − Analysis
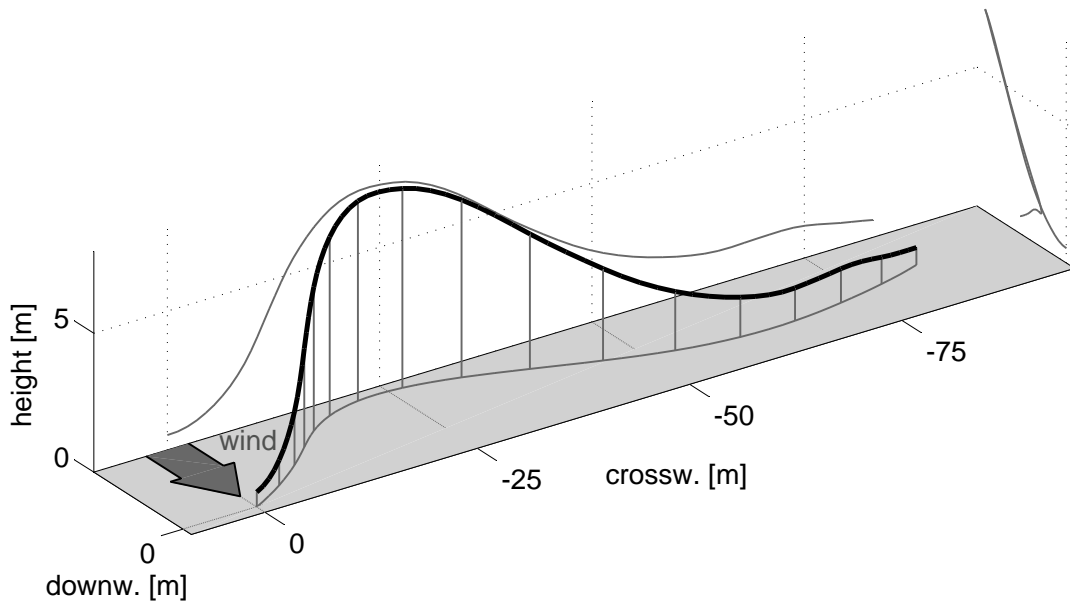
Figure D.11: 3m_1514_185364_185370 – Trajectory
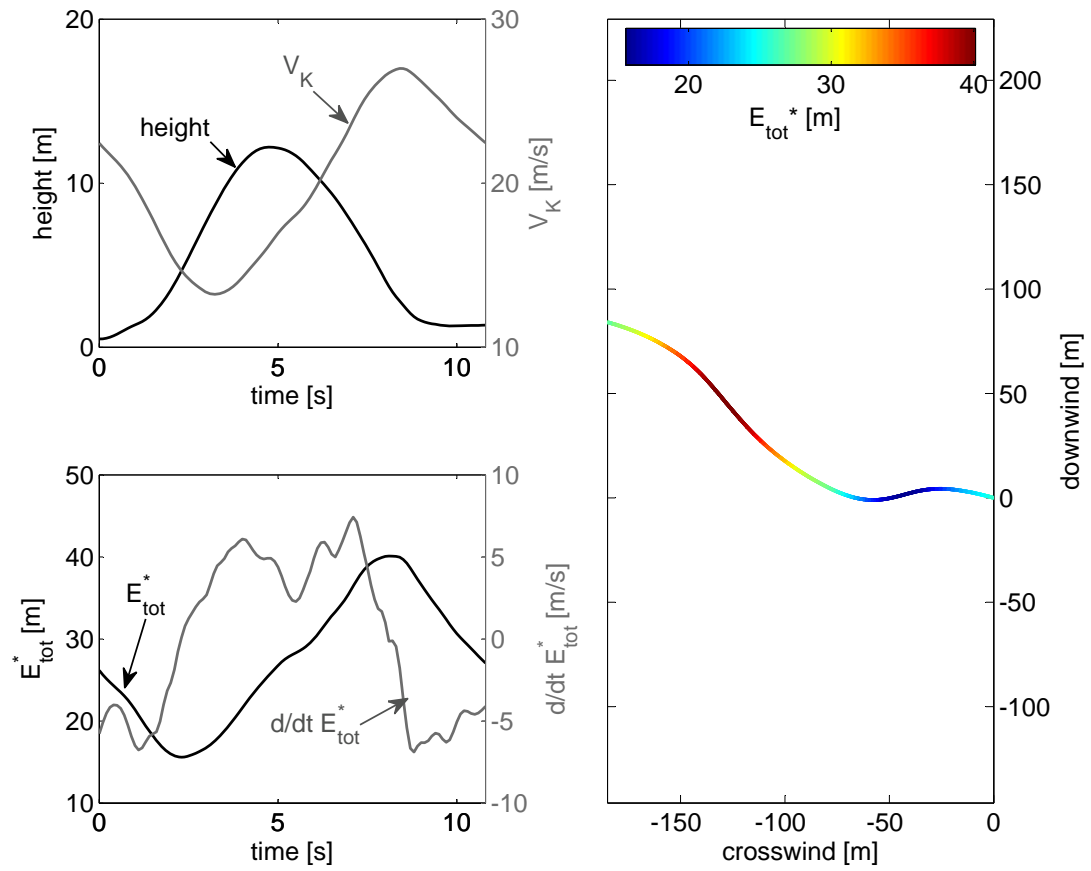
(a) Total energy
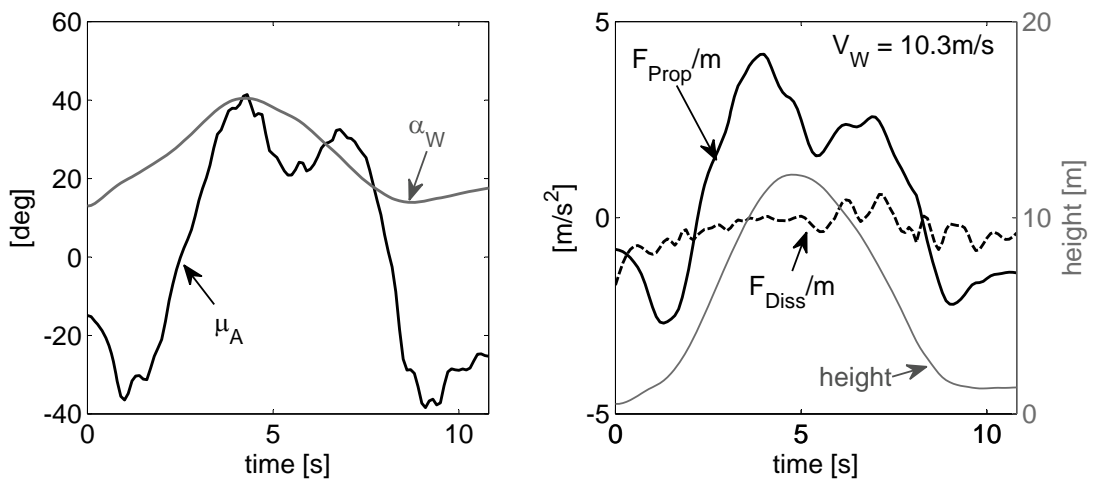
(b) Aerodynamics

Figure D.12: 3m_1514_185386_185397 – Analysis
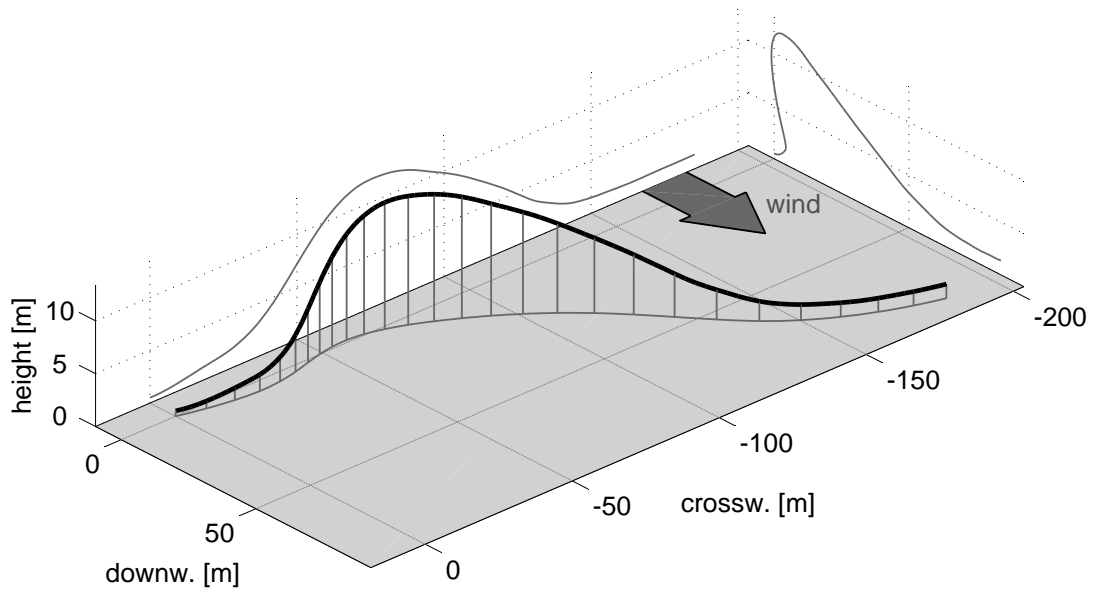
Figure D.13: 3m_1514_185386_185397 – Trajectory
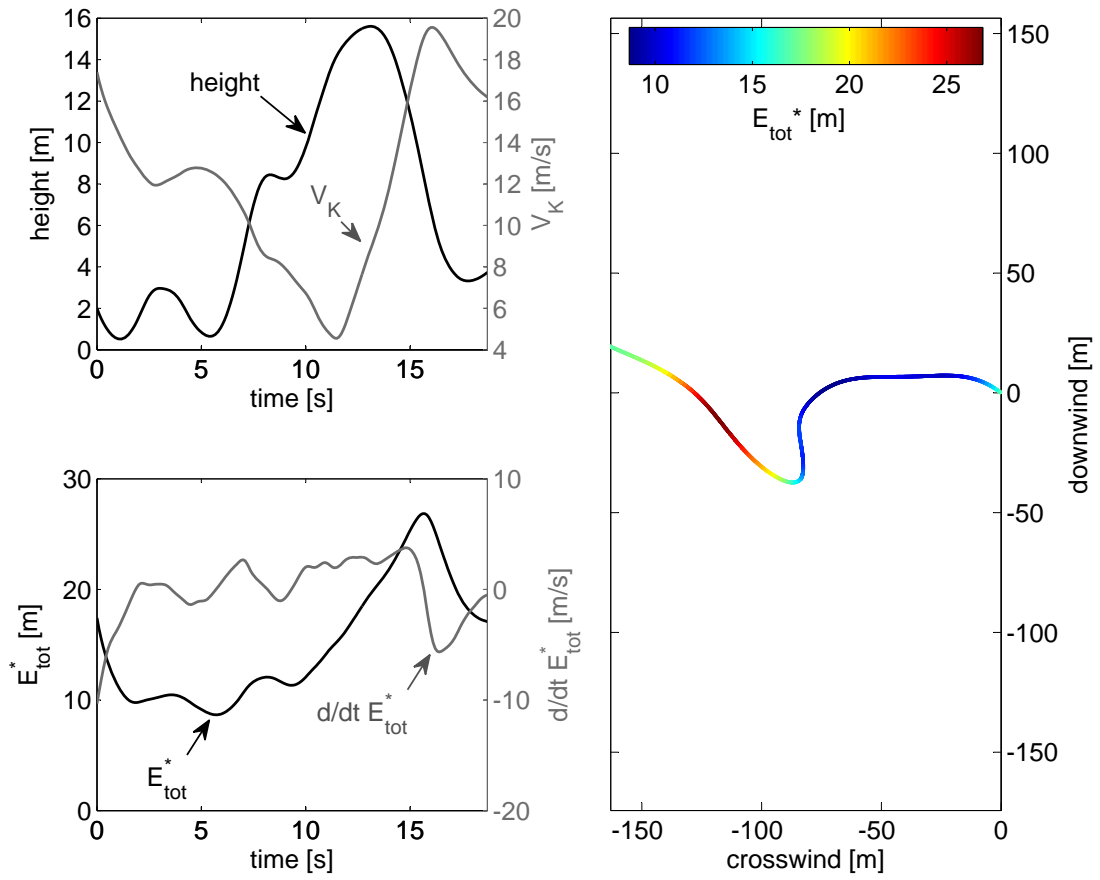
(a) Total energy
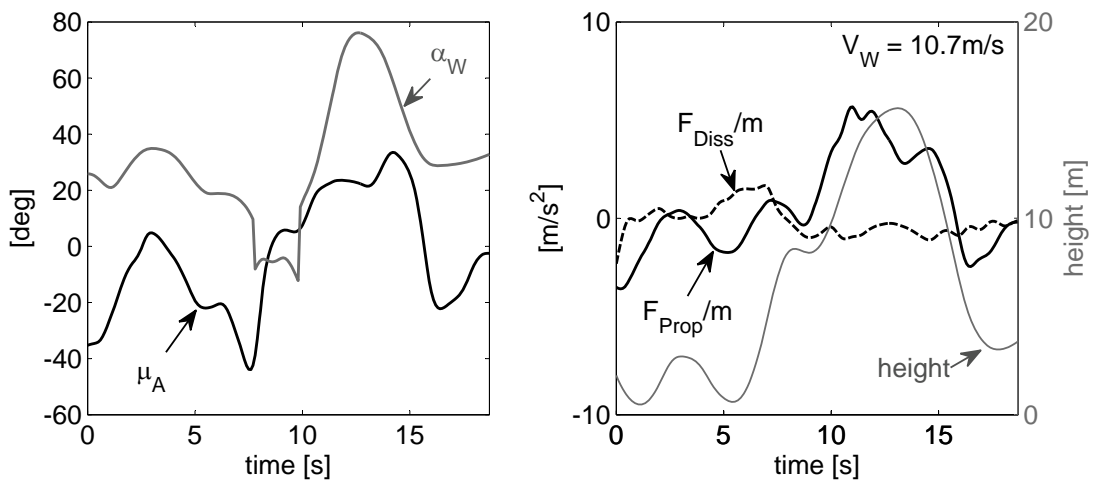
(b) Aerodynamics

Figure D.14: 91f_1514_492500_492519 – Analysis
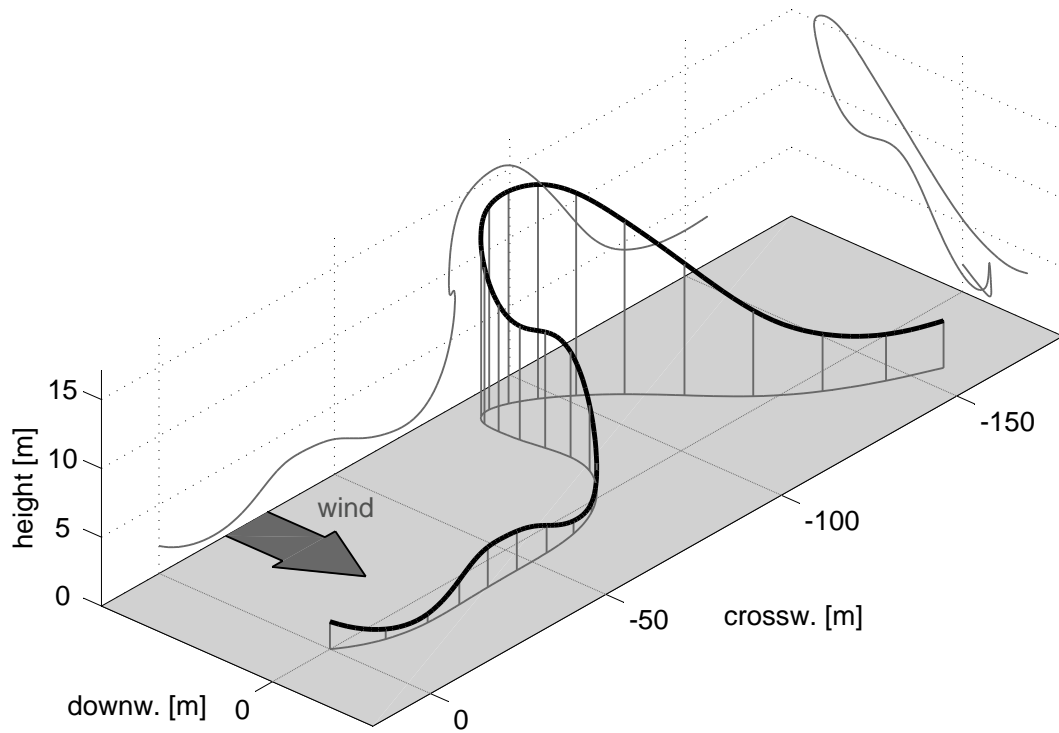
Figure D.15: 91f_1514_492500_492519 – Trajectory
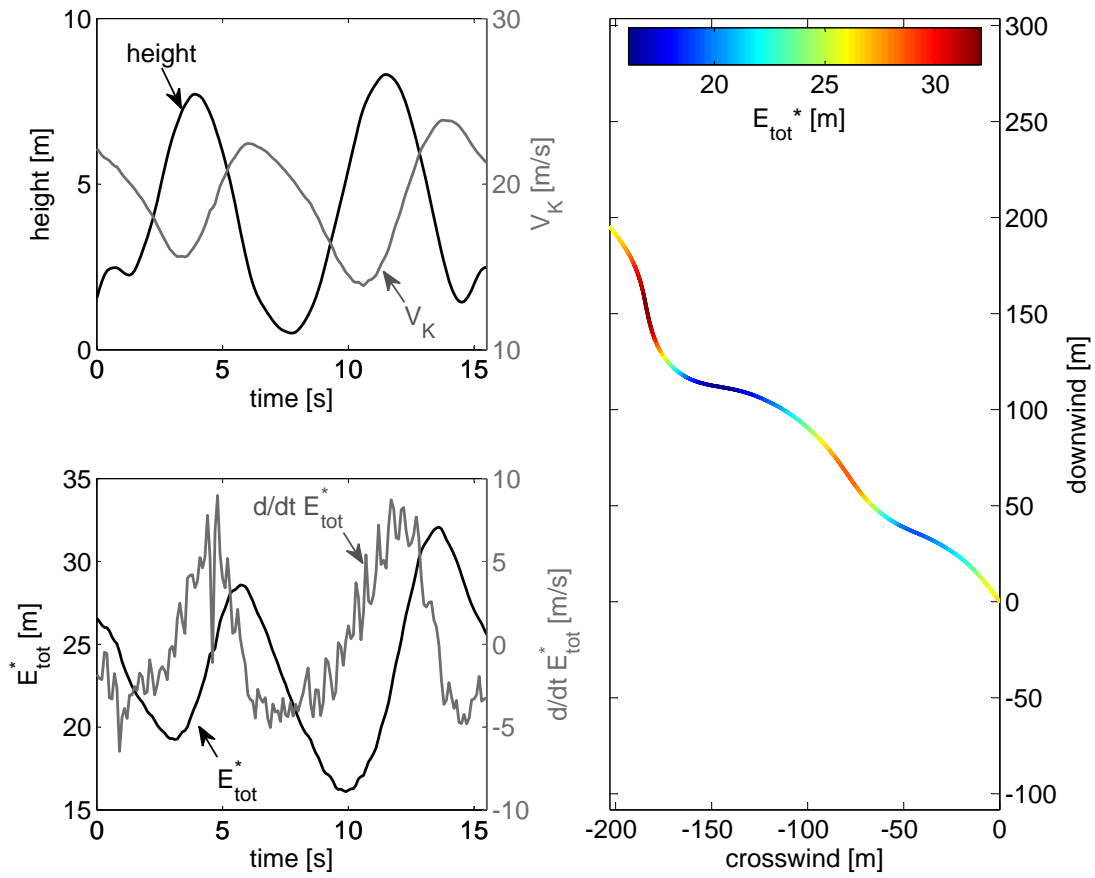
(a) Total energy
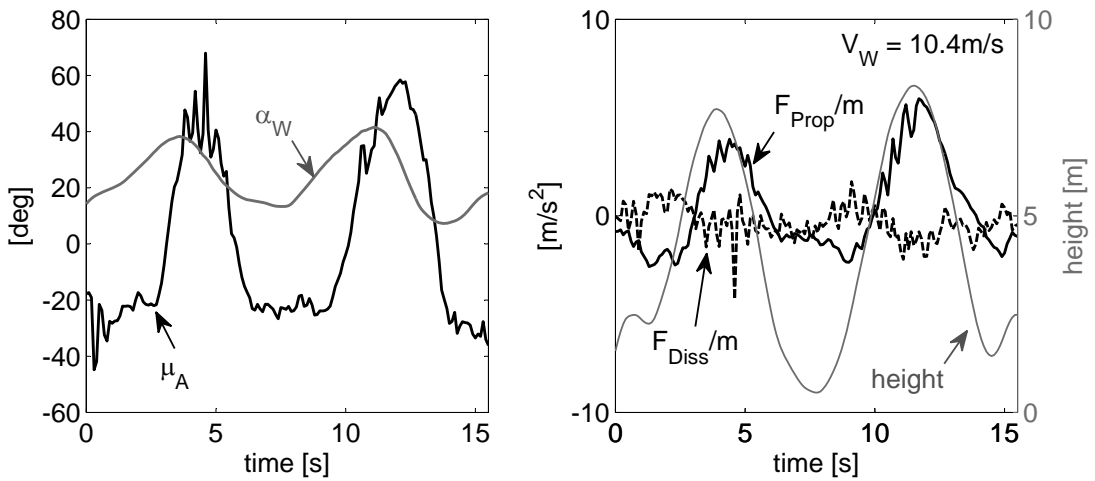
(b) Aerodynamics

Figure D.16: 94f_1513_230576_230592 − Analysis
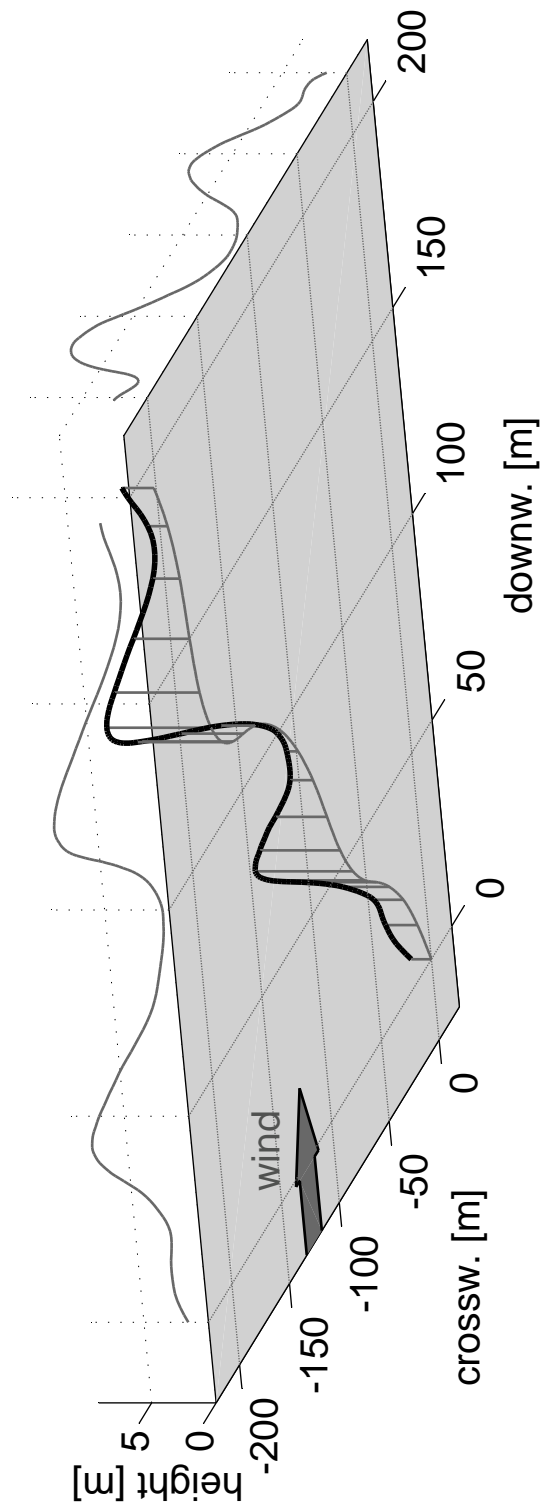
Figure D.17: 94f_1513_230576_230592 – Trajectory
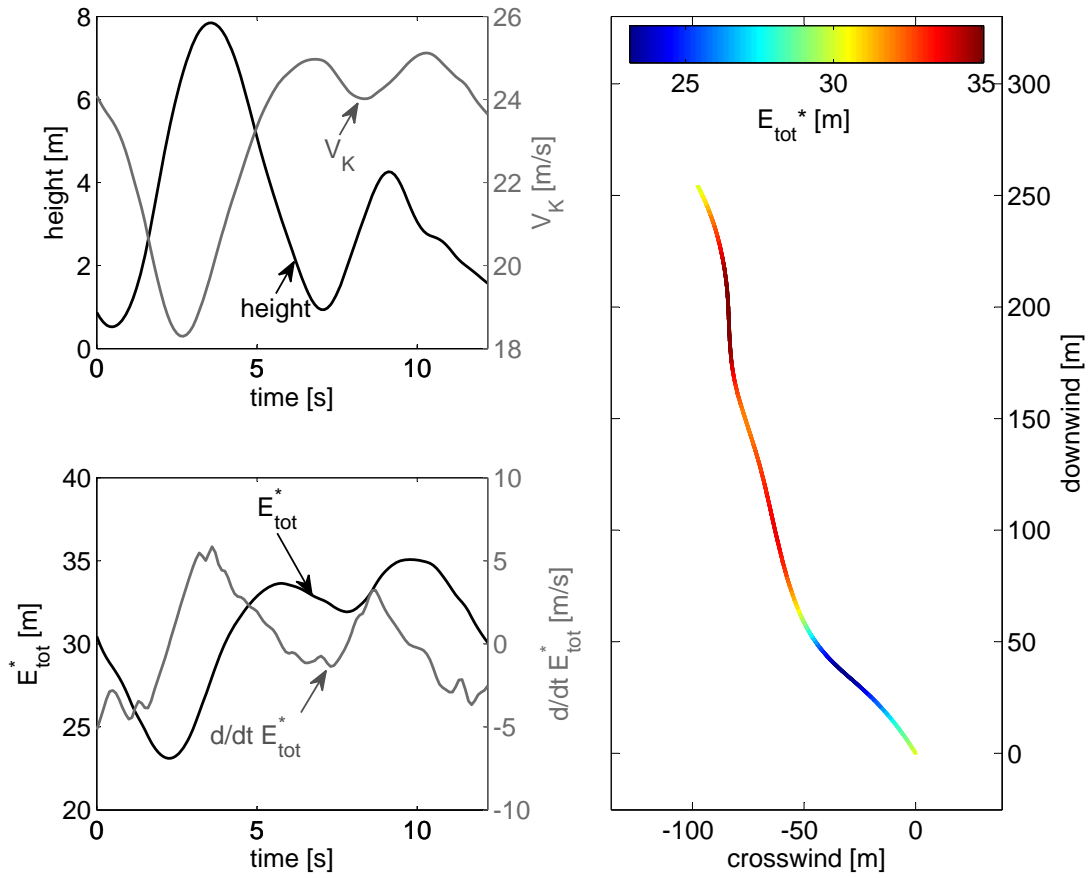
(a) Total energy
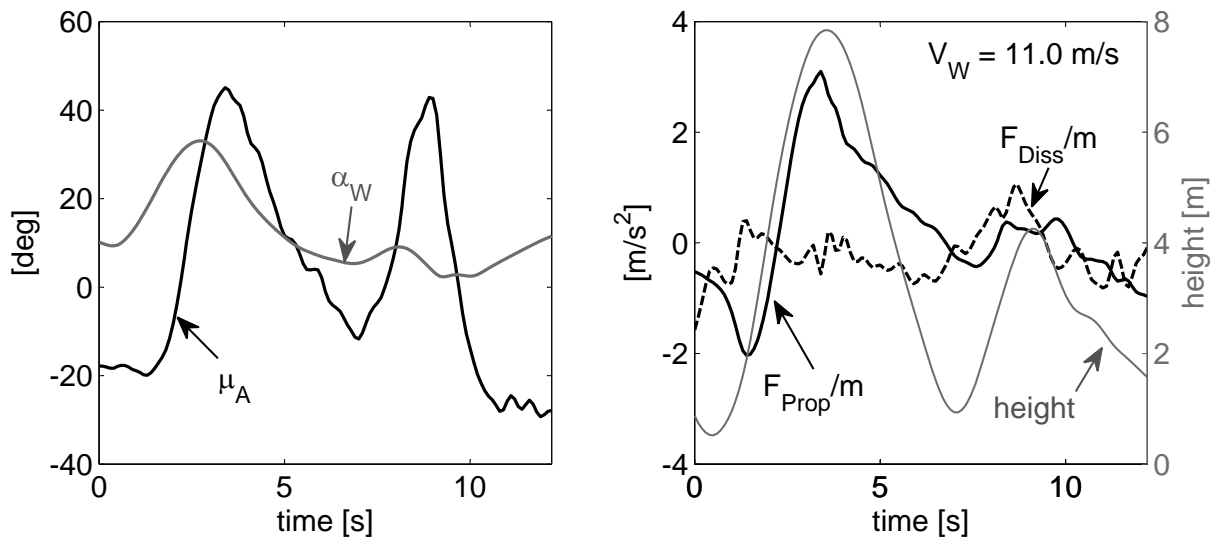
(b) Aerodynamics (wind direction altered by $-20°$)

Figure D.18: 941m_1514_317192_317205 – Analysis
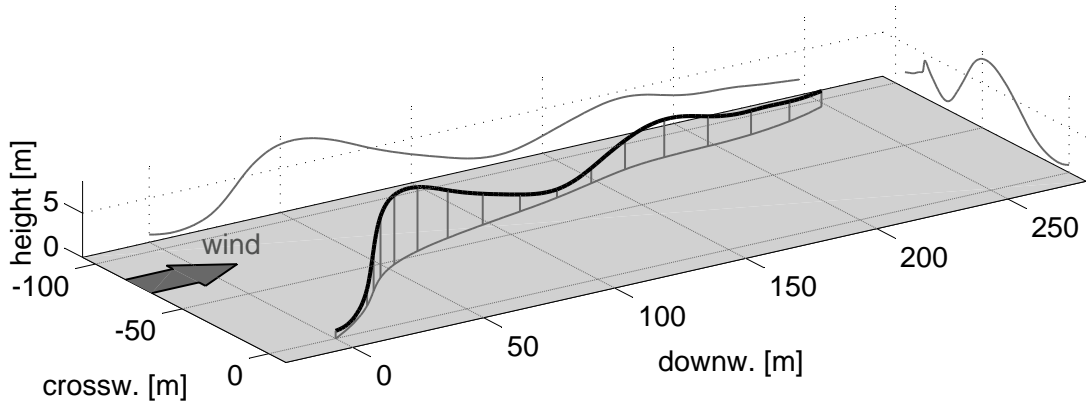
Figure D.19: 941m_1514_317192_317205 – Trajectory
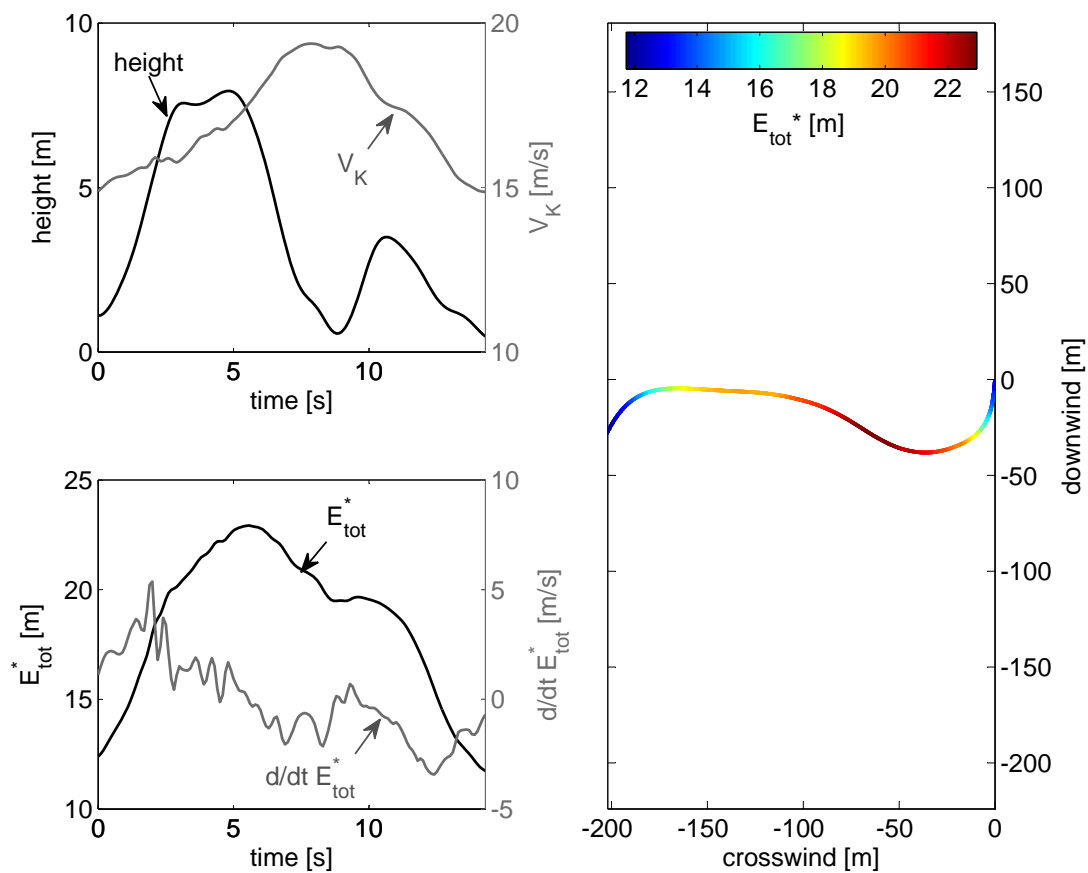
(a) Total energy
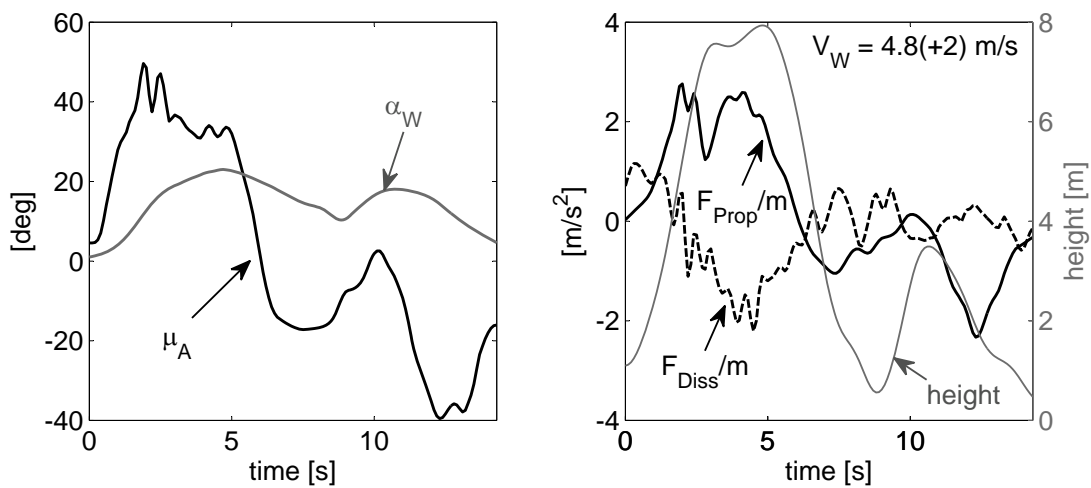
(b) Aerodynamics (wind direction altered by $-20°$)

Figure D.20: 81f_1512_219666_219685 – Analysis
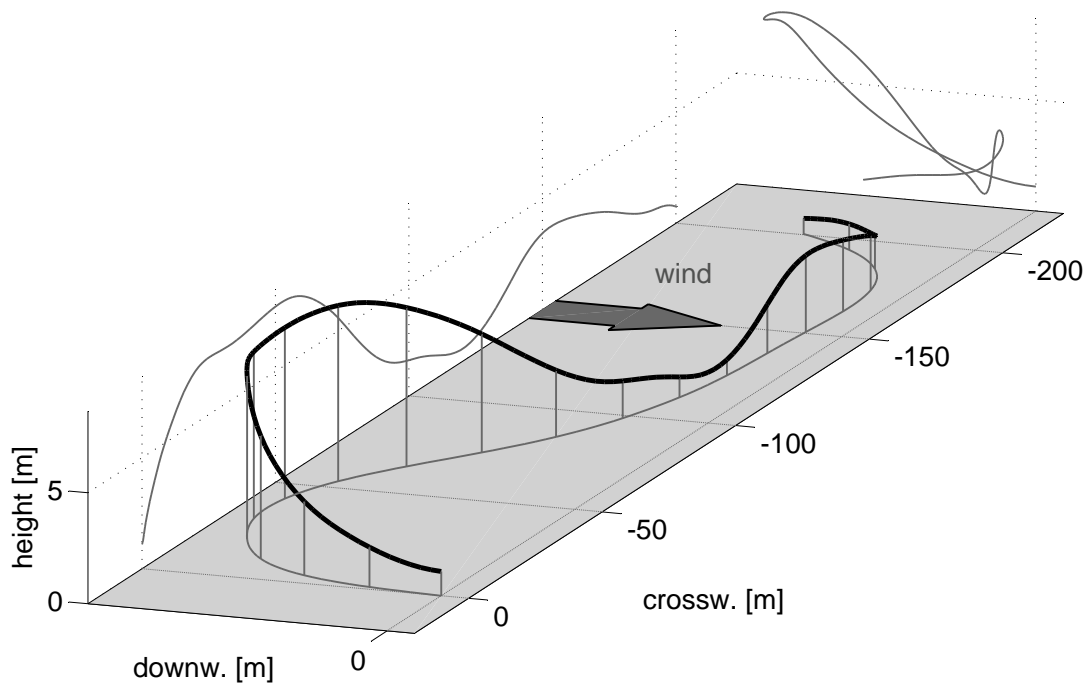
Figure D.21: 81f_1512_219666_219685 – Trajectory
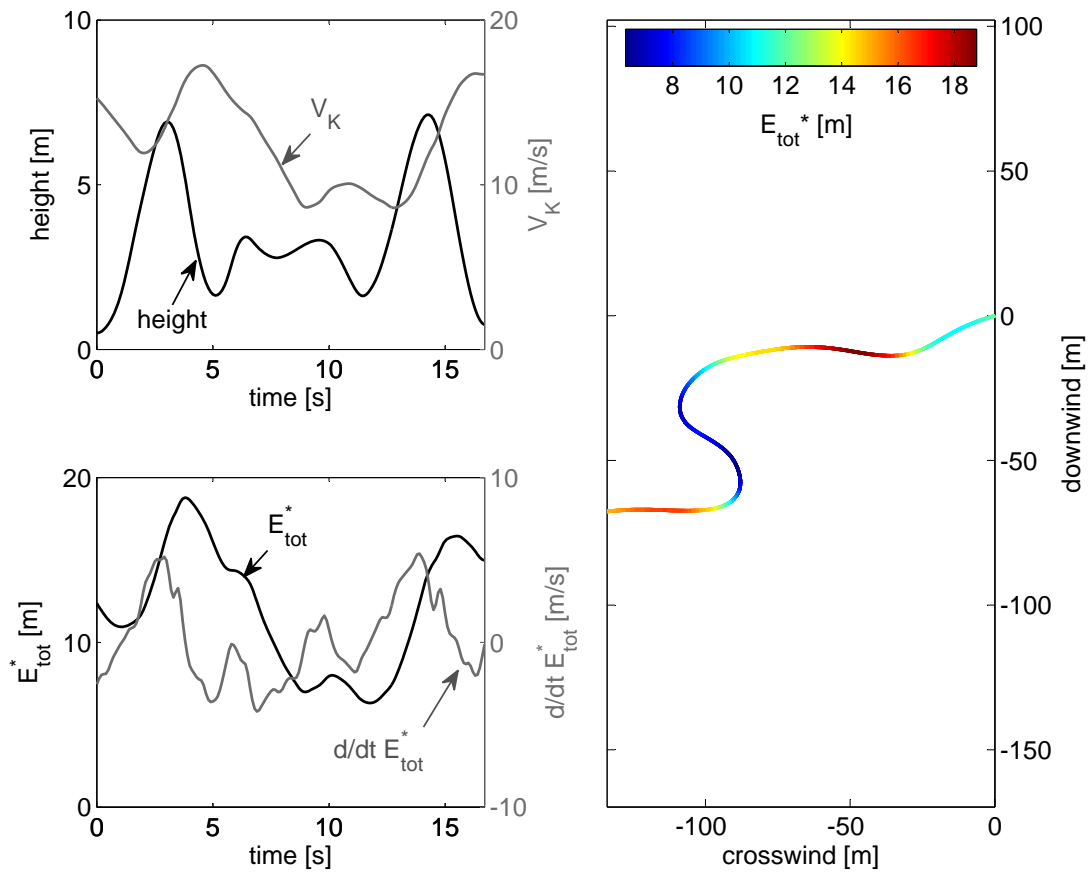
(a) Total energy
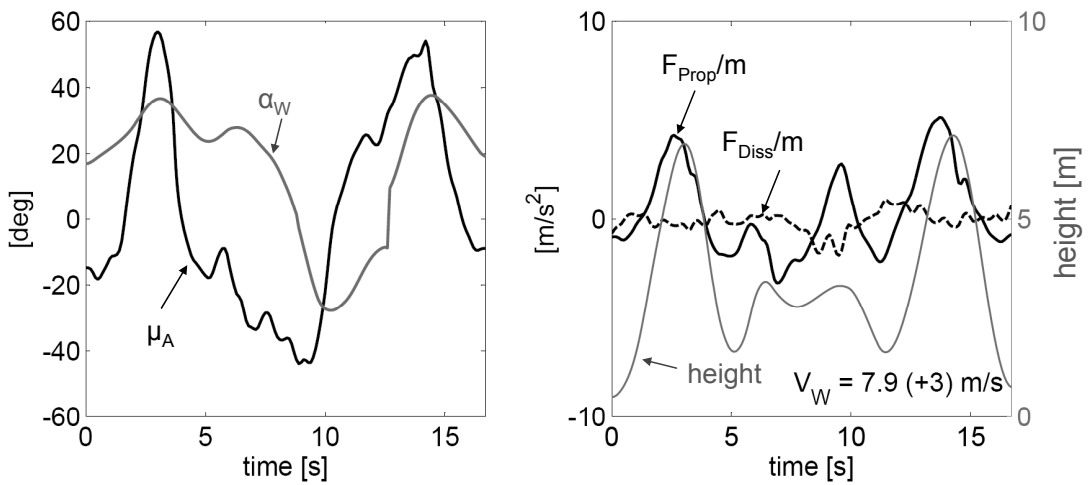
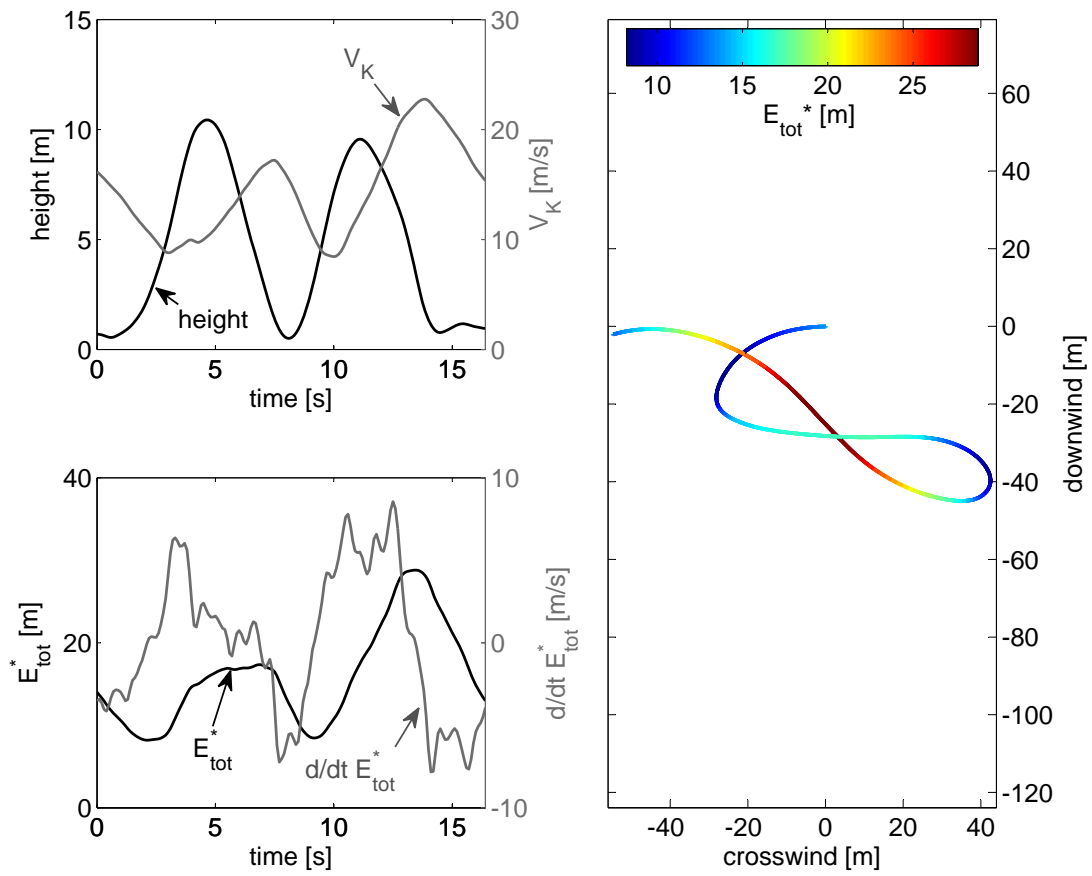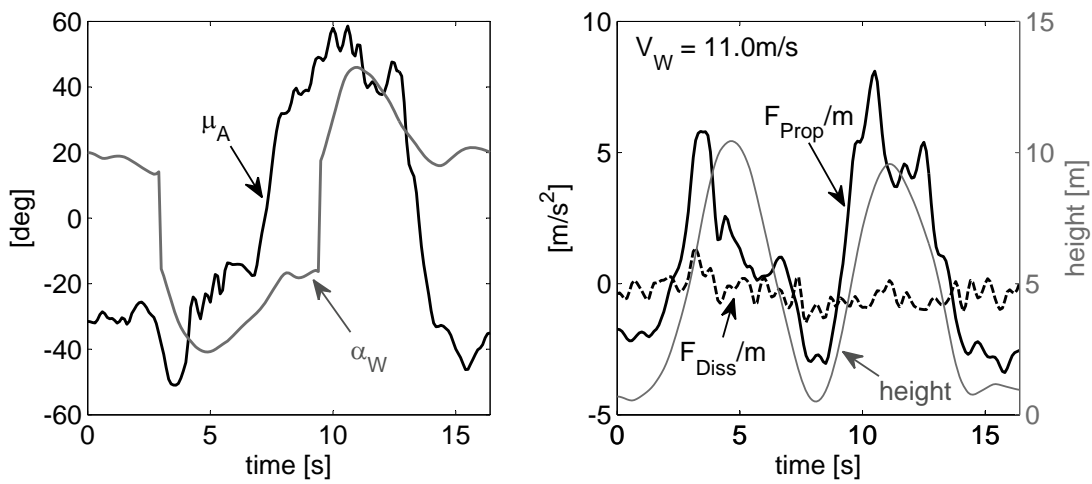(b) Aerodynamics

Figure D.22: 1m_1512_575448_575465 – Analysis
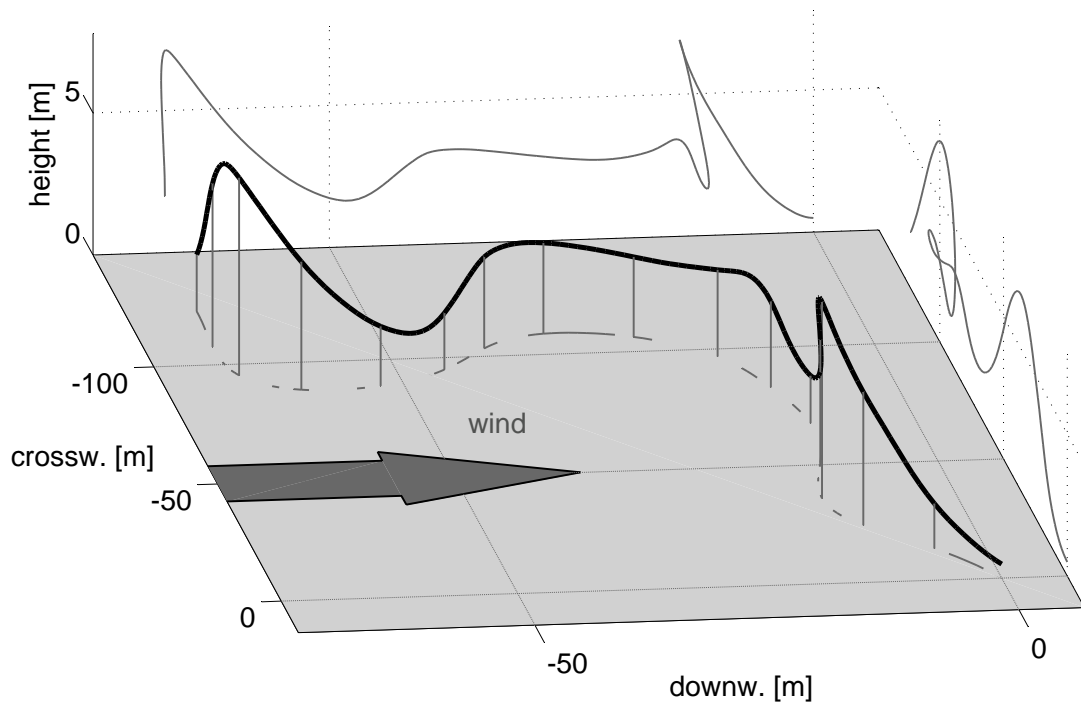
Figure D.23: 1m_1512_575448_575465 – Trajectory

(a) Total energy

(b) Aerodynamics
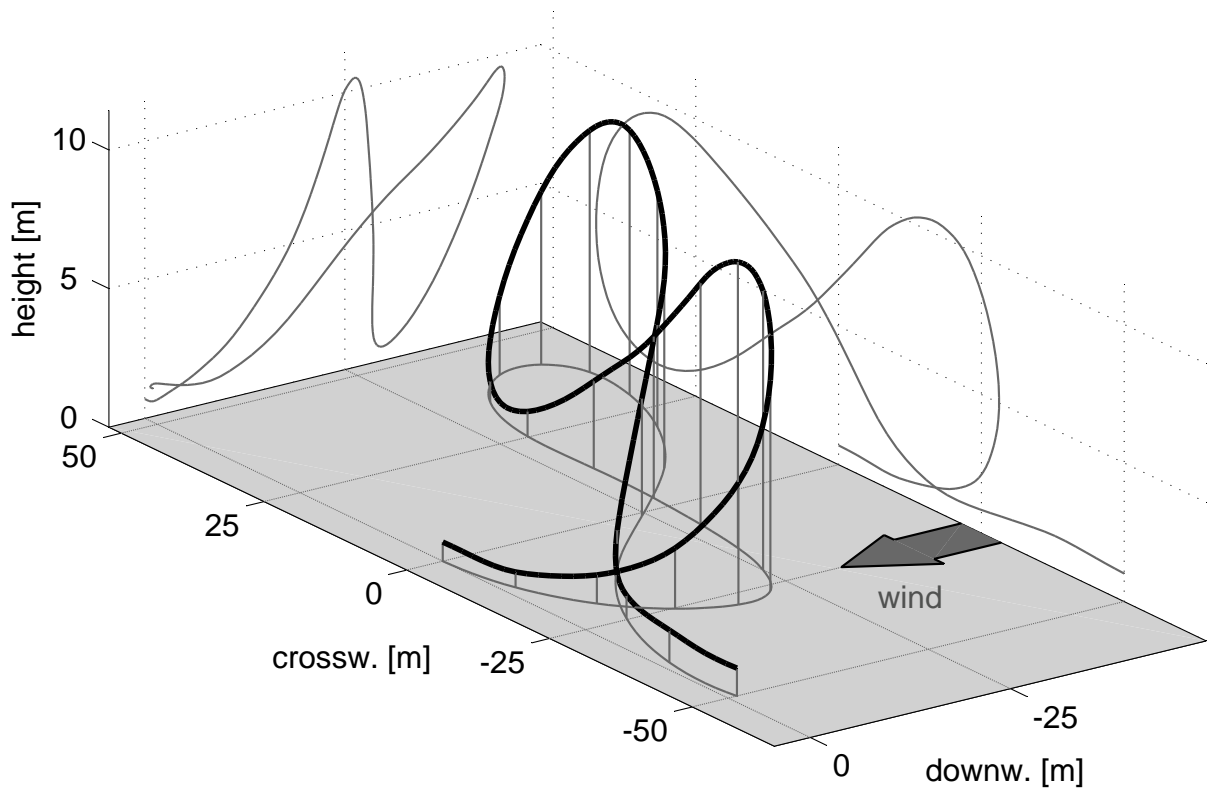
Figure D.24: 94f_1513_209330_209346 – Analysis

Figure D.25: 94f_1513_209330_209346 – Trajectory